Hydrodynamic excitation force estimation and forecasting for wave energy applications

Ollscoil
Mhá Nuad
Ollscoil na hÉireann
Má Nuad

Yerai Peña-Sanchez

A thesis submitted for the degree of
Doctor of Philosophy

Maynooth University

Faculty of Science and Engineering, Electronic Engineering Department
Centre for Ocean Energy Research

February 2020

Head of the department: Prof. Ronan Farrell
Supervisor: **Prof. John V. Ringwood**

Contents

Appendices

Abstract

Ocean waves represent a significant energy resource which can complement other renewable energy technologies during the transition to a low-carbon energy mix. Despite the large number of concepts suggested for the conversion of wave energy, none of the technologies has yet demonstrated economic viability. To this end, several solutions have been proposed in the literature, such as deploying Wave Energy Converters (WECs) in large arrays or optimal control of WECs.

The majority of WEC optimal control strategies require knowledge of the previous, current, and future excitation force acting on the device. However, for the WEC case, the excitation force is an unmeasurable quantity and, therefore, must first be estimated, based on available measurements, and then predicted in the future. The main objective of this thesis is to analyse the estimation/prediction techniques proposed for wave energy applications and to evaluate whether such techniques are ready to be applied for real WEC control strategies. To this end, a critical comparison of the available excitation force estimators is presented. Additionally, the performance of the autoregressive model as a predictor is analysed, showing that, the obtained prediction accuracy can get close to the theoretically best achievable prediction accuracy.

Based on the errors observed from the analysis of excitation force estimation/prediction techniques, a sensitivity analysis of an optimal control strategy to such errors is performed. As a result, this thesis provides an overview of the aspects which should be considered at the stage of tuning estimation/prediction techniques, to not affect the controller performance.

Since the estimation/prediction problem becomes more challenging for WEC arrays, due to the hydrodynamic interactions, an important question is whether the extra measurements from the array are sufficient to compensate for the greater complexity of the wave field. Thus, a global estimator/predictor, considering information from all the devices of the array, is developed and compared to a set of independent estimators/predictors.

Finally, this thesis introduces an identification strategy to obtain a parametric model of both the force-to-motion dynamics and/or the radiation force convolution term of the device. The strategy allows for the identification of low-order parametric models of WECs, which will simplify the implementation of optimal control strategies in real-time. Additionally, the proposed strategy is compared to the other approaches available in the literature.

Declaration of authorship

I, Yerai Peña Sanchez, declare that this thesis titled 'Hydrodynamic excitation force estimation and forecasting for wave energy applications' and the work presented in it are my own. I confirm that:

- This work was done wholly or mainly while in candidature for a research degree at this University.
- Where any part of this thesis has previously been submitted for a degree or any other qualification at this University or any other institution, this has been clearly stated.
- Where I have consulted the published work of others, this is always clearly attributed.
- Where I have quoted from the work of others, the source is always given. With the exception of such quotations, this thesis is entirely my own work.
- I have acknowledged all main sources of help.
- Where the thesis is based on work done by myself jointly with others, I have made clear exactly what was done by others and what I have contributed myself.

Date: ______________________

Signature: _________________________________

Acknowledgements

Personal

First and foremost, I would like to thank my supervisor, Professor John Ringwood, for the opportunity he gave me to become a PhD student at the COER, all the valuable advise he gave me related to my research work, technical English, as well as presentation skills, and, specially, for his support during my stay in Ireland. Additionally, I would like to thank all the staff members from the Electronic Engineering Department and, in particular, Carrie Anne Barry, Ann Dempsey, Joanne Bredin, Denis Buckley, and John Maloco for their support with any administrative or technical issue.

My warmest thanks to present and former members of the COER group, who have provided enjoyable conversations in the lab, during lunchtime, or in random pubs: Hafiz Ahsan Said, Hasana Bagnal, Jake Cunningham, Josh Davidson, Francisco Dores, Andrei Ermakov, Giuseppe Giorgi, Bingyong Guo, Fernando Jaramillo, Tom Kelly, Jost Kemper, Riccardo Novo, Francesco Paparella, Louis Papillon, Leonardo Pio Pistillo, Alix Untrau, LiGuo Wang.

Very special thanks to Marina García-Abril and Markel Penalba for all the support and help at the beginning of my PhD, to Alexis Mérigaud and Demián García-Violini for all their guidance during our collaborations and friendship, and, finally, to Christian Windt and Nicolás Faedo for their support and priceless advise during the writing of this thesis.

I would also like to thank my former lecturer Alain Ulazia, for inspiring me (like to many other students) during my bachelor degree, and encouraging me to apply for this PhD.

Last, but not least, I would like to thank my family and Olaia, for their understanding, support, and (specially) for their patience before and during my PhD.

Institutional

Gratitude is expressed to Science Foundation Ireland for supporting this work, under Grant no. 13/IA/1886, and to the Irish Marine Institute for providing the wave data fragments used in Chapter 6.

List of Figures

Nomenclature

A general convention adopted in this thesis is the use of the bold font style to represent the WEC array equivalents of the symbols used to describe the single-device case as, for example, $\boldsymbol{A}_\mathrm{r}(\omega)$ or $\boldsymbol{\chi}(t)$.

$A_\mathrm{r}(\omega)$	Matrix with radiation added mass coefficients for the considered DoFs
A_ss,B_ss,C_ss,D_ss	Matrices of the WEC dynamics SS model
$A_{\mathrm{r}_\mathrm{ss}}$,$B_{\mathrm{r}_\mathrm{ss}}$,$C_{\mathrm{r}_\mathrm{ss}}$,$D_{\mathrm{r}_\mathrm{ss}}$	Matrices of the radiation subsystem SS model
a_η	Wave amplitude
β_η	Incident wave propagation direction with respect to the x-axis
β^MM	Interpolation frequencies of the SS model identified with FOAMM
χ, $\dot{\chi}$, $\ddot{\chi}$	Position, velocity, and acceleration vectors of the device for the considered DoFs
χ_pto	Displacement of the PTO
$D_\mathrm{r}(\omega)$	Matrix with radiation damping coefficients for the considered DoFs
D_pto	PTO damping coefficient
d_b	Inter-device distance
$F(\omega)$	Fourier transform of the force vector f
$\hat{F}_\mathrm{e}(\omega)$	Vector with excitation force frequency domain coefficients for the considered DoFs
f_e	Vector with excitation force values for the considered DoFs
f_ext	Vector with external force values for the considered DoFs
f_h	Vector with hydrostatic force values for the considered DoFs
f_r	Vector with radiation force values for the considered DoFs
f_r^c	Vector with radiation convolution term force values for the considered DoFs
f_pto	Vector with PTO force values for the considered DoFs
$f_\mathrm{pto}^\mathrm{opt}$	Vector with optimal PTO force values for the considered DoFs

f_{w}	Vector with total wave force values for the considered DoFs
Φ_{d}	Diffraction velocity potential
Φ_{f}	Velocity potential of the fluid f
Φ_{i}	Incident wave velocity potential
Φ_{r}	Radiation velocity potential
g	Gravitational acceleration
γ	Peak-shape parameter of the JONSWAP spectrum
$H(\omega)$	Force-to-velocity frequency response matrix for the considered DoFs
H_{s}	Significant wave height
h_{wd}	Water depth
η	Free surface elevation
$K_{\text{r}}(\omega)$	Fourier transform of the vector k_{r}
k_{e}	Vector with the excitation force kernel for the considered DoFs
k_{r}	Vector with the radiation force kernel for the considered DoFs
κ_{η}	Wavenumber
M	Matrix with mass and inertia values for the considered DoFs
m	Mass
μ_{f}	Dynamic viscosity of the fluid f
μ_{∞}	Matrix with infinite frequency added mass coefficients for the considered DoFs
n_{b}	Number of bodies composing the array
n_{DoF}	Number of DoF
n_{dat}	Number of samples used to evaluate the error
n_{o}	Unit vector normal to a surface
n_{r}	Number of states of the radiation convolution SS approximation model
n_{ss}	Number of states of the WEC dynamics SS model
n_{tr}	Number of samples used to train the model
n_{w}	Number of samples considered in the receding window
p	Pressure
$R_{\eta\eta}$	Auto-covariance function of η

ρ	Density of a fluid
S_h	Matrix of hydrostatic stiffness coefficients for the considered DoFs
$S_{\eta\eta}$	Power spectral density of η
S_wet	Wetted surface of the device
t_caus	Causalisation time
t_del	Time delay
t_hor	Prediction horizon
T_p	Peak period
t_s	Sampling period
u_f	Flow velocity vector of the fluid f
$X(\omega)$	Fourier transform of the WEC position vector χ
$x(t)$	State vector of the WEC dynamics SS model
$x_\mathrm{r}(t)$	State vector of the radiation subsystem SS model
$y(t)$	Output vector of the WEC dynamics SS model

List of abbreviations

ACVF	Auto-CoVariance Function
AR	AutoRegressive
ARMA	AutoRegressive Moving Average
ARX	Autoregressive with eXogenous variable
AS	Assumption
ASMO	Adaptive Sliding Mode Observer
BC	Boundary Condition
BEM	Boundary Element Method
BEMIO	Boundary Element Method Input/Output
BL	Band Limited
CFD	Computational Fluid Dynamics
CNWT	CFD-based Numerical Wave Tank
CPWE	Convolution with Predicted Wave Elevation
DMS	Direct Multi-Step
DoF	Degree-of-Freedom
EKF	Extended Kalman Filter
EKFHO	Extended Kalman Filter Harmonic Oscillator
EKFPS	Extended Kalman Filter using Pressure Sensors
EnKF	Ensemble Kalman Filter
FAUIE	Fast Adaptive Unknown Input Estimation
FDI	Frequency Domain Identification
FFT	Fast Fourier Transform
FOAMM	Finite Order Approximation by Moment-Matching
HO	Harmonic Oscillator
KF	Kalman Filter
KFHO	Kalman Filter with Harmonic Oscillator

KFRW	Kalman Filter with Random Walk
LMI	Linear Matrix Inequality
LRPI	Long-Range Predictive Identification
LLS	Linear Least Squares
LS	Least Squares
LTI	Linear Time Invariant
MIMO	Multiple-Input Multiple-Output
MPC	Model Predictive Control
MSPI	Multi-Step Performance Index
nBL	non-Band-Limited
NLS	Nonlinear Least Squares
nOB	non-Optimisation-Based
NRMSE	Normalised Root Mean Square Error
NWT	Numerical Wave Tank
OB	Optimisation-Based
PADE	Pressure Acceleration Displacement Estimation
PTO	Power Take-Off
QP	Quadratic Programming
RE	Relative Error
RHE	Receding Horizon Estimation
RW	Random Walk
SDF	Spectral Density Function
SISO	Single-Input Single-Output
SS	State Space
SWL	Still Water Level
UIO	Unknown Input Observer
ULISE	Unified Linear Input & State Estimator
WEC	Wave Energy Converter

What you do makes a difference, and you have to decide
what kind of difference you want to make.

— Jane Goodall.

1

Introduction

Contents

It is well-known that access to energy is fundamental for social- and economical-welfare development, as well as for poverty mitigation [157]. Therefore, providing everyone in the world with enough energy access is an important challenge for global development. Historically, current energy supply systems have been led by fossil fuels (coal, oil, and gas), which have adverse environmental impacts. In particular, the use of such fossil fuels produce carbon dioxide (CO_2) and other greenhouse gases. Several studies suggest that the emission of such greenhouse gases is a main contributor to the global temperature increase [33]. In fact, 17 of the 18 warmest years occurred during the first 17 years of the 21st century, with an increase of almost 1°C in the average global temperature, compared to the average temperature of the 20th century [124].

Nowadays, as shown in Figure 1.1, the global primary energy consumption is around 15 times higher than at the beginning of the 20th century, which is induced, in part, by the increase in population. Additionally, the largest share of the primary energy mix (approximately 85%) is filled by natural gas, crude oil, and coal which, as mentioned before, have important negative environmental impacts. Considering the ever increasing worldwide energy demand, and the undeniable environmental impact associated with the combustion of fossil fuels, modifying the current energy mix is one of the most important challenges of this century [7]. Even including modern biofuels and hydropower, renewable energies still represent less than ten percent of the consumed primary energy, which means that there is a long way to go for a transition from a fossil-fuel-dominated energy mix to a low-carbon, renewable-dominated one [157].

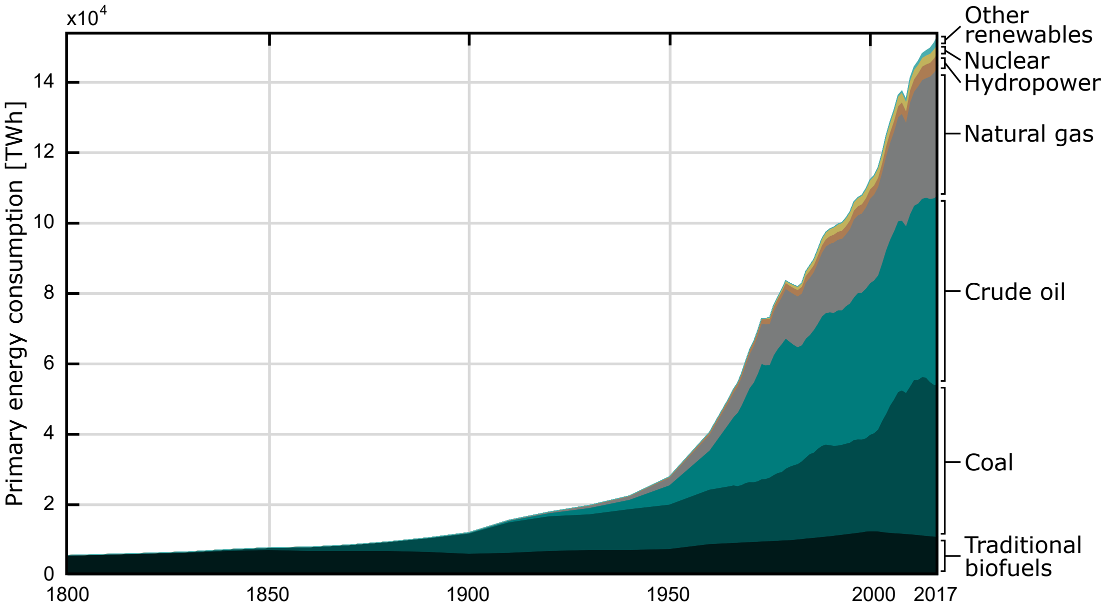

Figure 1.1: Global primary energy consumption and the energy resources, providing the energy per year, measured in TeraWatt-hours (TWh). Note that 'other renewables' represent renewable energy technologies not including hydropower and traditional biofuels (adapted from [157]).

In order to make the energy mix transition possible, investment in renewable energy technologies by public and private entities all over the planet is growing [157]. Such investment is driven, not only by global environment reasons but, to a considerable extent, by the increase in the price of the fossil fuels, which are more difficult and, therefore, more expensive to harvest (due to the limited amount of easily-accessible fossil fuels in the planet) [22].

Considering only global electricity production, the percentage contribution of renewable energy sources is higher than that considering the total primary energy consumption, with 30% of the worldwide power generation capacity and an estimate of 24.5% of the total electricity demand supply in 2016 [154]. Additionally, it is worth highlighting the contributions obtained by wind and solar Photo-Voltaic (PV) energies in different countries, since 37.6%, 27%, and 24% of electricity demand was covered by wind energy in Denmark, Ireland, and Portugal, respectively, in 2016; and 7.3%, 7.2%, and 6.4% were covered by PV solar in Italy, Greece, and Germany, respectively, in 2016 [154].

These trends in the global energy mix demonstrate the increasing contribution of modern renewable energy sources which, as shown in Figure 1.1, account for approximately 10% of the total energy consumption. However, in addition to the well-established traditional renewable energy sources, i.e. hydropower, wind, and solar energies, the contribution of other modern renewable sources in the energy mix is crucial for a transition to a low-carbon energy mix.
Among the other modern renewable energy sources, offshore renewable energy technologies, such as offshore wind (fixed and floating), tidal energy, thermal ocean energy conversion, and wave energy have the potential to significantly support traditional renewable energy sources in the future. The European wind energy association suggests that installed offshore wind power capacity could produce almost $2{\cdot}10^4$TWh annually by 2050 [117], about 13% of current energy consumption. Regarding the other offshore renewable energy systems (excluding offshore wind), the European commission estimates that the contribution could be around 10% of the total power demand in the European Union by 2050, with an annual energy production of around 350TWh [64]. In particular, since this thesis focuses on wave energy, the available resource estimate and the developed wave energy conversion technologies are introduced in the following section.

1.1 Wave Energy

Wave energy, which is yet an unexploited renewable energy source, has a higher power density than other renewable energy sources such as, for example, solar or wind energy [34]. Several studies in the literature estimated the global wave energy resource to be around $3.2{\cdot}10^4$TWh in [40, 118] or $1.8{\cdot}10^4$TWh in [82], which would cover 20% or 12% of current global energy consumption, respectively. However, as shown in Figure 1.2, a large proportion of the wave energy resource is located in remote areas where, due to the long distance between energy conversion and consumption areas, deployment of Wave Energy Converter (WEC) farms may be technically challenging. Additionally, recent studies [152, 108] show that part of the estimated wave energy resource may stem from storms, which are, usually, not exploitable. In fact, WECs are designed to generate energy within an operational space, usually defined by a specific range of wave heights, and, beyond such operational space, the strategy is to protect the WEC to avoid any critical damage. Finally, analyses of the trend of wave characteristics over the 20th century in different locations suggest that the wave energy resource is growing, in particular during the last decades, which may also cause more non-exploitable extreme events [175, 146].

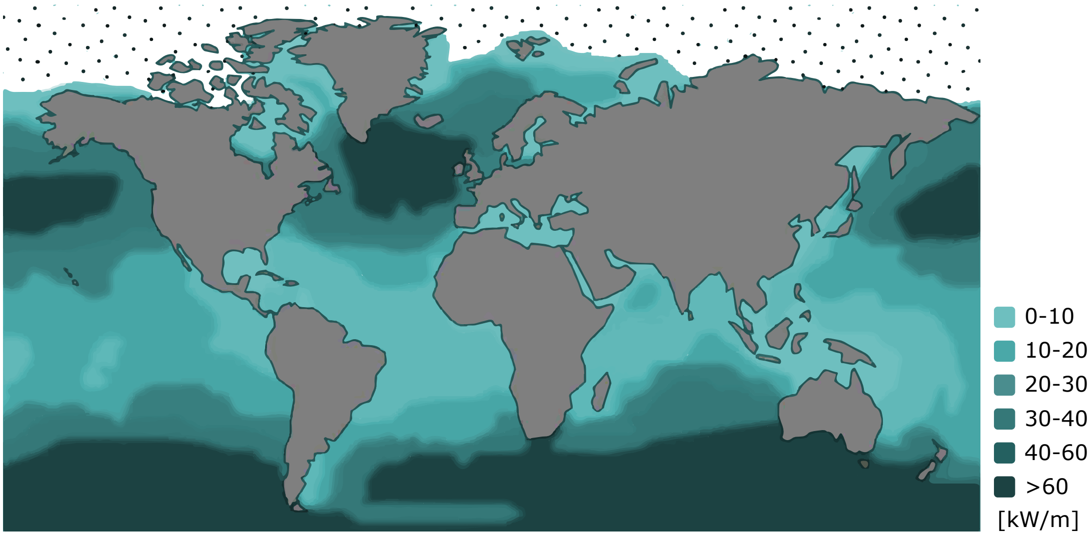

Figure 1.2: Approximation of the average annual wave energy (adapted from [87]).

Due to the uncertainty of the possible deployment areas, the early stage of development of the wave energy industry, and the uncertainties of its evolution in the future, the real exploitable wave energy resource potential is, as yet, unpredictable. Thus, future developments of the wave energy industry in the near future will define the position of wave energy within the global energy mix.

1.1.1 Wave Energy Converters

At this early stage of development, there is no profitable, standard WEC geometry and, therefore, different developers, researchers, or inventors have proposed several WEC concepts [53]. Given the large number of WEC concepts, different classifications have been proposed in the literature to organise the devices into groups, such as by their dimension and orientation with respect to the incoming waves, their working principle, or their proximity to the coastline.

Based on the dimension and orientation of WECs with respect to the incoming waves [38], as shown in Figure 1.3, three type of devices can be distinguished: point absorbers, attenuators, and terminators. Point absorbers are small devices with respect to the wavelength and are, in general, multi-directional devices. On the contrary, attenuators and terminators are large devices (similar to, or greater than, a wavelength) whose main dimensions are aligned with the waves direction, in the case of attenuators, and facing the waves, in the case of terminators.

A further classification is possible, based on the proximity of the device to the coastline [107]. Onshore devices refer to WECs located on the coastline, while WECs installed in the ocean are known as near-shore devices, when they are located close to shore

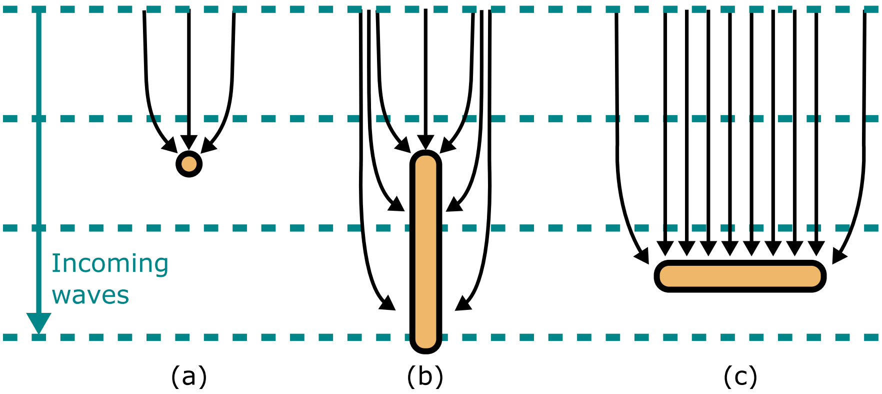

Figure 1.3: Different WEC configurations depending on their dimension and orientation with respect to the incoming waves: (a) is a point absorber, (b) an attenuator, and (c) a terminator. Adapted from [123].

and use the seabed as the reference point for motion, or as offshore devices, if located far from the coastline (water depths of about 100 m) and using loose mooring lines. Based on the working principle [107], four different groups can be distinguished: wave-activated floating bodies, pressure differential devices, overtopping devices, and impact devices. Power capture of wave-activated floating bodies can be induced either by a relative motion between two or more bodies, as shown in Figure 1.4(a), or by an absolute motion between the floating body and a fixed reference, illustrated in Figure 1.4(d). Pressure differential devices can be divided into two groups: Archimedes effect converters and Oscillating Water Columns (OWCs). Archimedes effect converters are submerged point absorbers, typically fixed to the seabed, that use the pressure difference generated between the wave crests and troughs over the device, shown in Figure 1.4(b). In OWC devices, as can be observed from Figure 1.4(f), waves force the water column in the bottom of the chamber to oscillate which, in turn, moves the air trapped in the chamber, spinning an air-turbine located at the top-end of the chamber. For overtopping devices, shown in Figure 1.4(c), ocean waves break on a ramp, capturing the water of the waves in a reservoir and, using the potential energy of the captured water, a turbine, located at the bottom of the floating structure, spins. Finally, impact devices or Oscillating Wave Surge Converters (OWSCs) are flaps, positioned perpendicular to the wave direction, which move back and forth due to wave impact, as illustrated in Figure 1.4(e).

Different WEC prototypes have been developed based on the WEC working principles shown in Figure 1.4. Remarkable examples comprise the Pelamis device [89] for the attenuator of Figure 1.4(a), or the Archimedes Wave Swing [177] for the pressure differential point absorber shown in Figure 1.4(b). It is also worth mentioning that, based on the Pelamis device, the Blue Star and the Blue Horizon devices (from Mocean Energy [43]) are two of the leading WEC concepts in the UK. Overtopping devices,

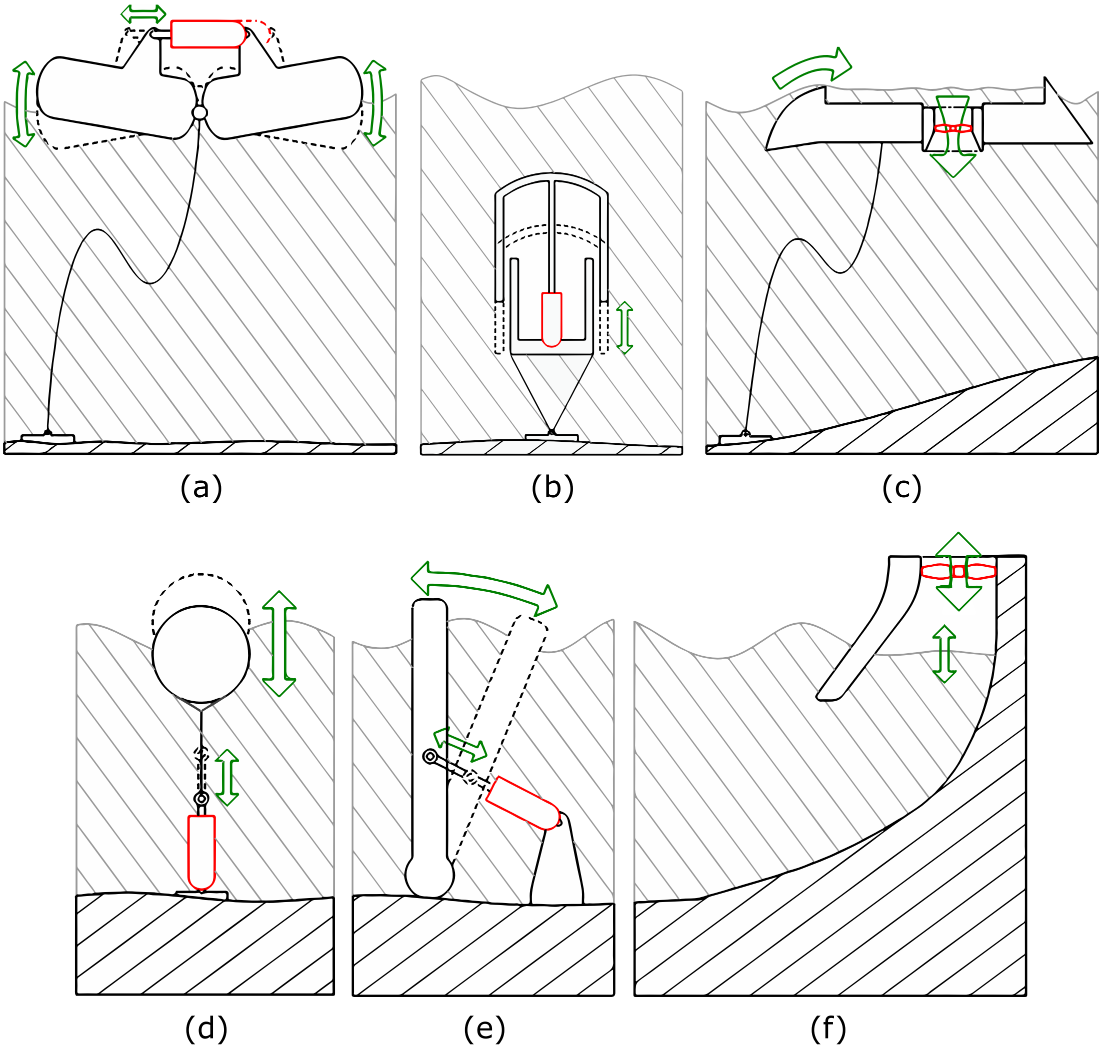

Figure 1.4: Different types of WECs: (a) is an attenuator, (b) a pressure differential point absorber, (c) an overtopping device, (d) a point absorber, (e) an OWSC, and (f) an OWC. Note that (a,b,c) represent offshore devices, (d,e) near-shore devices, and (f) an onshore device. The red part of each subfigure represents the PTO system.

illustrated in Figure 1.4(c), can be located offshore or onshore, such as the Wavedragon [98] and the TAPCHAN device [111], respectively. Figure 1.4(e) illustrates an OWSC located near-shore, which rotates around a reference point on the seabed, such as the Oyster device [183], but it can also be floating and deployed offshore, such as the Langlee concept [141]. The HPA shown in Figure 1.4(d), located near-shore as the Seabased device [81], can also be located offshore, e.g. the OPT Powerbuoy [112]. While the near-shore HPA uses the seabed as its reference point, offshore HPAs usually react against themselves (since are composed of two bodies). Finally, the onshore OWC shown in Figure 1.4(f), such as the Mutriku power plant [174], can also be floating and be deployed offshore, such as the Sparbuoy [79].

Even though the first WEC was patented in 1799 in Paris [158], the wave energy industry, as it is known nowadays, started to develop with the energy crisis originated as a consequence of the oil crisis in 1973. In fact, oil price and wave energy industry activity are strongly correlated, as can be observed from Figure 1.5, where both the number of wave energy patents and oil price are shown. Interestingly, in the 1980s, oil price became affordable again and, therefore, the number of patents decreased, as an indicator for a diminished interest in wave energy research. However, since late 1990s, driven by climate change awareness, governments, companies, and researchers are focusing on renewable energy sources, increasing the number of wave energy patents. Currently, there are over 1000 wave energy patents in the world. The interested reader is referred to [10] for a thorough review of the historical development of WECs.

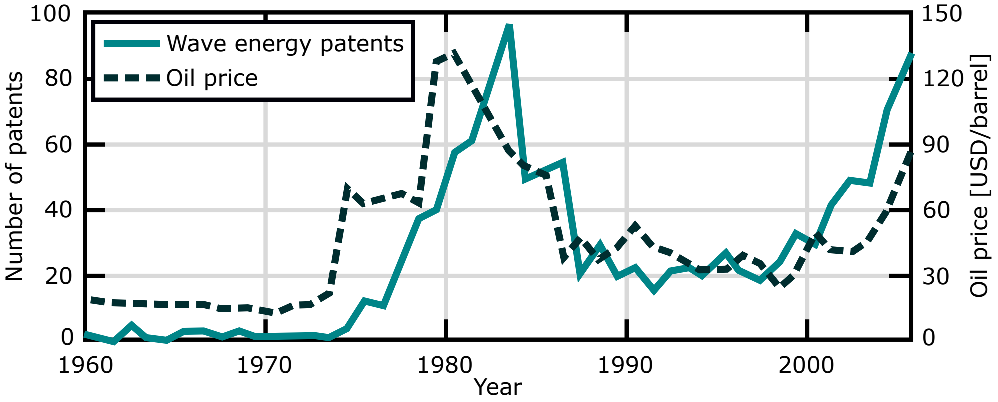

Figure 1.5: Number of wave energy patents and oil price (adapted from [18]).

Despite the number of prototypes suggested so far, none of them has shown commercial viability yet, and a significant number of important wave energy companies went into bankruptcy (e.g. Pelamis, Wavestar, or Aquamarine). However, the reasons that forced wave energy companies into bankruptcy may be their development strategy, rather than their specific technologies. Due to investors pressure, the companies installed their full-scale (or close to full-scale) prototypes in the ocean as soon as possible, which requires large financial investments, without fully developing the economical viability, i.e. without ensuring that their prototypes were cost-effective (the interested reader is referred to [181] for a comprehensive definition of the different technology development methodologies). In view of the economic bankruptcy of previous companies, several wave energy companies, like Mocean Energy [43] or Corpower Ocean [42], prioritise numerical modelling/optimisation and small-scale tank testing, to increase the likelihood that the full-scale device (to be deployed in the ocean) is economically viable.

To reduce the cost of energy associated with wave energy, different aspects of WECs need to be improved before deploying new full-scale prototypes in the ocean. In particular, three general challenges can be distinguished:

Maximising energy extraction: In addition to optimising the WEC configuration, such as the geometry or the operational Degrees of Freedom (DoF), which has been a subject of study since the beginning of the wave energy development, WECs can be controlled to maximise the extracted energy. Optimal control of WECs is crucial since, in theory, it ensures maximal energy extraction at every time instant, which should reduce the electricity generation cost. Additionally, the design of a specific Power Take-Off (PTO) system that allows for an efficient conversion from mechanical to electric energy is vital, since it strongly affects the final cost of the produced energy.

Deploy WECs in arrays: Given the harsh conditions of the offshore environment, construction, deployment, and maintenance of WECs is difficult and expensive. By deploying WECs in large arrays, some of the infrastructural costs (such as moorings or electrical connections) are shared within the devices of the array, which reduces the cost per device, diminishing the total cost of the generated electricity. Array configurations also need to be optimised, since the interactions between devices can be constructive or destructive depending on several aspects such as the array layout, inter-device distances, control strategy, etc.

Survivability: WECs have to survive in extreme conditions, such as storms. Therefore, a survivability strategy that minimises structural damage under such harsh conditions is essential to reduce the total cost. Several survivability strategies can be found in the literature as, for example, locking the PTO to prevent motion or life-extending control strategies [30].

Even though these specific issues individually affect the final cost of energy, they cannot be analysed independently when developing a WEC concept, since some of the issues are strongly connected. For example, the device geometry cannot be optimised without considering the controller, since the optimal shape of the geometry might differ when considering different control strategies, as shown in [180]. At the same time, the chosen control strategy is strongly affected by the considered PTO system, due to its speed capacities, constraints, etc. Similarly, a WEC configuration (dimensions, PTO system, controller, etc.) cannot be optimised without considering that devices will be deployed in an array since, depending on the inter-device distance of the WECs composing the array, the interactions can be constructive or destructive, which may affect the WEC configuration (mostly the controller). In particular, this thesis is focused on aspects related to maximising energy extraction and deployment in arrays and, therefore, survivability analysis is beyond the scope of this thesis.

1.2 Motivation of the thesis

To determine the optimal control input of WECs, the majority of energy maximising control strategies require knowledge of the instantaneous and future excitation force acting on the device (the force that WECs experience due to waves) [155], which is one of the inputs to the WEC system. However, excitation force is an unmeasurable quantity for non-fixed floating bodies (such as most WECs) and, therefore, needs to be estimated based on other related measurable quantities, such as device motion. Once the excitation force is estimated, if required, prediction strategies can be applied in order to supply the controller with future information of the excitation force. Given the large number of excitation force estimation/prediction strategies available in the literature [138], knowledge of their limitations as well as relative weaknesses and strengths is necessary to know which strategy is best suited for a specific scenario, or WEC configuration. Thus, by optimising the obtained excitation force estimate/prediction, optimal controller performance can be obtained, which, as pointed out in Section 1.1, is vital to reduce the cost involved with generating electricity.

Similarly, since WECs are likely to be deployed in arrays to reduce the final cost of the converted energy, analysing how the interactions between the devices of the array affect estimator/predictor performance is crucial, in order to ensure that, in the array case, the performance of the WEC array controller is optimal.

An additional challenge for optimal control strategies is the computational effort. The optimisation procedure associated with most of the optimal WEC controllers [45], in addition to the computational burden required by the estimation/prediction processes, can lead to computational requirements that exclude the real-time application of such control strategies. Depending on the controller, different methods can be applied to reduce the computational requirements [45]. A general approach consists of approximating the non-parametric radiation convolution term of Cummins' equation [35] (used to describe the WEC dynamics) using a suitable parametric model[1]. Several strategies can be found to obtain such a convolution term approximation; however, an ideal radiation convolution term approximation strategy should, apart from obtaining a good accuracy that monotonically decreases when increasing the order of the final model, preserve the physical properties of the radiation convolution term [47]. Since none of the strategies currently available in the literature satisfies such ideal characteristics, a development of a new identification application that fulfils those features is undertaken as part of the work presented in this thesis.

---

[1] Note that this is often required, since most of the modern control strategies are based on the availability of a state-space description of the system under analysis [45].

1.3 Objectives and contributions of the thesis

The main objectives and novel contributions of this thesis are summarised as follows:

1 The main purpose of the present thesis is to critically analyse the existing excitation force estimation and prediction strategies, and determine which of the strategies can be used for accurate real-time excitation force estimation/prediction for control purposes. In order to do so, the contributions regarding different excitation force estimation/prediction strategies are summarised as follows:

- **1.1** In order to analyse the different excitation force estimation and prediction strategies, it is of paramount importance to draw a complete picture of the strategies available in the literature. To this end, a comprehensive review of the state-of-the-art excitation force estimation and prediction techniques is first carried out. Work published in [138, 139].
- **1.2** Given the large number of excitation force estimators available in the literature, a critical comparison is performed to determine the relative strengths and weaknesses of the different strategies. Work published in [138].
- **1.3** Additionally, the difficulties associated with excitation force estimation using real motion measurements are shown, along with the results from real-time excitation force estimation obtained from physical wave tank experiments. Work published in [74].
- **1.4** Since the AutoRegressive (AR) model is found to be one of the simplest and most accurate predictors for wave energy applications by several researchers, a thorough analysis of different aspects of the AR model is performed, in order to determine its capabilities for excitation force or wave elevation prediction. Work published in [139].
- **1.5** It should be noted that different estimation/prediction errors can affect differently, and have more or less impact on, the performance achieved by the controller. In order to understand how different estimation and prediction errors affect the performance obtained by an optimal control strategy and, thus, to be able to determine which estimation/prediction strategies are the most convenient for control purposes, a sensitivity analysis of an optimal control strategy to estimation and prediction errors is shown. Work published in [50].

2 A further objective of this thesis is to analyse if, for excitation force estimation/prediction in WEC arrays, knowledge from all the bodies in the array is enough to account for the more complex wave field, caused by the radiated and diffracted waves from all the devices. To this end, an estimator/predictor that uses measurements from all the devices of the array is developed, and compared to a set of independent estimators/predictors that consider only measurements local to each device. Work published in [138].

3 Given the importance of radiation convolution term approximation strategies to obtain accurate low-order parametric models for control purposes, several objectives and contributions regarding such strategies can be found in this thesis:

3.1 It is important that the approximation strategy, used to identify the radiation convolution term, in addition to obtain accurate approximations that monotonically decrease when increasing the order of the parametric model, preserves the physical properties of the original system. Since, in the literature, there is no specific strategy that guarantees all the previously mentioned characteristics, a new identification strategy is introduced. Additionally, a MATLAB toolbox, termed Finite Order Approximation by Moment-Matching (FOAMM), that systematically applies such approximation strategy in a user-friendly fashion is developed. Work published in [47, 48, 134].

3.2 Since different researchers use different approximation strategies to obtain the parametric model of the convolution term, it is of interest to see the differences between all the available applications (including FOAMM), for which a comparison of the available radiation convolution term approximation applications is performed. Work published in [47, 135, 136].

3.3 Given the interaction between the devices comprising WEC arrays, the number of radiation convolution terms grows exponentially with the number of bodies, which significantly increases the computational burden associated with the simulation or the control of WEC arrays. To avoid such an issue, the moment-matching-based approximation strategy is extended to include the radiation convolution terms of all the devices comprising the array in a single parametric model. Work published in [49, 137].

4 Finally, as an additional contribution, the inconsistency between the results reported in two studies in the literature, with respect to the performance of AR and the AutoRegressive Moving Average (ARMA) models for prediction in wave energy applications, is clarified. Work published in [140].

1.3.1 List of publications

1.3.1.1 Conference publications

- **Y. Peña-Sanchez**, J. V. Ringwood, *"A Critical Comparison of AR and ARMA Models for Short-term Wave Forecasting"*, Proceedings of the 12th European Wave and Tidal Energy Conference (EWTEC), Cork, Ireland, pages 961–(1-6), 2017.
- **Y. Peña-Sanchez**, N. Faedo, J. V. Ringwood, *"Hydrodynamic Model Fitting for Wave Energy Applications Using Moment-Matching: A Case Study"*, Proceedings of the 28th International Offshore and Polar Engineering Conference (ISOPE), Sapporo, Japan, pages 641–648, 2018.
- N. Faedo, **Y. Peña-Sanchez**, J. V. Ringwood, *"Moment-Matching-Based Identification of Wave Energy Converters: the ISWEC Device"*, Proceedings of the 11th IFAC conference on Control Applications in Marine Systems (CAMS), Opatija, Croatia, pages 189–194, 2018.
- N. Faedo, **Y. Peña-Sanchez**, J. V. Ringwood, *"Passivity Preserving Moment-Based Finite-Order Hydrodynamic Model Identification for Wave Energy Applications"*, Proceedings of the 3rd International Conference on Renewable Energies Offshore (RENEW), Lisbon, Portugal, pages 351–359, 2018.
- **Y. Peña-Sanchez**, N. Faedo, J. V. Ringwood, *"A Critical Comparison Between Parametric Approximation Methods for Radiation Forces in Wave Energy Systems"*, Proceedings of the 29th International Offshore and Polar Engineering Conference (ISOPE), Honolulu, Hawaii, pages 174–181, 2019.
- **Y. Peña-Sanchez**, N. Faedo, J. V. Ringwood, *"Moment-Based Parametric Identification of Arrays of Wave Energy Converters"*, Proceedings of the 2019 American Control Conference (ACC), Philadelphia, EEUU, pages 4785–4790, 2019.
- **Y. Peña-Sanchez**, N. Faedo, M. Penalba, G. Giorgi, A. Mérigaud, C. Windt, D. Garcia Violini, L. Wang, J. V. Ringwood, *"Finite-Order hydrodynamic Approximation by Moment-Matching (FOAMM) toolbox for wave energy applications"*, Proceedings of the 13th European Wave and Tidal Energy Conference (EWTEC), Naples, Italy, pages 1448–(1-9), 2019.
- N. Faedo, **Y. Peña-Sanchez**, G. Giorgi, J. V. Ringwood, *"Moment-Matching-Based Input-Output Parametric Approximation for a Multi-DoF WEC Including Hydrodynamic Nonlinearities"*, Proceedings of the 13th European Wave and Tidal Energy Conference (EWTEC), Naples, Italy, pages 1449–(1-10), 2019.

- N. Faedo, **Y. Peña-Sanchez**, J. V. Ringwood, *"Parameterisation of Radiation Forces for a Multiple Degree-of-Freedom Wave Energy Converter Using Moment-Matching"*, Proceedings of the 29th International Offshore and Polar Engineering Conference (ISOPE), Honolulu, Hawaii, pages 166—173, 2019.
- N. Faedo, D. Garcia Violini, **Y. Peña-Sanchez**, J. V. Ringwood, *"Optimisation-VS non-Optimisation-based Energy-Maximising Control for Wave Energy Converters: A Case Study",* European Control Conference (ECC), Saint Petersburg, Russia, pages 843–848, 2020.
- D. Garcia Violini, **Y. Peña-Sanchez**, N. Faedo, C. Windt, J. V. Ringwood *"LTI energy-maximising control for the Wave Star wave energy converter: Identification, design, and implementation"*, IFAC World Congress, Berlin, Germany, 2020.

1.3.1.2 Journal publications

- **Y. Peña-Sanchez**, A. Mérigaud, J. V. Ringwood, *"Short-Term Forecasting of Sea Surface Elevation for Wave Energy Applications: The Autoregressive Model Revisited"*, IEEE Journal of Oceanic Engineering, 45(2), 462–471, 2018.
- **Y. Peña-Sanchez**, M. García-Abril, F. Paparella, J. V. Ringwood, *"Estimation and forecasting of excitation force for arrays of wave energy devices"*, IEEE Transactions on Sustainable Energy, 9(4), 1672–1680, 2018.
- N. Faedo, **Y. Peña-Sanchez**, J. V. Ringwood, *"Finite-order hydrodynamic model determination for wave energy applications using moment-matching"*, Ocean Engineering, 163, 251–263, 2018.
- **Y. Peña-Sanchez**, C. Windt, J. Davidson, J. V. Ringwood, *"A Critical Comparison of Excitation Force Estimators for Wave Energy Devices"*, IEEE Transactions on Control Systems Technology (early access), 2019.
- N. Faedo, **Y. Peña-Sanchez**, J. V. Ringwood, *"Parameterisation of radiation forces for multiple degree-of-freedom wave energy converters using moment-matching"*, International Journal of Ocean and Polar Engineering (IJOPE), in press, 2019.
- N. Faedo, **Y. Peña-Sanchez**, J. V. Ringwood, *"Receding-horizon energy-maximising optimal control of wave energy systems based on moments"*, IEEE Transactions on Sustainable Energy (early access), 2020.
- D. Garcia Violini, **Y. Peña-Sanchez**, N. Faedo, J. V. Ringwood, *"An energy-maximising Linear Time Invariant Controller (LiTe-Con) for wave energy devices"*, IEEE Transactions on Sustainable Energy (early access), 2020.

- N. Faedo, **Y. Peña-Sanchez**, J. V. Ringwood, *"Parametric representation of arrays of wave energy converters for motion simulation and unknown input estimation: a moment-based approach"*, Applied Ocean Research, 98, 102055, 2020.
- D. Garcia Violini, **Y. Peña-Sanchez**, N. Faedo, C. Windt, J. V. Ringwood, *"Experimental implementation and validation of a broadband LTI energy-maximising control strategy for the Wavestar device"*, submitted to IEEE Transactions on Control Systems Technology, 2020.

1.4 Thesis layout

The thesis consists of eight additional chapters, laid out as explained in the following part of this section:

- Chapter 2 introduces the theory behind the concepts used throughout this thesis to describe the wave-structure hydrodynamic interaction. To this end, the theoretical background of ocean waves, and how to (numerically) generate regular or irregular waves, is explained. Then, the fundamental aspects of potential flow theory are described in detail, along with the well-known Cummins' equation (for both a single device or a WEC array). Finally, the state-space representation of the radiation subsystem and the complete WEC dynamics, which are used throughout the thesis, are defined.
- Chapter 3 first explains why excitation force estimation and prediction is necessary for optimal control of WECs. Then, the chapter provides a comprehensive literature review of the excitation force estimation and forecasting strategies available in the literature, and highlights some of the gaps in the literature that this thesis aims to fill.
- Chapter 4 introduces the moment-matching-based approximation strategy proposed in this thesis to identify a state-space representation (introduced in Chapter 2) of the radiation subsystem and the WEC dynamics. Then, a comparison of the proposed strategy against competing available applications is provided and, finally, an extension of the moment-matching-based strategy to account for multiple-input multiple-output systems (such as WEC arrays) is described.
- In Chapter 5, all the excitation force estimation strategies available in the literature (reviewed in Chapter 3) are compared. Additionally, the results for real-time excitation force estimation carried out using physical wave tank data, obtained using one of the best estimators of the comparison, are shown.

- Chapter 6 provides a detailed analysis of the capabilities of the AR model since, from the review of Chapter 3, the AR model is found to be one of the simplest and more accurate predictors for wave energy applications. To this end, a comparison is initially shown that addresses the inconsistency between the results reported by two different researchers with respect to the relative performance of AR and ARMA models for wave elevation prediction. Then, the AR model is compared to two different theoretical accuracy limits of the prediction, in order to analyse the efficiency of the AR model as a predictor for wave energy applications.
- Chapter 7 shows the estimation and forecasting results for WEC arrays obtained using one of the best estimators, from the comparison of Chapter 5, along with the AR model for forecasting, analysed in Chapter 6. A comparison is performed to assess if the extra information from all the devices in the array is sufficient to compensate the more complex wave field resulting from the interactions between the devices.
- In Chapter 8, a sensitivity analysis of a WEC optimal control strategy, to excitation force estimation and prediction errors, is provided. To this end, information about the possible estimation/prediction errors, obtained from the analyses of Chapters 5 and 6, is used.
- Finally, the conclusions of the thesis are drawn in Chapter 9, along with a summary and a discussion on the contributions and results, as well as a brief discussion of future work.

2

WEC modelling

Contents

As mentioned in the introduction, one of the objectives of this thesis is to analyse the wave excitation force estimation strategies available. Since WEC systems are yet on an early-stage of development, the majority of excitation force estimation (and control) strategies in the literature are based on linear hydrodynamic models of WECs. On the contrary, several researchers have reported that, while linearised hydrodynamic models represent accurately (to some extent) WEC systems when no control is applied, such linear models are not representative any more under WEC control conditions[1] [77]. Therefore, considering that the estimation (and prediction) of the excitation force is carried out to be used by the WEC controller, and that under control conditions

---

[1] This is because control strategies tend to maximise WEC motion, while small device motion is one of the linear potential flow assumptions (further explained in Section 2.2.2).

linear models do not represent accurately the WEC system, one could argue that using linear models to describe the excitation force estimators is not sensible.

Nevertheless, at this stage, it is important to assess the performance of the estimation techniques using linear WEC models, before implementing nonlinear models for excitation force estimation. An additional reason for the researchers to use linear models for estimation is that, while no general nonlinear description of WECs can be found in the literature (since the descriptions are device-specific), the linear Cummins' equation (introduced in Section 2.2.3) can be considered as a general linear description of WECs (since is widely used by the majority of the authors). Therefore, and in order to assess such state-of-the-art estimation strategies, this chapter introduces the linear Cummins' equation, which is the model considered in this thesis and also commonly by other researchers in the literature. Additionally, the sets of assumptions the linearisation is based on, along with the linearisation process, are introduced, in order to better understand the limitations of the final (linear) WEC model.

Note that the author do not discard the idea of using linear WEC models for the estimators in a real scenario, since the sensitivity of the estimator to model uncertainties has never been addressed yet (to the author's knowledge) and, thus, it is unknown the effects that such combination could have on the controller performance. Additionally, it should be noted that, when considering nonlinear WEC models, the concept of excitation force may not hold any more, since superposition is a linear concept and, therefore, the forces acting on the device may not be divisible. However, such issues are out of the scope of this thesis, since the objective is to analyse the excitation force estimation problem from a linear perspective, in order to ease the transition to the nonlinear estimation (for future work).

2.1 Ocean waves

Ocean waves, generated mainly by wind activity, can be produced in many different ways. The simplest waves, from a signal-complexity point of view, are monochromatic waves, described by a sinusoidal signal with a single (constant) amplitude and frequency. On the contrary, an example of a more complex characterization of ocean waves would be three-dimensional, irregular, fully nonlinear waves. Since this thesis focuses on investigating WEC devices working in power production mode, only those waves that are of importance for power production are considered. Under such assumptions, extreme, highly nonlinear waves are not considered in this work. In fact, the wave resource, associated with operational conditions, can be described, in most cases, by linear wave theory [126].

It should be noted that, from now on, the dependence on the independent variable (as, for example, t or x) is dropped when its clear from the context.

2.1.1 Linear wave theory

Linear wave theory, or Airy's wave theory, is often used to characterise the propagation of waves on the free-surface [126]. For a better understanding of the definition of Airy's wave theory, Figure 2.1 presents a schematic of the wave characteristics, where a_η is the wave amplitude, $H_\eta = 2a_\eta$ the wave height, λ_η is the wavelength and h_{wd} the water depth. The coordinate system considered in this thesis is as in Figure 2.1, where the waves propagate in the positive sense of the x-axis, the positive sense of the y-axis is out of the page, and the z-axis is perpendicular to the free-surface, with the origin on the undisturbed free surface, or the Still Water Level (SWL).

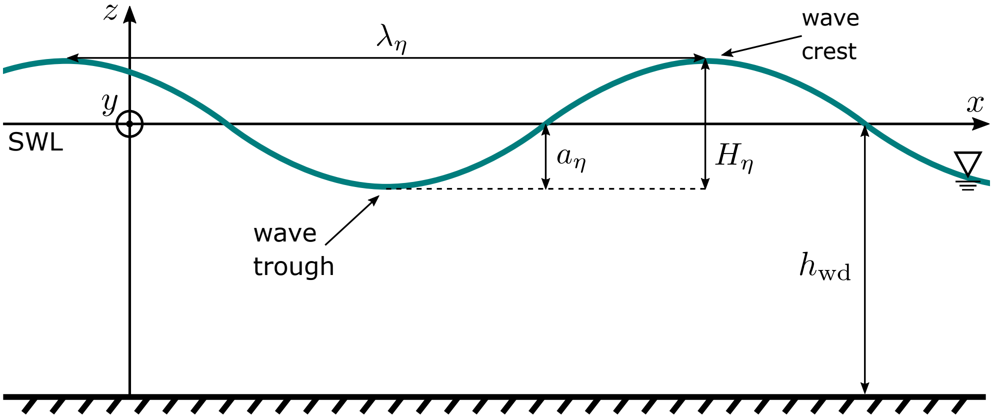

Figure 2.1: Schematic of the wave characteristics.

Airy's wave theory assumes deep water depths ($h_{\text{wd}} > 0.5\lambda_\eta$), and that the wave height H_η is small compared to the wavelength λ_η. Additionally, it is assumed that the fluid flow is inviscid, incompressible, and irrotational, assumptions that are recalled and better explained in Section 2.2.2. Thus, the free surface elevation η can be defined for monochromatic waves as

$$\eta(x,y,t) = \text{real}(a_\eta e^{\omega_\eta t - \jmath\kappa_\eta(x\cos\beta_\eta + y\sin\beta_\eta)+\phi_\eta}), \tag{2.1}$$

or, equivalently as

$$\eta(x,y,t) = a_\eta \cos\left(\omega_\eta t - \jmath\kappa_\eta\left(x\cos\beta_\eta + y\sin\beta_\eta\right) + \phi_\eta\right), \tag{2.2}$$

where the operator real $(\{\cdot\})$ (and imag $(\{\cdot\})$) refer to the real (and imaginary) part of $\{\cdot\}$, ω_η is the oscillating frequency of the wave (in rad/s), $\jmath$ the imaginary unit (which satisfies $\jmath^2 = -1$), β_η the propagation direction of the incident wave (with respect to the positive x-axis), ϕ_η the wave phase and κ_η is the wavenumber, which is related to the wave frequency ω_η via the dispersion relation

$$\frac{\omega_\eta^2}{g} = \kappa_\eta \tanh\left(\kappa_\eta h_{\text{wd}}\right), \tag{2.3}$$

which, since deep water depth is assumed, can be simplified to $\omega_\eta^2/g = \kappa_\eta$, where g is the gravitational acceleration.
However, since regular waves do not represent real ocean wave scenarios, irregular waves are commonly employed in the literature. The next subsection details the mathematical description of the irregular waves employed in this thesis.

2.1.2 Irregular wave description

Irregular waves are usually generated based on a given Spectral Density Function (SDF) that can represent a real sea state. Several formulations can be found in the literature that, using empirical measurements and physical considerations, allow the representation of spectral shapes under idealised conditions. Among such formulations, the most widely considered SDFs are the JONSWAP spectrum for wind-generated seas with fetch limitations [88], the Bretschneider spectrum for developing seas [20], and the Pierson-Moskowitz spectrum for fully-developed seas [151]. By way of example, Figure 2.2 shows how the JONSWAP spectrum varies when changing (a) the peak period (T_p), (b) the significant wave height (H_s), and (c) the peak-shape parameter (γ), which are the three parameters that characterise the JONSWAP spectrum as:

$$S_{\eta\eta}(\omega) = \frac{\alpha_s g^2}{\omega^5} e^{-\frac{5}{4}\left(\frac{\omega_\mathrm{p}}{\omega}\right)^4} \gamma^{r_s(\omega)} \tag{2.4}$$

where $r_s(\omega) = e^{-\frac{(\omega-\omega_\mathrm{p})^2}{2\sigma_s^2\omega_\mathrm{p}^2}}$, $\omega_\mathrm{p} = \frac{2\pi}{T_\mathrm{p}}$, and α_s and σ_s are constant values determined using data collected during the JONSWAP experiment [88].

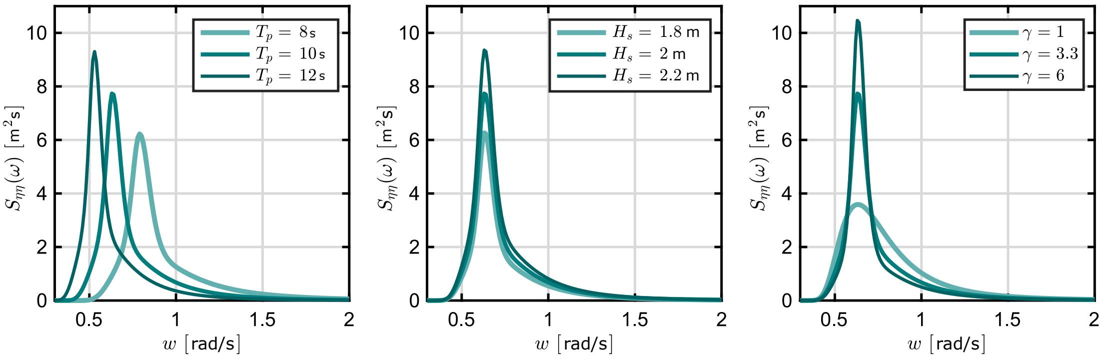

(a) H_s =2 m and $\gamma = 3.3$. **(b)** T_p =10 s and $\gamma = 3.3$. **(c)** T_p =10 s and H_s =2 m.

Figure 2.2: Examples of JONSWAP SDFs with varying parameters (a) T_p, (b) H_s, and (c) γ.

Once the target SDF is selected, several methods can be found in the literature to generate a finite-duration wave time series (or realisation) with the statistical properties of such a sea state. For example, irregular wave time series are approximated by superposing harmonic components, with frequency-dependent amplitudes (directly derived from the target wave spectrum) and phases, which can be chosen randomly [119]. Another well-known approach, is to compute the inverse Fourier transform of a random spectrum derived from the objective SDF as

$$\eta(t) = \mathscr{F}^{-1}\{S_{\eta\eta}(\omega)S_{ww}(\omega)\}, \tag{2.5}$$

where $\mathscr{F}^{-1}$ denotes the inverse Fourier transform, and $S_{\eta\eta}(\omega)$ and $S_{ww}(\omega)$ are the power spectral densities of the wave (for example, the JONSWAP SDF) and a white noise input signal, respectively, with the mean value of the white noise power spectrum $\frac{1}{n_\omega}\sum_{j=1}^{n_\omega} S_{ww}(j) \approx 1$. In particular, the random irregular waves are generated using the method of the inverse Fourier transform within this thesis, since it is a well-known method in the literature, which retains the spectral characteristics of the target SDF on every realisation [132].

By way of example, Figure 2.3 shows an irregular wave elevation η time series randomly generated, using the method explained in Equation (2.5), from a JONSWAP SDF with T_p =10 s, H_s =2 m, and $\gamma = 3.3$.

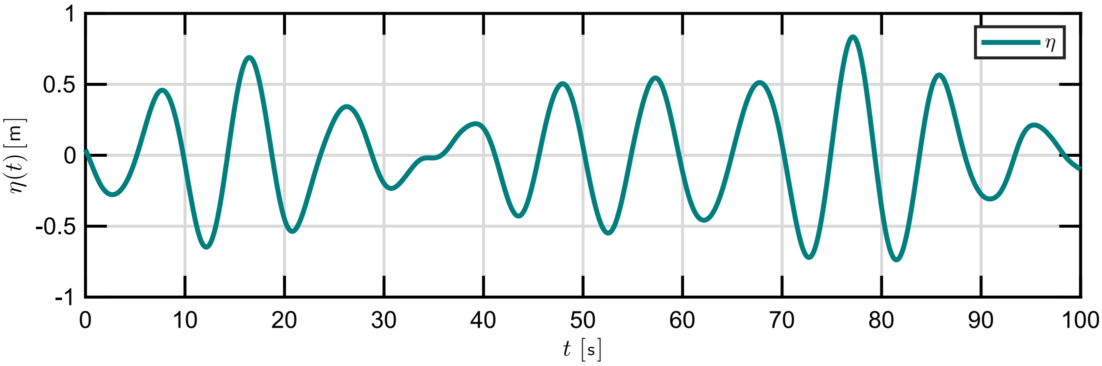

Figure 2.3: Example of a wave elevation time series generated from a JONSWAP SDF with T_p =10 s, H_s =2 m, and $\gamma = 3.3$.

2.2 Linear WEC modelling

As will be introduced in Section 2.2.3, Cummins' equation [35] is a linear differential equation used to characterise the motion of a floating body or, more specifically, a WEC in this case. However, in order to understand where the employed equations stem from, and under which set of assumptions these equations are valid, the following subsections describe what the Navier-Stokes equations and the potential flow theory are.

2.2.1 Navier-Stokes equations

The motion of viscous fluids (also the interactions between a viscous fluid substance and a solid structure, orqa between fluid substances) is described using a well-known set of nonlinear differential equations, called the Navier-Stokes equations [55]. In particular, the behaviour of such a fluid can be characterised using pressure and flow velocity, which are derived via the continuity and impulse equations, describing the conservation of mass and momentum, respectively

$$\frac{\delta \rho}{\delta t} + \nabla \cdot (\rho u_{\mathsf{f}}) = 0 \tag{2.6a}$$

$$\frac{\delta u_{\mathsf{f}}}{\delta t} + u_{\mathsf{f}}^{\mathsf{T}} \nabla u_{\mathsf{f}} = f - \frac{1}{\rho}\nabla p + \frac{\mu_{\mathsf{f}}}{\rho}\nabla^2 u_{\mathsf{f}}, \tag{2.6b}$$

where ρ is the density of the fluid under analysis, u_{f} the fluid flow velocity vector, f the external force vector per unit mass, p the pressure, and μ_{f} the fluid dynamic viscosity. The operators ∇, $\nabla\cdot$, and ∇^2 denote the divergence, the gradient, and the Laplacian, respectively, and $\{\cdot\}^{\mathsf{T}}$ denotes the transpose of $\{\cdot\}$. Since the system of equations (2.6) does not have an analytical solution, numerical discretization methods are required in order to obtain a solution. To this end, mathematical modelling approaches like the classic mesh-based Computational Fluid Dynamics (CFD) or the mesh-less Smoothed-Particle Hydrodynamics (SPH) are commonly used in the literature [185]. To avoid the computational expense of approaches like CFD, linear potential flow theory simplifies the system of equations (2.6) under a set of assumptions (introduced in Section 2.2.2), to obtain a computationally more efficient technique to solve the hydrodynamic wave-structure interaction.

2.2.2 Linear potential flow theory

In order to better understand the hypothesis proposed by linear potential flow theory [127] to simplify the Navier-Stokes equations, Figure 2.4 shows a schematic view of a floating body, where n_o denotes the unit vector normal to the body's surface, $\mathsf{S}_{\mathsf{wet}}$ the wetted surface of the floating body, and the equations refer to the different (linear) boundary conditions that will be introduced throughout this section.

The assumptions considered in the linear potential flow model to simplify the Navier-Stokes equations (Equation (2.6)) are the following:

AS.1 The fluid, in this case sea water, is incompressible $\left(\frac{\delta \rho}{\delta t} = 0\right)$,

AS.2 The fluid is inviscid ($\mu_{\mathsf{f}} = 0$),

AS.3 The flow is considered to be irrotational ($\nabla \times u_{\mathsf{f}} = 0$),

AS.4 The amplitude of the body motion is small compared to its dimensions,

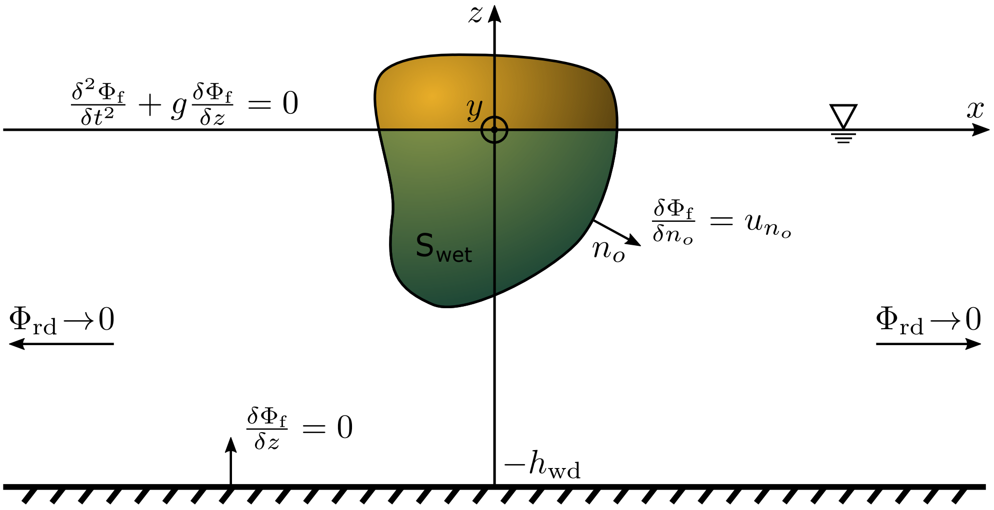

Figure 2.4: Schematic of a floating body with the linear boundary conditions introduced in Section 2.2.2.

AS.5 The wave amplitude is small with respect to the wavelength.

It should be noted that, though reasonable for an uncontrolled device case, some of the assumptions do not hold when the device is under optimal control conditions. By way of example, under optimal control conditions, the device motion is maximised (which directly invalidates **AS.4**), and the relative velocity between body and η increases, which raises the force that the device experiments due to the viscosity of the water, making, thus, **AS.2** is not a reasonable assumption. However, as mentioned at the beginning of the chapter, the objective of this thesis is to analyse the excitation force estimation problem from a linear perspective (in order to ease the transition to nonlinear excitation force estimation) and, therefore, the same set of assumptions considered for the standard Cummins' equation (introduced in Section 2.2.3) are considered in this thesis.

Since the fluid is assumed incompressible (**AS.1**), Equation (2.6a) can be expressed as

$$\nabla \cdot u_{\mathsf{f}} = 0. \tag{2.7}$$

Additionally, considering **AS.2-3**, there exists a scalar function Φ_{f} denoted as the velocity potential, such that

$$u_{\mathsf{f}} = \nabla \Phi_{\mathsf{f}}. \tag{2.8}$$

Thus, by substituting Equation (2.8) into Equation (2.7), the velocity potential Φ_{f} can be obtained by solving the Laplace equation

$$\nabla^2 \Phi_{\mathsf{f}} = 0, \tag{2.9}$$

and u_{f} can then be calculated using Equation (2.8). Additionally, since the fluid is considered inviscid (**AS.2**), the last term of Equation (2.6b) is 0. Then, by defining the external force as the gravitational force $\left(f = [0, 0, -\rho g]^{\mathsf{T}}\right)$, and integrating Equation (2.6b), one can obtain the Bernoulli equation, defined as

$$\frac{p}{\rho} + \frac{\delta \Phi_{\text{f}}}{\delta t} + \frac{1}{2} \left(\nabla \Phi_{\text{f}}\right)^2 + gz = C_{\text{int}}, \tag{2.10}$$

where C_{int} is an integration constant.

In order to determine the velocity potential and fluid pressure, a set of boundary conditions (shown in Figure 2.4) needs to be defined. The considered boundary conditions are the following:

BC.1 The seabed is assumed to be impermeable, i.e. no fluid enters or leaves the seabed, which means that the vertical component of the fluid velocity will be 0 at the seabed

$$\frac{\delta \Phi_{\text{f}}}{\delta z} = 0 \qquad \text{on } z = -h_{\text{wd}}. \tag{2.11}$$

BC.2 Similar to **BC.1**, the floating body is also assumed to be impermeable, which means that, at the body surface the fluid velocity component normal to the body surface (u_{n_o}) must be equal to the velocity of the body in the same direction

$$\frac{\delta \Phi_{\text{f}}}{\delta n_o} = u_{n_o} \qquad \text{on the body surface.} \tag{2.12}$$

BC.3-4 Regarding the free surface η, two boundary conditions must be fulfilled: the kinematic and dynamic boundary conditions. The kinematic boundary condition states that a fluid particle on the free surface is assumed to stay on the free surface and, therefore, the fluid velocity normal to the free surface must be equal the free surface velocity in that direction. The dynamic boundary condition states that the fluid pressure is equal to the atmospheric pressure (p_{atm}) on the free surface. Both kinematic and dynamic boundary conditions are formally defined as

$$\frac{\delta \eta}{\delta t} + \frac{\delta \Phi_{\text{f}}}{\delta x}\frac{\delta \eta}{\delta x} + \frac{\delta \Phi_{\text{f}}}{\delta y}\frac{\delta \eta}{\delta y} - \frac{\delta \Phi_{\text{f}}}{\delta z} = 0 \qquad \text{on } z = \eta, \tag{2.13a}$$

and

$$\frac{\delta \Phi_{\text{f}}}{\delta t} + \frac{1}{2} \left(\nabla \Phi_{\text{f}}\right)^2 + g\eta = 0 \qquad \text{on } z = \eta. \tag{2.13b}$$

BC.5 The last boundary condition specifies that, far away from the floating body, the wave field should be identical to the incoming wave field (undisturbed by the floating body). To this end, radiation and diffraction effects should fade out as the distance to the floating body increases:

$$\Phi_{\text{rd}} \approx 0 \qquad \text{as } d_{\text{r}} \to \infty, \tag{2.14}$$

where d_{r} is the radial distance, and $\Phi_{\mathsf{rd}} = \Phi_{\mathsf{r}} + \Phi_{\mathsf{d}}$ the potential of the perturbation, related to radiation and diffraction effects, where Φ_{r} and Φ_{d} are the radiation and diffraction potentials, respectively.

To linearise the nonlinear boundary conditions **BC.3-4**, two different simplifications are considered, based on **AS.4** and **AS.5**. The first simplification is to consider **BC.3-4** on the undisturbed free surface ($z = 0$) instead of at the instantaneous free surface ($z = \eta$), and, the second simplification, to neglect the higher order terms. Thus, as shown in Figure 2.4, such equations can be linearised as

$$\frac{\delta \eta}{\delta t} - \frac{\delta \Phi_{\mathsf{f}}}{\delta z} = 0 \qquad \text{on } z = 0, \tag{2.15a}$$

$$\frac{\delta \Phi_{\mathsf{f}}}{\delta t} + g\eta = 0 \qquad \text{on } z = 0, \tag{2.15b}$$

respectively. Furthermore, Equations (2.15a) and (2.15b) can now be combined as

$$\frac{\delta^2 \Phi_{\mathsf{f}}}{\delta t^2} + g\frac{\delta \Phi_{\mathsf{f}}}{\delta z} = 0 \qquad \text{on } z = 0. \tag{2.16}$$

Since linearity is assumed, the potential around the floating body can be decomposed into incident (Φ_{i}), diffracted, and radiated potential, as

$$\Phi_{\mathsf{f}} = \Phi_{\mathsf{i}} + \Phi_{\mathsf{d}} + \Phi_{\mathsf{r}}. \tag{2.17}$$

The incident wave field potential represents the incoming wave potential in the absence of the body, while the diffracted potential defines the interaction between the incident wave and the fixed body. Finally, the radiated potential results from the oscillations of the body in the absence of an incident wave field.

As mentioned in Section 2.1.1, it is assumed that, for deep water depth, the solution of the boundary problem takes a sinusoidal form. In fact, the velocity potential, which oscillates harmonically in time with angular frequency ω, can be written as

$$\Phi_{\mathsf{f}}(x, y, z, \omega, t) = \mathsf{real}(\hat{\Phi}_{\mathsf{f}}(x, y, z, \omega)e^{\jmath\omega t}), \tag{2.18}$$

where $\hat{\Phi}_{\mathsf{f}}$ represents the complex amplitude of the velocity potential. Even though real ocean waves are never truly monochromatic, Equation (2.18) considers a single wave frequency to simplify the problem, for illustration purposes. However, the extension to irregular waves can be done straightforwardly by superposing sinusoidal waves of different frequency and amplitude[2], as explained in Section 2.1.2.

---

[2] Note that this is just an approximation of real irregular waves, which are composed of an infinite number of frequencies.

According to Equation (2.18), the Laplace equation (2.9) can now be represented as

$$\nabla^2 \hat{\Phi}_{\mathsf{f}} = 0, \tag{2.19}$$

and the boundary conditions of Equations (2.11), (2.12) and (2.16) as

$$\frac{\delta \hat{\Phi}_{\mathsf{f}}}{\delta z} = 0 \qquad \text{on } z = -h_{\mathsf{wd}}, \tag{2.20a}$$

$$\frac{\delta \hat{\Phi}_{\mathsf{f}}}{\delta n_o} = u_{n_o} \qquad \text{on the body surface,} \tag{2.20b}$$

$$\frac{\delta^2 \hat{\Phi}_{\mathsf{f}}}{\delta t^2} + g\frac{\delta \hat{\Phi}_{\mathsf{f}}}{\delta z} = 0 \qquad \text{on } z = 0. \tag{2.20c}$$

Thus, based on Equations (2.18) and (2.20), the complex amplitude of the velocity potential of the incident wave can be computed following Equation (2.21) [61] as

$$\hat{\Phi}_{\mathsf{i}}(x, y, z, \omega) = \frac{\jmath g}{\omega} a_\eta(\omega) \frac{\cosh\left[\kappa_\eta(\omega)\,(z + h_{\mathsf{wd}})\right]}{\cosh\left(\kappa_\eta(\omega) h_{\mathsf{wd}}\right)} e^{-\jmath \kappa_\eta(\omega)(x\cos\beta_\eta + y\sin\beta_\eta)}. \tag{2.21}$$

It should be noted that, when h_{wd} tends to infinity, the decay function $\frac{\cosh[\kappa_\eta(\omega)(z+h_{\mathsf{wd}})]}{\cosh(\kappa_\eta(\omega)h_{\mathsf{wd}})}$ of Equation (2.21) turns into the exponential function $e^{\kappa_\eta(\omega)z}$.

The diffracted waves are generated by the interaction between the incident wave and the fixed body, and the diffraction potential must satisfy the boundary condition over the wetted surface of the fixed body, specifically

$$-\frac{\delta \hat{\Phi}_{\mathsf{d}}}{\delta n_o} = \frac{\delta \hat{\Phi}_{\mathsf{i}}}{\delta n_o} \qquad \text{on } \mathsf{S}_{\mathsf{wet}}. \tag{2.22}$$

The radiation potential must satisfy the boundary condition (2.20b) while the body oscillates in any Degree-of-Freedom (DoF). Thus, the radiation potential complex amplitude can be described as

$$\hat{\Phi}_{\mathsf{r}}(\omega) = \jmath\omega \sum_{i=1}^{n_{\mathsf{DoF}}} \hat{\chi}_i \phi_{\mathsf{r}_i}, \tag{2.23}$$

where n_{DoF} is the number of degrees-of-freedom (see Figure 2.5), $\hat{\chi}_i$ the complex amplitude of the motion of the body in DoF i, and ϕ_{r_i} the unit-amplitude radiation potential due to the motion in mode i.

According to Newton's second law, in the time-domain, the equation of motion of a floating body can be expressed as

$$M\ddot{\chi}(t) = \sum f_i(t), \tag{2.24}$$

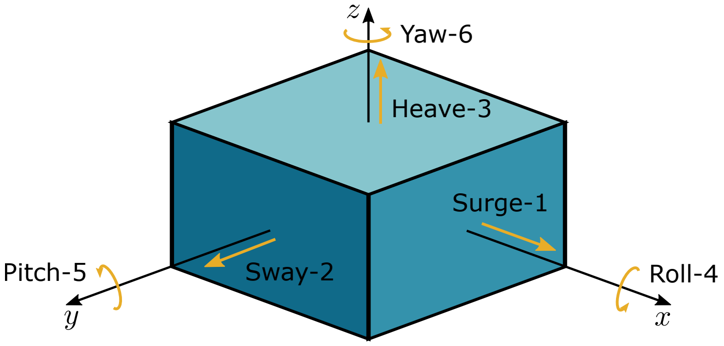

Figure 2.5: Schematic of the six degrees-of-freedom of a floating body, with their corresponding index numbers for the matrix notation.

where $f_i(t) \in \mathbb{R}^{n_{\mathsf{DoF}}}$ are the vectors of forces and moments acting on the floating body for the different modes of motion. $M \in \mathbb{R}^{n_{\mathsf{DoF}} \times n_{\mathsf{DoF}}}$ contains the mass (or inertia) values for all the DoFs and interactions as

$$M = \begin{bmatrix} m & 0 & 0 & 0 & mz_g & -my_g \\ 0 & m & 0 & -mz_g & 0 & mx_g \\ 0 & 0 & m & my_g & -mx_g & 0 \\ 0 & -mz_g & my_g & \mathsf{i}_{xx} & -\mathsf{i}_{xy} & -\mathsf{i}_{xz} \\ mz_g & 0 & -mx_g & -\mathsf{i}_{yx} & \mathsf{i}_{yy} & -\mathsf{i}_{yz} \\ -my_g & mx_g & 0 & -\mathsf{i}_{zx} & -\mathsf{i}_{zy} & \mathsf{i}_{zz} \end{bmatrix}, \tag{2.25}$$

where m is the mass of the body, (x_g, y_g, z_g) the coordinates of the centre of gravity, and i_{ij} are the moments of inertia about the different axes if $i = j$, or the products of inertia with respect to the centre of mass if $i \neq j$. It should be noted that the total force acting on the device can be represented as a sum of different forces, because the considered system is linear and, therefore, superposition holds. In particular, replacing the hydrodynamic forces considered in this thesis, Equation (2.24) can be redefined as

$$M\ddot{\chi}(t) = f_{\mathsf{e}}(t) + f_{\mathsf{r}}(t) + f_{\mathsf{h}}(t) + f_{\mathsf{ext}}(t), \tag{2.26}$$

where $f_{\mathsf{e}}(t)$ represents the excitation force (the force exerted by the incoming wave), $f_{\mathsf{r}}(t)$ the radiation force (the force of the waves generated by the oscillatory motion of the body), $f_{\mathsf{h}}(t)$ the hydrostatic force (results from the balance between the gravity and the buoyancy forces), and any external force $f_{\mathsf{ext}}(t)$, such as the Power-Take-Off (PTO) system force ($f_{\mathsf{pto}}(t)$), the mooring force ($f_{\mathsf{moo}}(t)$), etc.

Since the motion of the waves and the floating body can be considered to oscillate harmonically (because the system is linear), the body position, velocity, and acceleration vectors can be expressed, respectively, as

$$\chi(t) = \mathsf{real}(\hat{\chi} e^{\jmath\omega t}), \tag{2.27a}$$

$$\dot{\chi}(t) = \mathsf{real}(\jmath\omega\hat{\chi} e^{\jmath\omega t}), \tag{2.27b}$$

$$\ddot{\chi}(t) = \mathsf{real}(-\omega^2\hat{\chi} e^{\jmath\omega t}). \tag{2.27c}$$

Equally, Equation (2.26) can also be defined in the frequency domain as

$$M\ddot{X} = F_{\mathsf{e}} + F_{\mathsf{r}} + F_{\mathsf{h}} + F_{\mathsf{ext}}. \tag{2.28}$$

The excitation force $F_{\mathsf{e}}(\omega)$ can be divided into Froude-Krylov force ($F_{\mathsf{FK}}(\omega)$) and diffraction ($F_{\mathsf{d}}(\omega)$) force as

$$F_{\mathsf{e}}(\omega) = F_{\mathsf{FK}}(\omega) + F_{\mathsf{d}}(\omega) = \jmath\omega\rho \int_{\mathsf{S}_{\mathsf{wet}}} \hat{\Phi}_{\mathsf{i}} n_o d\mathsf{S}_{\mathsf{wet}} + \jmath\omega\rho \int_{\mathsf{S}_{\mathsf{wet}}} \hat{\Phi}_{\mathsf{d}} n_o d\mathsf{S}_{\mathsf{wet}}, \tag{2.29}$$

where $\mathsf{S}_{\mathsf{wet}}$ refers to the wetted surface of the floating body (see Figure 2.4). The radiation force in mode i can be expressed as

$$F_{\mathsf{r}_i}(\omega) = -\omega^2\rho \int_{\mathsf{S}_{\mathsf{wet}}} \sum_{i'=1}^{n_{\mathsf{DoF}}} X_{i'}(\omega)\phi_{\mathsf{r}_{i'}} n_{o_i} d\mathsf{S}_{\mathsf{wet}}, \tag{2.30}$$

or, using an electrical/mechanical analogy, as

$$F_{\mathsf{r}_i}(\omega) = -\jmath\omega \sum_{i'=1}^{n_{\mathsf{DoF}}} K_{\mathsf{r}_{i\,i'}}(\omega) X_{i'}(\omega), \tag{2.31}$$

where $K_{\mathsf{r}_{i\,i'}}(\omega)$ is an element of the radiation impedance matrix $K_{\mathsf{r}}(\omega)$, defined as

$$K_{\mathsf{r}_{i\,i'}}(\omega) = -\jmath\omega\rho \int_{\mathsf{S}_{\mathsf{wet}}} \phi_{\mathsf{r}_{i'}} n_{o_i} d\mathsf{S}_{\mathsf{wet}}. \tag{2.32}$$

The hydrostatic force $F_{\mathsf{h}}(\omega)$ can be calculated from the integration of the hydrostatic pressure over the instantaneous wetted surface of the floating body. Since calculating the instantaneous wetted surface of the device is computationally demanding, a linearised $F_{\mathsf{h}}(\omega)$ is usually considered which, for small body motions (**AS.4**), provides a reasonably accurate approximation of $F_{\mathsf{h}}(\omega)$. Thus, $F_{\mathsf{h}}(\omega)$ can be expressed as a force proportional to the displacement of the body as

$$F_{\mathsf{h}}(\omega) = -S_{\mathsf{h}} X(\omega), \tag{2.33}$$

where $S_{\mathsf{h}} \in \mathbb{R}^{n_{\mathsf{DoF}} \times n_{\mathsf{DoF}}}$ represents the hydrostatic stiffness.

2.2.3 Cummins' equation

The displacement of a multiple-DoF floating body can now be defined, replacing the different forces in Equation (2.28), as

$$\dot{X}(\omega) = \left(F_{\mathsf{e}}(\omega) + F_{\mathsf{ext}}(\omega)\right) H(\omega), \tag{2.34}$$

with the force-to-velocity[3] frequency response $H(\omega)$ defined as

$$H(\omega) = \left[\frac{S_{\mathsf{h}}}{\jmath\omega} + \jmath\omega\left(M + A_{\mathsf{r}}(\omega)\right) + D_{\mathsf{r}}(\omega)\right]^{-1}, \tag{2.35}$$

---

[3] Note that the force-to-position or force-to-acceleration frequency responses can be obtained by the integral or derivative (respectively) of Equation (2.35).

where $\{D_{\mathsf{r}}(\omega), A_{\mathsf{r}}(\omega)\} \subset \mathbb{R}^{n_{\mathsf{DoF}} \times n_{\mathsf{DoF}}}$ and are the so-called radiation damping and radiation added mass coefficients, respectively, which are the real and imaginary parts of the radiation impedance. Additionally, the excitation force can be defined as a function of the incident waves as $F_{\mathsf{e}}(\omega) = a_{\eta}(\omega)\hat{F}_{\mathsf{e}}(\omega)$, where $\hat{F}_{\mathsf{e}}(\omega)$ is a vector containing the complex amplitudes of excitation force (or torques) of the different DoF. The diagonal terms of the frequency response matrix $H(\omega)$ describe the inner dynamics of each DoF, while the off-diagonal terms describe the interaction between the different DoFs. The frequency response of the different terms in $H(\omega)$ depends, mostly, on the geometry of the device, i.e. some WECs can be designed to enhance, diminish, or cancel, the dynamics of specific DoFs and/or interactions [73].

All the hydrodynamic coefficients ($D_{\mathsf{r}}(\omega)$, $A_{\mathsf{r}}(\omega)$, $\hat{F}_{\mathsf{e}}(\omega)$ and S_{h}) are normally computed using Boundary Element Method (BEM) solvers. Such BEM solvers compute the linear potential hydrodynamic coefficients by solving (for a set of user-selected frequencies) the diffraction velocity potential of Equation (2.22) to obtain $\hat{F}_{\mathsf{e}}(\omega)$, and the radiation velocity potential of Equation (2.23) to obtain $D_{\mathsf{r}}(\omega)$ and $A_{\mathsf{r}}(\omega)$. To this end, several software codes can be found that compute the linear BEM hydrodynamic parameters, in the frequency or the time domain. Among the different available BEM solvers, ACHIL3D [110] in the time domain, and the commercially-available WAMIT [93] and the open-source NEMOH [12] in the frequency domain are the most commonly used utilities.

As an example, Figure 2.6 shows the frequency domain hydrodynamic coefficients for the heave motion of a 5 m radius and 10 m draft cylinder. Figures 2.6 (a) and (b) depict the hydrodynamic coefficients related to the radiation force $D_{\mathsf{r}}(\omega)$, and $A_{\mathsf{r}}(\omega)$, respectively, where $\mu_{\infty} \in \mathbb{R}^{n_{\mathsf{DoF}} \times n_{\mathsf{DoF}}}$ represents the infinite frequency added mass coefficient, which is the value of $A_{\mathsf{r}}(\omega)$ when $\omega \to \infty\,\mathsf{rad}/s$. Figures 2.6 (c) and (d) show the magnitude and phase values of the complex coefficient $\hat{F}_{\mathsf{e}}(\omega)$, respectively.

As first introduced by Cummins in [35], the time domain equivalent of Equation (2.28) can be formulated as

$$(M + \mu_{\infty})\ddot{\chi}(t) = -S_{\mathsf{h}}\chi(t) - \int_{-\infty}^{t} k_{\mathsf{r}}(t-\tau)\dot{\chi}(\tau)d\tau + f_{\mathsf{ext}}(t) + f_{\mathsf{e}}(t), \tag{2.36}$$

where the excitation force can be computed from the free-surface elevation as

$$f_{\mathsf{e}}(t) = \int_{-\infty}^{\infty} k_{\mathsf{e}}(t-\tau)\eta(\tau)d\tau. \tag{2.37}$$

The excitation force kernel $k_{\mathsf{e}}(t) \in \mathbb{R}^{n_{\mathsf{DoF}}}$ can be computed by applying the inverse Fourier transform to the excitation force frequency domain coefficients shown in Figure 2.6(a) and (b). Additionally, the radiation force kernel $k_{\mathsf{r}}(t) \in \mathbb{R}^{n_{\mathsf{DoF}} \times n_{\mathsf{DoF}}}$ can be

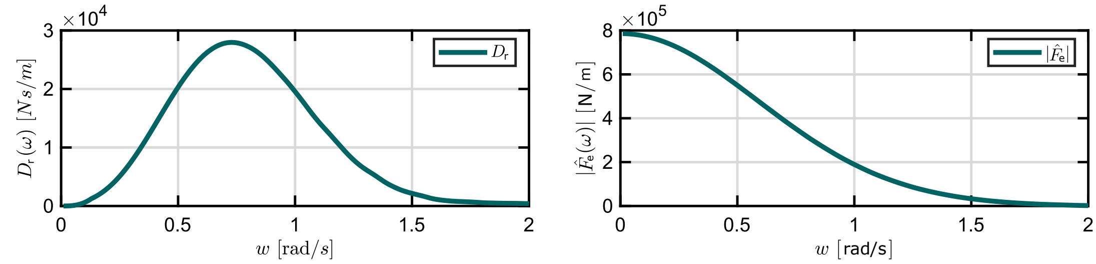

(a) Radiation damping. **(b)** Magnitude of the excitation force coefficients.

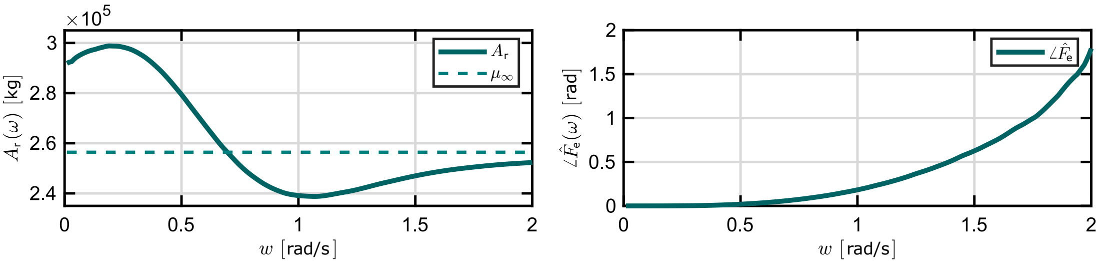

(c) Radiation added mass and infinite added mass. **(d)** Angle of the excitation force coefficients.

Figure 2.6: Hydrodynamic coefficients for the heave mode of a 5 m radius cylinder with 10 m draft.

computed from the frequency domain hydrodynamic parameters $A_r(\omega)$ and $D_r(\omega)$ through Ogilvie's relations which are defined, from the frequency to the time domain, as

$$k_r(t) = \frac{2}{\pi}\int_0^\infty D_r(\omega)\cos(\omega t)d\omega, \tag{2.38a}$$

and from the time to the frequency domain as

$$D_r(\omega) = \int_0^\infty k_r(t)\cos(\omega t)dt, \tag{2.38b}$$

$$A_r(\omega) = \mu_\infty - \frac{1}{\omega}\int_0^\infty k_r(t)\sin(\omega t)dt. \tag{2.38c}$$

Solving a convolution integral at every time-step, to compute the radiation force, is inconvenient for several reasons, as will be detailed in Section 2.2.4. Thus, the convolution term is usually approximated using a Linear Time Invariant (LTI) system, which can be defined using a State-Space (SS) representation. The next subsection provides a brief literature review of the available methods to compute the SS approximation for the convolution term.

2.2.4 Radiation convolution term approximation

The convolution term of Equation (2.36), accounting for the fluid memory effect associated with radiation forces, can represent a drawback for several ocean engineering applications. In particular, this convolution term represents a drawback from a simulation point of view, given that computing the numerical solution of such a term requires a relatively high computational effort. Additionally, from an estimation/control point of view, it can be inconvenient, since state-of-the-art model-based estimation/control techniques are usually based on the availability of a parametric SS representation of the system under analysis [45]. In order to overcome these drawbacks, researchers usually approximate the non-parametric convolution term using a suitable parametric structure. To this end, several options can be found in the literature, which attempt to compute an approximating parametric model for the convolution term introduced by Cummins. Regardless of the strategy used to identify the parametric model that approximates the radiation convolution term, the obtained SS will be defined as

$$\dot{x}_{\mathsf{r}}(t) = A_{\mathsf{r_{ss}}} x_{\mathsf{r}}(t) + B_{\mathsf{r_{ss}}} \dot{\chi}(t) \tag{2.39a}$$

$$f_{\mathsf{r}}^{\mathsf{c}}(t) = C_{\mathsf{r_{ss}}} x_{\mathsf{r}}(t) + D_{\mathsf{r_{ss}}} \dot{\chi}(t), \tag{2.39b}$$

with the velocity of the device as input and the radiation force convolution term ($f_{\mathsf{r}}^{\mathsf{c}}$) as output, where $x_{\mathsf{r}}(t) \in \mathbb{R}^{n_{\mathsf{r}}}$ is the state vector of the radiation convolution SS representation, and the matrices $A_{\mathsf{r_{ss}}} \in \mathbb{R}^{n_{\mathsf{r}} \times n_{\mathsf{r}}}$, $B_{\mathsf{r_{ss}}} \in \mathbb{R}^{n_{\mathsf{r}} \times n_{\mathsf{DoF}}}$, $C_{\mathsf{r_{ss}}} \in \mathbb{R}^{n_{\mathsf{DoF}} \times n_{\mathsf{r}}}$, and $D_{\mathsf{r_{ss}}} \in \mathbb{R}^{n_{\mathsf{DoF}}}$ can be obtained by any of the methods available in the literature. Ideally, as explained in Section 4.1, the matrix $D_{\mathsf{r_{ss}}}$ should be 0 if the physical properties of the radiation convolution term are respected.

Additionally, as will be explained in Section 4.3, the SS of the radiation convolution term of a multiple-DoF WEC, which is a Multiple-Input Multiple-Output (MIMO) SS system, can be defined using set of Single-Input Single-Output (SISO) SS systems, or identifying directly the MIMO frequency response of the radiation system. Due to its structure, the dimension of the MIMO SS model generated using multiple SISO SS systems is usually much larger than the dimension of the MIMO SS model identified using the MIMO frequency response of the device.

One of the well-established parameterisation methods was developed in [148] at the Norwegian University of Science and Technology and proposes a frequency-domain parametric identification strategy. To this end, the frequency response that this method attempts to identify can be obtained by computing the Fourier transform of Equation (2.38a) as

$$K_{\mathsf{r}}(\omega) = D_{\mathsf{r}}(\omega) + \jmath w \left[A_{\mathsf{r}}(\omega) - \mu_{\infty} \right]. \tag{2.40}$$

One year after the theory of this strategy was presented, and as an independent component of the Marine System Simulator [65], the authors developed a MATLAB toolbox to systematically apply the method [149], termed the *Frequency-Domain Identification* (FDI) toolbox[4]. The toolbox acts as an user interface where the

---

[4] Note that this toolbox differs from the original MATLAB toolbox (also termed FDI toolbox) developed in [99].

hydrodynamic coefficients are loaded, the different options of the toolbox (specified better in Section 4.2.1) are selected, and the MATLAB function *invfreqs* is called to identify the system. However, since *invfreqs* is a general frequency domain identification tool (it is not specifically developed for wave-energy applications), it has some problems when identifying some of the radiation convolution systems, which leads to unstable models, as shown in Section 4.2.3.

Another available application for the radiation parametric identification is associated with the WEC motion simulator *WEC-Sim* [189]. This utility, termed *Boundary Element Method Input/Output* (BEMIO) [171], is specifically used within WEC-Sim to obtain a state-space approximation of the radiation force convolution term. Unlike the FDI toolbox, which computes the SS approximated model using frequency domain data, BEMIO identifies the parametric model using time domain data, i.e. the radiation kernel $k_{\text{rad}}(t)$. To this end, BEMIO uses the singular value decomposition on the Hankel matrix of the radiation impulse-response function, as was first shown in [188].

Even though there is no specific general purpose software application developed for wave energy applications based on Prony's method [37], this method should be mentioned here, since it is still commonly used within the ocean engineering literature. Briefly, this strategy is based on identifying the radiation SS coefficients from the impulse response function (similar to the BEMIO application), and it has been used in noteworthy studies, such as those involving the SEAREV WEC [11] and the Spar-buoy WEC [79].

Finally, the only other available radiation convolution approximation utility, to the best of the author's knowledge, is the moment-matching-based identification method for both the radiation convolution term and the complete force-to-motion (input-output) dynamics, which has recently been developed by the Centre for Ocean Energy Research (COER) [47]. This strategy has its foundation in recent advances on model order reduction by moment-matching, developed over several studies such as [8] or [161]. This method allows for the computation of a model that *exactly* matches the frequency response of the original (target) system at a set of user-selected frequencies, providing an efficient method to compute a state-space representation for the dynamics of floating bodies with zero forward speed. In 2019, the *Finite-Order Approximation by Moment-Matching* (FOAMM) MATLAB application was developed within the COER [134], that systematically applies the moment-based strategy using, as the FDI toolbox, frequency-domain data.

The theory behind the FOAMM application, along with the different options and modes of operations that it comprises, and a comparison with the aforementioned other available applications, is provided in Section 4.1.

2.2.5 WEC state-space representation

The approximation of the non-parametric convolution term in Equation (2.36) with a suitable parametric model, allows the representation of the complete WEC dynamics in a SS form. The continuous-time SS analogue of Equation (2.36) can be defined as

$$\dot{x}(t) = A_{\mathsf{ss}} x(t) + B_{\mathsf{ss}} f_{\mathsf{e}}(t) \tag{2.41a}$$

$$y(t) = C_{\mathsf{ss}} x(t) + D_{\mathsf{ss}} f_{\mathsf{e}}(t), \tag{2.41b}$$

where $x(t) = \begin{bmatrix} \chi(t) & \dot{\chi}(t) & x_{\mathsf{r}}(t) \end{bmatrix}^{\mathsf{T}} \in \mathbb{R}^{n_{\mathsf{ss}}}$, $y(t) = \begin{bmatrix} \chi(t) & \dot{\chi}(t) & \ddot{\chi}(t) \end{bmatrix}^{\mathsf{T}} \in \mathbb{R}^{q_{\mathsf{ss}}}$, and the matrices $A_{\mathsf{ss}} \in \mathbb{R}^{n_{\mathsf{ss}} \times n_{\mathsf{ss}}}$, $B_{\mathsf{ss}} \in \mathbb{R}^{n_{\mathsf{ss}} \times p_{\mathsf{ss}}}$, $C_{\mathsf{ss}} \in \mathbb{R}^{q_{\mathsf{ss}} \times n_{\mathsf{ss}}}$, and $D_{\mathsf{ss}} \in \mathbb{R}^{q_{\mathsf{ss}} \times p_{\mathsf{ss}}}$ are given by

$$\begin{aligned} A_{\mathsf{ss}} &= \begin{bmatrix} 0 & \mathbb{I}_{n_{\mathsf{DoF}}} & 0 \\ -M^* S_{\mathsf{h}} & 0 & -M^* C_{\mathsf{r_{ss}}} \\ 0 & B_{\mathsf{r_{ss}}} & A_{\mathsf{r_{ss}}} \end{bmatrix}, B_{\mathsf{ss}} = \begin{bmatrix} 0 \\ M^* \\ 0 \end{bmatrix}, \\ C_{\mathsf{ss}} &= \begin{bmatrix} \mathbb{I}_{n_{\mathsf{DoF}}} & 0 & 0 \\ 0 & \mathbb{I}_{n_{\mathsf{DoF}}} & 0 \\ -M^* S_{\mathsf{h}} & 0 & -M^* C_{\mathsf{r_{ss}}} \end{bmatrix} \text{ and } D_{\mathsf{ss}} = \begin{bmatrix} 0 \\ 0 \\ M^* \end{bmatrix}, \end{aligned} \tag{2.42}$$

where $M^* = (M + \mu_\infty)^{-1}$. The symbol $\mathbb{I}_{n_{\mathsf{DoF}}}$ denotes an identity matrix of size n_{DoF}, the symbol 0 stands for any zero element dimensioned according to the context, with $p_{\mathsf{ss}} = n_{\mathsf{DoF}}$ and $q_{\mathsf{ss}} = 3n_{\mathsf{DoF}}$.

It should be noted that the formulation of System (2.41) can represent a general SS system, corresponding to a multiple DoF WEC. However, the definition of such a system can change throughout this thesis, according to the device or the case analysed in each section. For example, the most common variation is to consider a single DoF, which considerably reduces the size of System (2.41), simplifying the problem. Another variation is not to consider position, velocity, and acceleration as outputs, but just some of them (for example, position and velocity only), which is done by modifying the dimensions of matrices C_{ss} and D_{ss}. If necessary, the performed variations will be indicated when referring to System (2.41).

2.2.6 WEC array modelling

This subsection aims to introduce the expansion of the single WEC equation of motion (2.36), to consider an array of n_{b} bodies. Since Equation (2.36) is already defined as multiple-input multiple-output, the expansion to consider multiple bodies is straightforward. The displacement vector of the i^{th} body ($\chi_i(t)$) can be included into a new vector containing all the states as

$$\boldsymbol{\chi}(t) = \sum_{i=1}^{n_{\mathsf{b}}} \mathbb{e}_i^{n_{\mathsf{b}}} \otimes \chi_i(t), \tag{2.43}$$

where $\boldsymbol{\chi}(t) \in \mathbb{R}^n$, $n = n_{\mathsf{b}} n_{\mathsf{DoF}}$, the symbol $\mathbb{e}_i^q \in \mathbb{R}^q$ denotes a vector with 1 in the i^{th} component and 0 elsewhere (similarly, $\mathbb{e}_{ij}^{qp} \in \mathbb{R}^{q \times p}$ denotes a matrix with 1 in the ij^{th} component and 0 elsewhere), and the symbol $\otimes$ denotes the *Kronecker product* [21]. Thus, the equation of motion for an array of n_{b} bodies can be expressed as

$$(\boldsymbol{M} + \boldsymbol{\mu}_\infty)\ddot{\boldsymbol{\chi}}(t) = -\boldsymbol{S}_{\mathsf{h}}\boldsymbol{\chi}(t) - \int_{-\infty}^{t} \boldsymbol{k}_{\mathsf{r}}(t-\tau)\dot{\boldsymbol{\chi}}(\tau)d\tau + \boldsymbol{f}_{\mathsf{ext}}(t) + \boldsymbol{f}_{\mathsf{e}}(t). \tag{2.44}$$

Note that the bold symbols in Equation (2.44) are used to represent the WEC array equivalents of the symbols in Equation (2.36). Thus, $\boldsymbol{M} = \mathbb{I}_{n_{\mathsf{b}}} \otimes M \in \mathbb{R}^{n \times n}$ contains the information of the mass (or inertia) of the different bodies, and $\boldsymbol{S}_{\mathsf{h}} = \mathbb{I}_{n_{\mathsf{b}}} \otimes S_{\mathsf{h}} \in \mathbb{R}^{n \times n}$ the hydrostatic coefficients. Similarly, $\boldsymbol{\mu}_\infty \in \mathbb{R}^{n \times n}$ and $\boldsymbol{k}_{\mathsf{r}}(t) \in \mathbb{R}^{n \times n}$ contain the infinite added mass and radiation kernel, respectively, of each device's DoFs inner dynamics in the diagonal terms, and the interactions between the different DoFs of the bodies composing the array in the off-diagonal terms.

In the frequency domain, the displacement of the different devices of the array is expressed as

$$\dot{\boldsymbol{X}}(\omega) = \left(\boldsymbol{F}_{\mathsf{e}}(\omega) + \boldsymbol{F}_{\mathsf{ext}}(\omega)\right)\boldsymbol{H}(\omega), \tag{2.45}$$

where $\dot{\boldsymbol{X}}(\omega)$, $\boldsymbol{F}_{\mathsf{e}}(\omega)$, and $\boldsymbol{F}_{\mathsf{ext}}(\omega)$ are the frequency domain analogues of $\dot{\boldsymbol{\chi}}(t)$, $\boldsymbol{f}_{\mathsf{e}}(\omega)$, and $\boldsymbol{f}_{\mathsf{ext}}(\omega)$. The force-to-velocity frequency response of the array $\boldsymbol{H}(\omega)$ can be defined as

$$\boldsymbol{H}(\omega) = \left[\frac{\boldsymbol{S}_{\mathsf{h}}}{\jmath\omega} + \jmath\omega\left(\boldsymbol{M} + \boldsymbol{A}_{\mathsf{r}}(\omega)\right) + \boldsymbol{D}_{\mathsf{r}}(\omega)\right]^{-1}, \tag{2.46}$$

with $\{\boldsymbol{D}_{\mathsf{r}}(\omega), \boldsymbol{A}_{\mathsf{r}}(\omega)\} \subset \mathbb{R}^{(n_{\mathsf{DoF}} n_{\mathsf{b}}) \times (n_{\mathsf{DoF}} n_{\mathsf{b}})}$ containing the radiation damping and radiation added mass coefficients, respectively, of all the devices of the array (in the diagonal terms) and interactions between devices (in the off-diagonal terms).

By way of example, consider a 4 heaving spherical device (5 m radius and 5 m draft) array arranged in a square layout, with an inter-device distance, along one side of the square, of d_{b} =20 m (see Figure 2.7). As shown in Figure 2.7, due to the specific layout geometry, only three dynamics are differentiated: the inner dynamics of each body (diagonal terms), and two different interactions (off-diagonal terms). The different colours of Figure 2.7 show how the different dynamics are arranged in the frequency domain matrices as in, for example, $\boldsymbol{A}_{\mathsf{r}}(\omega)$, $\boldsymbol{B}_{\mathsf{r}}(\omega)$ or $\boldsymbol{H}(\omega)$.

Figure 2.8 shows the frequency response of the force-to-velocity dynamics (computed as shown in Equation (2.46)) for the array layout depicted in Figure 2.7, using the same colour code of Figure 2.7. One could notice that the motion of a given device is driven (mainly) by its inner dynamics, since the amplitude of the inner dynamics,

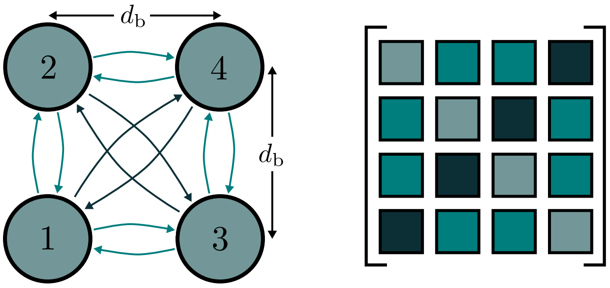

Figure 2.7: Example array layout of 4 spherical bodies of 5 m radius and 5 m draft, and an inter-device distance (along one side of the square) of d_b =20 m.

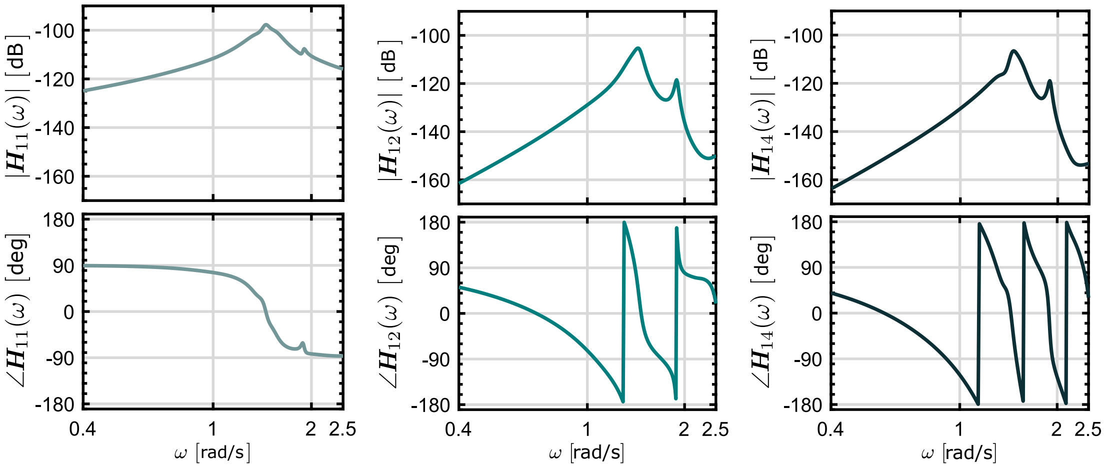

(a) Force-to-velocity frequency response of the inner dynamics.

(b) Force-to-velocity frequency response of the interaction with the closest body.

(c) Force-to-velocity frequency response of the diagonal interaction.

Figure 2.8: Force-to-velocity frequency responses of (a) the inner dynamics of each device of the array, (b) the closest interactions, and (c) the interaction with the device on the other diagonal of the array for the array introduced in Figure 2.7.

shown in Figure 2.8(a), is larger than the amplitude of the interactions, shown in Figures 2.8(b) and (c). However, since the inter-device distance is only 20 m (i.e. two device diameters), the interactions with the other bodies of the array have considerable influence on the motion of different WECs. Depending on the array design, the interactions between the devices can be constructive or destructive [72], i.e. can increase or diminish the motion of the devices. Thus, optimising the design of the complete WEC array (which includes the design of the layout, device geometry, control, moorings, etc.) is of paramount importance in order to maximise energy extraction and, therefore, improve wave energy profitability.

3

Wave excitation force estimation and prediction literature review

Contents

3.1 Overview

The majority of the energy maximising control strategies require knowledge of the instantaneous and future excitation force f_{e} acting on the WEC, in order to determine the optimal control input $f_{\mathrm{pto}}^{\mathrm{opt}}$ [155]. For a fixed body, f_{e} can be derived from a total pressure measurement or by integrating the pressure over the submerged body surface. However, for a non-fixed body, f_{e} is an unmeasurable quantity, since the integrated pressure over the submerged body surface represents the excitation force plus other hydrodynamic forces, e.g. radiation force f_{r}, hydrostatic force f_{h}, etc. Therefore, for a moving device, such as a WEC, f_e can only be estimated. To this end, various strategies have been proposed in the literature, which attempt to estimate f_e based on measurable quantities, such as the device position and velocity (as exemplified in Figure 3.1 for a typical control loop) or the pressure on the WEC hull.

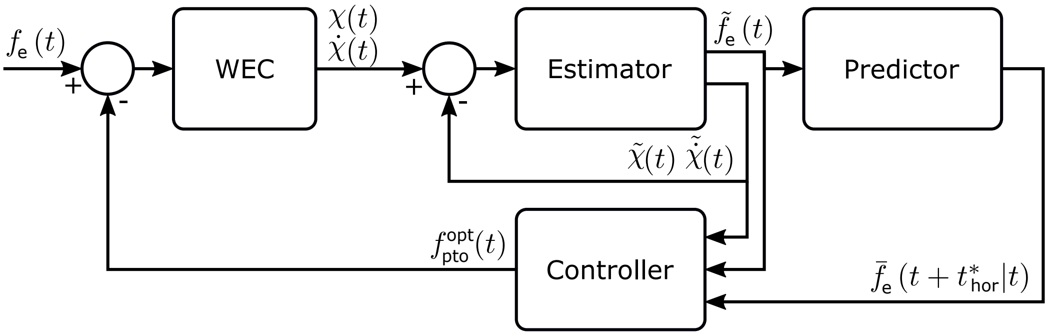

Figure 3.1: Example of a control loop diagram, where the estimator uses position and velocity of the WEC. The controller requires estimated and predicted f_e, as well as position and velocity of the WEC.

Figure 3.1 shows an example of a WEC control loop diagram, where the inputs to the WEC block are $f_e(t)$ and $f_{pto}^{opt}(t)$. The measurements of the device motion are used to estimate the instantaneous excitation force ($\tilde{f}_e(t)$). Then, using $\tilde{f}_e(t)$, a predictor[1] is used to forecast future excitation force values ($\bar{f}_e(t + t^*_{hor}|t)$), where $\bar{f}_e(t + t^*_{hor}|t)$ is the excitation force value at $t + t^*_{hor}$ predicted from the time instant t, $t^*_{hor} \in \{0, ..., t_{hor}\}$, and t_{hor} is the prediction horizon. The controller of the example shown in Figure 3.1 needs both $\tilde{f}_e(t)$ and $\bar{f}_e(t + t^*_{hor}|t)$, along with estimated position and velocity of the device, to calculate the optimal control force $f_{pto}^{opt}(t)$. This is further explained in Chapter 8 where, for the presented energy-maximising optimal control strategy, energy maximisation can only be achieved by having full (instantaneous and future) knowledge of the excitation force. In other words, the external input $f_e(t)$ has to be known over the time window in which energy absorption is being optimised. However, it should be noted that Figure 3.1 shows just one possible control loop diagram as an example, but different researchers have shown different approaches to calculate the optimal control force [45].

A possible variation of the diagram in Figure 3.1 is to change the measurements used by the estimator. As shown in Section 3.2, the measurements used by the estimator do not necessarily have to be position and velocity of the device, although most of the f_e estimators in the literature use position and velocity measurements of the device. It should be noted that, the estimation strategy to be applied on a real WEC should

---

[1] Note that the words forecast and predict (as well as their derived forms) are used interchangeably.

be chosen at the design stage of the device, since the measurements required by the estimator could affect the equipment installed on the device.

Another possible variation of the diagram in Figure 3.1 is that the controller may not require knowledge of future f_e (as shown, for example, in [70, 122, 164]) and, in such a case, the block with the predictor can be omitted. However, since the majority of the energy maximising control strategies require knowledge of f_e in the near future [45, 155], short-term f_e predictors are essential and, hence, different available short-term forecasting strategies should be studied.

A review of the different f_e estimation and short-term forecasting techniques available in the literature is carried out in Sections 3.2 and 3.3, respectively. In the case of the forecasting techniques review, it should be noted that most of the f_e predictors available in the literature are adapted from studies focused on wave elevation η prediction, which is a wider topic. Therefore, not only short-term f_e forecasting techniques are reviewed in Section 3.3, but also short-term η forecasting strategies.

Finally, it should be clarified that, in this thesis, only short-term η or f_e forecasting is addressed, which differs from mean sea water level [178], significant wave-height [44] or, more generally, sea-state forecasting [153]. Sea-state forecasting consists of predicting wave statistics, for time horizons ranging from 1 to 48 hours, as opposed to short-term wave elevation forecasting, which predicts η a few seconds into the future. The reader interested in sea-state forecasting is referred to [153] for a comparison between methods based on meteorological models and time series-based approaches, for significant wave-height forecasting.

3.2 Excitation force estimation

For the sake of clarity, the f_e estimation strategies reviewed here are separated into three groups, depending on the measurements they use. To this end, the first set of estimators only consider wave elevation measurements to estimate f_e, while the estimators belonging to the second group only consider measurements of the device motion (χ, $\dot{\chi}$, and/or $\ddot{\chi}$). Finally, the third group of estimation strategies consider both device motion, and pressure measurements measured over the hull of the device.

3.2.1 Estimators using η measurements

The first estimation strategy, which only considers η measurements, is based on the convolution product between the wave elevation η and the excitation force kernel k_e, as shown in Equation (2.37). In spite of the simplicity associated with obtaining the f_e estimate by solving a convolution product, this estimator has three main drawbacks, which hampers its implementation in a real sea scenario:

1. The excitation force kernel k_e is non-causal [54]. Hence, future η values (at the device location) are required in order to estimate the instantaneous f_e acting on the device and, therefore, η must be predicted. For the prediction, the required prediction horizon time t_hor depends on the causalisation time (t_caus) of $k_\mathsf{e}(t)$. The causalisation time is the time that $k_\mathsf{e}(t)$ has to be shifted, to move all the non-zero values to positive t values; i.e. $k_\mathsf{e}(t) = k_\mathsf{e}^\mathsf{caus}(t + t_\mathsf{caus})$, with a sufficiently large t_caus so that $k_\mathsf{e}^\mathsf{caus}(t) = 0$ for any $t < 0$. In practice, t_caus depends on the geometry (and the size) of the device under analysis.
2. For non-axisymmetric bodies, k_e will be different, depending on the wave direction. Therefore, in a real sea-state scenario, the different directional components of η need to be known (or estimated) to estimate f_e.
3. Obtaining reliable η measurements in a real, multi-directional, sea scenario is a non-trivial task [5]. In fact, for floating devices, it is not possible to measure η at the WEC location, for obvious reasons. Therefore, it has to be estimated based on other measurable quantities from the device, or η measurements taken in the near proximity of the WEC (as explained in Section 3.3).

The estimator that only uses η measurements to compute the f_e estimate is further exemplified in Figure 3.2. It is shown that, using only past η measurements, the estimator first predicts future η values and then computes an estimate of the excitation force by solving a convolution term defined by the excitation force kernel k_e.

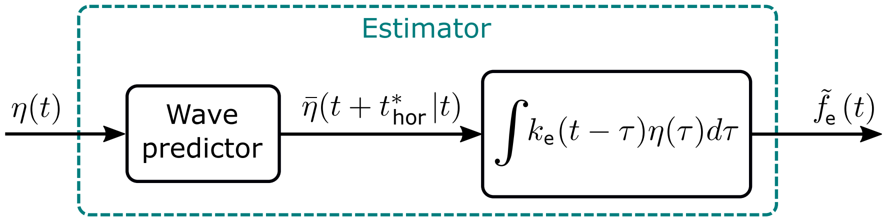

Figure 3.2: Diagram of a f_e estimator that uses wave elevation measurements to compute the excitation force estimate.

Due to its estimation principle, the strategy based on solving a Convolution with Predicted Wave Elevation is referred to as CPWE hereinafter. Despite the aforementioned drawbacks, the CPWE strategy is used in [83] and [84] to successfully estimate f_e in real tank tests, for a 0.15 m radius and 0.25 m draft cylinder. Due to the small scale of the device, the required casualisation time is around 1 s, for which an AR model gives reasonably accurate predictions of η, using only past values. However, by way of example, it should be noted that the causalisation time required for a 5 m radius and 10 m draft cylinder is ≈6 s, for which, depending on the sea state, an AR model may not provide an accurate enough η prediction. In [84], the η measurements are obtained by measuring η on a sensor placed laterally with respect to the WEC, perpendicular to the wave direction, where the wave measurement can be assumed equal to η at the WEC location, since unidirectional waves are considered.

In [25], the CPWE strategy is used to estimate not only actual, but future, values of f_e (between 8 and 24 s in the future), for a floating WEC subject to multidirectional waves. To this end, the prediction of η is carried out using up-wave information, provided by a Doppler radar positioned at the WEC location, using an Ensemble Kalman Filter (EnKF). Thus, the predicted η is used to estimate the actual and future f_e, which is then used to calculate the optimal control force $f_\mathrm{pto}^\mathrm{opt}$, using Model Predictive Control (MPC). Generally, it can be stated that the accuracy of the f_e estimate, using the CPWE strategy, depends on both the accuracy of the η prediction, and the precision of k_e. k_e can be calculated via the inverse Fourier transform of the frequency response function of the excitation force $\hat{F}_\mathrm{e}(\omega)$ which, in turn, can be computed using BEM codes, as for the example shown in Figure 2.6 (c) and (d); or it can be directly identified from physical or numerical wave tank tests, as shown in [78].

3.2.2 Estimators using WEC motion measurements

Omitting the use of η, the following estimation techniques require WEC motion measurements only to estimate f_e. Given the similarities between the estimation strategies which use motion measurements, they can all be described by the diagram shown in Figure 3.3. The only possible difference between the generic diagram and the strategies introduced in this subsection are the required measurements, which do not necessarily have to be the full set of three (position, velocity, and acceleration), as exemplified in Figure 3.3. It is shown that the observer estimates both f_e and motion of the WEC and, by use of the error in the estimate of the WEC motion (the motion estimate is compared with the real motion information), the f_e estimate is corrected.

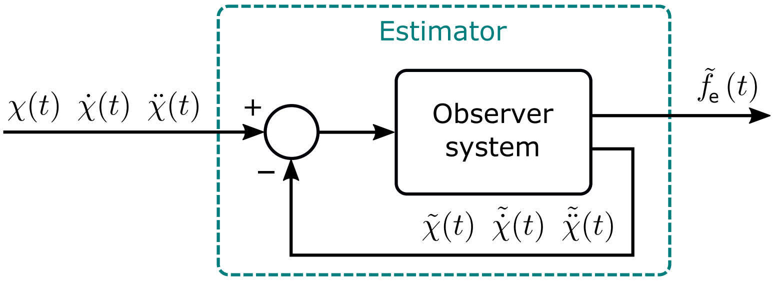

Figure 3.3: Example of a f_e estimation diagram that uses motion measurements from the WEC to compute the f_e estimate.

The first strategy, introduced in [121], considers f_e as an unknown input to the system, and estimates the force based exclusively on the device motion measurements, using a Kalman Filter (KF). The position and velocity of the device (along with its corresponding f_e) are estimated and compared to the measured position and velocity which, based on internal model principle [66], provides a surrogate measure of the accuracy of the f_e estimate. Therefore, the accuracy of the obtained f_e estimate depends on how accurate the model, used in the KF, represents the actual WEC. Since the dynamical model used to describe f_e is given by a Random Walk (RW) model, this strategy is termed KFRW. The KFRW strategy is also used in [190], in order to validate the estimator proposed in that study.

While the KFRW estimator uses a RW model to describe the f_e dynamics, the KFHO estimator uses a KF, in conjunction with a Harmonic Oscillator (HO) model, to describe the dynamics of f_e. This is the most commonly used excitation force estimation strategy in the literature. In [71, 106], the KFHO strategy is used along with a f_e predictor to illustrate how the estimated f_e can be used to predict future excitation force values, to be used for control purposes. Additionally, [105] proposes an extension of [106], where an approach for the calculation of the best parameters for the KFHO estimator, based on an optimisation process, is introduced. In [100], the KFHO estimator is used, in wave tank tests, to obtain a f_e estimate to apply observer-based control to a scaled Wave Star device [109]. The KFHO approach is used, along with a MIMO model of a WEC array in [138][2] and [193], to estimate the excitation force of different bodies of an array.

In [71, 105], a modification of the KFHO estimator is included, where the HO model is described by time-varying frequencies, allowing for estimation of the dominant frequencies of f_e. Since, for the treatment of time-varying frequencies, an Extended KF (EKF) needs to be employed, this strategy is hereinafter referred to as EKFHO. It should be noted that, in [71, 105], the researchers conclude that there is no significant improvement in performance using the EKFHO estimator, compared to the KFHO strategy. In addition to estimating the frequency of the instantaneous f_e, Fusco et al. [70] adapt the EKFHO approach to also estimate its instantaneous amplitude, which is required by their controller. A further extension is presented in [116], where the amplitude, frequency, and phase of the different components of the f_e signal are estimated.

Also considering f_e as an unknown input, the Receding Horizon Estimation (RHE) strategy estimates the excitation force without assuming any dynamical model for f_e, employing a receding horizon approach [121]. The authors of [121] claim that avoiding a dynamical model for f_e improves the obtained results. To this end, at each receding window, f_e is estimated by minimising a Quadratic Programming (QP)

---

[2] Note that the array expansion, along with the obtained estimation results, of [138] are shown in Chapter 7.

problem or, if no constraint for the device motion or control force is considered, the QP problem can be solved analytically.

Abdelrahman et al. [5] introduce the Fast Adaptive Unknown Input Estimation (FAUIE) strategy, which attempts to ensure fast and accurate estimation of f_e, by using proportional and integral terms of the state estimation error. The observer, which is designed by solving a set of Linear Matrix Inequalities (LMIs), is based on a fault estimation technique and considers nonlinear Lipschitz systems, which can be used to account for nonlinearities in the WEC device. In [5], the obtained f_e estimate is used as a reference signal for the proposed tracking control system.

The authors of the FAUIE present another estimation strategy, termed the Unknown Input Observer (UIO) [3]. The UIO strategy is designed by solving a set of LMIs, to robustly estimate the excitation force, along with other system states, while considering model uncertainties. Such an estimator is also used in [84] where, as in [3], f_e is estimated along with the velocity of the device, using measurements of the WEC position and the electric current of the PTO.

Coe et al. introduce, in [29], the Unified Linear Input & State Estimator (ULISE), which can be considered as a generalisation of the KF for systems with unknown inputs [187]. While a standard KF is composed of two stages (a *time update* and a *measurement update*) [32], the ULISE approach has a third stage, to account for estimation of the unknown input. Two variants of the ULISE strategy are presented in [29], one using only WEC motion information and another one using pressure measurements. For the estimator using pressure measurements, a model that relates total pressure to f_e is required which, in [29], is identified through wave tank tests (as detailed in [14]).

Using position and velocity measurements, the Adaptive Sliding Mode Observer (ASMO) strategy estimates f_e using an adaptive sliding mode observer [190]. The authors of this approach claim that the observer is robust to model uncertainties and that the estimate convergence time is low. In [190] and [191], the ASMO is compared to the KFRW and KFHO estimators, respectively, and, in both studies, the ASMO is shown to outperform the KF-based strategies.

3.2.3 Estimators using motion and pressure measurements

Among the set of estimators using measurements of both device motion and pressure over the WEC hull, the first strategy is termed EKFPS, since it uses an EKF along with Pressure Sensors measurements [1, 2]. Here, f_e estimation is carried out recursively by an EKF, using measurements of device position and pressure on the WEC hull. f_e is then modelled as the integration of the excitation pressure over the wetted WEC surface (S_wet in Figure 2.4), which assumes that f_e is given only by the Froude-Krylov force, neglecting the diffraction forces (see Equation (2.29)). Note that the EKFPS estimator is also described by the diagram shown in Figure 3.3, if only position $\chi(t)$ and pressure $p(t)$ measurements are considered (as opposed to position, velocity, and acceleration of the device).

The final estimation technique found in the reviewed literature is the Pressure Acceleration Displacement Estimation (PADE), proposed in [84]. As shown in Figure 3.4, PADE estimates f_e by subtracting all hydrodynamic forces (estimated using the measured WEC motion), other than f_e, from the total wave force (f_w), which can be calculated by integrating the pressure over the wetted surface of the WEC [84].

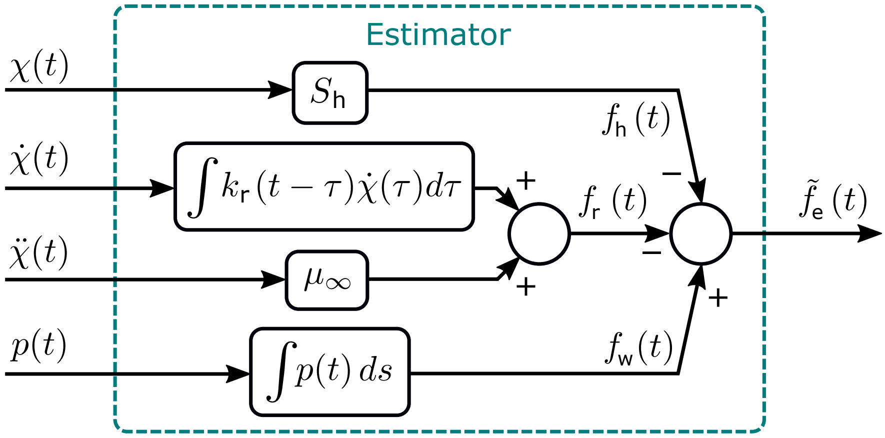

Figure 3.4: Diagram describing the PADE estimation strategy, as shown in [84].

3.3 Excitation force and η prediction

As mentioned in Section 3.1, most of the short-term forecasting strategies developed for wave energy applications deal with forecasting of η, rather than f_e. However, the strategies for η prediction can also be applied, in an analogous mode, for the prediction of f_e. In fact, the only studies that directly predict f_e, namely, [69, 103, 120, 138] and [163], use forecasting techniques that have been previously developed for short-term η forecasting as, for example, in [67]. Therefore, in order to provide a more comprehensive review of the short-term forecasting strategies developed for wave energy applications, this section focuses on the approaches developed for short-term η forecasting, although the studies that predict f_e are also mentioned.

In the literature, two main approaches are found for short-term η forecasting [67]. The first method predicts future η values at the WEC location, based on measurements taken at one or more points located at a certain distance from the WEC, as shown in Figure 3.5(a). The number of measurement points, required to obtain an accurate prediction, depends mainly on the directional spreading of the incoming waves and, for unidirectional sea-states, a single up-wave measurement point would lead to a deterministic prediction of η [115].

The second method, shown in Figure 3.5(b), uses only past measurements at the WEC location to predict η; that is, considering the measurements of η as a time series, future values can be predicted as a function of past values. From a hardware requirement point of view, the second method is simpler, mainly because it uses only measurements from the WEC itself, while the first method requires more equipment to measure η at different points. However, knowledge of up-wave information may improve the prediction, compared to that achieved by using only past measurements taken at the WEC location.

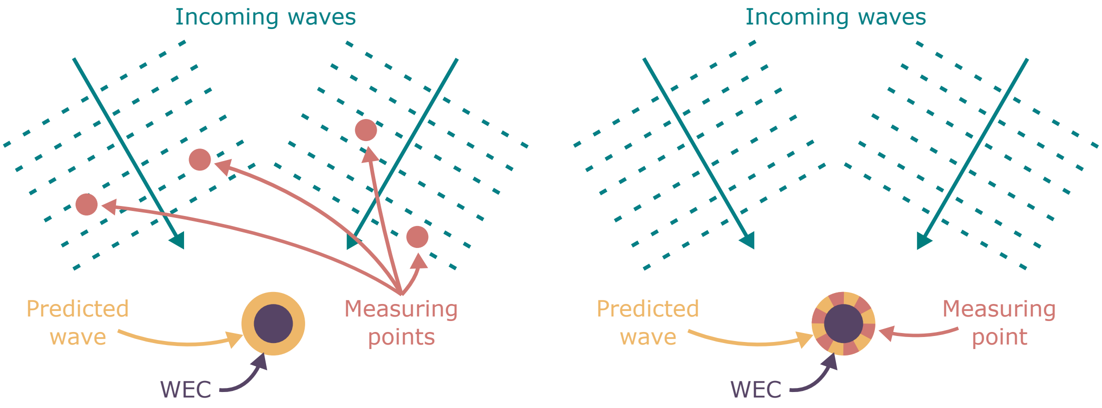

(a) Using distant measurements. **(b)** Based on the measurements of a single point.

Figure 3.5: Schematic of the two main methods to forecast free surface elevation: (a) using distant measurements and (b) based on the measurements of a single point.

Since several prediction strategies can be found in the literature for the two the methods shown in Figure 3.5, both methods are reviewed separately in the subsequent sections. To this end, Section 3.3.1 reviews the strategies using up-wave measurements, while the forecasting strategies that consider only past η measurements taken at the WEC location are mentioned in Section 3.3.2.

3.3.1 Strategies using up-wave measurements

Starting with the strategies using up-wave measurements, most of the approaches in the literature do not consider multidirectional waves, with the exception of [25] and [115]. In [25], an EnKF is used to predict the wave elevation at the WEC location, using wave elevation data in the vicinity of the WEC recorded with a Doppler radar. The strategy used in [115], which uses information of the wave spectrum, should theoretically lead to the optimal prediction of η, as explained in Section 6.2.1 for the unidirectional wave case.

Regarding the strategies using up-wave measurements, but without considering multi-directional waves, three different prediction strategies are found in the literature. The first two predictors are based on using a Finite Impulse Response (FIR) model [57, 114, 130, 131, 169], which only considers up-wave information, or using an AutoRegressive with eXogenous variables (ARX) model [114, 130, 131, 138], which considers both up-wave measurements and past η values at the WEC location. The third strategy decomposes the wave elevation into individual frequencies using the Fast Fourier Transform (FFT), propagates each frequency component using the dispersion relation, and reconstructs η at a different temporal and spatial point, as shown in [85, 86, 179].

3.3.2 Strategies using only past measurements

Regarding the methods that consider only past η (or f_e) measurements taken at the WEC location, shown in Figure 3.5(b), a number of forecasting approaches have been proposed as, for example, grey models [102, 104], cyclical models [114], sinusoidal extrapolation with an EKF [67], neural-networks [103], Direct Multi-Step (DMS) models [59, 139], ARMA models [76, 140], orthogonal basis function models [162], Gaussian process models [165] or, the most commonly used approach, the AR model [68, 69, 84, 120, 176].

In [67], a comparison between different prediction strategies (cyclical models, sinusoidal extrapolation using EKF, AR, neural networks, ARMA and particle filters) is carried out, and the simple AR model is found to achieve the most accurate predictions for the case of low-frequency swell waves, which are the most energetic waves and, thus, offer the most potential for wave energy conversion. In fact, since [67] was published, several researchers that propose new prediction strategies compare their results with those obtained using an AR model, usually concluding that there is no significant improvement with respect to the AR [114, 130, 162, 166]. However, even though Fusco and Ringwood [67] conclude that using an ARMA model does not result in any significant improvement with respect to the AR model, in [76], the authors claim that the predictions obtained using an ARMA model are more accurate than those obtained using an AR model.

3.4 Conclusions

After reviewing the state-of-the-art of the estimation and prediction of excitation force (or η in the case of prediction) for wave energy applications, it is possible to identify several areas for which further investigation is required. Some of these areas were addressed by the author during the course of the PhD, and compose the main contributions of this thesis.

- Given the large number of published excitation force estimation strategies, knowledge of their relative strengths and weaknesses is important and, to the author's knowledge, such a comprehensive comparison has not yet been performed. Reviews of different f_e estimators have been presented in [71, 84, 121] and [190]; however, these existing reviews only consider a maximum of three different estimation strategies. Additionally, most of the methods are evaluated using different sea data, making quantitative comparison impossible. Therefore, a critical and fair comparison of all estimation strategies available in the literature (11 strategies in total) is carried out, which is presented in Section 5.1.
- In Section 3.3.2, some inconsistency within the η forecasting results obtained in [67] (AR model) and [76] (ARMA model) is reported. To clarify the identified inconsistency and determine the advantages and disadvantages of the two approaches under the same conditions, a critical comparison of the AR and ARMA models is carried out in Section 6.1. Real wave data from three different locations is used in the comparison to test the models under realistic conditions.
- In [67], the AR model is found to be one of the most accurate η predictors. To assess the capabilities of the AR model for wave energy applications, an analysis of the performance of the AR models is carried out in Section 6.2. To this end, two accuracy limits for the theoretical best achievable prediction are used to evaluate to what extent the AR model can be improved.
- Finally, given that the objective of estimating and forecasting the excitation force is to provide an input to optimal control strategies, it is important to know the sensitivity of such an optimal control strategy to the accuracy of the f_e estimate and forecast. Thus, Chapter 8 studies how the f_e estimation/forecasting errors, which are reported in Chapters 5 and 6, affect the performance of a receding-horizon moment-matching-based optimal control strategy.

4

Radiation convolution term approximation

Contents

As introduced in Section 2.2.4, several methods can be found in the literature that attempt to approximate the radiation convolution term of Cummins' equation (Equation (2.36)), which accounts for the memory effects of the fluid. Among the different identification utilities, the Finite Order Approximation by Moment-Matching, or FOAMM, toolbox is, to the author's knowledge, the most recent one. The following section (briefly) introduces the theory behind FOAMM, along with an application case. Note that, for brevity, the details of the structure, organisation, characteristics, operation modes, and options of the toolbox, along with a step-by-step example and some using recommendations are given in Appendix A.

A comparison between FOAMM and the other available radiation convolution approximation utilities is detailed in Section 4.2. Finally, in Section 4.3, an application case of the extension of the moment-based identification strategy for MIMO systems, which is yet not included in the FOAMM toolbox, is presented.

4.1 Finite-Order Approximation by Moment-Matching

The identification application FOAMM is based on recent advances in model order reduction by moment-matching, which has been developed over several studies (see, for example, [8, 161]), and is able to compute a parametric model of both the radiation convolution term and the complete force-to-velocity WEC dynamics (wave excitation force to device velocity) [47]. The main characteristic of the moment-matching strategy is that the identified parametric model *exactly* matches the frequency response of the target system, at a set of user-selected frequencies. Additionally, this moment-based strategy preserves some of the physical properties of the identified model, such as input-output stability.

In the following subsections, the theoretical background behind the moment-based strategy, along with an application case, are given.

4.1.1 Moment-based theory

For an extensive discussion on the specific underlying mathematical principles, the interested reader is referred to [47]. First, the theory of the force-to-velocity approximation is defined and, then, the theory of the radiation convolution term approximation. Similar to other available identification utilities, the FOAMM toolbox is developed for SISO systems and, therefore, when referring to the WEC equations of Section 2.2.3, it should be noted that a WEC with a single DoF is considered.

4.1.1.1 Force-to-velocity approximation

Since the development of model order reduction by moment-matching theory is based on a state-space representation of the target system, Equation (2.36) needs to be re-written in a more suitable structure, for which the following state-space representation is proposed:

$$\dot{x}^{\mathsf{MM}}(t) = A_{\mathsf{ss}}^{\mathsf{MM}} x^{\mathsf{MM}}(t) + B_{\mathsf{ss}}^{\mathsf{MM}} f_{\mathsf{ext}}^{\mathsf{MM}}(t), \tag{4.1a}$$

$$y^{\mathsf{MM}}(t) = C_{\mathsf{ss}}^{\mathsf{MM}} x^{\mathsf{MM}}(t), \tag{4.1b}$$

where $x^{\mathsf{MM}}(t) = [\chi(t),\, \dot{\chi}(t)]^{\intercal} \in \mathbb{R}^2$ is the state-vector of the continuous-time model and $y^{\mathsf{MM}}(t) = \dot{\chi}(t) \in \mathbb{R}^1$ the output of the system, assuming velocity as the measurable output of the device. Since the radiation convolution term is non-parametric, at this point, it is included as one of the inputs of System (4.1), $f_{\text{ext}}^{\text{MM}}(t) \in \mathbb{R}$, as

$$f_{\text{ext}}^{\text{MM}}(t) = f_{\text{e}}(t) - \int_{-\infty}^{t} k_{\text{r}}(t-\tau)\dot{\chi}(\tau)d\tau, \tag{4.2}$$

while the matrices $A_{\text{ss}}^{\text{MM}} \in \mathbb{R}^{2\times 2}$, $B_{\text{ss}}^{\text{MM}} \in \mathbb{R}^{2}$ and $C_{\text{ss}}^{\text{MM}} \in \mathbb{R}^{2}$ are given by

$$A_{\text{ss}}^{\text{MM}} = \begin{bmatrix} 0 & 1 \\ -M^{*}S_{\text{h}} & 0 \end{bmatrix}, \; B_{\text{ss}}^{\text{MM}} = \begin{bmatrix} 0 \\ M^{*} \end{bmatrix}, \; C_{\text{ss}}^{\text{MM}} = \begin{bmatrix} 0 \\ 1 \end{bmatrix}^{\text{T}}, \tag{4.3}$$

respectively. Note that if the WEC under analysis has any other linear stiffness or damping term, it should be included in the definition of System (4.1), to allow for an identification of the complete force-to-velocity dynamics. The input f_{e} is expressed as a *signal generator*, written in implicit form as

$$\dot{x}_{\text{e}}^{\text{MM}}(t) = A_{\text{sg}}^{\text{MM}} x_{\text{e}}^{\text{MM}}(t), \tag{4.4a}$$

$$f_{\text{e}}(t) = C_{\text{sg}}^{\text{MM}} x_{\text{e}}^{\text{MM}}(t), \tag{4.4b}$$

where $x_{\text{e}}^{\text{MM}}(t) \in \mathbb{R}^{n_{\text{ss}}}$, $A_{\text{sg}}^{\text{MM}} \in \mathbb{R}^{n_{\text{ss}}\times n_{\text{ss}}}$, $C_{\text{sg}}^{\text{MM}} \in \mathbb{R}^{n_{\text{ss}}}$ and the triple $\left(C_{\text{sg}}^{\text{MM}}, A_{\text{sg}}^{\text{MM}}, x_{\text{e}}^{\text{MM}}(0)\right)$ is assumed to be minimal[1]. The matrix $A_{\text{sg}}^{\text{MM}}$ can be written, in a real block-diagonal form, as

$$A_{\text{sg}}^{\text{MM}} = \bigoplus_{i=1}^{\beta^{\text{MM}}} \begin{bmatrix} 0 & \omega_i \\ -\omega_i & 0 \end{bmatrix}, \tag{4.5}$$

where $n_{\text{ss}} = 2\beta^{\text{MM}}$, with $\beta^{\text{MM}} > 0$ the number of interpolation frequencies, and the matrix $C_{\text{sg}}^{\text{MM}}$ is chosen so that $\left(C_{\text{sg}}^{\text{MM}}, A_{\text{sg}}^{\text{MM}}\right)$ is observable. In Equation (4.5), the symbol $\bigoplus_{i=1}^{\beta^{\text{MM}}}$ stands for the direct sum of β^{MM} matrices. Note that each $\omega_i > 0$ represents a desired interpolation frequency for the moment-matching-based model reduction process, i.e. a frequency where the transfer function of the parametric model exactly matches the transfer function of the target system.

Following the theory developed in [47], the family of models (parametrised on G^{MM}) for the force-to-velocity response of the target WEC, achieving moment-matching at the set of frequencies $\mathcal{F} = \{\omega_1, ..., \omega_{\beta^{\text{MM}}}\}$, can be described as

$$\tilde{H}_{\mathcal{F}} : \begin{cases} \dot{\Theta}^{\text{MM}}(t) = (A_{\text{sg}}^{\text{MM}} - G^{\text{MM}} C_{\text{sg}}^{\text{MM}})\Theta^{\text{MM}}(t) + G^{\text{MM}} f_{\text{e}}(t), \\ \theta^{\text{MM}}(t) = V^{\text{MM}}\Theta^{\text{MM}}(t), \end{cases} \tag{4.6}$$

---

[1] The minimality of the triple $(C_{\text{sg}}^{\text{MM}}, A_{\text{sg}}^{\text{MM}}, x_{\text{e}}^{\text{MM}}(0))$ implies the observability of $(C_{\text{sg}}^{\text{MM}}, A_{\text{sg}}^{\text{MM}})$ and the excitability of $(A_{\text{sg}}^{\text{MM}}, x_{\text{e}}^{\text{MM}}(0))$ [129].

where $\theta^{\mathsf{MM}}(t) \approx \dot{\chi}(t)$, and V^{MM} represents the so-called *moment-domain equivalent* of the velocity of the device $\dot{\chi}(t)$ [47], which can be computed using the frequency-domain data, obtained by BEM solvers, as

$$V^{\mathsf{MM}} = C_{\mathsf{e}}^{\mathsf{MM}} \Phi^{\mathsf{MM}}, \tag{4.7a}$$

$$\Phi^{\mathsf{MM}} = \left[\left(\mathbb{I}_{n_{\mathsf{ss}}} + \phi^{\mathsf{MM}} R^{\mathsf{MM}^{\intercal}} \right)^{-1} \phi^{\mathsf{MM}} \right]^{\intercal}, \tag{4.7b}$$

$$\phi^{\mathsf{MM}} = (\mathbb{I}_{n_{\mathsf{ss}}} \otimes C_{\mathsf{ss}}^{\mathsf{MM}}) \left(A_{\mathsf{sg}}^{\mathsf{MM}} \hat{\oplus} A_{\mathsf{ss}}^{\mathsf{MM}} \right)^{-1} (\mathbb{I}_{n_{\mathsf{ss}}} \otimes -B_{\mathsf{ss}}^{\mathsf{MM}}). \tag{4.7c}$$

In Equation (4.7), the symbol $\hat{\oplus}$ denotes the *Kronecker sum* [21] and $R^{\mathsf{MM}} \in \mathbb{R}^{n_{\mathsf{ss}} \times n_{\mathsf{ss}}}$ is a block-diagonal matrix defined by

$$R^{\mathsf{MM}} = \bigoplus_{i=1}^{\beta^{\mathsf{MM}}} \begin{bmatrix} \mathsf{real}\,(K_{\mathsf{r}}(\omega_i)) & \mathsf{imag}\,(K_{\mathsf{r}}(\omega_i)) \\ -\mathsf{imag}\,(K_{\mathsf{r}}(\omega_i)) & \mathsf{real}\,(K_{\mathsf{r}}(\omega_i)) \end{bmatrix}, \tag{4.8}$$

where K_{r} is defined as shown before in Equation (2.40). It should be noted that the model of System (4.6) has the same dimension of the final finite order parametric model, $n_{\mathsf{ss}} = 2\beta^{\mathsf{MM}}$. In order to better understand the concept of family of models, Figure 4.1 shows the frequency response of different models contained in the same family, along with the target frequency response. It can be observed that all the frequency responses coincide at the interpolation frequency (≈2 rad/s).

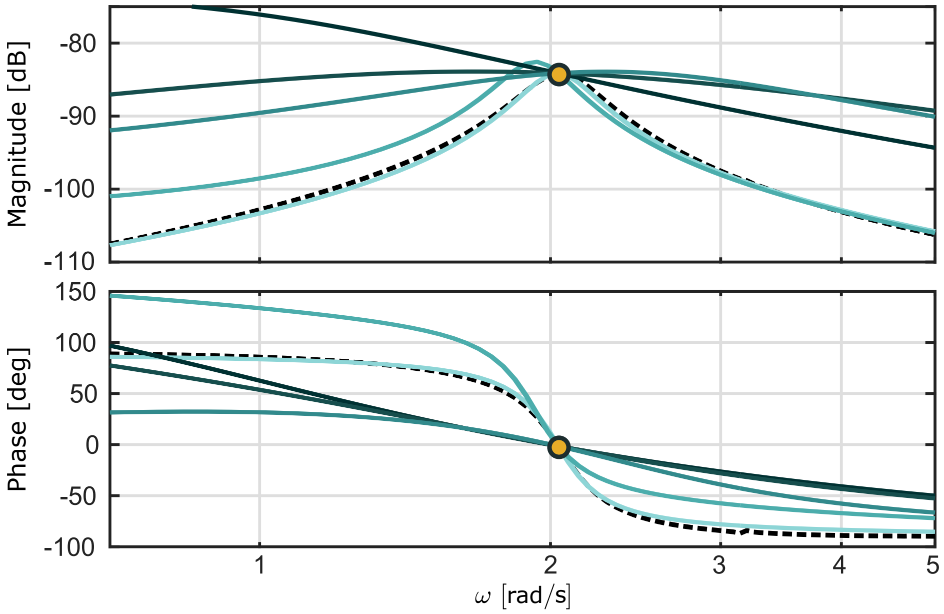

Figure 4.1: Example of a family of models, along with the target frequency response (dashed-black line), and the interpolation frequency (orange dot).

The additional flexibility provided by G^{MM}, can be exploited to arbitrarily assign the eigenvalues of the reduced order model of System (4.6). In FOAMM, the set of desired eigenvalues is chosen within an optimisation formulation, which minimises the Euclidean distance between the device force-to-velocity frequency response $H(\omega)$, shown in Equation (2.35), and the frequency response of the parametric family of Equation (4.6) $\tilde{H}(\omega)$ which, for the set of frequencies $\mathcal{F}$, can be obtained from the transfer function

$$\tilde{H}_{\mathcal{F}}(s) = V^{\mathsf{MM}} \left[s\mathbb{I}_{n_{\mathsf{ss}}} - (A_{\mathsf{ss}}^{\mathsf{MM}} - G^{\mathsf{MM}} C_{\mathsf{sg}}^{\mathsf{MM}}) \right]^{-1} G^{\mathsf{MM}}. \tag{4.9}$$

Note that the frequency-dependent device parameters $A_{\mathsf{r}}(\omega)$ and $B_{\mathsf{r}}(\omega)$ are calculated at a finite number of user-defined frequencies, using BEM solvers. However, the approximation of the parametric model can be computed on a reduced (also user-selected) frequency range, with a frequency step of $\Delta\omega$, and lower and upper bound frequencies of the range given by ω_l and ω_u, respectively. As further discussed in Section 4.1.2, the definition of such a frequency range depends explicitly on the application under analysis. Defining the complex-valued vectors H_{fr} and $\tilde{H}_{\mathsf{fr}}$ as,

$$\begin{aligned} H_{\mathsf{fr}} &= \begin{bmatrix} H(\omega_l) & H((\omega_l + \Delta\omega)) & \cdots & H((\omega_u)) \end{bmatrix}, \\ \tilde{H}_{\mathsf{fr}} &= \begin{bmatrix} \tilde{H}_{\mathcal{F}}(\omega_l) & \tilde{H}_{\mathcal{F}}((\omega_l + \Delta\omega)) & \cdots & \tilde{H}_{\mathcal{F}}((\omega_u)) \end{bmatrix}, \end{aligned} \tag{4.10}$$

respectively, the proposed optimisation procedure to assign the eigenvalues $\Sigma_{\mathsf{opt}}^{\mathsf{MM}}$ of the parametric model of System (4.6) can be formulated using least-squares optimization, via:

$$\Sigma_{\mathsf{opt}}^{\mathsf{MM}} = \arg \min_{\Sigma^{\mathsf{MM}}} \| H_{\mathsf{fr}} - \tilde{H}_{\mathsf{fr}} \|_2^2, \tag{4.11}$$

where the elements of the set $\Sigma_{\mathsf{opt}}^{\mathsf{MM}}$ are chosen to have a negative real part, so that System (4.6) is internally stable.

4.1.1.2 Radiation convolution term approximation

Since the radiation convolution term represents an LTI system by itself, with the velocity of the device $\dot{\chi}$ as input, an analogous procedure to the one presented for the force-to-velocity identification can be applied to such a system. To this end, the velocity can be expressed as a linear signal generator, as shown for f_{e} in System (4.4),

$$\dot{x}_{\dot{\chi}}^{\mathsf{MM}}(t) = A_{\mathsf{sg}}^{\mathsf{MM}} x_{\dot{\chi}}^{\mathsf{MM}}(t), \tag{4.12a}$$

$$\dot{\chi}(t) = C_{\mathsf{sg}}^{\mathsf{MM}} x_{\dot{\chi}}^{\mathsf{MM}}(t). \tag{4.12b}$$

Thus, as in System (4.6), a family of models can be defined for the convolution term subsystem, that achieve moment-matching at the set of frequencies $\mathcal{F}$, as

$$\tilde{K}_{\mathsf{r}_{\mathcal{F}}} : \begin{cases} \dot{\Theta}^{\mathsf{MM}}(t) = (A_{\mathsf{sg}}^{\mathsf{MM}} - G^{\mathsf{MM}} C_{\mathsf{sg}}^{\mathsf{MM}}) \Theta^{\mathsf{MM}}(t) + G^{\mathsf{MM}} \dot{\chi}(t), \\ \theta^{\mathsf{MM}}(t) = Y_K^{\mathsf{MM}} \Theta^{\mathsf{MM}}(t), \end{cases} \tag{4.13}$$

where, for the radiation convolution term approximation, $\theta^{\mathsf{MM}}(t) \approx f_{\mathsf{r}}^{\mathsf{c}}(t)$, and the moment-domain equivalent of the output (radiation convolution force), is now given as $Y_K^{\mathsf{MM}} = C_{\mathsf{sg}}^{\mathsf{MM}} R^{\mathsf{MM}}$. Finally, the new G^{MM} can be obtained solving the following optimisation procedure

$$\Sigma_{\mathsf{opt}}^{\mathsf{MM}} = \arg\min_{\Sigma^{\mathsf{MM}}} \|K_{\mathsf{r_{fr}}} - \tilde{K}_{\mathsf{r_{fr}}}\|_2^2, \tag{4.14}$$

where, as shown in Equation (4.10), the vectors $K_{\mathsf{r_{fr}}}$ and $\tilde{K}_{\mathsf{r_{fr}}}$ can be obtained from the frequency response $K_{\mathsf{r}}(\omega)$ (defined as shown in Equation (2.40)) and from the frequency response of the identified model, respectively.

4.1.2 Application Case Study

To illustrate the performance of the moment-matching-based identification method, the float body of an OPT-like (Ocean Power Technologies) [112] full-scale heaving point absorber WEC is selected as application case, which is shown in Figure 4.2. The hydrodynamic coefficients $D_{\mathsf{r}}(\omega)$ and $A_{\mathsf{r}}(\omega)$, computed using the BEM solver WAMIT, along with the force to velocity and the radiation convolution frequency responses $H(\omega)$ and $K_{\mathsf{r}}(\omega)$, respectively, are shown in Figure 4.3.

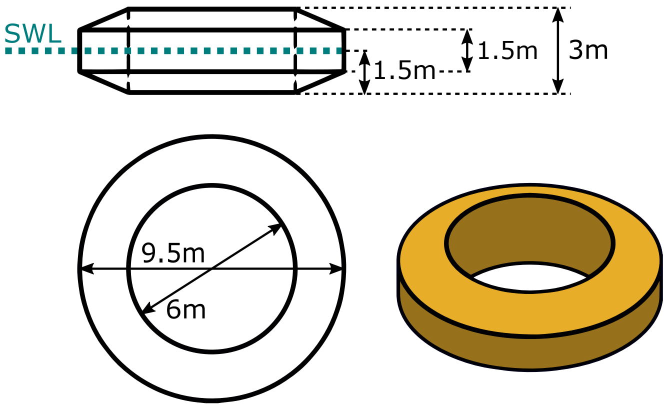

Figure 4.2: Sketch of the float of an OPT-like device, with the considered dimensions.

It can be seen in Figure 4.3 that the hydrodynamic coefficients have been computed over a frequency range from 0.01 to 10 rad/s. However, ocean peak periods are usually between 3 and 16 s [145], which implies that the frequency range of the input of the system, lies, approximately, between 0.4 and 2.1 rad/s. Therefore, by choosing a frequency range from ω_l =0.3 rad/s and ω_u =3 rad/s for the frequency domain identification method, it can be ensured that the identified models will accurately represent the target system for all the relevant input frequencies.

The irregular waves, considered in this application case, are generated from a JONSWAP spectrum (H_{s} = 2 m, T_{p} = 8 s, and γ = 3.3). As shown in Figure

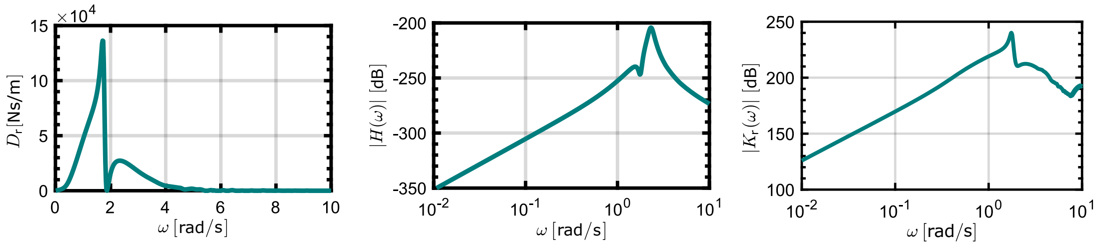

(a) Radiation damping D_r.

(b) $H(\omega)$ magnitude.

(c) $K_r(\omega)$ magnitude.

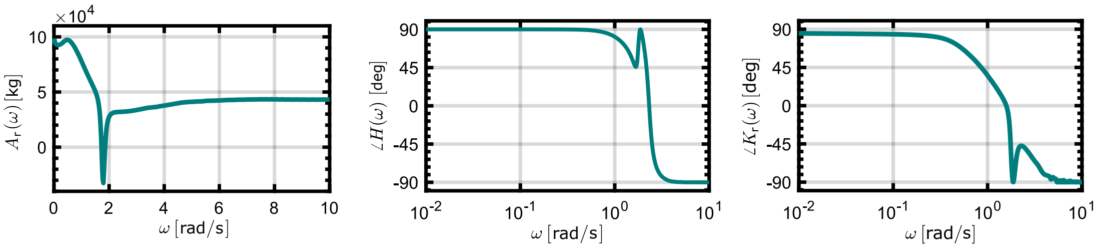

(d) Radiation added mass A_r.

(e) $H(\omega)$ phase.

(f) $K_r(\omega)$ phase.

Figure 4.3: Device characteristics: (a) radiation damping, (d) radiation added-mass, force-to-velocity frequency response $H(\omega)$ ((b) magnitude, (e) phase), and radiation convolution frequency response $K_r(\omega)$ ((c) magnitude, (f) phase).

4.4, all the non-zero values of the spectrum lie in the frequency range selected to approximate the parametric model, which is highlighted with a white area in all the following graphs of this section.

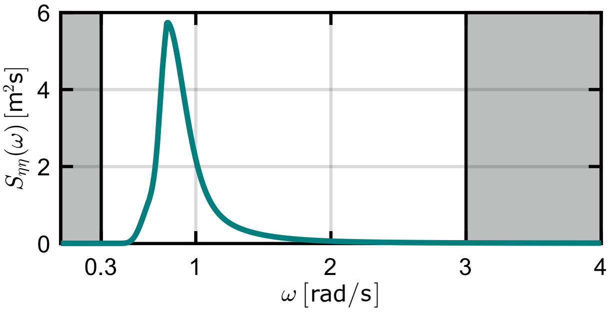

Figure 4.4: JONSWAP SDF with $H_s = 2$ m, $T_p = 8$ s, and $\gamma = 3.3$.

4.1.2.1 Force-to-velocity parametric model identification

In this subsection, the results obtained for the model order reduction of the force-to-velocity frequency response $H(\omega)$ are discussed. After the frequency range is selected, which is done by inspecting the spectrum of the input, depicted in Figure 4.4, the first step of the moment-matching-based identification technique is to select a set of suitable interpolation frequencies. A sensible choice for a first interpolation point can be made by inspecting $H(\omega)$ (Figures 4.3 (b) and (e)): the resonant frequency of the device represents a key interpolation point, which, in this case, is approximately 2.3 rad/s. Figure 4.5(a) shows the target frequency response of the WEC $H(\omega)$, computed with the hydrodynamic coefficients, along with the frequency response of the parametric model obtained by applying the moment-matching technique $\tilde{H}_{\{2.3\}}(\omega)$. It can be immediately observed that the approximated model exactly matches the target frequency response at the chosen interpolation point (2.3 rad/s). Furthermore, when choosing three interpolation points, the approximation of $H(\omega)$ improves significantly, as illustrated in Figure 4.5(b).

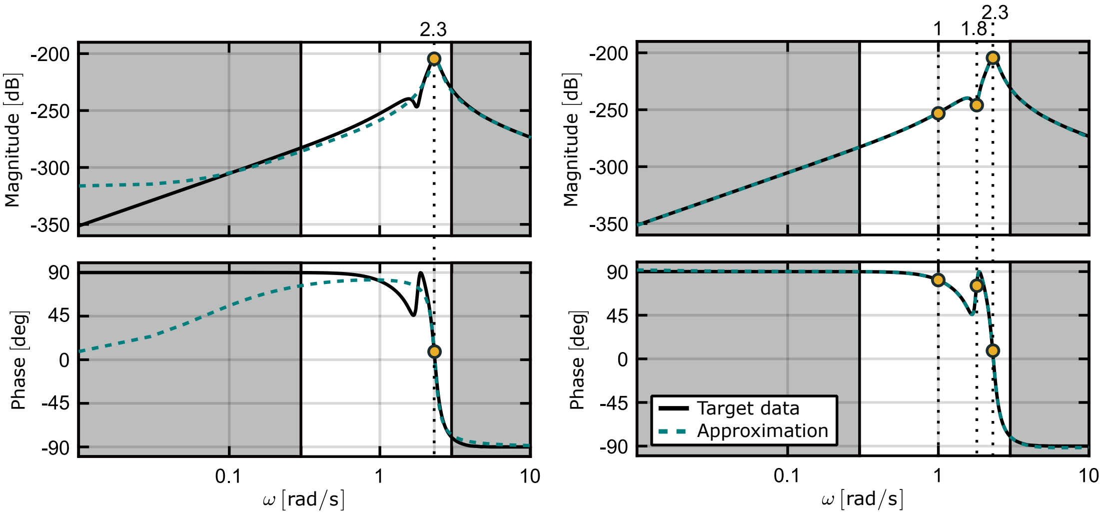

(a) Approximation using a single interpolation frequency (orange dot). MAPE≈0.25.

(b) Approximation using three interpolation frequencies (orange dots). MAPE≈0.002.

Figure 4.5: Force-to-velocity frequency response computed with the target frequency-domain hydrodynamic coefficients and the moment-matching parametric model frequency response for (a) one and (b) three interpolation frequencies (orange dots).

Figure 4.6 shows the time-domain response of the reduced order model $\tilde{H}_{\{1,1.8,2.3\}}$ for irregular waves, along with the steady-state response computed from $H(\omega)$ for the same wave input. It can be observed that, after the transient response, the steady-state behaviour of the approximated model converges to the target steady-state output. Note that, since FOAMM is a frequency-domain identification method, it can only guarantee steady-state matching for a set of user selected frequencies, and not transient behaviour. However, if required, such transient behaviour can be shaped with an appropriate selection of the internal dynamics of the computed model.

4.1.2.2 Radiation impulse response parametric model identification

In this subsection, the moment-matching identification framework is applied to obtain a parametric form for the radiation kernel $K_r(\omega)$, as defined in Equation (2.40). Figure 4.7(a) shows the Bode diagram of the radiation convolution frequency

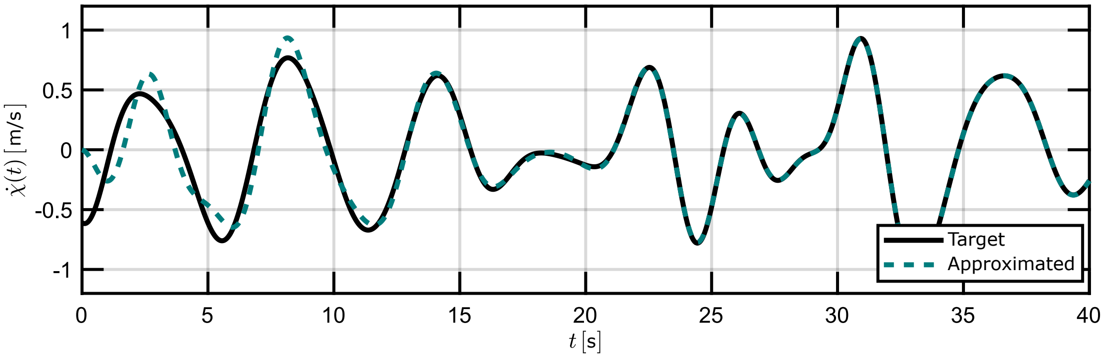

Figure 4.6: Comparison between the time-domain output of the reduced order model $\tilde{H}_{\{1,1.8,2.3\}}(\omega)$ (solid-blue), and the force-to-velocity frequency response $H(\omega)$ (dashed-black).

response computed from the frequency-domain hydrodynamic coefficients and the obtained parametric model frequency response considering a single interpolation point $\tilde{K}_{\mathrm{r}_{\{1.75\}}}(\omega)$. From Figure 4.7, the improvement on the approximation accuracy when considering three interpolation points (Figure 4.7(b)), as opposed to a single approximation frequency (Figure 4.7(a)), can be observed.

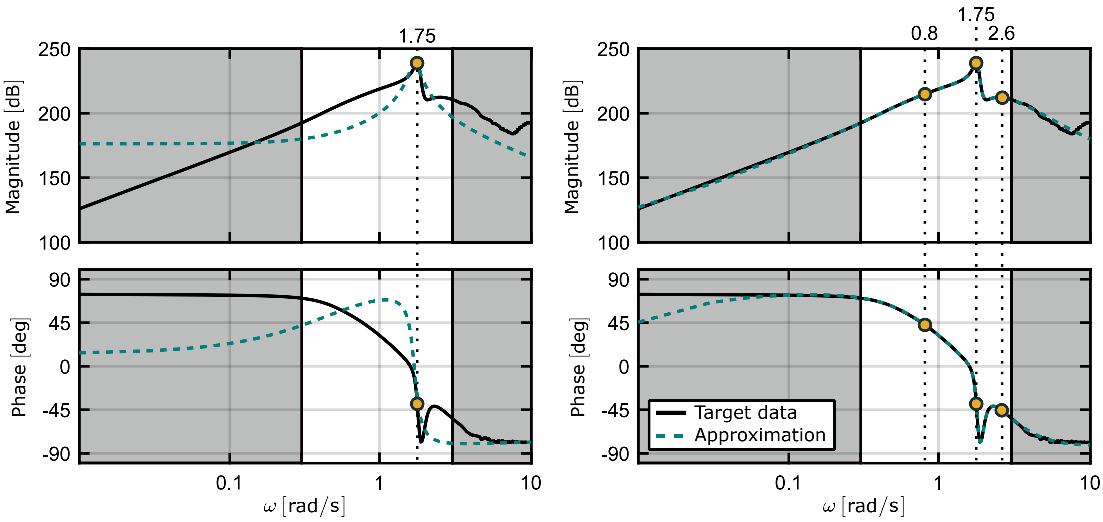

(a) Approximation using a single interpolation frequency (orange dot). MAPE≈0.63.

(b) Approximation using three interpolation frequencies (orange dots). MAPE≈0.004.

Figure 4.7: Radiation impulse frequency response computed with the target frequency-domain hydrodynamic coefficients and the moment-matching parametric model frequency response for (a) one and (b) three interpolation frequencies (orange dots).

As mentioned in Section 2.2.4, the frequency response of the radiation kernel has a set of particular properties [148] which, ideally, the identified parametric model should preserve. Among the implication of those physical properties, the transfer function of the device has the following structural characteristics. To begin with, since the impulse response kernel of the radiation should tend to 0 ($\lim_{t\to\infty} k_{\text{r}}(t) = 0$), the first property of the radiation subsystem is that it should be input-output stable. Furthermore, since the radiation frequency response is 0 when ω tends to 0 or infinity ($\lim_{\omega\to 0} K_{\text{r}}(\omega) = 0$ and $\lim_{\omega\to\infty} K_{\text{r}}(\omega) = 0$, respectively), the obtained model should have a zero at the origin, and be strictly proper. Figure 4.8(a) depicts the pole-zero map of the transfer function of the approximated model obtained using three interpolation frequencies. It can be seen that such a parametric model displays all the desired properties: a zero in the origin, one pole more than the number of zeros (therefore, is strictly proper), and all the poles have a negative real part (the model is stable).

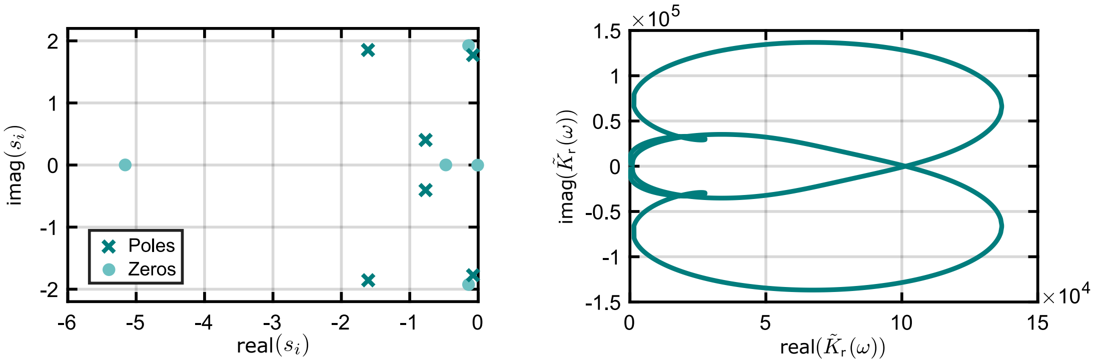

(a) Pole-zero map of $\tilde{K}_{\text{r}_{\{0.8,1.75,2.6\}}}(\omega)$, where the set s_i indicates the set of poles of $\tilde{K}_{\text{r}_{\{0.8,1.75,2.6\}}}(\omega)$.

(b) Nyquist diagram of $\tilde{K}_{\text{r}_{\{0.8,1.75,2.6\}}}(\omega)$.

Figure 4.8: (a) Pole-zero map, and (b) Nyquist diagram, of the moment-matching parametric model of the radiation force kernel $\tilde{K}_{\text{r}_{\{0.8,1.75,2.6\}}}(\omega)$.

The last, but no less important, of the properties of the radiation convolution subsystem is passivity. Provided that the results obtained from the BEM solver are accurate, $K_{\text{r}}(\omega)$ should be passive and so should $\tilde{K}_{\text{r}}(\omega)$. To demonstrate that the models approximated by the moment-matching technique are usually inherently passive, Figure 4.8(b) depicts the Nyquist diagram of $\tilde{K}_{\text{r}_{\{0.8,1.75,2.6\}}}(\omega)$. It is shown that the real-part of the approximated frequency response is always positive and, therefore, the system is passive (the reader is referred to [97] for a comprehensive demonstration on the passivity conditions for a linear system). Note that passivity is not explicitly ensured by FOAMM; however, as discussed in [48], a nonlinear constraint can be added to the optimisation process defined in Equation (4.14) to explicitly guarantee passivity, which will be included in FOAMM in the future.

In Figure 4.9, the quality of the time-domain response of the approximated model is further exemplified, where the similarities of both radiation impulse responses, computed using the target $K_{\text{r}}(\omega)$ and the reduced order model $\tilde{K}_{\text{r}_{\{0.8,1.75,2.6\}}}(\omega)$, are shown.

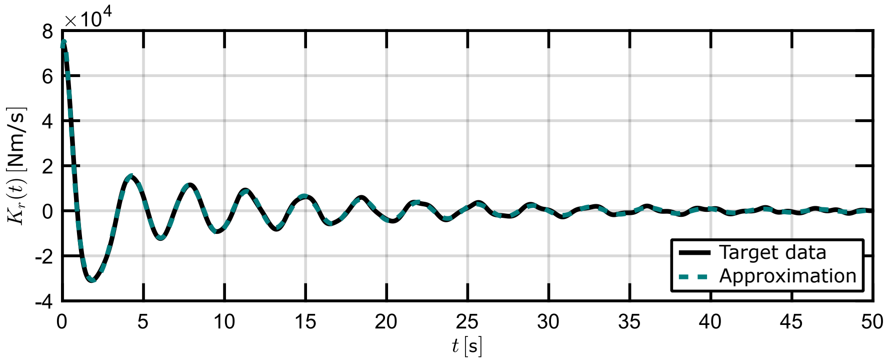

Figure 4.9: Comparison between the radiation impulse response computed with the target frequency-domain data and the impulse response of $\tilde{K}_{\{0.8,1.75,2.6\}}$.

From Figures 4.5 and 4.7, one can notice that, for the same model order, the approximation error obtained for $H(\omega)$ is usually lower[2] than that obtained for $K_{\text{r}}(\omega)$. This can be reasoned by the fact that the dynamics of the radiation convolution system are absorbed by the force-to-velocity dynamics of the device [47].

Additionally, as shown in System (2.41), two states more have to be added to the radiation convolution SS model in order to define a SS model that characterises the complete WEC dynamics, while the force-to-velocity SS model represents the complete WEC system. Therefore, considering the two extra states, needed to express the complete force-to-motion dynamics of the device, in addition to the higher order, usually required to accurately parametrise $K_{\text{r}}(\omega)$ as opposed to $H(\omega)$, using the force-to-velocity mode of FOAMM represents a more sensible choice than using approximating the radiation convolution subsystem. However, it should be noted that the choice of the approximation mode (force-to-velocity or radiation subsystem) of FOAMM highly depends on the application case. For example, even though low-order force-to-velocity SS models are optimal for WEC motion simulation due to their computational requirements, they may not be valid for some optimal control strategies, for which an accurate definition of the radiation convolution system is required.

4.2 Comparison of identification methods

In order to show the comparative performance of FOAMM, this section provides a critical comparison, both in the frequency and time domain, between the different utilities available to identify parametric models of radiation convolution subsystems, namely, FDI toolbox, BEMIO application, and Prony's method, which have been

---

[2] Such difference is more clear for the example provided in Section A.2, where an order two SS system is enough to characterise the complete force-to-velocity dynamics, while (at least) 4 states are necessary to approximate the radiation subsystem.

previously introduced in Section 2.2.4. The methods are compared in terms of approximation quality, model order, and preservation of the physical characteristics of the radiation subsystem. To cover a broad range of application cases and highlight potential shortcoming of identification methods, a total of six different WEC systems is considered.

4.2.1 Radiation subsystem parameterisation utilities

In this subsection, the options that the different radiation convolution subsystem parameterisation utilities, currently available in the literature, comprise are introduced. It should be noted that the underlying theory of each different method is kept to minimum herein and, therefore, the reader is referred to the relevant references (mentioned in each subsection). Additionally, the different utilities are introduced in order of release date, starting with the earliest strategy[3].

4.2.1.1 FDI toolbox

This software runs in MATLAB, and it requires the user to have the commercially available *signal processing toolbox* in order to operate it. However, as explained in [149], alternative functions can be implemented by the user in order to avoid using the signal processing toolbox. The application can be downloaded for free from [172]. The FDI toolbox requires the user to provide the vectors containing the frequency-domain hydrodynamic coefficients $A_{\text{r}}(\omega)$ and $B_{\text{r}}(\omega)$, along with a vector containing the corresponding set of frequencies ω. Additionally, the infinite-frequency added mass μ_∞ and a structure containing information about the options of the software can also be defined.

The FDI toolbox allows the user to choose a desired frequency range over which to perform the parametric approximation and to remove any outliers in the frequency data. Such option aims to remove any possible information that the user considers unrealistic, as could happen for irregular frequencies [143].

Subsequently, the FDI toolbox explicitly calls the MATLAB function *invfreqs* to identify the system. *Invfreqs* identifies a continuous-time transfer function defined as

$$\tilde{K}_{\text{r}_{\text{fdi}}}(s) = \frac{b_{\text{fdi}}(1)s^{(n_{\text{ord}}^{\text{num}})} + b_{\text{fdi}}(2)s^{(n_{\text{ord}}^{\text{num}}-1)} + \cdots + b_{\text{fdi}}(n_{\text{ord}}^{\text{num}}+1)}{a_{\text{fdi}}(1)s^{(n_{\text{ord}}^{\text{den}})} + a_{\text{fdi}}(2)s^{(n_{\text{ord}}^{\text{den}}-1)} + \cdots + a_{\text{fdi}}(n_{\text{ord}}^{\text{den}}+1)}, \tag{4.15}$$

where the scalars $n_{\text{ord}}^{\text{num}}$ and $n_{\text{ord}}^{\text{den}}$ are the orders of the numerator and denominator, respectively, with $n_{\text{ord}}^{\text{num}} < n_{\text{ord}}^{\text{den}}$ to ensure the obtained parametric model is strictly

---

[3] Note that Prony's method is introduced at the end of this subsection since there is no specific application for wave energy that applies such method.

proper. To identify the numerator and denominator coefficients, b_{fdi} and a_{fdi} respectively, a nonlinear LS fitting optimisation technique is considered in the FDI toolbox. As shown in [149], three different methods can be followed to solve such a nonlinear optimisation problem

- Linearise the optimisation problem and solve a LLS problem.
- Solve an Iterative LS (ILS) problem.
- Use the linear LS solution to initialise a Nonlinear LS (NLS) problem (solved using a Gauss-Newton method).

The FDI toolbox automatically estimates the final order of the approximation, by linearly increasing the model order and computing the corresponding approximation error, as a function of both the approximated and the target radiation added mass, as well as damping coefficients. Once this approximation error falls below a predefined threshold, or the maximum order (specified by the user) is reached, the software stops increasing the order and the obtained model output is plotted along with the target data. As output, the FDI toolbox returns the numerator and denominator coefficients of the estimated transfer function for the radiation force subsystem, as well as the estimate of μ_∞ (if it was not supplied by the user). Thus, in order to obtain the SS representation of the radiation impulse response, the user needs to compute a realisation of the obtained transfer function (for example, by computing any canonical realisation [167]).

4.2.1.2 BEMIO toolbox

In contrast to the FDI toolbox, the BEMIO toolbox identifies the parametric model of the radiation convolution term using time-domain data, i.e. $k_{\mathsf{r}}(t)$. There are both Matlab and Python versions available. However, since the conversion from Python to Matlab was specifically made to implement BEMIO in WEC-Sim (which only runs in Matlab), the Python-based BEMIO code is no longer supported by the developers. It is important to highlight that BEMIO does not require any other additional toolbox to run, and can be downloaded for free from [62] for Matlab or from [63] for Python.

BEMIO is capable of reading the output files from NEMOH, WAMIT, or AQUA [92] and converts them into a standardised format. After pre-processing the hydrodynamic data, the utility computes $k_{\mathsf{r}}(t)$ following Ogilvie's relations, shown in Section 2.2.3, which is then used to compute the SS model of the radiation impulse response. As mentioned in Section 2.2.5, the BEMIO application computes the realisation of the radiation SS system following the Hankel singular value decomposition procedure, as

$$\Gamma_{k_{\mathsf{r}}(t)} = \begin{bmatrix} U_1^{\mathsf{H}} & U_2^{\mathsf{H}} \end{bmatrix} \begin{bmatrix} \Sigma_1^{\mathsf{H}} & 0 \\ 0 & \Sigma_2^{\mathsf{H}} \end{bmatrix} \begin{bmatrix} V_1^{\mathsf{H}^\intercal} \\ V_2^{\mathsf{H}^\intercal} \end{bmatrix} \approx U_1^{\mathsf{H}} \Sigma_1^{\mathsf{H}} V_1^{\mathsf{H}^\intercal}, \tag{4.16}$$

where $\Gamma_{k_{\mathsf{r}}(t)}$ is the Hankel matrix [150] defined using $k_{\mathsf{r}}(t)$. Then, the matrices U_1^{H} and $V_1^{\mathsf{H}^{\mathsf{T}}}$ are partitioned into three matrix blocks as

$$U_1^{\mathsf{H}} = \begin{bmatrix} U_{11}^{\mathsf{H}} \\ U_{12}^{\mathsf{H}} \\ U_{13}^{\mathsf{H}} \end{bmatrix} \quad V_1^{\mathsf{H}^{\mathsf{T}}} = \begin{bmatrix} V_{11}^{\mathsf{H}} \\ V_{12}^{\mathsf{H}} \\ V_{13}^{\mathsf{H}} \end{bmatrix}. \tag{4.17}$$

Finally, the matrices of the radiation convolution SS model are given by

$$\begin{aligned} A_{\mathsf{ss_r}} &= \Sigma_1^{\mathsf{H}^{-\frac{1}{2}}} \begin{bmatrix} U_{11}^{\mathsf{H}} \\ U_{12}^{\mathsf{H}} \end{bmatrix}^{\mathsf{T}} \begin{bmatrix} U_{12}^{\mathsf{H}} \\ U_{13}^{\mathsf{H}} \end{bmatrix} \Sigma_1^{\mathsf{H}^{-\frac{1}{2}}}, & B_{\mathsf{ss_r}} &= \Sigma_1^{\mathsf{H}^{-\frac{1}{2}}} V_{11}^{\mathsf{H}}, \\ C_{\mathsf{ss_r}} &= U_{11}^{\mathsf{H}} \Sigma_1^{\mathsf{H}^{-\frac{1}{2}}}, & D_{\mathsf{ss_r}} &= k_{\mathsf{r}}(0). \end{aligned} \tag{4.18}$$

The only mode offered by BEMIO is the automatic order selection mode, where the user selects the maximum order, and the accuracy threshold for the fit, of the SS realisation. With this approach, the code increases the model order until the selected maximum order is reached. Though the computational time, required by the toolbox is relatively low, the implemented method is inherently sub-optimal with regard to its computational capabilities, given that the software always computes the totality of the parametric models ranging from order 1, up to the final order.

4.2.1.3 FOAMM toolbox

FOAMM is based on the moment-matching-based identification strategy developed in Section 4.1. It is developed for Matlab and it does not require any additional toolbox to run. As the FDI toolbox, FOAMM identifies the parametric models in the frequency-domain (using $K_{\mathsf{r}}(\omega)$), and it requires the user to provide the vectors containing the frequency domain hydrodynamic coefficients.

Unlike the other two toolboxes, FOAMM can not only identify a parametric model of the radiation convolution subsystem, but also the complete force-to-velocity dynamics of the device which, as shown in Section 4.1.2, have some advantages with respect to parametrising the radiation convolution term.

Note that detailed information on the theory behind FOAMM and on the options that FOAMM provides can be found in Section 4.1 and Appendix A, respectively.

4.2.1.4 Prony's method

As mentioned in Section 2.2.4, even though there is no specific toolbox developed to apply Prony's method in wave energy systems, this method is included in this comparison, since it is broadly used in the community [11, 79]. Regarding the algorithm, it can be coded by the user (as performed for the current comparison), or the Matlab built-in function *prony.m* can be used. Prony's method assumes that the radiation impulse response $k_{\text{r}}(t)$ can be expressed as

$$\tilde{k}_{\text{r}}(t) = \sum_{i=1}^{n_{\text{ss}}} \alpha_{\text{p}}(i) e^{-\beta_{\text{p}}(i)t}, \tag{4.19}$$

where α_{p} and β_{p} are the amplitude and phase components, respectively, and can be obtained by solving two linear LS problems, as explained in [90]. Then, the matrices of the SS model are defined as

$$\begin{aligned} A_{\text{ss}_\text{r}} &= \text{diag}(-\alpha_{\text{p}}(1), -\alpha_{\text{p}}(2), \cdots, -\alpha_{\text{p}}(n_{\text{ss}})), \\ B_{\text{ss}_\text{r}} &= \begin{bmatrix} \beta_{\text{p}}(1) & \beta_{\text{p}}(2) & \cdots & \beta_{\text{p}}(n_{\text{ss}}) \end{bmatrix}^{\text{T}}, \\ C_{\text{ss}_\text{r}} &= \mathbb{1}_{1,n_{\text{ss}}}. \end{aligned} \tag{4.20}$$

4.2.2 Test cases

The geometries considered for the comparison performed in this section are depicted in Figure 4.10 along with all relevant dimensions. The first geometry (**G1**), shown in Figure 4.10(a), is a CETO-like device [58], a device similar to the float of the OPT WEC [112] (used for the application case of Section 4.1.2) is chosen for the second geometry (**G2**), as illustrated in Figure 4.10(b). The third geometry (**G3**) is an ISWEC-like device [19], depicted in Figure 4.10(c), the fourth (**G4**) and fifth (**G5**) devices are a spherical and a cylindrical device, shown in Figures 4.10(d) and (e), respectively. Finally, the last geometry considered (**G6**) is a CorPower-like device [170], shown in Figure 4.10(f).

G1 and **G2** are chosen due to the complexity of their frequency responses, while **G3** and **G6** are chosen because they are based on well-known state-of-the-art WECs. Finally, even though **G4** and **G5** are not based on any real WEC prototype, and their frequency responses are not especially complex, they are chosen since, due to their geometrical simplicity, they are widely used devices within the researchers.

Table 4.1 shows the selected DoF, mass m, S_{h}, μ_∞, and D_{pto} (which defines the PTO force as $f_{\text{pto}}(t) = D_{\text{pto}}\dot{\chi}(t)$) of the different geometries considered in this section. The units of m, S_{h}, μ_∞, and D_{pto} are given in kg, N/m, kg, and Ns/m, respectively, except for the pitching device **G3**, for which the units are kgm, Nm/rad, kgm, and Nms/rad, respectively. Note that D_{pto} is only considered to reduce the convergence time of the simulated results of this comparison, and that the values of D_{pto} are selected to be proportional to the magnitude of the radiation damping $D_{\text{r}}(\omega)$ of each device.

The frequency responses of the different geometries are shown in Figure 4.11. As depicted in Figure 4.11(a), the frequency response of **G1** has two resonance frequencies (at, approximately, 1 and 2 rad/s), which increases its complexity when it comes to

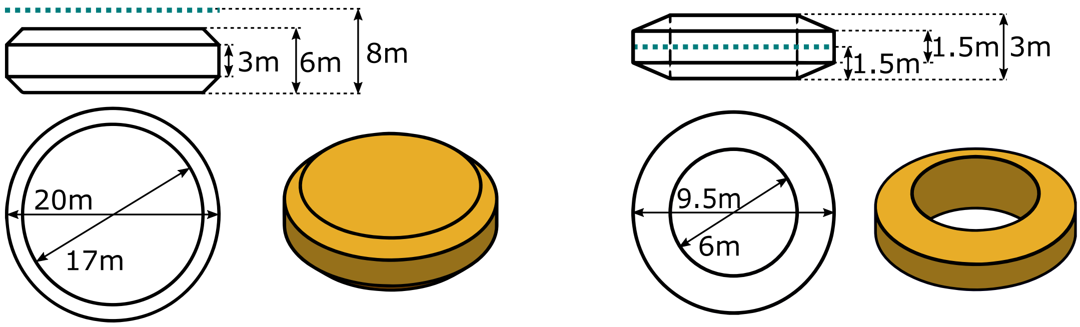

(a) CETO-like device (**G1**), with the considered dimensions.

(b) Float of an OPT-like device (**G2**), with the considered dimensions.

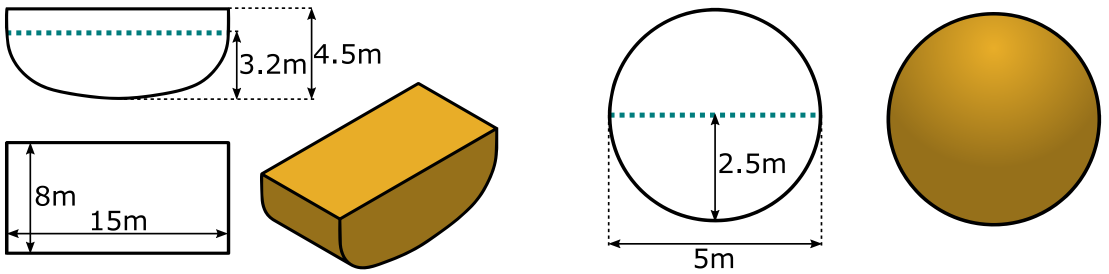

(c) ISWEC-like device (**G3**), with the considered dimensions.

(d) Spherical device (**G4**), with the considered dimensions.

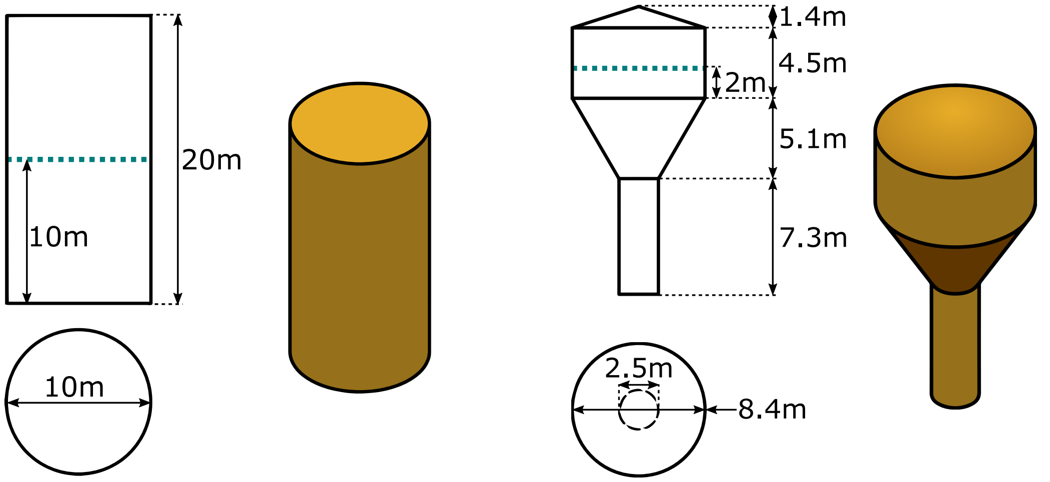

(e) Cylindrical device (**G5**), with the considered dimensions.

(f) CorPower-like device (**G6**), with the considered dimensions.

Figure 4.10: Sketches of all the devices considered in this chapter, where the blue-dotted line in each sketch represents the SWL.

parametric approximation, as shown in [47]. Similarly, the moon-pool of **G2** also makes the identification of a parametric model for the radiation subsystem more complex [135], as depicted in Figure 4.11(b). Finally, even though the frequency responses of **G3**, **G4**, **G5**, and **G6** appear to be 'simpler' than those of the previous cases, it is attractive to evaluate the capabilities of the identification applications to approximate the radiation

Table 4.1: Considered DoF, m, S_h, μ_∞, and D_pto values of the different geometries.

	G1	**G2**	**G3**	**G4**	**G5**	**G6**
DoF	1	3	5	3	3	3
m	$1.79{\cdot}10^6$	$4.79{\cdot}10^4$	$4.62{\cdot}10^6$	$3.35{\cdot}10^4$	$8.05{\cdot}10^5$	$3.35{\cdot}10^5$
S_h	0	$4.28{\cdot}10^5$	$1.51{\cdot}10^7$	$1.97{\cdot}10^5$	$1.55{\cdot}10^6$	$5.56{\cdot}10^5$
μ_∞	$4.39{\cdot}10^5$	$4.46{\cdot}10^4$	$1.69{\cdot}10^6$	$1.68{\cdot}10^4$	$2.46{\cdot}10^5$	$5.74{\cdot}10^4$
D_pto	$4{\cdot}10^4$	$1{\cdot}10^4$	$1{\cdot}10^5$	$4{\cdot}10^3$	$2{\cdot}10^3$	$5{\cdot}10^3$

force frequency response of such devices, since they are widely used geometries.

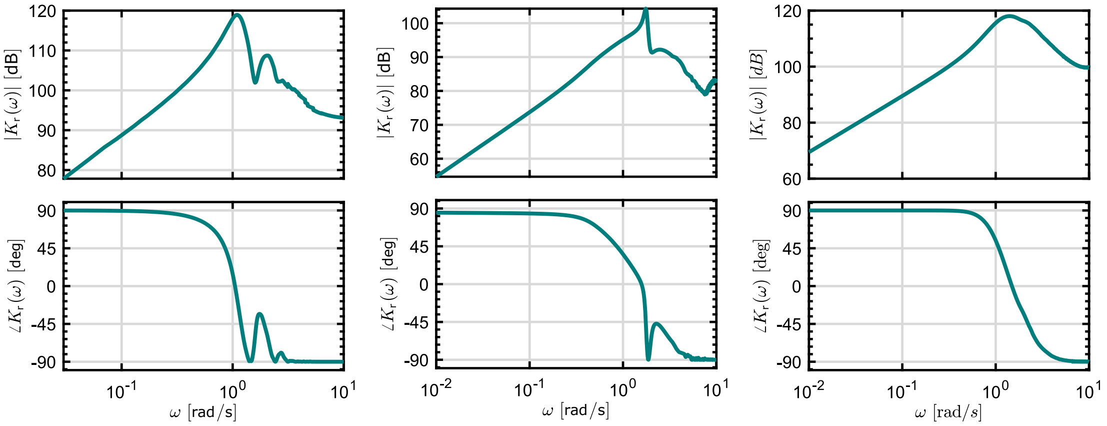

(a) $K_\mathsf{r}(\omega)$ of **G1** (surge). **(b)** $K_\mathsf{r}(\omega)$ of **G2** (heave). **(c)** $K_\mathsf{r}(\omega)$ of **G3** (pitch).

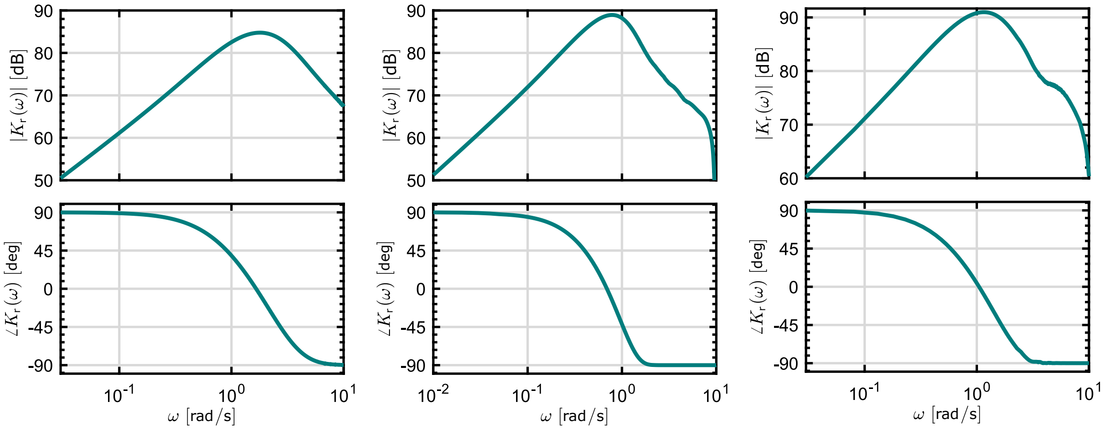

(d) $K_\mathsf{r}(\omega)$of **G4** (heave). **(e)** $K_\mathsf{r}(\omega)$ of **G5** (heave). **(f)** $K_\mathsf{r}(\omega)$ of **G6** (heave).

Figure 4.11: Radiation impulse response kernel k_r for the different geometries considered.

Finally, Figure 4.12 depicts the impulse response function $k_\mathsf{r}(t)$ for each of the six different geometries, obtained through Ogilvie's relations, as shown in Section 2.2.3. It can be seen how, for **G3**, **G4**, **G5**, and **G6**, the impulse response function diminishes to 0 in approximately 10 s while, for **G1** and **G2**, keeps oscillating until around 30 s and 50 s, respectively. Additionally, from the oscillations of each $k_\mathsf{r}(t)$, **G4** has the slowest dynamics, followed by **G6** and **G5**, **G3**, **G1**, and **G2** with the fastest dynamics.

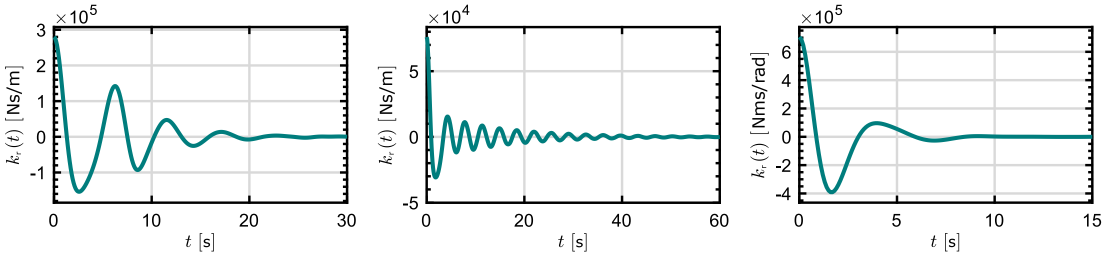

(a) $k_{\mathrm{r}}(t)$ of **G1** (surge). **(b)** $k_{\mathrm{r}}(t)$ of **G2** (heave). **(c)** $k_{\mathrm{r}}(t)$ of **G3** (pitch).

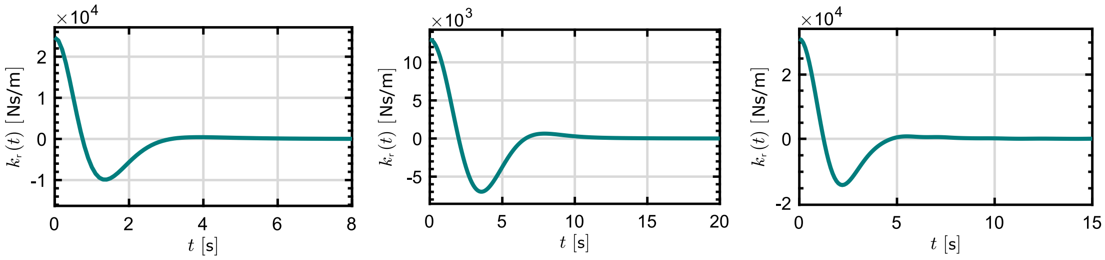

(d) $k_{\mathrm{r}}(t)$of **G4** (heave). **(e)** $k_{\mathrm{r}}(t)$ of **G5** (heave). **(f)** $k_{\mathrm{r}}(t)$ of **G6** (heave).

Figure 4.12: Radiation impulse response kernel k_{r} for the different geometries considered.

4.2.3 Comparison results

In this subsection, the results obtained by the different identification toolboxes are discussed. First, an analysis is carried out on how the different options of each application affect the obtained results. Finally, the comparison of the results obtained by the different toolboxes is provided, along with a discussion of such results.

It should be noted that the accuracy of the frequency, or time, responses of the identified models is given in terms of the Normalised Root Mean Square Error (NRMSE), which is defined as follows:

$$\mathrm{NRMSE}_f = \sqrt{\frac{\sum_{i=1}^{n_{\mathrm{dat}}} \left(f(i) - \tilde{f}(i) \right)^2}{\sum_{i=1}^{n_{\mathrm{dat}}} f(i)^2}}, \tag{4.21}$$

where n_{dat} is the number of points used to evaluate the approximation error, f represents the target frequency response $K_{\mathrm{r}}(\omega)$ or the impulse response $k_{\mathrm{r}}(t)$, depending on the context, and $\tilde{f}$ stands for the approximated f.

4.2.3.1 FDI toolbox

The first step when using the FDI (and FOAMM) toolbox is choosing the frequency range within which the approximation is computed. As explained in Section 4.1.2, the choice of the frequency range depends on the input ocean waves frequencies. Since the BEMIO application or the Prony's method do not have the option to select the frequency range over which the approximation is computed, the complete frequency range (shown in Figure 4.11) is selected for the approximation by FDI and FOAMM toolboxes. Note that this is also the frequency range over which the NRMSE$_{K_\mathrm{r}(\omega)}$ is computed.

Figure 4.13 depicts the accuracy of the obtained approximating model for the different identification methods contained in the FDI toolbox, and different model orders, for the six geometries under analysis. For the comparison, the maximum model order is set to 14, since the obtained parametric models of order 14 are (usually) sufficiently accurate for all the cases, and considering higher orders does not bring any significant improvement. It can be observed that the LLS method gives, overall, the highest errors. Furthermore, even though the ILS and NLS methods give similar results, it can be seen that for **G2**, **G4**, and **G5**, for some model orders, the performance obtained by the NLS is worse than that obtained by the ILS. Furthermore, since the NLS is based on solving a nonlinear LS problem, it requires higher computational time than the other two methods. Therefore, the ILS is the identification method used in the reminder of this comparison, which is also the method recommended by the developers of the FDI toolbox in [149], due to its good trade-off between computational speed and accuracy.

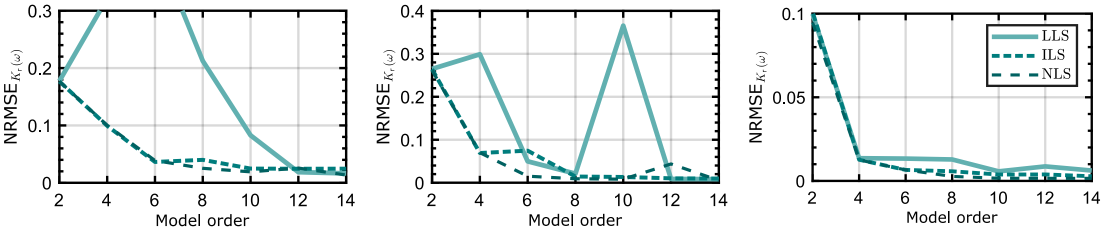

(a) NRMSE$_{K_\mathrm{r}(\omega)}$ for different model orders, considering **G1**.

(b) NRMSE$_{K_\mathrm{r}(\omega)}$ for different model orders, considering **G2**.

(c) NRMSE$_{K_\mathrm{r}(\omega)}$ for different model orders, considering **G3**.

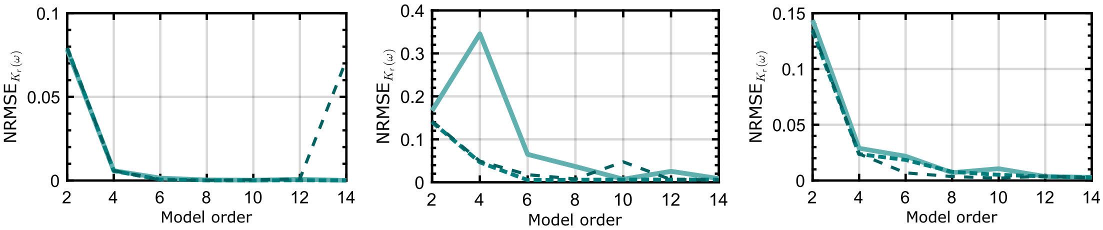

(d) NRMSE$_{K_\mathrm{r}(\omega)}$ for different model orders, considering **G4**.

(e) NRMSE$_{K_\mathrm{r}(\omega)}$ for different model orders, considering **G5**.

(f) NRMSE$_{K_\mathrm{r}(\omega)}$ for different model orders, considering **G6**.

Figure 4.13: NRMSE$_{K_\mathrm{r}(\omega)}$ for different model orders using the different identification methods of the FDI toolbox, for all the geometries considered.

Additionally, from Figure 4.13, it can be observed that the results obtained for **G1** and **G2** are, overall, less accurate than the results obtained for the other geometries; which is due to the complexity of their frequency responses, shown in Figure 4.11(a) and (b), respectively.

4.2.3.2 BEMIO toolbox

Since, as mentioned in Section 4.2.1, BEMIO has no other user-defined option than the fitting accuracy threshold and the maximum model order, the quality of the obtained model depends only on the calculation of $k_\mathrm{r}(t)$. In fact, since the time-length of the $k_\mathrm{r}(t)$ functions is given by the time for which the function is approximately 0 (as shown in Figure 4.12), the only variable that can affect the parametric model obtained by BEMIO is the time-step[4] used for the definition of $k_\mathrm{r}(t)$.

Figure 4.14 shows, for **G1**[5], how the accuracy of the approximation varies when considering different time-steps for the definition of $k_\mathrm{r}(t)$. As shown in Figure 4.14(a), the accuracy improvement in the time-domain (NRMSE$_{k_\mathrm{r}(t)}$) is not significant when reducing the time-step to less than 0.04 s (all the lines overlap behind the 0.04 s line). However, as shown in Figure 4.14(b), the approximation error of the frequency response of the obtained parametric model (NRMSE$_{K_\mathrm{r}(\omega)}$) is, indeed, improving when reducing the time-step more than 0.04 s. Therefore, the time-step selected for the definition of $k_\mathrm{r}(t)$ is 0.01 s, since further reducing the time-step does not improve the accuracy of the approximated model in the time or frequency domain.

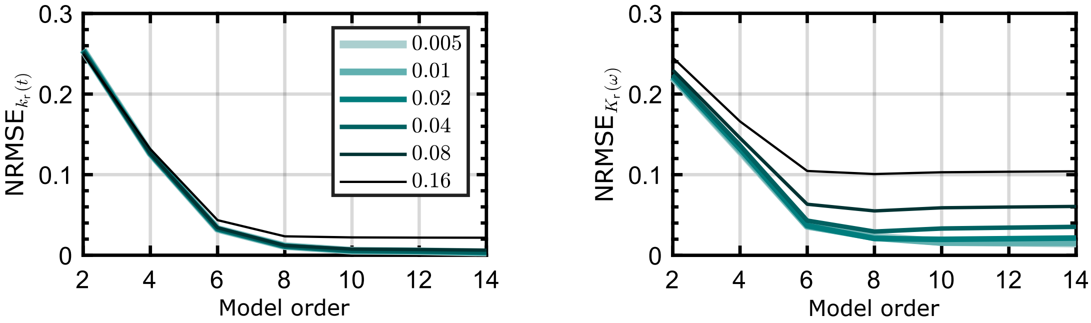

(a) NRMSE$_{k_\mathrm{r}(t)}$ for different model orders and time-steps.

(b) NRMSE$_{K_\mathrm{r}(\omega)}$ for different model orders and time-steps.

Figure 4.14: NRMSE$_{k_\mathrm{r}(t)}$ and NRMSE$_{K_\mathrm{r}(\omega)}$ for different model orders and time-steps using the BEMIO toolbox for **G1**.

4.2.3.3 FOAMM toolbox

For the FOAMM toolbox, the most characteristic frequencies of each frequency response are preselected, which are shown in Table 4.2. In fact, the interpolation

---

[4] Note that both the time-length and the time-step of $k_\mathrm{r}(t)$ are strongly related with the frequency discretisation considered for the calculation of $K_\mathrm{r}(\omega)$. Therefore, the hydrodynamic data used for the analysis of this section is defined until a sufficiently high frequency, in order to ensure that the time-step of the definition of $k_\mathrm{r}(t)$ can be reduced consistently, guaranteeing that the FFT of $K_\mathrm{r}(\omega)$ is calculated correctly [128].

[5] Note that only the results obtained for **G1** are shown, because similar accuracy improvement (with respect to the time-step) is obtained for the other devices.

frequencies shown in Table 4.2 correspond to the peak values of the frequency responses, shown in Figure 4.11. Since the frequency response of **G1** and **G2** have two peaks, two different interpolation frequencies are preselected; while a single interpolation frequency is preselected for the rest of the devices. For the model orders that require more interpolation frequencies than those specified in Table 4.2, the automatic mode of FOAMM is utilised to optimise their position. Note that this identification method is selected for FOAMM since, for this case, the value of the interpolation frequencies, apart from those specified in Table 4.2, is not important.

Table 4.2: Interpolation frequencies considered by FOAMM for the different devices.

	G1	**G2**	**G3**	**G4**	**G5**	**G6**
$\mathcal{F}_{K_\mathrm{r}(\omega)}$	1	1.75	1.37	1.78	0.78	1.1
	2	0.8				

4.2.3.4 Prony's method

As for the BEMIO toolbox, the only variable that can affect the approximation for Prony's method is the time step used to define $k_\mathrm{r}(t)$. However, unlike for the BEMIO toolbox, using small time-steps leads to numerically ill-conditioned LS problems (as discussed in [56] and [96]) and, therefore, to incorrect parametric models. Such an ill-conditioning problem arises from the fact that, to solve the LS problem, a matrix (generated using the values of $k_\mathrm{r}(t)$) needs to be inverted and, when decreasing the time-step, the differences between the values of the rows/columns of the regression matrix decreases and becomes nearly rank-deficient. Thus, in order to avoid such numerical instabilities while, at the same time, having a sufficiently accurate discretisation ok $k_\mathrm{r}(t)$, the time-step considered to compute the radiation impulse response used for Prony's method is set to 0.04 s. Note that the results obtained using Prony's method could be potentially improved (for some model orders) by further reducing the time-step used to compute $k_\mathrm{r}(t)$. However, as explicitly discussed before in this subsection, reducing the time-step can lead to numerically ill-conditioned LS problems (especially for high model orders), potentially generating convergence problems in the corresponding minimisation procedure.

4.2.3.5 Comparison of the approximation applications

As shown in Figure 4.15, in the frequency domain, the results obtained by FOAMM and FDI are similar for all the cases analysed, especially for **G3** and **G4**, illustrated in Figures 4.15(c) and (d), respectively. Additionally, overall, FOAMM and FDI obtain a lower NRMSE$_{K_\mathrm{r}(\omega)}$ than BEMIO and Prony's method, which stems from the fact that both

FDI and FOAMM identify the radiation convolution parametric model by minimising the error in the frequency-domain. It should be highlighted that, while the results obtained using the BEMIO application are slightly less accurate than those obtained using FOAMM and FDI, one can notice that the results obtained by applying Prony's method are significantly less accurate than those obtained by the other three strategies.

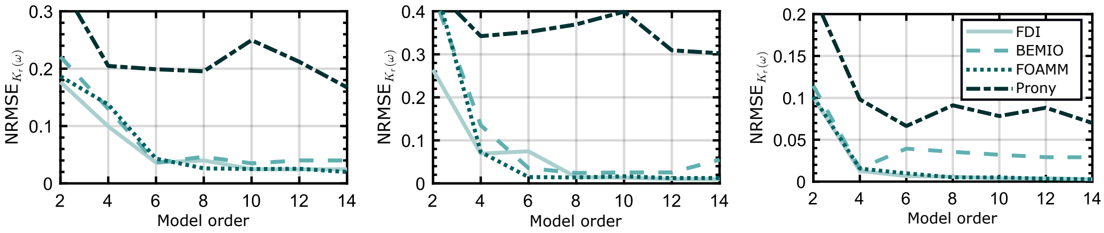

(a) NRMSE$_{K_\mathrm{r}(\omega)}$ for different model orders, considering **G1**.

(b) NRMSE$_{K_\mathrm{r}(\omega)}$ for different model orders, considering **G2**.

(c) NRMSE$_{K_\mathrm{r}(\omega)}$ for different model orders, considering **G3**.

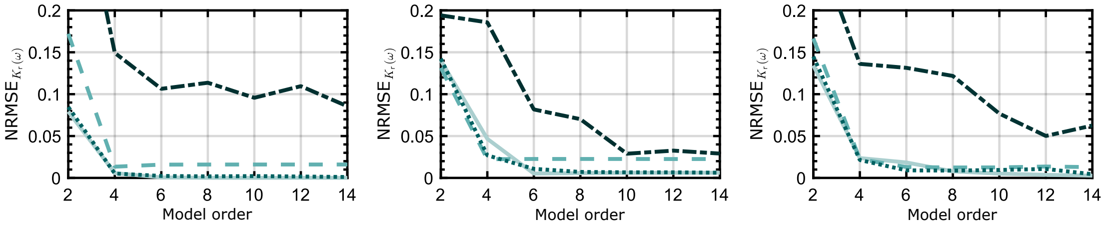

(d) NRMSE$_{K_\mathrm{r}(\omega)}$ for different model orders, considering **G4**.

(e) NRMSE$_{K_\mathrm{r}(\omega)}$ for different model orders, considering **G5**.

(f) NRMSE$_{K_\mathrm{r}(\omega)}$ for different model orders, considering **G6**.

Figure 4.15: NRMSE$_{K_\mathrm{r}(\omega)}$ for different model orders, for the different toolboxes and geometries.

In Figure 4.15, it is shown that the obtained NRMSE$_{K_\mathrm{r}(\omega)}$ for **G3**-**6** is below 0.05 for orders higher than 4, for all the utilities except Prony's method. On the contrary, for **G1**-**2**, apart from the fact that a model order of 6-8 is required to get a NRMSE$_{K_\mathrm{r}(\omega)}$ which is below 0.05, the obtained accuracy is, overall, worse than that obtained for **G3**-**6**. Figure 4.16 shows the error on the obtained parametric model impulse response $k_\mathrm{r}(t)$ for the different identification utilities, model orders and geometries. Since Prony's method and BEMIO applications identify the parametric model by minimising the error between target and obtained impulse response function, the error obtained by such methods should decrease considerably with respect to the error shown in Figure 4.15. However, it is noteworthy that the results obtained using Prony's method do not improve as expected. This is not the case for the BEMIO toolbox, which obtains, overall, the lowest NRMSE$_{k_\mathrm{r}(t)}$ among the different strategies. Regarding the FDI and FOAMM toolboxes, the obtained NRMSE$_{k_\mathrm{r}(t)}$ are, overall, worse than the NRMSE$_{K_\mathrm{r}(\omega)}$ shown in Figure 4.15. This can be reasoned by the fact that these strategies minimise the error between target and approximated frequency responses, rather than $k_\mathrm{r}(t)$.

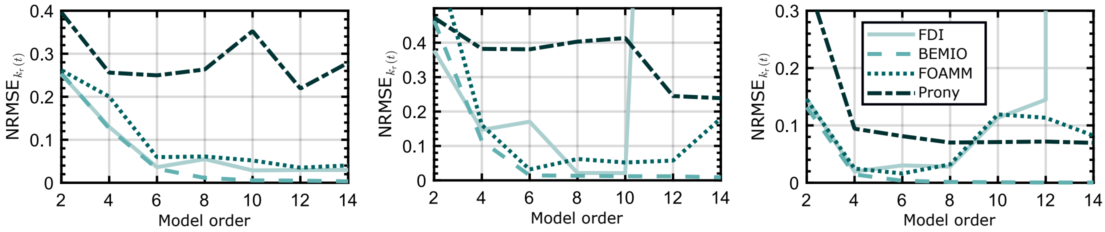

(a) NRMSE$_{k_\mathrm{r}(t)}$ for different model orders, considering **G1**.

(b) NRMSE$_{k_\mathrm{r}(t)}$ for different model orders, considering **G2**.

(c) NRMSE$_{k_\mathrm{r}(t)}$ for different model orders, considering **G3**.

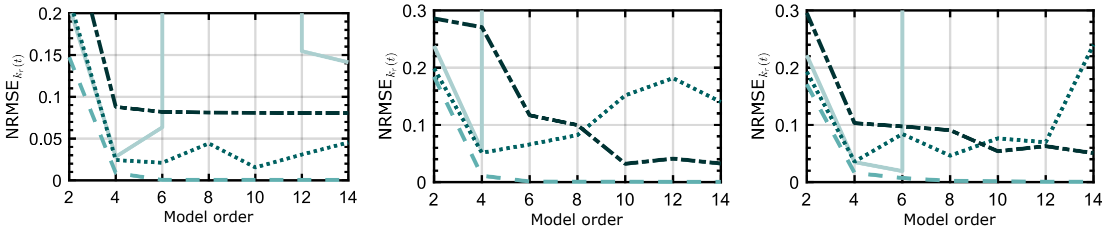

(d) NRMSE$_{k_\mathrm{r}(t)}$ for different model orders, considering **G4**.

(e) NRMSE$_{k_\mathrm{r}(t)}$ for different model orders, considering **G5**.

(f) NRMSE$_{k_\mathrm{r}(t)}$ for different model orders, considering **G6**.

Figure 4.16: NRMSE$_{k_\mathrm{r}(t)}$ for different model orders, for the different toolboxes and geometries.

In particular, among the results obtained with the FDI toolbox, there are some cases where the obtained NRMSE$_{k(t)}$ is particularly high, which happens especially for high model orders or for the geometrically simplest devices (**G4**-**6**). This has been already reported in [149], where the developers specify that, if the order of the proposed model is too large, there will be over-fitting and, therefore, the approximation error will increase. In such cases, the obtained parametric model is unstable, which leads to divergence of the impulse response and, thus, the obtained NRMSE$_{k_\mathrm{r}(t)}$. It should be noted that, as mentioned in [149], such over-fitting problems can be avoided by selecting a different frequency range , which can be selected using the built-in frequency-range-selection option of the toolbox. Finally, as shown in Figure 4.15, the NRMSE$_{k_\mathrm{r}(t)}$ obtained using BEMIO decreases faster for **G3**-**6** than for **G1**-**2**, due to the simplicity associated, this time, with the radiation impulse response kernels of **G3**-**6**, shown before in Figure 4.12(c)-(f).

Figure 4.17 shows the NRMSE$_{\dot{\chi}(t)}$ obtained by the different toolboxes, for each of the geometries analysed, which is the error between the velocity obtained by the simulation of the device motion using the identified parametric models (constructing the WEC system as in Equation (2.41)) and the steady-state response computed using the frequency domain data. Such simulations are carried out using irregular waves described by a JONSWAP spectrum ($T_\mathrm{p} = 6\,\mathrm{s}$, $H_\mathrm{s} = 1.5\,\mathrm{m}$ and $\gamma = 3.3$) and the results are averaged using 50 random simulations (computed as explained in Section 2.1.2), in order to get representative results.

As explained for Figure 4.16, there are some model orders for which, due to over-fitting, the result obtained from the FDI toolbox diverges. However, it should be noted that, for all the geometries where over-fitting happens, the NRMSE$_{\dot{\chi}(t)}$ obtained by the FDI toolbox for the highest model order before the divergence, is as low (or lower) as the NRMSE$_{\dot{\chi}(t)}$ obtained by the other methods. Unsurprisingly, as for figures 4.15 and 4.16, the NRMSE$_{\dot{\chi}(t)}$ obtained using Prony's method is the highest among the different toolboxes. Note that, for **G6**, the parametric models of order 12 and 14 obtained using Prony's method are unstable since, as the FDI toolbox, stability is not enforced in the employed Prony's method formulation. Finally, the results obtained by both BEMIO and FOAMM are similar for all the model orders and geometries analysed obtaining, always, stable parametric models. It should be highlighted that, even though all the SS models obtained by both FOAMM and BEMIO are stable, FOAMM is the only toolbox that, as explained in Section 4.1, explicitly enforces stability in the identification process.

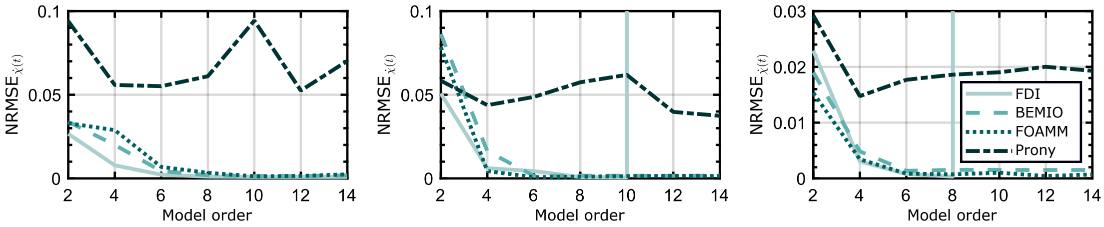

(a) NRMSE$_{\dot{\chi}(t)}$ for different model orders, considering **G1**.
(b) NRMSE$_{\dot{\chi}(t)}$ for different model orders, considering **G2**.
(c) NRMSE$_{\dot{\chi}(t)}$ for different model orders, considering **G3**.

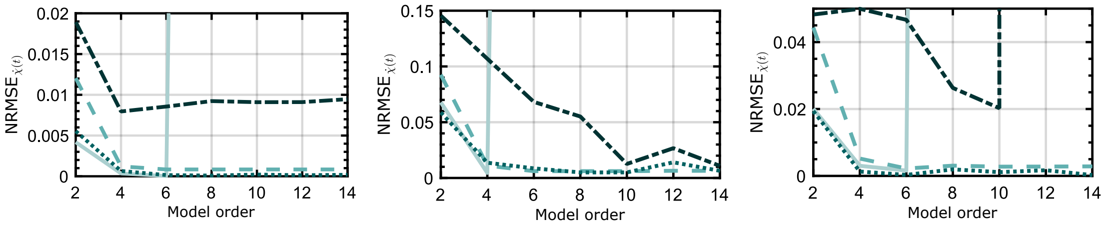

(d) NRMSE$_{\dot{\chi}(t)}$ for different model orders, considering **G4**.
(e) NRMSE$_{\dot{\chi}(t)}$ for different model orders, considering **G5**.
(f) NRMSE$_{\dot{\chi}(t)}$ for different model orders, considering **G6**.

Figure 4.17: NRMSE$_{\dot{\chi}(t)}$ for different model orders, for the different toolboxes and geometries analysed.

4.2.3.6 Preservation of physical properties

In this subsection, the models identified in Section 4.2 are analysed, to assess to what extent the different toolboxes are able to preserve the properties of the radiation subsystem. The first property analysed is input-output stability. As mentioned before, both FOAMM and BEMIO obtain always stable SS models[6], however, stability is not preserved for some of the cases when using the FDI and Prony's methods.

Even though the FDI toolbox is the only utility enforcing the parametric model to have a zero at the origin, the models obtained by BEMIO and FOAMM always have a zero close to the origin; on the contrary, most of the models obtained using Prony's method do not have a zero at the origin. It should be noted that, even though is not implemented in FOAMM yet, it is possible to enforce a zero at the origin within the moment-based formulation, as shown in [48]. Regarding the property that the model should be strictly proper, all but the BEMIO toolbox are able to preserve it, which being the only utility that employs a feed through matrix D_{ss} on the final SS model, does not provide strictly proper models.

Finally, even though none of the toolboxes explicitly guarantee passivity, BEMIO and FOAMM are the ones obtaining the higher number of passive models (around 75% of the cases). In fact, for the case of the FOAMM toolbox, a particular selection of the interpolation frequencies can be used to obtain a passive model, since there exists a relation between the interpolation frequencies, the spectral zeros of a system, and its passivity which, as for the zero at the origin, can be enforced (though is not implemented within the FOAMM toolbox yet) [48].

4.3 MIMO approach

As mentioned in Section 2.2.6, commercial WECs are likely to be deployed in arrays to minimise the Levelized Cost of Energy (LCOE) associated with WECs [159]. Additionally, most of the WECs are not expected to move in a single DoF, due to the cost related to building a structure to restrict the other DoFs. However, the majority of the literature only considers the SISO WEC case and the researchers that consider MIMO WEC cases compute the MIMO SS system as a set of SISO SS systems, where the different radiation subsystems are identified separately and gathered together in an augmented SS model [192, 193]. Such multi-SISO WEC systems require a separate impulse response function for each cross-coupling component (arising from inter-device and inter-DoF interactions) and, therefore, the number of radiation SS models increases quadratically with the number of bodies[7].

Even though the multi-SISO approach is still computationally more efficient than solving all the convolutions, the dimension of the final SS system still increases exponentially, which can hamper global control techniques to the point of being intractable for

---

[6] Although FOAMM is the only strategy that explicitly ensures stability.

[7] Note that it does not increase quadratically with respect to the number of DoF since the interactions between DoF can be 0 for some cases.

real-time applications [45]. Additionally, the structure of the SS system obtained by the multi-SISO approach is suboptimal, since it ignores any connection between the different subsystems. To address such an issue, an extension of the moment-matching-based identification framework, presented in Section 4.1, for MIMO systems was developed in [137] and [49]. The following subsection shows, through an application example, the advantages of this new MIMO identification strategy compared to the approach of defining the MIMO WEC SS system as a multi-SISO SS system.

4.3.1 Application case

For the application case showing the advantages of using the MIMO moment-matching identification approach, the same WEC array system used as an example in Section 2.2.6 is considered, shown in Figure 2.7, with four spherical heaving devices (5 m radius and 5 m draft) arranged in a square layout with an inter-device distance, along one side of the square, of $d_\text{b} = 20$ m. It should be noted that, for the numerical examples of this subsection, the irregular waves are described by a JONSWAP spectrum with $T_\text{p} = 6$ s, $H_\text{s} = 1.5$ m and $\gamma = 3.3$.
To test the MIMO identification strategy, the results obtained using identified parametric models of different orders are compared. As explained in Section 4.1.2 for the SISO case, the selection of the interpolation frequencies has to be done in a sensible manner, picking the most representatives frequencies. By way of example, four different interpolation frequency sets $\mathcal{F}$ are considered:

$$\mathcal{F}_1 = \{1.45\}, \qquad \mathcal{F}_3 = \{1.45,\ 1.89,\ 1.14\},$$
$$\mathcal{F}_2 = \{1.45,\ 1.89\}, \qquad \mathcal{F}_4 = \{1.45,\ 1.89,\ 1.14,\ 2.2\}.$$

Figure 4.18 presents the target force-to-velocity frequency response $\boldsymbol{H}(\omega)$ of the WEC array computed as shown in Equation (2.45), along with the identified frequency response of the model $\tilde{\boldsymbol{H}}_{\mathcal{F}_1}$. In particular, Figure 4.18(a) presents the Bode diagram for the element $\{1,1\}$ (the inner dynamics of the bodies), 4.18(b) the Bode diagram for the element $\{1,2\}$ (the interactions with the direct neighbours), and Figure 4.18(c) the bode diagram for the element $\{1,4\}$ (the interactions between the bodies in the diagonal). For $\mathcal{F}_1$, the interpolation point is chosen as the frequency where the maximum amplitude peak of the target frequency response occurs (≈ 1.45 rad/s). Even though the approximation of $\tilde{\boldsymbol{H}}_{\mathcal{F}_1}$ seems to be poor, especially in the case of the $\{1,4\}$ element, the model is able to capture the most significant dynamics of the array, as a consequence of the sensible choice of the interpolation point, obtaining an approximation error of $\text{NRMSE}_{\boldsymbol{H}(\omega)} = 0.24$.

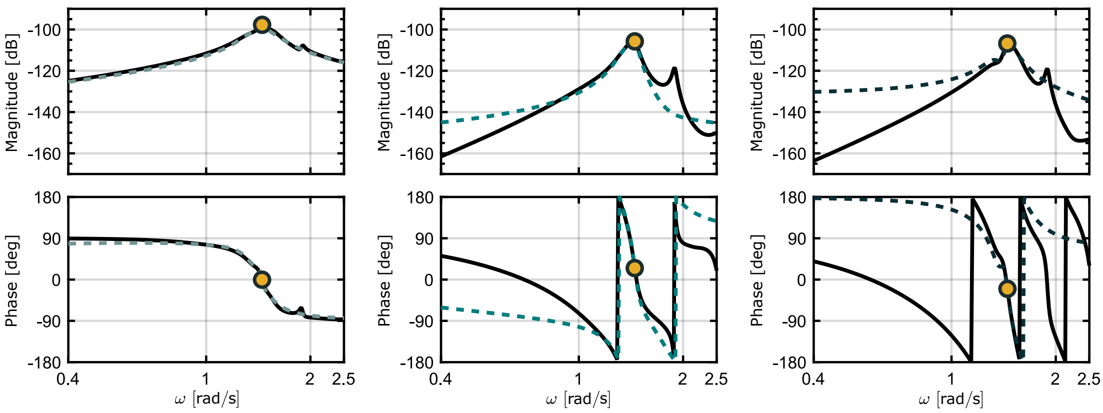

(a) Identification of the inner dynamics.
(b) Identification of the interaction with the closest neighbour.
(c) Identification of the diagonal interaction.

Figure 4.18: Frequency response of the MIMO parametric model considering a single frequency (dashed line, following the colour code of Figure 2.7) along with the target frequency domain data (solid-black-line), and the interpolation frequencies (orange-dots). Obtained NRMSE$_{\boldsymbol{H}(\omega)} = 0.24$.

Similarly, Figure 4.19 shows the approximation results, obtained with the parametric model that uses the set of interpolation frequencies $\mathcal{F}_4$. In this case, the set of interpolation frequencies naturally includes $\mathcal{F}_1$, and increases the number of interpolation points by adding the frequency where the second peak occurs (≈ 1.89 rad/s), along with lower and higher frequency components (arbitrarily chosen). The approximation error decreases, from $\tilde{\boldsymbol{H}}_{\mathcal{F}_1}$ to $\tilde{\boldsymbol{H}}_{\mathcal{F}_4}$, can be appreciated directly from Figures 4.18 and 4.19, or more precisely from Table 4.3.

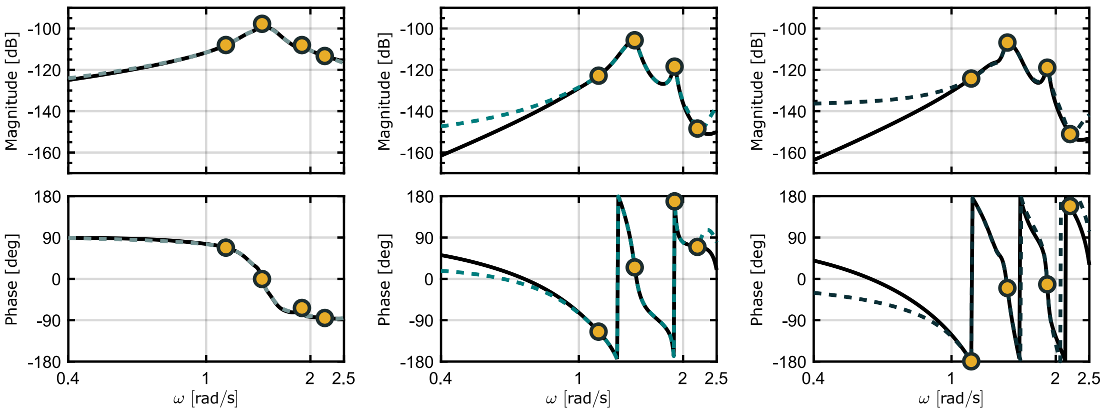

(a) Identification of the inner dynamics.
(b) Identification of the interaction with the closest neighbour.
(c) Identification of the diagonal interaction.

Figure 4.19: Frequency response of the MIMO parametric model considering 4 frequencies (dashed line, following the colour code of Figure 2.7) along with the target frequency domain data (solid-black-line), and the interpolation frequencies (orange-dots). Obtained NRMSE$_{\boldsymbol{H}(\omega)} = 0.04$.

Figure 4.20 shows the time-domain response of $\tilde{\boldsymbol{H}}_{\mathcal{F}_4}$ for an irregular wave input. Due to the layout of the array (and the wave direction β_η), the velocity of devices 1 and 2 (Figure 4.20(a)), and devices 3 and 4 (Figure 4.20(b)) are the same. It can be observed that, in steady-state, the output of the identified MIMO parametric model coincides with the motion results obtained from the target model frequency response.

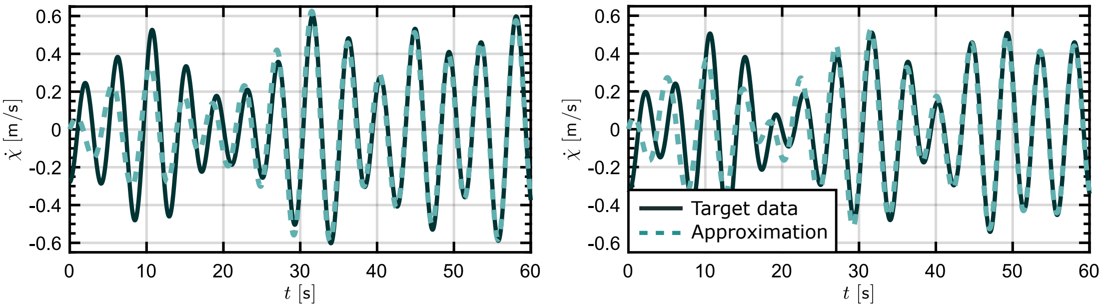

(a) Velocity of device 1 (and 2).

(b) Velocity of device 3 (and 4).

Figure 4.20: Comparison between the time-domain outputs of the identified parametric model $\tilde{\boldsymbol{H}}_{\mathcal{F}_4}$ (dashed-light-blue) and the steady-state response computed from $\boldsymbol{H}(\omega)$ (solid-dark-blue). Note that only two graphs are shown since, due to the layout of the array, the velocity of devices 1 and 2 (a), and devices 3 and 4 (b) are the same.

Finally, Table 4.3 shows the results of the numerical evaluation of each of the computed models in terms of the following characteristics:

Dim Dimension of the identified force-to-velocity parametric model.

NRMSE$_{\boldsymbol{H}(\omega)}$ Approximation error computed against the target MIMO WEC array frequency response (for $\omega \in [0.3, 2.5]$ $^{\text{rad}}/_{\text{s}}$).

NRMSE$_{\dot{\chi}(t)}$ NRMSE computed against the target steady-state responses averaged over 10 different simulations.

N-Time The time required[8] for the time-domain simulation normalised against the fastest model, in this case the one computed with $\tilde{\boldsymbol{H}}_{\mathcal{F}_1}$.

The results of **NRMSE**$_{\boldsymbol{H}(\omega)}$, shown in Table 4.3, represent the mean of the **NRMSE**$_{\boldsymbol{H}(\omega)}$ obtained for the different cross-coupling components of $\boldsymbol{H}(\omega)$. Similarly, the **NRMSE**$_{\dot{\chi}(t)}$ is the mean of the approximation error in the velocity $\dot{\chi}(t)$ of the four bodies.
As mentioned in Section 4.1.2 for the SISO case, the dynamics of the radiation force subsystem often require a higher order approximation, than the force-to-motion dynamics, to successfully represent its relevant features. Therefore, as can be observed from Table 4.3, the multi-SISO model (of dimension 104) obtains similar force-to-motion results to those computed by $\tilde{\boldsymbol{H}}_{\mathcal{F}_1}$ (of dimension 8), while requiring more than twice the computational time required by $\tilde{\boldsymbol{H}}_{\mathcal{F}_1}$.

---

[8] Measured using the MATLAB functions `Tic` and `Toc`.

Table 4.3: Results obtained with the different identified MIMO and the multi-SISO parametric models of the force-to-velocity of the WEC array.

Model	**Dim**	**NRMSE**$_{\boldsymbol{H}(\omega)}$	**NRMSE**$_{\dot{\mathcal{X}}(t)}$	**N-Time**
multi-SISO	104	0.2007	0.0998	2.3670
$\tilde{\boldsymbol{H}}_{\mathcal{F}_1}$	8	0.2391	0.1043	1
$\tilde{\boldsymbol{H}}_{\mathcal{F}_2}$	16	0.0914	0.0658	1.0070
$\tilde{\boldsymbol{H}}_{\mathcal{F}_3}$	24	0.0552	0.0233	1.0581
$\tilde{\boldsymbol{H}}_{\mathcal{F}_4}$	32	0.0383	0.0126	1.0951

Additionally, it should be highlighted that, when considering a parametric form for each of the radiation force subsystems, the dimension of the model increases quadratically with the number of bodies of the array while, with the proposed MIMO identification strategy, the order increases linearly. Therefore, the differences shown in Table 4.3 would be more significant when considering arrays larger than the one considered for this example.

4.4 Conclusions

One of the main conclusions that can be drawn from this chapter is the importance of choosing the correct identification mode (force-to-motion or radiation force subsystem) for each application. As shown in Section 4.1.2, higher order parametric models are usually required to represent the WEC SS model using the parametric model of the radiation convolution system, as opposed to directly identifying the complete force-to-motion dynamics of the device. However, such approach is not optimal for every application since, even though the obtained force-to-motion dynamics approximation is correct, it is not guaranteed that the definition of the radiation force subsystem is accurately described. Thus, while SS models identified using the force-to-velocity approach are optimal for WEC motion simulation (due to their computational requirements), identifying the radiation force subsystem separately may be necessary for some optimal control strategies, for which an accurate definition of the radiation subsystem is required.

The main argument of some researchers in the literature against identifying the complete force-to-motion dynamics is that, by identifying the radiation force subsystem separately, they are able to introduce nonlinearities into the WEC description, such as nonlinear restoring, Froude-Krylov, or viscous damping forces. However, as shown in [46], it is possible to include nonlinear terms into force-to-motion parametric models, as feedback terms, thus obtaining an accurate and computationally efficient nonlinear representation of WEC systems.

With regard to the force-to-motion dynamics identification, it is worth to highlight that, among the parametric identification utilities developed for wave energy applications, FOAMM is the only one including such an identification mode. Additionally, it should be noted that, while none of the radiation subsystem identification utilities is able to preserve all the radiation convolution system properties, the only properties that FOAMM does not explicitly enforce are passivity and the zero at the origin. However, as demonstrated in [48], both passivity and the zero at the origin can be ensured by using a nonlinear optimisation procedure within the moment-matching-based identification scheme, which will be added to the FOAMM toolbox in the future, making FOAMM the only identification application capable of preserving all the physical properties of the radiation system.

Finally, to characterise a WEC array using a SS representation, it is important to directly identify the MIMO SS model from the complete array MIMO system, as opposed to compute the MIMO SS model a set of multiple SISO SS systems. The number of radiation convolution terms increases proportional to the square of the number of bodies of a WEC array, and so does the number of radiation SISO SS models required to describe the WEC array MIMO SS system. In contrast, by directly identifying the WEC array MIMO force-to-motion system, the order of the final model increases linearly with the number of bodies composing the array, representing, thus, a more suitable identification method to characterise large WEC arrays.

5

Excitation force estimation

Contents

5.1 Comparison of excitation force estimators

As introduced in Section 3.2, several excitation force f_e estimators (11 strategies in total) can be found in the literature. Given the large number of f_e estimators, knowledge of the relative strengths and weaknesses of each strategy is important; however, an exhaustive comparison has not yet been performed. Thus, this section aims to compare all the different wave excitation force estimation techniques available in the literature. Nevertheless, comparing different estimators is not a trivial task. Since, as explained in Section 3.1, the f_e on a moving body is an unmeasurable quantity, the definition of an unbiased reference for the comparison poses a challenge.

Therefore, a CFD simulation is employed to measure the excitation force, from pressure measurements in the hull, used as a benchmark for the comparison presented in this section. As further explained in Section 5.1.3, since the description of the model used for the CFD simulation differs from the model used in the estimators, using CFD allows the definition of an unbiased f_{e} reference and, therefore, the execution of a critical and fair comparison of the different estimation techniques. A 5 m diameter heaving sphere point absorber WEC (see Figure 4.10(d)) is chosen as the case study for the presented comparison. The device is exposed to irregular waves, and a nonlinear hydraulic PTO [142], with a resistive controller, is implemented in the model.

It should be noted that, even though CFD is used to simulate the motion of the device, the considered case reduces the motion of the WEC, such that the simulation can be considered linear. This is necessary since the only way to define an unbiased f_{e} reference is to perform a diffraction test (as further explained in Section 5.1.3) which, as introduced in Section 2.2.2, only holds for linear systems. This is consistent with the fact that most of the excitation force estimators only consider linear WEC dynamics and, therefore, considering nonlinear WEC dynamics would hamper the application of most of the estimation strategies. However, it should be noted that, if required, some of the estimation strategies can directly accommodate non-linearities on the WEC description. In particular, the estimators able to consider non-linear WEC models are the EKFHO, FAUIE, EKFPS, and PADE strategies. Additionally, the KFRW, KFHO, and ULISE estimators can be extended to account for a non-linear WEC model by using an EKF. Finally, it should be further noted that the UIO strategy can be designed to be robust to model uncertainties, which could be enough to account for the differences between linear and non-linear WEC model.

5.1.1 Estimation strategies

The theory behind every different f_{e} estimation technique is introduced in the following. Information on the theory of the different estimation strategies is kept concise, for brevity. The interested reader is referred to the references, provided for each strategy, for a more comprehensive description of the approaches.

The SS model describing the WEC device is defined as in System (2.41). Since most of the estimation strategies are defined for SISO systems, a single-DoF WEC is considered. Moreover, even though the default outputs of System (2.41) are position, velocity, and acceleration of the device, matrices C_{ss} and D_{ss} are changed according to the measurements (within the set of position, velocity, and acceleration) used by the different estimators. The discrete-time equivalent of System (2.41) (which can be computed as shown in [26]) is represented using the superscript $\{\cdot\}^{\mathsf{d}}$, with a discrete-time index k ($t = kt_{\mathsf{s}}$) and a sampling period t_{s}. Finally, as explained in Section 5.1.3, in order to dampen the motion of the device and keep the simulation of the comparison relatively linear, a resistive controller proportional to the WEC velocity is considered. Therefore, a damping coefficient for the PTO force, defined as $f_{\mathsf{pto}}(t) = D_{\mathsf{pto}}\dot{\chi}(t)$, has to be added to the SS model describing the WEC system, in particular, to the A_{ss} matrix of Equation (2.42).

5.1.1.1 Convolution with Predicted Wave Elevation - CPWE

As shown in [84], having identified the excitation force kernel k_{e} (which, as explained in Section 3.2.1, can be obtained from BEM codes or from wave tank tests), the estimated $f_{\mathsf{e}}(t)$ for the CPWE strategy ($\tilde{f}_{\mathsf{e}}^{\mathsf{CPWE}}(t)$) is given by

$$\tilde{f}_{\mathsf{e}}^{\mathsf{CPWE}}(t) = \int_0^{t+t_{\mathsf{caus}}} k_{\mathsf{e}}^{\mathsf{caus}}(t + t_{\mathsf{caus}} - \tau)\eta^*(\tau)d\tau, \tag{5.1}$$

where $k_{\mathsf{e}}^{\mathsf{caus}}(t+t_{\mathsf{caus}}) = k_{\mathsf{e}}(t)$ is the casualised $k_{\mathsf{e}}(t)$ and, as explained in Section 3.2.1, t_{caus} is sufficiently large so that $k_{\mathsf{e}}^{\mathsf{caus}}(t) = 0$ for any $t < 0$ or, in other words, is causal. In Equation (5.1), $\eta^*(\tau)$ refers to past values of $\eta(t)$ for $\tau < t$, instantaneous $\eta(t)$ for $\tau = t$, and predicted values of $\eta(t)$ for $\tau > t$. Equation (5.1) is defined using the causalised kernel $k_{\mathsf{e}}^{\mathsf{caus}}$, instead of k_{e}, as in Equation (2.37), since the causalised kernel can be approximated using a finite order parametric model which, as shown in [84], reduces the computational burden associated with evaluating the convolution product.

5.1.1.2 Kalman Filter with Random Walk - KFRW

As shown in [121], the dynamical model describing the excitation force, which is given by a RW model, is defined as

$$f_{\mathsf{e}}^{\mathsf{KFRW}}(k+1) = f_{\mathsf{e}}^{\mathsf{KFRW}}(k) + \epsilon_{f_{\mathsf{e}}}(k), \tag{5.2}$$

where $\epsilon_{f_{\mathsf{e}}}(k)$ is a random number (independently and identically distributed in size). This random walk model assumes that, at each sampling time k, $f_{\mathsf{e}}^{\mathsf{KFRW}}(k)$ takes a random step ($\epsilon_{f_{\mathsf{e}}}$) away from its previous value, at $k-1$. As mentioned in Section 3.2, this strategy is based on the internal model principle and, therefore, the model, describing the excitation force, needs to be included into the WEC system state space. Thus, the augmented SS model of the WEC system, including the dynamical description of $f_{\mathsf{e}}^{\mathsf{KFRW}}(k)$, is defined as

$$x_{\mathsf{a}}(k+1) = A_{\mathsf{a}}^{\mathsf{d}} x_{\mathsf{a}}(k) + \epsilon_{\mathsf{n}}(k) \tag{5.3a}$$

$$y(k) = C_{\mathsf{a}} x_{\mathsf{a}}(k) + \mu_{\mathsf{n}}(k). \tag{5.3b}$$

Here, the subscript $\{\cdot\}_{\mathsf{a}}$ refers to the augmented $\{\cdot\}$, $x_{\mathsf{a}}(k) \in \mathbb{R}^{(n_{\mathsf{ss}}+1)}$, $A^{\mathsf{d}}_{\mathsf{a}} \in \mathbb{R}^{(n_{\mathsf{ss}}+1)\times(n_{\mathsf{ss}}+1)}$, and $C_{\mathsf{a}} \in \mathbb{R}^{q_{\mathsf{ss}}\times(n_{\mathsf{ss}}+1)}$ are given by

$$x_{\mathsf{a}}(k) = \begin{bmatrix} x(k) \\ f_{\mathsf{e}}^{\mathsf{KFRW}}(k) \end{bmatrix}, \; A^{\mathsf{d}}_{\mathsf{a}} = \begin{bmatrix} A^{\mathsf{d}}_{\mathsf{ss}} & B^{\mathsf{d}}_{\mathsf{ss}} \\ 0 & 1 \end{bmatrix}, \; C_{\mathsf{a}} = \begin{bmatrix} C_{\mathsf{ss}} & 0 \end{bmatrix}. \tag{5.4}$$

In Equation (5.4), $\epsilon_{\mathsf{n}}(k)$ and $\mu_{\mathsf{n}}(k)$ are the process and measurement white-noises, whose covariance matrices are $Q_{\epsilon_{\mathsf{n}}}$ and $R_{\mu_{\mathsf{n}}}$, respectively. Additionally, C_{ss} is modified in this strategy to obtain just position and velocity as outputs. Once the augmented system is described, it is possible to define the linear, discrete-time KF used by KFRW as

Time Update (*A Priori*) :

$$\tilde{x}^{-}_{\mathsf{a}}(k) = A^{\mathsf{d}}_{\mathsf{a}}\tilde{x}_{\mathsf{a}}(k-1), \tag{5.5a}$$

$$P^{-}_{\mathsf{kf}}(k) = A^{\mathsf{d}}_{\mathsf{a}}P_{\mathsf{kf}}(k-1)A^{\mathsf{d}^{\mathsf{T}}}_{\mathsf{a}} + Q_{\epsilon_{\mathsf{n}}}. \tag{5.5b}$$

Measurement Update (*A Posteriori*) :

$$K_{\mathsf{kf}}(k) = P^{-}_{\mathsf{kf}}(k)C^{\mathsf{T}}_{\mathsf{a}}(C_{\mathsf{a}}P^{-}_{\mathsf{kf}}(k)C^{\mathsf{T}}_{\mathsf{a}} + R_{\mu_{\mathsf{n}}})^{-1}, \tag{5.5c}$$

$$P_{\mathsf{kf}}(k) = (\mathbb{I}_{n_{\mathsf{ss}}+1} - K_{\mathsf{kf}}(k)C_{\mathsf{a}})P^{-}_{\mathsf{kf}}(k), \tag{5.5d}$$

$$\tilde{x}_{\mathsf{a}}(k) = \tilde{x}^{-}_{\mathsf{a}}(k) + K_{\mathsf{kf}}(k)\left(y(k) - C_{\mathsf{a}}\tilde{x}^{-}_{\mathsf{a}}(k)\right). \tag{5.5e}$$

In Equation (5.5), the superscript $\{\cdot\}^{-}$ denotes the *a priori* estimate of $\{\cdot\}$. K_{kf} and P_{kf} stand for the Kalman gain and the error covariance matrices, respectively. The reader is referred to [32] for more information on the KF.

5.1.1.3 Kalman Filter with Harmonic Oscillator - KFHO

The same process introduced for KFRW can be used for KFHO, with an adaptation of the matrices of the augmented SS model, shown in Equation (5.4), which now include a HO model (instead of the RW model) to describe the dynamics of $f_{\mathsf{e}}^{\mathsf{KFHO}}$. Thus, the matrices of the augmented WEC system for the KFHO estimator are now given by:

$$A^{d}_{a} = \begin{bmatrix} A^{d}_{\mathsf{ss}} & B^{d}_{\mathsf{ss}}C^{\mathsf{HO}} \\ 0 & \Omega^{\mathsf{HO}} \end{bmatrix}, \; x_a(k) = \begin{bmatrix} x(k) \\ \Theta(k) \end{bmatrix}, \tag{5.6}$$

where $C^{\mathsf{HO}} = \mathbb{1}_{1,n_\omega} \otimes \begin{bmatrix} 1 & 0 \end{bmatrix}$, and the matrix $\mathbb{1}_{i,j} \in \mathbb{R}^{i\times j}$ is a matrix of ones of size $i \times j$. In Equation (5.6), $\Omega^{\mathsf{HO}} \in \mathbb{R}^{2n_\omega\times 2n_\omega}$ and $\Theta(k) \in \mathbb{R}^{2n_\omega}$ are defined as

$$\Omega^{\mathsf{HO}} = \bigoplus_{i=1}^{n_\omega} \begin{bmatrix} 0 & \omega_i \\ -\omega_i & 0 \end{bmatrix}, \; \Theta(k) = \sum_{i=1}^{n_\omega} \mathbb{e}^{n_\omega}_i \otimes \begin{bmatrix} f^{\mathsf{KFHO}}_{e_{\omega_i}}(k) \\ \dot{f}^{\mathsf{KFHO}}_{e_{\omega_i}}(k) \end{bmatrix}, \tag{5.7}$$

where $f^{\mathsf{KFHO}}_{e_{\omega_i}}(k)$ are the different components of the HO model describing $f_{\mathsf{e}}^{\mathsf{KFHO}}(k)$, and ω_i are the frequencies of those components, with $i = (1, 2, \ldots n_\omega)$. Thus, the estimated excitation force from the KFHO estimator is given by

$$\tilde{f}_{\mathsf{e}}^{\mathsf{KFHO}}(k) = C^{\mathsf{HO}}\tilde{\Theta}(k). \tag{5.8}$$

It should be noted that, by using a KF, both KFRW and KFHO can optimally handle the measurement noise (if the measurement noise is Gaussian, which is usually a good approximation of the noise generated by the sensors in many real-world applications [133]).

5.1.1.4 Extended Kalman Filter Harmonic Oscillator - EKFHO

As mentioned in Section 3.2, several variations of the EKFHO estimators can be found in the literature. In particular, the most complete variation is chosen for the comparison in this work, estimating the amplitude, frequency, and phase of f_e [116]. With that, $f_\mathsf{e}^\mathsf{EKFHO}$ is defined using multiple harmonic signals as

$$f_\mathsf{e}^\mathsf{EKFHO}(t) = \sum_{i=1}^{n_\omega} a_{\mathsf{e}_i} \mathsf{sin}(\omega_{\mathsf{e}_i} t + \phi_{\mathsf{e}_i}), \tag{5.9}$$

where a_{e_i}, ω_{e_i}, and ϕ_{e_i} are the amplitudes, frequencies and phases of the harmonic signals defining $f_\mathsf{e}^\mathsf{EKFHO}$.

The only difference between the continuous-discrete EKF[1], used by the EKFHO strategy, and the KF shown in System (5.5), is the Time Update part (Equations (5.5a) and (5.5b)). In the EKFHO, $\tilde{x}_\mathsf{a}^-(k)$ is obtained by propagating the state at the previous measurement time, $\tilde{x}_\mathsf{a}(k-1)$, as

$$\dot{\tilde{x}}_\mathsf{a}(t) = A_\mathsf{a} \tilde{x}_\mathsf{a}(t) + B_\mathsf{a} \tilde{f}_\mathsf{e}^\mathsf{EKFHO}(t) + \epsilon(t), \tag{5.10}$$

where $A_\mathsf{a} \in \mathbb{R}^{(n_\mathsf{ss}+3n_\omega)\times(n_\mathsf{ss}+3n_\omega)}$ and $\tilde{x}_\mathsf{a}(t) \in \mathbb{R}^{(n_\mathsf{ss}+3n_\omega)}$ are defined as

$$A_\mathsf{a} = \begin{bmatrix} A_\mathsf{ss} & 0 \\ 0 & 0 \end{bmatrix}, \; \tilde{x}_\mathsf{a}(t) = \begin{bmatrix} \tilde{x}(t)^\mathsf{T} & \tilde{\Lambda}(t)^\mathsf{T} & \tilde{\Omega}(t)^\mathsf{T} & \tilde{\Phi}(t)^\mathsf{T} \end{bmatrix}^\mathsf{T}. \tag{5.11}$$

$\tilde{\Lambda}(t), \tilde{\Omega}(t), \tilde{\Phi}(t) \in \mathbb{R}^{n_\omega}$ are vectors containing the estimates of a_e, ω_e, and ϕ_e, respectively. The *a priori* estimate of the covariance matrix $P_\mathsf{kf}^-(k)$, is propagated from the previous measurement time, $P_\mathsf{kf}(k-1)$, using the following algebraic Riccati equation:

$$\dot{P}_\mathsf{kf}(t) = \Upsilon(\tilde{x}_\mathsf{a}(t)) P_\mathsf{kf}(t) + P_\mathsf{kf}(t) \Upsilon(\tilde{x}_\mathsf{a}(t))^\mathsf{T} + Q_{\epsilon_\mathsf{n}}, \tag{5.12}$$

where Υ is the Jacobian matrix defined as

$$\Upsilon(\tilde{x}_\mathsf{a}(t)) = \begin{bmatrix} A_\mathsf{ss} & B_\mathsf{ss} \Psi(\tilde{x}_\mathsf{a}(t)) \\ 0 & 0 \end{bmatrix}, \tag{5.13}$$

which is evaluated at $\tilde{x}_\mathsf{a}(k-1)$, as

$$\Psi(\tilde{x}_\mathsf{a}(t)) = \left[\frac{\partial f_\mathsf{e}^\mathsf{EKFHO}}{\partial \Lambda}^\mathsf{T} \quad \frac{\partial f_\mathsf{e}^\mathsf{EKFHO}}{\partial \Omega}^\mathsf{T} \quad \frac{\partial f_\mathsf{e}^\mathsf{EKFHO}}{\partial \Phi}^\mathsf{T} \right] \Bigg|_{\tilde{x}_\mathsf{a}(t) = \tilde{x}_\mathsf{a}(k-1)}. \tag{5.14}$$

---

[1] Note that the continuous-discrete EKF combines continuous-time nonlinear models with discrete-time measurements and, therefore, the notation corresponding to both continuous- and discrete-time are mixed in the definition of the strategy, as shown in [2] and [32].

5.1.1.5 Receding Horizon Estimation - RHE

In receding horizon estimation, at every time instant $k > n_{\text{w}}$, f_{e} is estimated by minimising a QP problem over the receding window (of size n_{w}), as shown in [121]. Since no constraint is considered for the estimator comparison, as mentioned in Section 3.2, the unique analytical solution of the QP problem of RHE can be obtained as:

$$\tilde{\xi}^*(k) = (P^{\text{RHE}} + \Psi_s^{\text{T}} R^{\text{RHE}} \Psi_s)^{-1} \begin{bmatrix} S^{\text{RHE}\text{T}} & \Psi_s^{\text{T}} R^{\text{RHE}\text{T}} \end{bmatrix} \begin{bmatrix} \tilde{f}_{\text{e}}^{\text{RHE}}(k - n_{\text{w}}) \\ \tilde{x}(k - n_{\text{w}}) \\ Y^{\text{RHE}}(k) \end{bmatrix}, \tag{5.15}$$

where $R^{\text{RHE}} \in \mathbb{R}^{q_{\text{ss}} n_{\text{w}} \times q_{\text{ss}} n_{\text{w}}}$ is a diagonal weighting matrix to account for the measurement noise, $Y^{\text{RHE}}(k) \in \mathbb{R}^{q_{\text{ss}} n_{\text{w}}}$ a vector containing all the values of y from $k - n_{\text{w}} + 1$ to k (assuming position and velocity as outputs), $\Psi_s = \begin{bmatrix} \Psi_y & \Phi_y & \Gamma_y \end{bmatrix} \in \mathbb{R}^{q_{\text{ss}} n_{\text{w}} \times (n_{\text{w}} + n_{\text{ss}} + n_{\text{ss}} n_{\text{w}})}$, and the matrices $P^{\text{RHE}} \in \mathbb{R}^{(n_{\text{w}} + n_{\text{ss}} + n_{\text{ss}} n_{\text{w}}) \times (n_{\text{w}} + n_{\text{ss}} + n_{\text{ss}} n_{\text{w}})}$, $\Gamma_y \in \mathbb{R}^{q_{\text{ss}} n_{\text{w}} \times n_{\text{ss}} n_{\text{w}}}$, $\Phi_y \in \mathbb{R}^{q_{\text{ss}} n_{\text{w}} \times n_{\text{ss}}}$, $\Psi_y \in \mathbb{R}^{q_{\text{ss}} n_{\text{w}} \times n_{\text{w}}}$, and $S^{\text{RHE}} \in \mathbb{R}^{(1 + n_{\text{w}}) \times (n_{\text{w}} + n_{\text{ss}} + n_{\text{ss}} n_{\text{w}})}$ are defined as

$$P^{\text{RHE}} = \begin{bmatrix} \Lambda_1 & 0 & 0 \\ 0 & P_0^{-1} & 0 \\ 0 & 0 & Q^{\text{RHE}} \end{bmatrix}, \quad \Gamma_y = \begin{bmatrix} C_{\text{ss}} & 0 & \cdots & 0 \\ C_{\text{ss}} A_{\text{ss}} & C_{\text{ss}} & \cdots & 0 \\ \vdots & \vdots & \ddots & \vdots \\ C_{\text{ss}} A_{\text{ss}}^{n_{\text{w}}-1} & C_{\text{ss}} A_{\text{ss}}^{n_{\text{w}}-2} & \cdots & C_{\text{ss}} \end{bmatrix},$$

$$\Phi_y = \begin{bmatrix} C_{\text{ss}} A_{\text{ss}} \\ C_{\text{ss}} A_{\text{ss}}^2 \\ \vdots \\ C_{\text{ss}} A_{\text{ss}}^{n_{\text{w}}} \end{bmatrix}, \quad \Psi_y = \begin{bmatrix} C_{\text{ss}} B_{\text{ss}} & 0 & \cdots & 0 \\ C_{\text{ss}} A_{\text{ss}} B_{\text{ss}} & C_{\text{ss}} B_{\text{ss}} & \cdots & 0 \\ \vdots & \vdots & \ddots & \vdots \\ C_{\text{ss}} A_{\text{ss}}^{n_{\text{w}}-1} B_{\text{ss}} & C_{\text{ss}} A_{\text{ss}}^{n_{\text{w}}-2} B_{\text{ss}} & \cdots & C_{\text{ss}} B_{\text{ss}} \end{bmatrix}, \tag{5.16}$$

$$S^{\text{RHE}} = \begin{bmatrix} Q_0^{-1} & 0 & 0 & 0 \\ 0 & 0 & P_0^{-1} & 0 \end{bmatrix}, \quad \Lambda_1 = \begin{bmatrix} Q_0^{-1} + \lambda^{\text{s}} & -\lambda^{\text{s}} & 0 & \cdots & 0 \\ -\lambda^{\text{s}} & 2\lambda^{\text{s}} & -\lambda^{\text{s}} & \cdots & 0 \\ 0 & -\lambda^{\text{s}} & 2\lambda^{\text{s}} & \cdots & 0 \\ \vdots & \vdots & \vdots & \ddots & \vdots \\ 0 & 0 & 0 & \cdots & \lambda^{\text{s}} \end{bmatrix}.$$

$P_0^{-1} \in \mathbb{R}^{n_{\text{ss}} \times n_{\text{ss}}}$ and $Q^{\text{RHE}} \in \mathbb{R}^{n_{\text{ss}} n_{\text{w}} \times n_{\text{ss}} n_{\text{w}}}$ are diagonal weighting matrices, penalising the error in the state estimate and process noise, respectively, and $Q_0^{-1} \in \mathbb{R}$ a scalar, penalising the error in the f_{e} estimate. The size of the second column of S^{RHE} (which is full of zeros) is $(n_{\text{ss}} + 1) \times (n_{\text{ss}} + 1)$, and $\lambda^{\text{s}} \in \mathbb{R}$ is a scalar to exploit the fact that f_{e} is smooth, which was first considered in [121]. Finally, the value of $\tilde{f}_{\text{e}}^{\text{RHE}}(k)$ is given by the n_{w}^{th} value of the vector $\tilde{\xi}^*(k) \in \mathbb{R}^{(n_{\text{w}} + n_{\text{ss}} + n_{\text{ss}} n_{\text{w}})}$ of Equation (5.15).

5.1.1.6 Unknown Input Observer - UIO

The UIO strategy, proposed in [3], uses WEC position and PTO current measurements to estimate f_{e} and $\dot{\chi}$. However, since no PTO current measurements are available in the comparison carried out here, the UIO strategy is adapted to use device position and velocity measurements. Before defining the required observer, the following augmented system needs to be formulated:

$$\dot{x}_{\mathsf{a}}(t) = A_{\mathsf{a}} x_{\mathsf{a}}(t) + D_{\mathsf{a}} d^{\mathsf{UIO}}(t, x_{\mathsf{a}}), \tag{5.17a}$$

$$y(t) = C_{\mathsf{a}} x_{\mathsf{a}}(t), \tag{5.17b}$$

where $x_{\mathsf{a}}(t) \in \mathbb{R}^{n_{\mathsf{ss}}+2}$, $A_{\mathsf{a}} \in \mathbb{R}^{(n_{\mathsf{ss}}+2)\times(n_{\mathsf{ss}}+2)}$, $D_{\mathsf{a}} \in \mathbb{R}^{(n_{\mathsf{ss}}+2)\times 3}$, and $C_{\mathsf{a}} \in \mathbb{R}^{q_{\mathsf{ss}}\times(n_{\mathsf{ss}}+2)}$ are defined as

$$\begin{gathered} x_{\mathsf{a}}(t) = \begin{bmatrix} x(t) \\ F_{\mathsf{e}}^{\mathsf{UIO}}(t) \\ \xi^*(t) \end{bmatrix}, \quad A_{\mathsf{a}} = \begin{bmatrix} A_{\mathsf{ss}} & B_{\mathsf{ss}} & 0 \\ 0 & 0 & 0 \\ 0 & 0 & 0 \end{bmatrix}, \quad D_{\mathsf{a}} = \begin{bmatrix} D^* & 0 & 0 \\ 0 & 1 & 0 \\ 0 & 0 & 1 \end{bmatrix}, \\ C_{\mathsf{a}} = \begin{bmatrix} C_{\mathsf{ss}} & 0 & \Xi^* \end{bmatrix}, \quad D^* = \begin{bmatrix} 0 & 1 \end{bmatrix}^{\mathsf{T}}, \quad \Xi^* = \begin{bmatrix} -2 & 2 \end{bmatrix}^{\mathsf{T}}. \end{gathered} \tag{5.18}$$

The term $d^{\mathsf{UIO}}(t, x_{\mathsf{a}})$ can represent a model disturbance, while $\xi^*(t) \in \mathbb{R}^{n_{\mathsf{sf}}}$ stands for any measurement noise or sensor fault, with $n_{\mathsf{sf}} = 1$, for this work, representing only measurement noise. The following observer is then used to estimate the augmented state $x_{\mathsf{a}}(t)$:

$$\dot{\zeta}^{\mathsf{UIO}}(t) = \mathcal{M}^{\mathsf{UIO}} \zeta^{\mathsf{UIO}}(t) + L^{\mathsf{UIO}} y(t), \tag{5.19a}$$

$$\tilde{x}_a(t) = \zeta^{\mathsf{UIO}}(t) + H^{\mathsf{UIO}} y(t), \tag{5.19b}$$

where the matrices $\mathcal{M}^{\mathsf{UIO}} \in \mathbb{R}^{(n_{\mathsf{ss}}+1+n_{\mathsf{sf}})\times(n_{\mathsf{ss}}+1+n_{\mathsf{sf}})}$, $L^{\mathsf{UIO}} \in \mathbb{R}^{(n_{\mathsf{ss}}+1+n_{\mathsf{sf}})\times q_{\mathsf{ss}}}$, and $H^{\mathsf{UIO}} \in \mathbb{R}^{(n_{\mathsf{ss}}+1+n_{\mathsf{sf}})\times q_{\mathsf{ss}}}$ are obtained by solving a set of LMIs. In particular, the set of LMIs to be solved for the UIO estimator are shown in Equation (5.20). Thus, the system associated with the error dynamics defined by $e_x(t) = x(t) - \tilde{x}(t)$ (denoted Σ_e^{UIO}) is stable and H_∞ performance is guaranteed[2], with an attenuation level of $\gamma^{\mathsf{UIO}} > 0$, i.e. $\|\Sigma_e^{\mathsf{UIO}}\|_\infty < \gamma^{\mathsf{UIO}}$, if there exists a symmetric positive definite matrix $P_{\mathsf{L}} \in \mathbb{R}^{(n_{\mathsf{ss}}+1+n_{\mathsf{sf}})\times(n_{\mathsf{ss}}+1+n_{\mathsf{sf}})}$ and the following LMI constraint holds:

$$\begin{bmatrix} he(P_{\mathsf{L}} A_{\mathsf{a}} - M_1 C_{\mathsf{a}} A_{\mathsf{a}} - M_2 C_{\mathsf{a}}) & P_{\mathsf{L}} D_{\mathsf{a}} & C_{\mathsf{a}}^{\mathsf{T}} \\ \star & -\gamma^{\mathsf{UIO}} \mathbb{I}_{(q_{\mathsf{ss}}+1+n_{\mathsf{sf}})} & 0 \\ \star & \star & -\gamma^{\mathsf{UIO}} \mathbb{I}_{q_{\mathsf{ss}}} \end{bmatrix} < 0, \tag{5.20}$$

where $M_1 = P_{\mathsf{L}} H^{\mathsf{UIO}}$, $M_2 = P_{\mathsf{L}} L_1$, $L^{\mathsf{UIO}} = L_1 + L_2$, $L_2 = (E^{\mathsf{UIO}} A_{\mathsf{a}} - L_1 C_{\mathsf{a}}) H^{\mathsf{UIO}}$, $E^{\mathsf{UIO}} = \mathbb{I}_{(n_{\mathsf{ss}}+1+n_{\mathsf{sf}})} - H^{\mathsf{UIO}} C_{\mathsf{a}}$, $\mathcal{M}^{\mathsf{UIO}} = E^{\mathsf{UIO}} A_{\mathsf{a}} - L_1 C_{\mathsf{a}}$, and $\star$ denotes the symmetric image components of the matrix.

The two main advantages of the UIO strategy are that the LMIs can be designed such that the observer is robust against model uncertainties, and that measurement noise can be accounted for.

---

[2] Which means the gain L^{UIO} is designed such that the effect of the exogenous input d^{UIO} on the estimation error $e_x(t)$ is attenuated below certain level γ^{UIO}.

5.1.1.7 Adaptive Sliding Mode Observer - ASMO

The adaptive sliding mode observer, proposed in [190], is defined as

$$\begin{aligned}
\dot{h}^{\mathsf{sl}}(t) &= \frac{S_{\mathsf{h}}}{M^*}\chi(t) + \frac{C_{\mathsf{r_{ss}}}}{M^*}x_{\mathsf{r}}(t) - \frac{1}{M^*}\tilde{f}_{\mathsf{e}}^{\mathsf{ASMO}}(t), && (5.21a)\\
s^{\mathsf{sl}}(t) &= \dot{\chi}(t) + h^{\mathsf{sl}}(t), && (5.21b)\\
\dot{c}^{\mathsf{sl}}(t) &= \mathsf{sign}(s^{\mathsf{sl}}(t)), && (5.21c)\\
\tilde{f}_{\mathsf{e}}^{\mathsf{ASMO}}(t) &= M^*\left(R^{\mathsf{sl}}|s^{\mathsf{sl}}(t)|^{\frac{1}{2}}\dot{c}^{\mathsf{sl}}(t) + Q^{\mathsf{sl}}c^{\mathsf{sl}}(t)\right), && (5.21d)
\end{aligned}$$

where s^{sl} is the sliding variable and the gains R^{sl} and Q^{sl} are defined as

$$\begin{aligned}
R^{\mathsf{sl}}(t) &= |\dot{\chi}(t)||s^{\mathsf{sl}}(t)|, && (5.22a)\\
Q^{\mathsf{sl}}(t) &= 0.5\mu^{\mathsf{sl}}R^{\mathsf{sl}}(t) + 0.5\mu^{\mathsf{sl}^2} + 0.5\kappa^{\mathsf{sl}}, && (5.22b)
\end{aligned}$$

respectively, with μ^{sl} and κ^{sl} as positive scalar values. In Equation (5.21), the radiation force state vector $x_{\mathsf{r}}(t)$ is obtained, as shown in System (2.39), using the measured device velocity $\dot{\chi}(t)$ as input. The main disadvantage of this approach, as for some of the other estimation strategies introduced before, is that there is no term to account for the measurement noise and, therefore, the accuracy of the estimated f_{e} can be significantly affected by such measurement noise.

5.1.1.8 Unified Linear Input & State Estimator - ULISE

As mentioned in Section 3.2, there is a variant of the ULISE strategy using pressure measurements. However, since the model that relates the total pressure on the hull and f_{e} would have to be identified from CFD experiments (in [14] the model is identified through wave tank tests), the estimator using such model would have an advantage over the other strategies. Therefore, only the ULISE estimator using motion measurements is employed in this comparison. The three-phase filter proposed in [29] for the ULISE approach is defined as:

Time Update:

$$\begin{aligned}
\tilde{x}^-(k) &= A_{\mathsf{ss}}^{\mathsf{d}}\tilde{x}(k-1) + B_{\mathsf{ss}}^{\mathsf{d}}\tilde{f}_{\mathsf{e}}^{\mathsf{ULISE}}(k-1), && (5.23a)\\
P_x^-(k) &= A_{\mathsf{ss}}^{\mathsf{d}}P_x(k-1)A_{\mathsf{ss}}^{\mathsf{d}\,\mathsf{T}} + B_{\mathsf{ss}}^{\mathsf{d}}P_{xf_{\mathsf{e}}}(k-1)^{\mathsf{T}}A^{\mathsf{d}\mathsf{T}} + A_{\mathsf{ss}}^{\mathsf{d}}P_{xf_{\mathsf{e}}}(k-1)B_{\mathsf{ss}}^{\mathsf{d}\,\mathsf{T}}\\
&\quad + B_{\mathsf{ss}}^{\mathsf{d}}P_{f_{\mathsf{e}}}(k-1)B_{\mathsf{ss}}^{\mathsf{d}\,\mathsf{T}} + Q_{\epsilon_{\mathsf{n}}}, && (5.23b)\\
\check{R}^-(k) &= C_{\mathsf{ss}}P_x^-(k)C_{\mathsf{ss}}^{\mathsf{T}}. && (5.23c)
\end{aligned}$$

Measurement Update:

$$\begin{aligned}
\check{L}(k) &= P_x^-(k)C_{\mathsf{ss}}^{\mathsf{T}}\check{R}^-(k)^{-1}\left(\mathbb{I}_{n_{\mathsf{ss}}} - D_{\mathsf{ss}}(D_{\mathsf{ss}}^{\mathsf{T}}\check{R}^-(k)^{-1}D_{\mathsf{ss}})^{-1}D_{\mathsf{ss}}^{\mathsf{T}}\check{R}^-(k)^{-1}\right), && (5.23d)\\
\tilde{x}(k) &= \tilde{x}^-(k) + \check{L}(k)\left(y(k) - C_{\mathsf{ss}}\tilde{x}^-(k)\right), && (5.23e)\\
P_x(k) &= \left(\mathbb{I}_{n_{\mathsf{ss}}} - \check{L}(k)C_{\mathsf{ss}}\right)P_x^-(k)\left(\mathbb{I}_{n_{\mathsf{ss}}} - \check{L}(k)C_{\mathsf{ss}}\right)^{\mathsf{T}} + \check{L}(k)R_{\mu_{\mathsf{n}}}\check{L}(k)^{\mathsf{T}}. && (5.23f)
\end{aligned}$$

Estimation of unknown input:

$$\check{R}(k) = \left(\mathbb{I}_{n_{\mathsf{ss}}} - C_{\mathsf{ss}}\check{L}(k)\right)\check{R}^{-}(k)\left(\mathbb{I}_{n_{\mathsf{ss}}} - C_{\mathsf{ss}}\check{L}(k)\right)^{\mathsf{T}}, \tag{5.23g}$$

$$P_{f_{\mathsf{e}}}(k) = \left(D_{\mathsf{ss}}^{\mathsf{T}}\check{R}(k)^{-1}D_{\mathsf{ss}}\right)^{-1}, \tag{5.23h}$$

$$\tilde{f}_{\mathsf{e}}^{\mathsf{ULISE}}(k) = \left(P_{f_{\mathsf{e}}}(k)D_{\mathsf{ss}}^{\mathsf{T}}\check{R}(k)^{-1}\right)\left(y(k) - C_{\mathsf{ss}}\tilde{x}(k)\right), \tag{5.23i}$$

$$P_{xf_{\mathsf{e}}}(k) = -P_x(k)C_{\mathsf{ss}}^{\mathsf{T}}\left(P_{f_{\mathsf{e}}}(k)D_{\mathsf{ss}}^{\mathsf{T}}\check{R}(k)^{-1}\right)^{\mathsf{T}} + \check{L}(k)R_{\mu_{\mathsf{n}}}\left(P_{f_{\mathsf{e}}}(k)D_{\mathsf{ss}}^{\mathsf{T}}\check{R}(k)^{-1}\right)^{\mathsf{T}}, \tag{5.23j}$$

where $P_x(k) \in \mathbb{R}^{n_{\mathsf{ss}} \times n_{\mathsf{ss}}}$, $P_{f_{\mathsf{e}}}(k) \in \mathbb{R}$, and $P_{xf_{\mathsf{e}}}(k) \in \mathbb{R}^{n_{\mathsf{ss}}}$ are the covariance matrices related to the state, f_{e}, and the relation between the state and f_{e}, respectively. Since only position and acceleration measurements are used by ULISE, only the 1st and 3rd row of C_{ss} and D_{ss}, from System (2.41), are considered.

5.1.1.9 Fast Adaptive Unknown Input Estimation - FAUIE

The observer proposed for the FAUIE strategy [5], which uses proportional and integral terms of the state estimation error, is defined as[3]:

$$\dot{\tilde{x}}(t) = A_{\mathsf{ss}}\tilde{x}(t) + B_{\mathsf{ss}}\tilde{f}_{\mathsf{e}}^{\mathsf{FAUIE}}(t) - L_1 e_y(t) - L_2 \dot{e}_y(t), \tag{5.24a}$$

$$\tilde{y}(t) = C_{\mathsf{ss}}\tilde{x}(t), \tag{5.24b}$$

where the estimated excitation force is given by

$$\tilde{f}_{\mathsf{e}}^{\mathsf{FAUIE}}(t) = -\Gamma^{\mathsf{FAUIE}} L_3 C(\dot{e}_x(t) + \sigma^* e_x(t)), \tag{5.25}$$

and the output and state errors can be obtained as $e_y = \tilde{y} - y$ and $e_x = \tilde{x} - x$, respectively. $\Gamma^{\mathsf{FAUIE}} \in \mathbb{R}$ is the user defined learning rate, $L_2 \in \mathbb{R}^{n_{\mathsf{ss}} \times q_{\mathsf{ss}}}$ and $\sigma^* \in \mathbb{R}$ are design parameters, and both $L_1 \in \mathbb{R}^{n_{\mathsf{ss}} \times q_{\mathsf{ss}}}$ and $L_3 \in \mathbb{R}^{q_{\mathsf{ss}}}$ are obtained by solving the following set of LMIs:

$$\begin{bmatrix} \Pi_{11} & \Pi_{12} & P_{\mathsf{L}} & 0 \\ \star & \Pi_{22} & 0 & B_{\mathsf{ss}}P_{\mathsf{L}} \\ \star & \star & -\alpha^*\mathbb{I}_{n_{\mathsf{ss}}} & 0 \\ \star & \star & \star & \Pi_{44} \end{bmatrix} < 0, \tag{5.26a}$$

$$\begin{bmatrix} \nu^*\mathbb{I}_{n_{\mathsf{ss}}} & B_{\mathsf{ss}}P_{\mathsf{L}} - L_3 C_{\mathsf{ss}} \\ \star & \nu^*\mathbb{I}_{n_{\mathsf{ss}}} \end{bmatrix} > 0. \tag{5.26b}$$

Here, $\Pi_{11} = he(P_{\mathsf{L}}A_{\mathsf{ss}} - Y_{\mathsf{L}}C_{\mathsf{ss}})$, $Y_{\mathsf{L}} = P_{\mathsf{L}}L_1$, $\Pi_{12} = \frac{\gamma^*}{\sigma^*}(C_{\mathsf{ss}}^{\mathsf{T}}Y_{\mathsf{L}}^{\mathsf{T}}B_{\mathsf{ss}} - A_{\mathsf{ss}}^{\mathsf{T}}P_{\mathsf{L}}B_{\mathsf{ss}})$, $\Pi_{22} = -\frac{2\gamma^*}{\sigma^*}B_{\mathsf{ss}}^{\mathsf{T}}P_{\mathsf{L}}B_{\mathsf{ss}} + \frac{G_{\mathsf{L}}}{\sigma^*\mu^*}$, $\Pi_{44} = -\frac{\beta^*\sigma^*}{\gamma^*}\mathbb{I}_{n_{\mathsf{ss}}}$, $he(\{\cdot\}) = \{\cdot\} + \{\cdot\}^{\mathsf{T}}$, and $\{\alpha^*, \beta^*, \mu^*, \gamma^*\} > 0 \in \mathbb{R}$ are design parameters. Although the matrix C_{ss} of Equation (5.24) is modified to obtain only position and velocity, measurements of the WEC acceleration are also needed due to the term $\dot{e}_y$. To this end, the observer of Equation (5.24) will give

---

[3] Since the model considered in this thesis is linear, the Lipschitz term in [5], accounting for the nonlinearities, has been removed.

bounded estimation errors, e_x and e_{f_e}, if positive definite matrices $P_\mathrm{L} \in \mathbb{R}^{n_\mathrm{ss} \times n_\mathrm{ss}}$ and $G_\mathrm{L} \in \mathbb{R}$ exist, and the constraints imposed in Equation (5.26) hold while, at the same time, $\nu^* > 0 \in \mathbb{R}$ is minimised.

The main drawback of the FAUIE estimator is that there is no term to account for the measurement noise, which may significantly affect the accuracy of the estimated f_e.

5.1.1.10 Extended Kalman Filter with Pressure Sensors - EKFPS

The EKFPS [1, 2], assumes that $\tilde{f}_\mathrm{e}^\mathrm{EKFPS}$ is defined as

$$\tilde{f}_\mathrm{e}^\mathrm{EKFPS}(t) = \rho g \sum_{j=1}^{n_\mathrm{p}} \mathrm{S}_j^\mathrm{s} n_{o_j} \sum_{i=1}^{n_\omega} a_{\mathrm{e}_i} e^{\kappa_{\mathrm{e}_i} z_j^\mathrm{s}} \cos(\kappa_{\mathrm{e}_i} x_j^\mathrm{s} - \omega_{\mathrm{e}_i} t + \phi_{\mathrm{e}_i}), \tag{5.27}$$

where the wavenumber, $\kappa_{\mathrm{e}_i} = {\omega_{\mathrm{e}_i}^2}/{g}$, is calculated as shown in Equation (2.3)[4], S_j^s is the surface area around the sensor j, n_{o_j} the normal vector to S_j^s, and x_j^s and z_j^s are the coordinates of the j^{th} sensor in the x and z axes, respectively. It is also assumed, for this f_e estimator, that the pressure at each sensor can be described as

$$p_j(t) = \rho g \sum_{i=1}^{n_\omega} a_{\mathrm{e}_i} e^{\kappa_{\mathrm{e}_i} z_j^\mathrm{s}} \cos(\kappa_{\mathrm{e}_i} x_j^\mathrm{s} - \omega_{\mathrm{e}_i} t + \phi_{\mathrm{e}_i}) - \rho g(\chi(t) + x_j^\mathrm{s}) - \frac{C_\mathrm{r} x_\mathrm{r}(t)}{\mathrm{S}_\mathrm{wet}}, \tag{5.28}$$

and the output vector is given by $\tilde{y}(t) = \begin{bmatrix} \tilde{\chi}(t)^\mathsf{T} & \tilde{p}_1(t)^\mathsf{T} & \cdots & \tilde{p}_{n_\mathrm{p}}(t)^\mathsf{T} \end{bmatrix}^\mathsf{T}$, with n_p the number of pressure sensors.

The continuous-discrete EKF, used by the EKFPS, differs from that used for the EKFHO strategy. While the outputs of the EKFHO ($\chi(t)$ and $\dot{\chi}(t)$) are part of the state vector, the output of the EKFPS strategy is given by the nonlinear combination of the states shown in Equation (5.28). Therefore, the estimation process required by the EKFPS can be summarised as:

- Propagate the state $\tilde{x}_a$, to obtain $\tilde{x}_a^-(k)$ from $\tilde{x}_a(k-1)$, using

$$\dot{\tilde{x}}_a(t) = \begin{bmatrix} \dot{\tilde{\chi}}(t) \\ M^* \tilde{f}_\mathrm{tot}(t) \\ B_{\mathrm{r_{ss}}} \dot{\tilde{\chi}}(t) + A_{\mathrm{r_{ss}}} \tilde{x}_\mathrm{r}(t) \\ 0 \end{bmatrix}, \tag{5.29}$$

  where $f_\mathrm{tot}(t)$ is the sum of all the forces, including $\tilde{f}_\mathrm{pto}(t)$, $\tilde{f}_\mathrm{e}^\mathrm{EKFPS}(t)$, $\tilde{f}_\mathrm{r}(t) = C_{\mathrm{r_{ss}}} \tilde{x}_\mathrm{r}(t)$, and $\tilde{f}_\mathrm{h}(t)$, which for the EKFPS is given by

$$\tilde{f}_\mathrm{h}(t) = -\rho g \sum_{i=1}^{n_\mathrm{p}} \mathrm{S}_i^\mathrm{s} n_{o_i} (\tilde{\chi}(t) + z_i^\mathrm{s}). \tag{5.30}$$

---

[4] Note that this definition of κ only holds for deep water depth which, as introduced in Section 2.1.1, is assumed throughout this thesis.

- Propagate the covariance matrix to get $P^{-}_{\mathsf{kf}}(k)$ using the Riccati equation (5.12). However, the Jacobian $\Upsilon(\tilde{x}(t), t)$, shown in Equation (5.13), is now computed considering $\tilde{f}_{\mathsf{e}}^{\mathsf{EKFPS}}(t)$ (instead of $\tilde{f}_{\mathsf{e}}^{\mathsf{EKFHO}}(t)$), and the new description of $\tilde{f}_{\mathsf{h}}(t)$ (instead of the term S_{h} of the matrix A_{ss} of Equation (5.11)).

- The Kalman gain is now given by

$$K_{\mathsf{kf}}(k) = P^{-}_{\mathsf{kf}}(k)\check{\Xi}(\tilde{x}^{-}_{a}(k))^{\mathsf{T}} \left(\check{\Xi}(\tilde{x}^{-}_{a}(k))P^{-}_{\mathsf{kf}}(k)\check{\Xi}(\tilde{x}^{-}_{a}(k))^{\mathsf{T}} + R_{\mu_{\mathsf{n}}}\right)^{-1}, \quad (5.31)$$

  where $\check{\Xi}(\tilde{x}^{-}_{a}(k)) = \frac{\delta y}{\delta x_a}\Big|_{\tilde{x}^{-}_{a}(k)} \in \mathbb{R}^{(n_{\mathsf{p}}+1)\times(n_{\mathsf{ss}}+3n_{\omega})}$ is the Jacobian matrix of the output, evaluated using $\tilde{x}^{-}_{a}(k)$.

- Finally, update the covariance $P^{-}_{\mathsf{kf}}(k)$ and the current state $\tilde{x}^{-}_{a}(k)$ using:

$$\tilde{x}_{a}(k) = \tilde{x}^{-}_{a}(k) + K_{\mathsf{kf}}(k)\left(y(k) - \tilde{y}(k)\right), \quad (5.32a)$$

$$P_{\mathsf{kf}}(k) = \left(\mathbb{I}_{n_{\mathsf{ss}}+3n_{\omega}} - K_{\mathsf{kf}}(k)\check{\Xi}(\tilde{x}^{-}_{a}(k))\right) P^{-}_{\mathsf{kf}}(k). \quad (5.32b)$$

5.1.1.11 Pressure Acceleration Displacement Estimation - PADE

The last estimation technique considered in the comparison of this section, the PADE strategy proposed in [84], assumes that the instantaneous excitation force can be approximated as:

$$\tilde{f}_{\mathsf{e}}^{\mathsf{PADE}}(t) = f_{\mathsf{w}}(t) - f_{\mathsf{r}}(t) - f_{\mathsf{h}}(t) - gm, \quad (5.33a)$$

$$f_{\mathsf{w}}(t) = \sum_{j=1}^{n_{\mathsf{p}}} p_j(t)\mathsf{S}^{\mathsf{s}}_{j} n_{o_j}, \quad (5.33b)$$

where p_j is the total pressure measured by the j^{th} sensor. Although the product between the gravitational constant and the mass of the device gm is not included in [84], it was found that this term is required to cancel out an offset on the total pressure p. The main disadvantage of PADE is that, since it computes the hydrodynamic forces directly from the motion measurements, it does not handle measurement noise.

5.1.2 Classification of estimators

From the review of the f_{e} estimators given in Sections 5.1.1.1-5.1.1.11, different classifications of the estimators can be proposed. A first class distinguishes between open-loop and closed-loop estimators. While CPWE and PADE are the only open-loop strategies, the remaining estimators are closed-loop. It can be argued that closed-loop estimators have an advantage since, due to the feedback mechanism, closed-loop estimators can better handle possible measurement or process uncertainty (noise).

Another possible classification is linear vs. nonlinear. Some estimators require a nonlinear combination of the states to characterise f_e. Thus, the group of linear estimators is composed of the CPWE, KFRW, KFHO, RHE, UIO, ASMO, ULISE, FAUIE, and PADE strategies, while the EKFHO and EKFPS estimation techniques are inherently nonlinear.

A final classification relies on the required measurements. Three different groups of estimators can be distinguished via this classification scheme: using η measurements, using device motion measurements, or using device motion and pressure measurements. The group of estimators using η measurements includes just the CPWE. The group using only WEC motion measurement embraces the KFRW, KFHO, EKFHO, RHE, ASMO, UIO, ULISE, and FAUIE strategies. Using WEC motion and pressure measurements, the EKFPS and the PADE strategies constitute the last group of this class.

Since the availability of measurement data is defined at the stage of device design and construction, some measurements, required for the f_e estimator, may not be available and, hence, rule out some strategies. Consequently, Section 5.1.5 follows the classification based on the required measurements, since this appears to be most important for the practical implementation of the estimator.

5.1.3 Comparison methodology

To compare the performance of the f_e estimators, the calculation of a reference value for the 'true' excitation force is required, to determine the accuracy of each strategy. However, as mentioned before, the excitation force is, in general, an unmeasurable quantity for an oscillating device. To date, common practice in the literature for the determination of a f_e reference, is to simply generate a random f_e signal or calculate the signal from η data. By using a (linear or nonlinear) hydrodynamic model for motion simulation, the corresponding response of the device is determined using the f_e reference signal as an input to the simulation model. f_e is subsequently estimated, from the simulated motion of the device, and compared to the f_e reference.

Although this procedure is common practice in the field, an important drawback can be identified. Assuming that a specific hydrodynamic model is used for the simulation of the device motion and an identical model is also used within the estimation strategy, an unbiased comparison of these estimators to those with different underlying hydrodynamic models is impossible. Therefore, to avoid the use of the same model in both the WEC motion simulation and the f_e estimation stages, a CFD-based Numerical Wave Tank (CNWT) is employed for motion simulation of the analysed WEC. This not only decouples the reference definition and estimation stages, but delivers more realistic results, compared to commonly used hydrodynamic models, since the CNWT inherently captures all the relevant nonlinearities by directly solving the Navier-Stokes equations (Equation (2.6)) [186, 185]. Thus, for the f_e reference definition, the following methodology, adopted from [78, 100] and [121], is used in this comparison: A set of waves is generated in the CNWT, in which the device is fixed in its equilibrium position. For this diffraction test case, since the device is not moving, radiation and hydrostatic forces are zero and the total wave force f_w, measured on the device, is f_e. Since f_w and, thus, f_e is given by the integral of the pressure over the wetted surface of the device, it can be measured using numerical pressure gauges at specific locations on the hull of the device. For that, a finite number of numerical pressure probes is used, to mimic a realistic, physical, test setup. A detailed description of the CNWT, and the case study, is given in Section 5.1.4.

Using the same input wave series, as for the above described wave diffraction test, simulations are performed with an unconstrained device, free to move[5]. From these simulations, measurements of the required quantities for the different estimators are taken, i.e. η, WEC motion (χ, $\dot{\chi}$, $\ddot{\chi}$), and pressure over the hull of the WEC. The acquired data are then used in the different f_e estimators, and the results are compared to the f_e measured in the wave diffraction tests.

It is important to note that the calculation of f_e, obtained from the wave diffraction test, as a reference for the motion simulation, only holds under linear conditions. For large amplitude relative motion between the body and η, the excitation force may become nonlinear, and equality between f_e in the wave diffraction, and motion tests, will not hold since, as explained in Section 2.2.2, linear potential flow assumes small relative motion between the body and η. To ensure and verify linear behaviour, some metrics and methodologies are provided in the literature, detailed in Section 5.1.4.

In order to quantify the accuracy of the analysed strategies, the estimation error is given in terms of the NRMSE (see Equation (4.21)). However, in order to avoid the estimation transient times, and obtain meaningful results, only the last 40% of the simulation time (the last 60 s) is considered to compute the NRMSE. Since the NRMSE is used to quantify both estimation and prediction errors in this section, for the sake of clarity, in addition to the subscript specifying the variable over which the error is computed, a superscript is added to specify if the error is computed using estimated or forecasted data; by way of example, the estimation error of f_e is referred to as $\mathrm{NRMSE}^{\mathrm{est}}_{f_\mathrm{e}}$, or $\mathrm{NRMSE}^{\mathrm{pred}}_{\eta}$ for the predicted η.

Throughout the comparison, f_e is not only estimated using the noiseless measures of η, WEC motion (χ, $\dot{\chi}$, $\ddot{\chi}$), and pressure from the CNWT. The numerical measurements are artificially polluted, in a post-processing step to the motion simulation, to deliver

---

[5] Note that unconstrained here does not necessarily imply motion in all six DoFs, but rather motion in the design DoFs.

more realistic characteristics of the input data, simulating real measurement from physical sensors. In particular, the noise added to the measurement signals is normally distributed, with zero mean, and standard deviations as specified in Table 5.1.

Table 5.1: Standard deviation of the measurements noise.

Measurement	η [m]	χ [m]	$\dot{\chi}$ [$^{\text{m}}/_{\text{s}}$]	$\ddot{\chi}$ [$^{\text{m}}/_{\text{s}^2}$]	p [Pa]
Standard deviation	0.003	0.003	0.005	0.007	100

5.1.4 Case study

In this section, the case study for the critical comparison of the f_{e} estimators will be described. As mentioned in the introduction of the comparison, the chosen device is a heaving sphere point absorber WEC (see Figure 4.10(d)), with a diameter of 5 m and a draft of 2.5 m. The hydraulic PTO system is modelled using the nonlinear wave-to-wire model proposed in [142]. Resistive control, with a damping factor of $D_{\text{pto}} = 170\,^{\text{kNs}}/_{\text{m}}$, is employed on the PTO system[6]. The sea state is chosen to be representative of real sea conditions, with waves generated based on a JONSWAP spectrum, with $H_{\text{s}} = 1.5$ m, $T_{\text{p}} = 8$ s, and $\gamma = 3.3$. It should be noted that both the PTO system and the sea state are selected so that the obtained simulation is linear, as explained in Section 5.1.3. The water depth is set to $h_{\text{wd}} = 70$ m (deep water waves), and the simulation length is 160 s, with a sampling period of $t_{\text{s}} = 0.01$ s.

5.1.4.1 CNWT

Numerical Wave Tanks (NWTs) are commonly used in ocean engineering to analyse wave-structure interaction [168]. Lower-fidelity NWTs are useful tools for parametric studies, which require fast computation. Reduction of the computational burden, when solving the wave-structure interaction problem, is achieved by linearising the governing equations, which can be carried out using a BEM framework, as shown in Chapter 2. Commonly solving the Laplace equation in a BEM framework, to account for the wave-structure interaction, and, therefore, requiring relatively modest computational power, lower-fidelity models cannot fully replicate realistic conditions. In contrast, high-fidelity CNWTs are able to provide a realistic, numerical, test bench for wave-structure interaction experiments, but are associated with relatively high computational cost. However, with the continuing increase in high-performance computing power, CNWTs for WEC experiments are nowadays more commonly implemented (see review in [184]).

---

[6] The damping factor D_{pto} is optimised to maximise energy absorption via exhaustive search algorithm [142].

The CNWT model in this chapter is based on the open-source CFD software OpenFOAM [182]. The hydrodynamics in the CNWT are captured by solving the incompressible Navier-Stokes equations, introduced before in Equation (2.6), describing the conservation of mass and momentum. The Volume of Fluid (VoF) method, proposed by Hirt [91], is used to capture the water wave advection following

$$\frac{\partial \alpha_{\mathsf{wat}}}{\partial t} + \nabla \cdot (\alpha_{\mathsf{wat}} u_{\mathsf{f}}) = 0 \tag{5.34a}$$

$$\Phi^{\mathsf{q}}_{\mathsf{tot}} = \alpha_{\mathsf{wat}} \Phi^{\mathsf{q}}_{\mathsf{wat}} + (1 - \alpha_{\mathsf{wat}}) \Phi^{\mathsf{q}}_{\mathsf{air}}, \tag{5.34b}$$

where α_{wat} denotes the volume fraction of water and $\Phi^{\mathsf{q}}_{\{\cdot\}}$ is a quantity of the fluid $\{\cdot\}$, such as density or viscosity. The turbulence is modelled using a standard k-ω Shear Stress Transport (SST) turbulence model [113], with standard wall functions for the turbulent kinetic energy $\mathsf{k_e}$, the turbulence frequency ω_{t}, and the eddy viscosity. Regarding wave generation and absorption in a CNWT, a range of numerical wave makers are available [184]. For the present case study, the relaxation zone method is employed, implemented as in the *waves2FOAM* toolbox [95]. The relaxation zone layout is depicted in Figure 5.1(a). The symmetry of the test case is exploited by implementing a symmetry boundary condition in the domain, which reduces the computational burden, while retaining the accuracy of the results. A schematic of the CNWT domain, with all relevant dimensions, is depicted in Figure 5.1(b). For more details on the spatial and temporal problem discretisation, as well as the mesh layout, the interested reader is referred to [142].

To measure η, the CNWT is equipped with numerical wave probes. Wave Probe 1 (WP1) is located in line with the device centre, at a distance of 5 m in the y direction, perpendicular to the wave direction. WP2 is located up-wave from the WEC's centre, at a distance of 20 m. The measurements for the WEC position, velocity, and acceleration are directly given from the motion solver implemented in OpenFOAM. For the pressure measurements, numerical pressure probes are positioned at specific locations on the WEC hull, as illustrated in Figure 5.2.

Although the CNWT is used for the diffraction and motion simulation, BEM hydrodynamic coefficients, required by the different estimators, also have to be computed. This is done using the open-source software NEMOH. Additionally, the SS model, to approximate the radiation convolution term, has been calculated using FOAMM, following the method shown in Section 4.1.

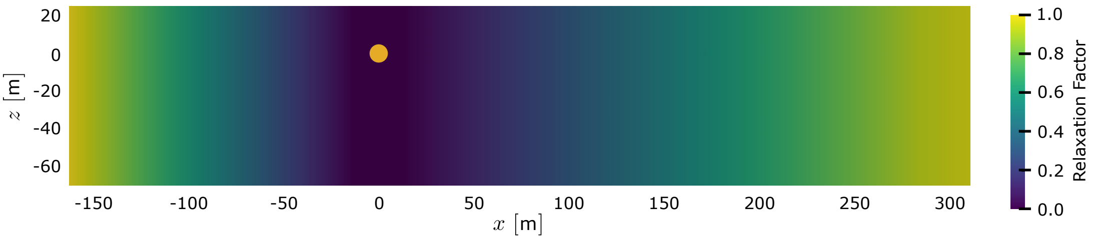

(a) Relaxation zone layout.

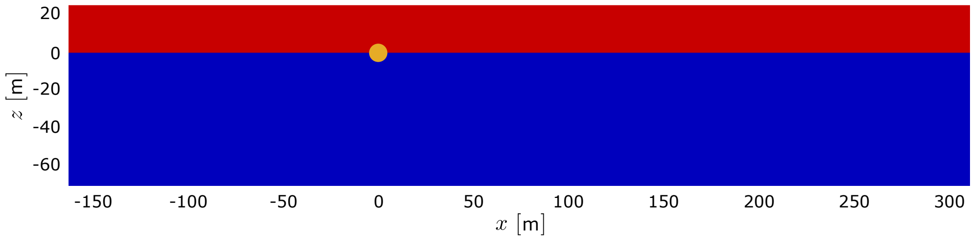

(b) Domain layout.

Figure 5.1: (a) Relaxation zone and (b) domain layouts of the considered CNWT, where the orange dot represents the WEC.

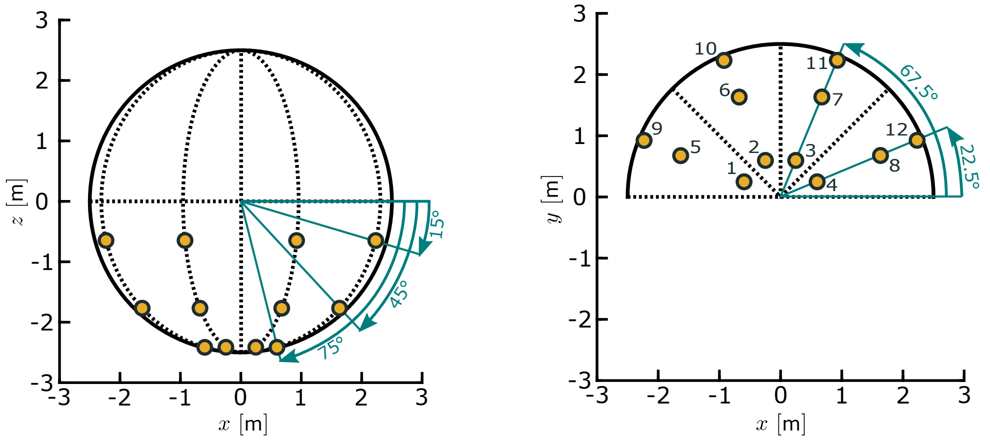

(a) Side view sketch. **(b)** Top view sketch.

Figure 5.2: (a) Side- and (b) top-view of the considered WEC, with the locations of the numerical pressure probes, where the still water line is located at $z = 0\,\text{m}$.

5.1.4.2 Linearity of the case study

It was stated, in Section 5.1.3, that linear conditions are required in order to use the f_{e} obtained from the wave diffraction tests as a reference for the case of a moving WEC. To verify the linearity of the considered case study, the nonlinearity measure proposed by [144] can be consulted. By comparing the steady-state response of a model against the *best linear approximation*, identified through a minimisation problem, the nonlinearity of the wave-device interaction can be quantified. The obtained nonlinearity measure is 0.01 (with a range from 0 to 1) for the case study at hand, confirming that the case is practically linear[7].

To further validate the linearity of the case study, a linear hydrodynamic model, based on Equation (2.36), was developed using data obtained from a BEM solver. The device is excited with the f_e measured from the CNWT wave diffraction test. The resulting device motion from the linear model can then be compared to the motion measured in the CNWT. If the models coincide, linearity is further validated. In Figure 5.3, the position and velocity, obtained using both the BEM model and the CFD simulation, are plotted. A relatively small deviation in the peaks of the signal can be seen, which is expected due to some nonlinear effects, such as nonlinear Froude-Krylov forces (note that the spherical WEC has a non-uniform cross-sectional area) or viscous effects, which are neglected in the linear hydrodynamic model.

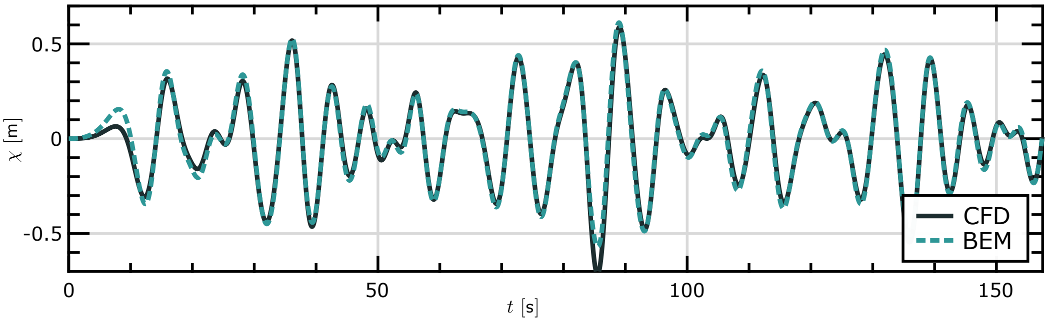

(a) Position comparison.

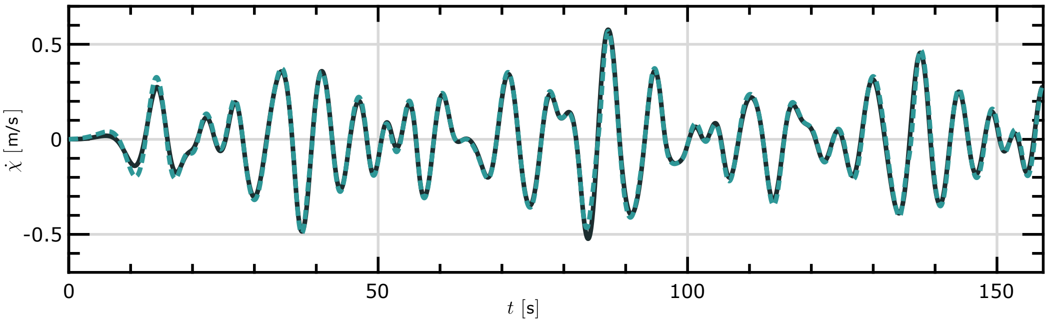

(b) Velocity comparison.

Figure 5.3: Comparison between the position (a) and velocity (b) obtained from CFD and from the simulation with the linear BEM-based model for polychromatic waves.

5.1.5 Comparison results

For the sake of clarity, the results obtained by the different f_e estimators are shown in three different subsections, classified by the required measurements (as explained

---

[7] Even though the case is practically linear, as explained in Section 5.1.3, the use of CFD is necessary to define an unbiased f_e reference for the comparison.

in Section 5.1.2). The first subsection (Section 5.1.5.1) only considers f_e estimators requiring η measurements, while in the following Section 5.1.5.2, estimators using measurements of the WEC motion only are analysed. The third subsection, Section 5.1.5.3, considers f_e estimators using measurements of the WEC motion and pressure on the WEC hull. Additionally, in Section 5.1.5.4, a summarising table along with some discussion is presented.

5.1.5.1 Using $\eta(t)$ measurements

Although only one estimator uses η measurements (CPWE), three different approaches are analysed here, to show how the forecasting accuracy of η affects the estimation (of f_e) accuracy for this strategy:

- CPWE_perf - Assuming perfect knowledge of η at the WEC location,
- CPWE_past - Considering only past η values at the WEC location,
- CPWE_up - Using up-wave measurements.

It should be noted that the η values used for CPWE_perf are measured in a simulation with no body present. Additionally, the CPWE_past requires knowledge of η values at the WEC location which, since in the analysed case waves are unidirectional, can be considered approximately equal to the wave elevation measured at probe WP1 (placed laterally with respect to the WEC, as defined in Section 5.1.4.1). Finally, due to the same assumption of unidirectional waves, a unique up-wave measurement point can provide full information of the expected η at the WEC, for which measurements at probe WP2 are used.

As mentioned in Section 5.1.1, when computing the convolution between k_e and η, shown in Equation (5.1), the value at $t = 0\,\text{s}$ of $k_\mathsf{e}(t)$, shown in Figure 5.4, is multiplied by the instantaneous η. The k_e values for positive time instances are multiplied by past η values, and the forecasted η is multiplied by the k_e values at negative time instances. Thus, the required t_hor is defined by the non-zero components of k_e for negative time instances. For this case, as shown in Figure 5.4, shifting the response $t_\text{hor} = 4\,\text{s}$ is enough to move all the non-zero components of k_e to positive time instances or, in other words, to causalise it ($t_\text{caus} = t_\text{hor} = 4\,\text{s}$).

As explained in Section 2.2.4 for the radiation force, the convolution term required by the CPWE estimator to obtain $\tilde{f}_\mathsf{e}^\text{CPWE}$ can be approximated using a parametric model. However, as explained in [84], the excitation force kernel needs to be causal in order to approximate it with a parametric model (see k_e^caus in Figure 5.4). It should be noted that, in the comparison carried out in this chapter, $\tilde{f}_\mathsf{e}^\text{CPWE}$ is computed solving the convolution shown in Equation (5.1), and not with a parametric model, in order

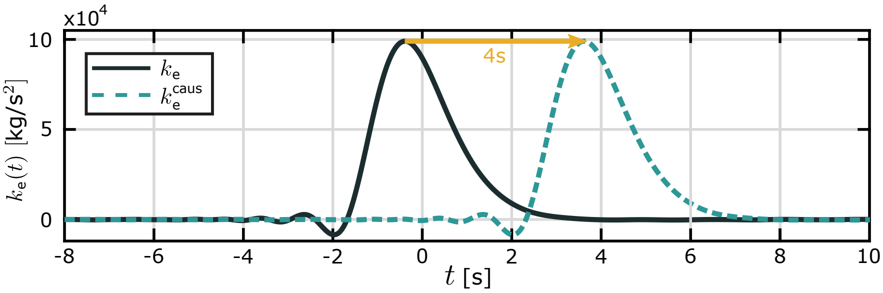

Figure 5.4: The non-causal and causalised $k_\mathrm{e}(t)$ for the analysed spherical WEC device.

to avoid any possible error associated with the approximation of such a parametric model. However, as shown in Section 5.1.5.4, even solving the convolution term, the CPWE estimator is the fastest strategy of this comparison.

The forecasting strategy used for the CPWE is the AR$_\mathrm{LLS}$ predictor[8], introduced in Section 6.1.1.1. In order to reduce the size of the predictor, η is re-sampled with $t_\mathrm{s} = 0.1\,\mathrm{s}$ (from $t_s = 0.01\,\mathrm{s}$), as explained in Section 7.3.2.

As shown in Figure 5.5(a), the best predictor orders are 15, for the CPWE$_\mathrm{past}$, and 60 for the CPWE$_\mathrm{up}$, achieving NRMSE$_{f_\mathrm{e}}^\mathrm{est}$ values of 0.143 and 0.128, respectively. One could argue that the results obtained by both the CPWE$_\mathrm{past}$ and the CPWE$_\mathrm{up}$ are similar while, in theory, using up-wave measurements should lead to considerably better results, compared to using only past information [115]. However, CPWE$_\mathrm{past}$ achieves accurate estimation because, even though NRMSE$_\eta^\mathrm{pred}$ increases faster than for the CPWE$_\mathrm{up}$, the results obtained over $t_\mathrm{hor} = [0{,}1]$ s are better (see Figure 5.5(b)); i.e. where the values of k_e are higher and, therefore, where the prediction accuracy has more effect on the NRMSE$_{f_\mathrm{e}}^\mathrm{est}$ (see time 0 to -1 s in Figure 5.4). Additionally, it should be noted that the NRMSE$_{f_\mathrm{e}}^\mathrm{est}$ achieved by the CPWE$_\mathrm{perf}$ estimator is 0.124, which means that the CPWE$_\mathrm{up}$ obtains almost the same estimation accuracy as CPWE$_\mathrm{perf}$, where perfect knowledge of η is considered.

Figure 5.6 shows the estimated f_e obtained using the CPWE$_\mathrm{past}$, the CPWE$_\mathrm{up}$ and the CPWE$_\mathrm{perf}$ strategies, when no measurement noise is considered. It can be observed that, although the achieved accuracy is similar for the three CPWE variations, the estimated f_e signals show some differences.

Surprisingly, even though the CPWE strategies do not have a term to account for the measurement noise, the obtained results, when considering measurement noise (see Figure 5.7), are similar to those obtained when no noise is considered, only increasing the NRMSE$_{f_\mathrm{e}}^\mathrm{est}$ by 0.003 and 0.001 for the CPWE$_\mathrm{past}$ and CPWE$_\mathrm{up}$, respectively. This can be explained by the fact that the AR prediction strategy acts as a low pass filter, if the order is correctly chosen.

---

[8] Note that, a variation of the AR model, termed ARX model (shown in Section 7.2.2), is employed for the CPWE$_\mathrm{up}$ estimator, which uses up-wave η values.

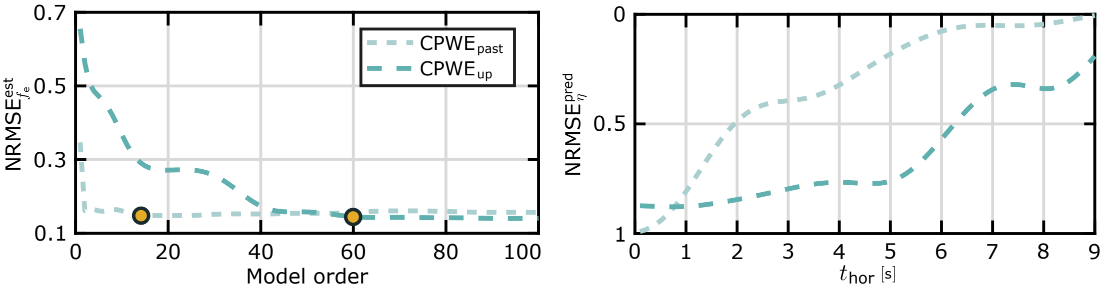

(a) Estimation error for different predictor orders.

(b) Prediction error for different t_{hor}.

Figure 5.5: (a) The estimation error depending on the order used for the predictor, and (b) prediction error for different t_{hor} obtained using $\text{CPWE}_{\text{past}}$ and CPWE_{up}. The orange dots of (a) represent the chosen model orders.

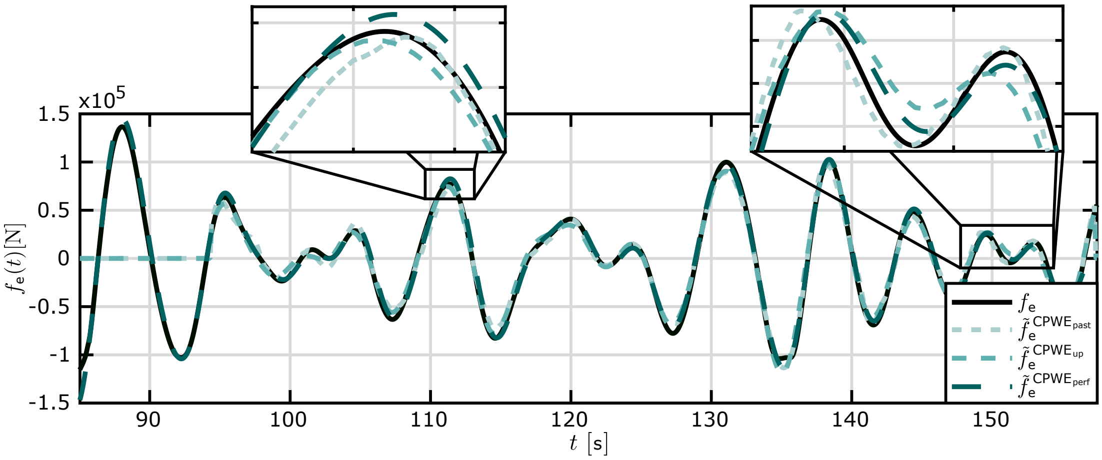

Figure 5.6: $f_e(t)$ estimation, when no measurement noise is considered, using $\text{CPWE}_{\text{past}}$, CPWE_{up}, and $\text{CPWE}_{\text{perf}}$ with an obtained estimation error of 0.143, 0.128, and 0.124, respectively.

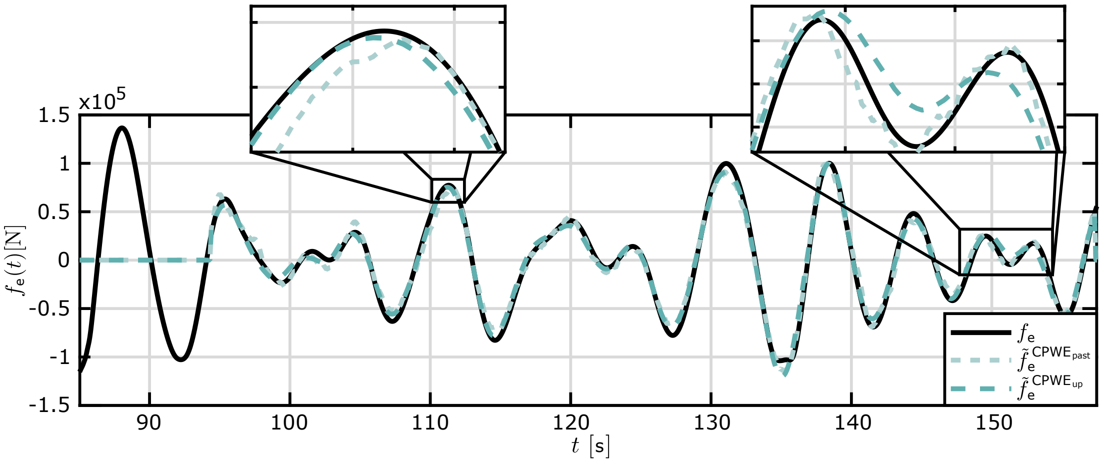

Figure 5.7: $f_e(t)$ estimation, considering measurement noise, using both $\text{CPWE}_{\text{past}}$ and CPWE_{up}, with an obtained estimation error of 0.146 and 0.129, respectively.

5.1.5.2 Using motion measurements

For the shake of clarity, the results obtained by the strategies that use motion measurements are shown in three different sets.

First, an analysis of the effect of the HO model order n_ω on estimation accuracy is carried out, when using the KFHO and the EKFHO strategies. As shown in Figure 5.8, while the $\text{NRMSE}_{f_\text{e}}^{\text{est}}$ achieved by the KFHO approach decreases when increasing n_ω, no corresponding decrease can be observed for EKFHO. This is consistent with the findings in [70]. Compared to the EKFHO estimator, where the frequencies ω are adaptive, the KFHO strategy has an additional potential pitfall, which is the choice of the frequencies of the HO. For the presented test case, these frequencies are chosen to be linearly spaced between 0.5 and 2 rad/s. However, the $\text{NRMSE}_{f_\text{e}}^{\text{est}}$ shown in Figure 5.8 may decrease further, if the value of the frequencies used by KFHO is optimised for every n_ω [138].

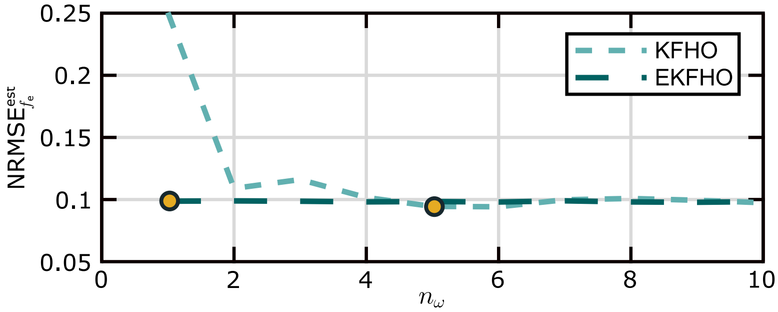

Figure 5.8: The obtained NRMSE by the KFHO and EKFHO strategies for different HO orders n_ω. The chosen orders for KFHO and EKFHO are $n_\omega = 5$ and 1, respectively (orange-dots).

Starting with the KF-based estimators, one can notice, from Figure 5.9, that the KFRW, KFHO, and EKFHO estimators obtain accurate estimates of f_e ($\text{NRMSE}_{f_\text{e}}^{\text{est}}$ =0.109, 0.093 and 0.097, respectively) for the case without measurement noise. Furthermore, it can be seen that the three strategies obtain very similar values of $\text{NRMSE}_{f_\text{e}}^{\text{est}}$; however, this is not the case when measurement noise is introduced.

As depicted in Figure 5.10, the EKFHO shows the highest error among the three, being the most affected by measurement noise (the $\text{NRMSE}_{f_\text{e}}^{\text{est}}$ is 0.066 higher when considering noise). Although the $\text{NRMSE}_{f_\text{e}}^{\text{est}}$ achieved by the KFRW is only increased by 0.026, when introducing noise, the resulting estimated f_e is the noisiest among the three signals (see Figure 5.10). In contrast, since the model of the HO gives the KF some information about the expected f_e dynamics, the KFHO estimate is the least noisy, resulting in an increase in the $\text{NRMSE}_{f_\text{e}}^{\text{est}}$ of 0.005 with respect to the result obtained when no noise is considered.

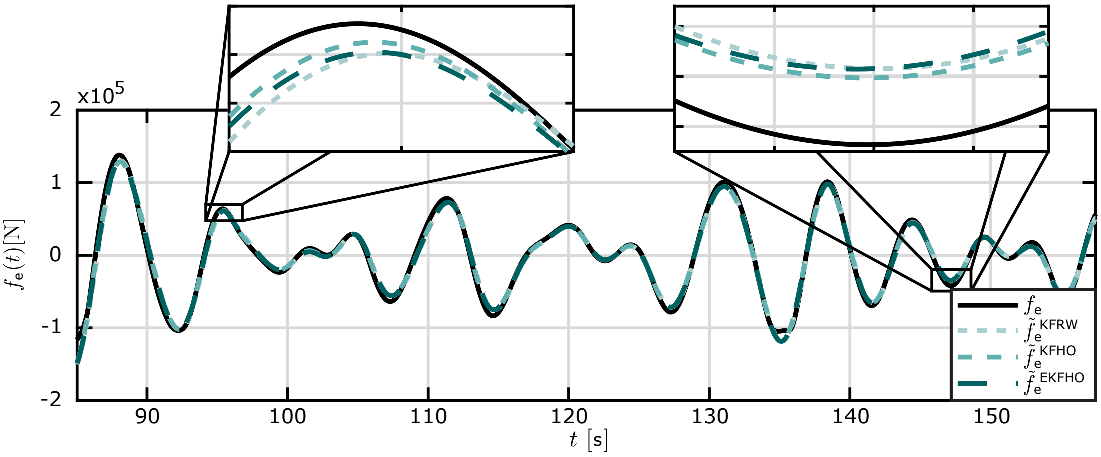

Figure 5.9: f_e estimation, when no measurement noise is considered, using the KFRW, KFHO, and EKFHO strategies obtaining a $\text{NRMSE}^{\text{est}}_{f_e}$ of 0.109, 0.093, and 0.097, respectively.

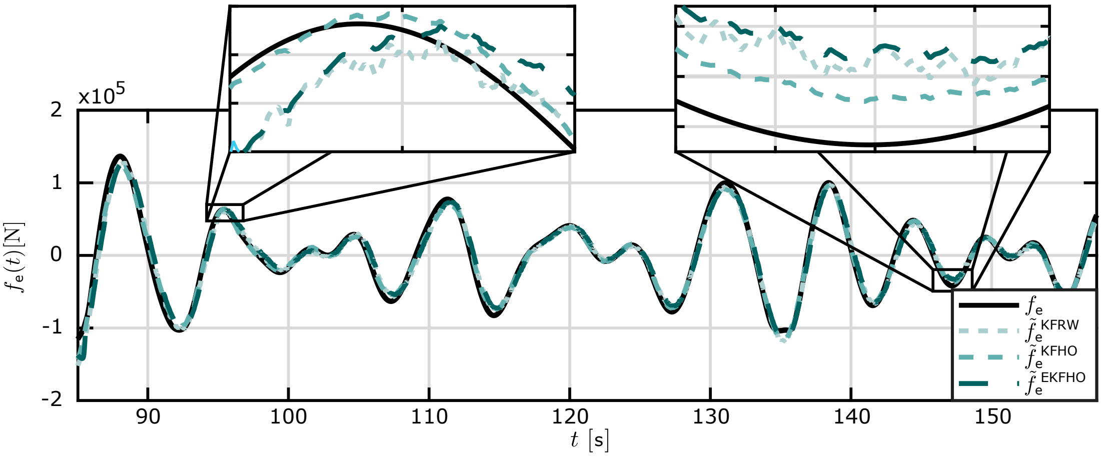

Figure 5.10: f_e estimation, considering measurement noise, using the KFRW, KFHO, and EKFHO strategies obtaining a $\text{NRMSE}^{\text{est}}_{f_e}$ of 0.135, 0.098, and 0.163, respectively.

Even though the UIO approach includes a term to account for the measurement noise, from a visual inspection of Figures 5.11 and 5.12, it can be seen that the UIO estimate is significantly affected by the presence of measurement noise and, thus, the $\text{NRMSE}^{\text{est}}_{f_e}$ increases by 0.04. For the RHE strategy, the window length is selected such that, for the chosen design parameters and for the case where no noise is considered, the obtained NRMSE is minimised. For this case, with $n_w = 8$, a $\text{NRMSE}^{\text{est}}_{f_e}$ of 0.153 is obtained. The $\text{NRMSE}^{\text{est}}_{f_e}$ achieved by the RHE strategy is relatively unaffected by the introduction of measurement noise and only increases from 0.153 to 0.172.

For the ASMO estimator, shown in Figure 5.12, even with no measurement noise the obtained estimation appears noisy at some time instances (as in the first zoomed-window of Figure 5.12). This is due to a well-known phenomenon, in the sliding-mode literature, called chattering [41]. As can be observed from Figure 5.11, the chattering phenomenon gets amplified when considering measurement noise, increasing the obtained $\mathrm{NRMSE}^{\mathrm{est}}_{f_\mathrm{e}}$ by 0.155.

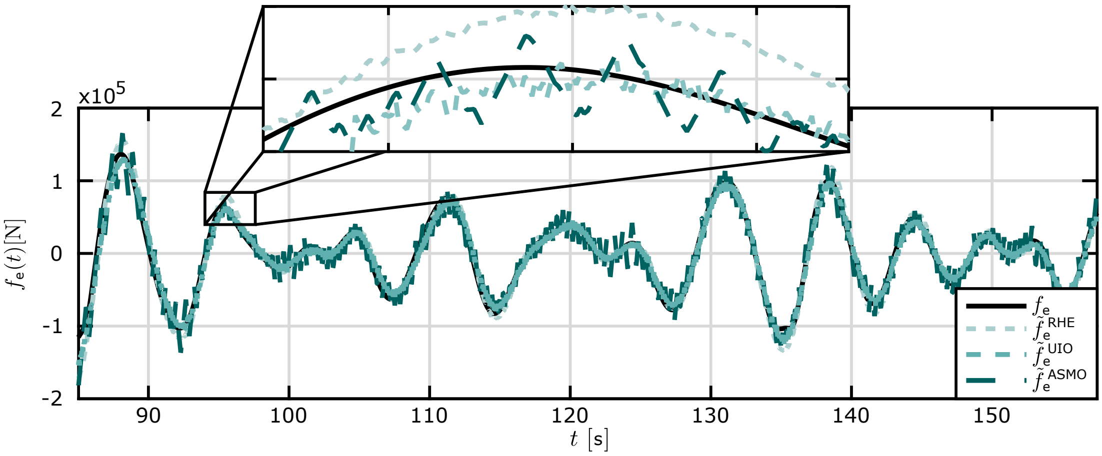

Figure 5.11: f_e estimation, considering measurement noise, using the RHE, UIO, and ASMO strategies obtaining a $\mathrm{NRMSE}^{\mathrm{est}}_{f_\mathrm{e}}$ of 0.172, 0.144, and 0.257, respectively.

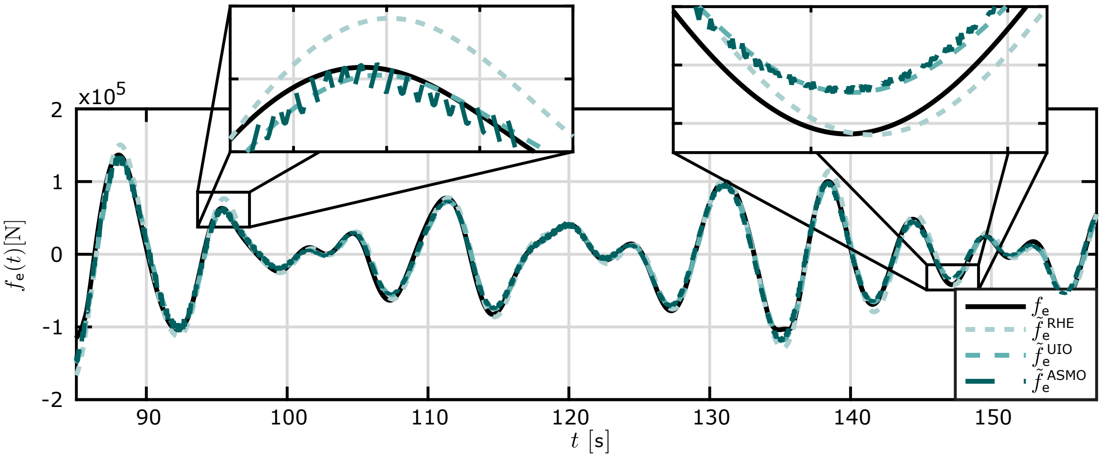

Figure 5.12: f_e estimation, when no measurement noise is considered, using the RHE, UIO, and ASMO strategies obtaining a $\mathrm{NRMSE}^{\mathrm{est}}_{f_\mathrm{e}}$ of 0.153, 0.104, and 0102. respectively.

The effectiveness of the ULISE to handle measurement noise is highlighted, with an increase of the $\mathrm{NRMSE}^{\mathrm{est}}_{f_\mathrm{e}}$ of only 0.002 when measurement noise is considered, which is also indicated when comparing the time traces in Figures 5.13 and 5.14. The effectiveness could be due to the fact that, as shown in Section 5.1.1, the ULISE strategy is based on a KF which, as mentioned before, can optimally handle measurement noise (if the noise is Gaussian, as it in this case).

As shown in Figure 5.14, the FAUIE strategy produces a relatively noisy estimate, and the $\mathrm{NRMSE}^{\mathrm{est}}_{f_\mathrm{e}}$ increases by 0.125 compared to the noise free case (see Figure 5.13). This is expected, since there is no explicit term to account for the measurement noise, as shown in Section 5.1.1. The results obtained by FAUIE could possibly be improved by low-pass filtering the measurements in a pre-processing step; however, due to the phase delay of a realistic filter, it would increase the delay of the excitation force estimate significantly.

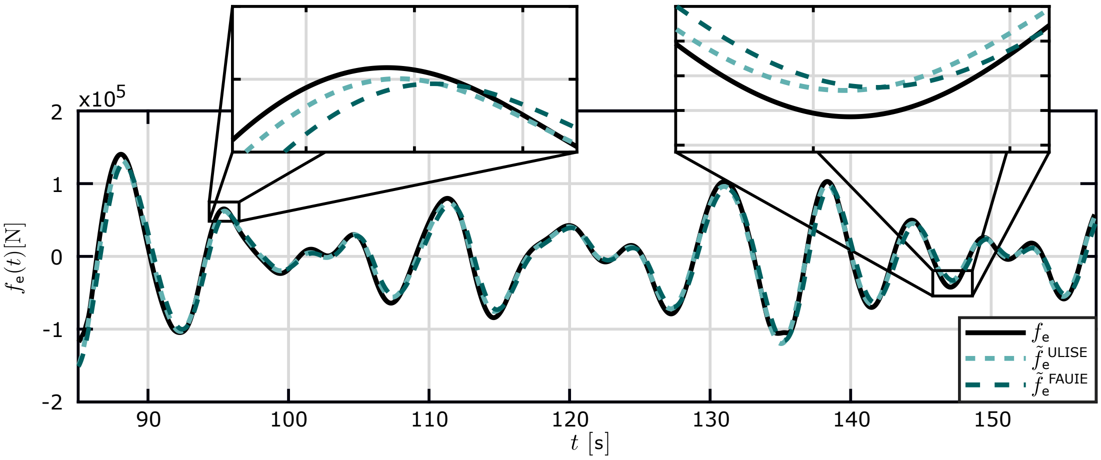

Figure 5.13: f_e estimation, when no measurement noise is considered, using the ULISE and FAUIE strategies obtaining a $\text{NRMSE}^{\text{est}}_{f_e}$ of 0.097 and 0.188, respectively.

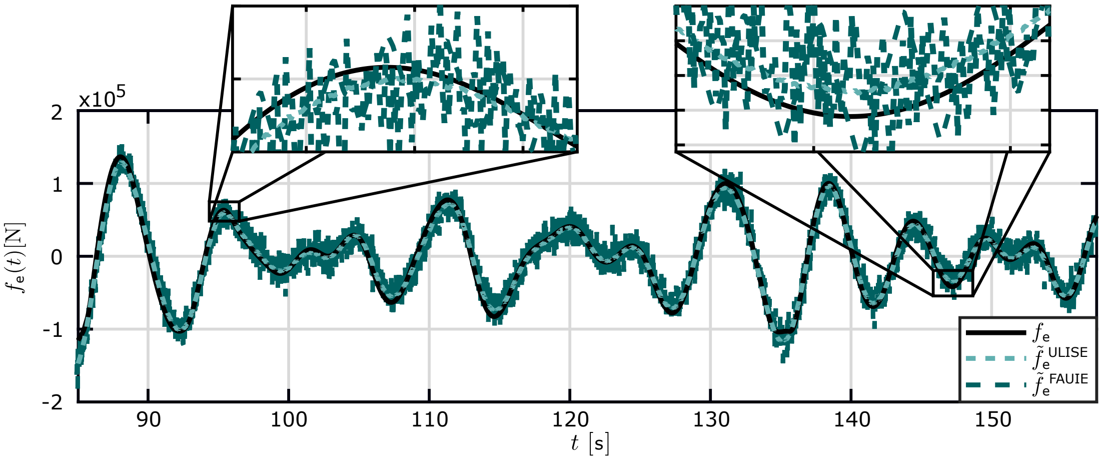

Figure 5.14: f_e estimation, considering measurement noise, using the ULISE and FAUIE strategies obtaining a $\text{NRMSE}^{\text{est}}_{f_e}$ of 0.099 and 0.312, respectively.

5.1.5.3 Using motion and pressure measurements

Regarding the set of estimators using motion and pressure measurements, it has been found that, for the PADE strategy, the number of pressure sensors directly affects the accuracy of the total wave force f_w estimate. In the present test case, the error in the estimation of f_w leads to an offset in $\tilde{f}_e^{\text{PADE}}$ compared to f_e (see Figures 5.15 and 5.16). However, even though the noisy measurements are directly used to estimate f_e, the obtained results are not affected, which may be explained by possible destructive interference of the different noisy signals.

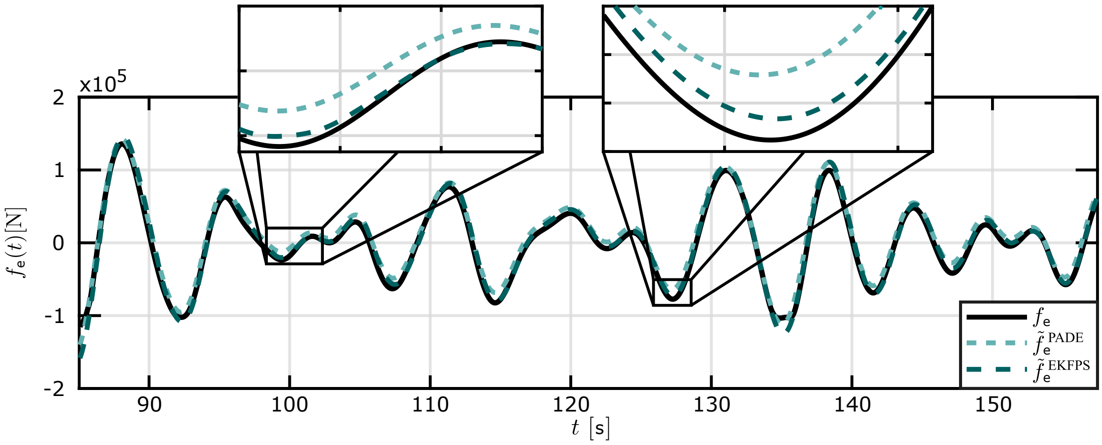

Figure 5.15: f_e estimation, when no measurement noise is considered, using the PADE and EKFPS strategies obtaining a $\text{NRMSE}^\text{est}_{f_\text{e}}$ of 0.207 and 0.128, respectively.

In contrast, the EKFPS strategy (of order $n_\omega = 4$) gives a more accurate estimate, obtaining a $\text{NRMSE}^\text{est}_{f_\text{e}}$ of 0.128 (compared to the 0.207 obtained by PADE) for the case where measurement noise is not considered, and 0.178 for the case where noise is included (compared to the 0.208 obtained by PADE).

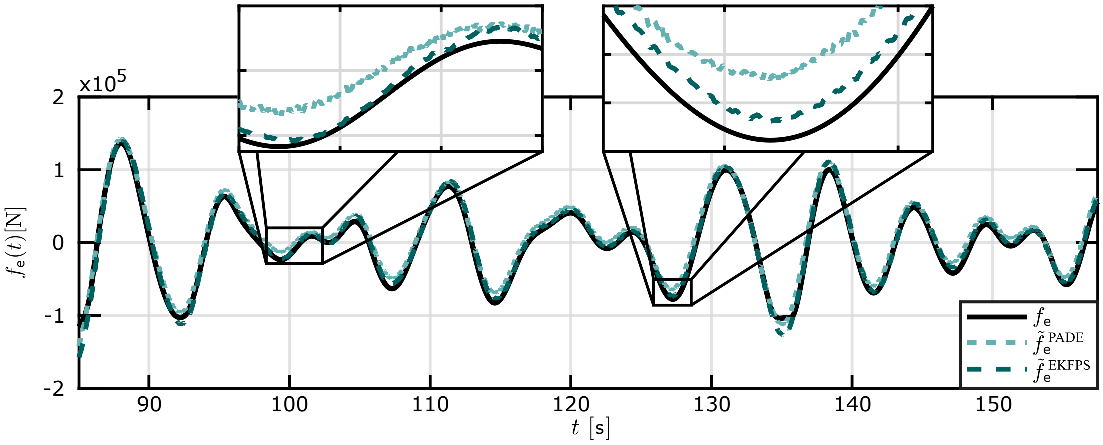

Figure 5.16: f_e estimation, considering measurement noise, using the PADE and EKFPS strategies obtaining a $\text{NRMSE}^\text{est}_{f_\text{e}}$ of 0.208 and 0.178, respectively.

5.1.5.4 Comparison summary

This subsection summarises the results presented above in tabulated form. For each f_e estimator, Table 5.2 shows the measurements required and the obtained error for the cases with, and without, measurement noise. Furthermore, Table 5.2 includes the time delay of $\tilde{f}_\text{e}$, relative to the reference f_e, obtained via cross-correlation. Finally, the required time for estimation, normalised against the fastest strategy, is listed (**N-Time**). In terms of delay time, one can notice that the open-loop estimators

(CPWE and PADE) are the only strategies obtaining a negative delay[9], while the KFHO, EKFHO, ASMO, and ULISE estimators are in phase with respect to f_{e}, and the rest of the analysed strategies are delayed.

Table 5.2: Comparison table with the results obtained by the different estimators.

Name	**Input Data**					**NRMSE**$^{\mathrm{est}}_{f_{\mathrm{e}}}$		**Delay** [s]	**N-Time**
	η	χ	$\dot{\chi}$	$\ddot{\chi}$	p	without noise	with noise		
CPWE$_{\mathrm{past}}$	•	–	–	–	–	0.143	0.146	-0.03	1
CPWE$_{\mathrm{up}}$	•	–	–	–	–	0.128	0.129	-0.06	1
KFRW	–	•	•	–	–	0.109	0.135	0.04	25
KFHO	–	•	•	–	–	0.093	0.098	0	28
EKFHO	–	•	•	–	–	0.097	0.163	0	$4{\cdot}10^3$
RHE	–	•	•	–	–	0.153	0.172	0.07	30
UIO	–	•	•	–	–	0.104	0.144	0.09	117
ASMO	–	•	•	–	–	0.102	0.257	0	377
ULISE	–	•	–	•	–	0.097	0.099	0	98
FAUIE	–	•	•	•	–	0.187	0.312	0.16	$1{\cdot}10^3$
EKFPS	–	•	–	–	•	0.128	0.178	0.03	$9{\cdot}10^3$
PADE	–	•	•	•	•	0.207	0.208	-0.01	29

Regarding the estimation time, it is found that CPWE is the fastest strategy to estimate f_{e}, requiring about $1{\cdot}10^{-6}$s for one f_{e} estimate update[10], with $t_{\mathrm{s}} = 0.01\,\mathrm{s}$. Note that, for the CPWE strategy, the convolution term is computed, so it could be even faster if the convolution is approximated using a parametric model [84]. The CPWE is followed by the KFRW, KFHO, PADE, RHE, ULISE, UIO, and ASMO strategies which, although they are slower than CPWE, may still be considered fast, in absolute terms, since they are still significantly below real time. Finally, FAUIE, EKFHO, and EKFPS are the slowest strategies which, in the case of EKFHO and EKFPS, is expected, since the estimators are inherently nonlinear and require linearisation of the function describing f_{e} at each step. In the FAUIE estimator, the computational burden is associated with the derivative error $\dot{e}_y$ (see Equation (5.24)), which creates an algebraic loop, slowing down the estimation process[11].

In terms of measurement requirements, WEC motion measurements are the easiest/cheapest to obtain using, for example, Inertial Measurement Units (IMUs).

---

[9] Note that a delay of $-t_{\mathrm{del}}$ represents that the estimated f_{e} is, overall, t_{del} seconds ahead on time with respect to the reference f_{e}.

[10] The tests have been carried out using MATLAB, on a desktop computer with an intel CORE i7 and 8GB of RAM.

[11] Note that a new version of the FAUIE estimator is presented in [4], where the algebraic loop is avoided. Therefore, the results shown in this chapter for the FAUIE estimator may improve if the version presented in [4] is implemented.

In contrast, it should be noted that pressure sensors are relatively expensive (and potentially unreliable) and the estimators using pressure measurements do not show any particular improvement with respect to the strategies using motion measurements alone. Additionally, past η values, at the WEC location, are physically unmeasurable and, therefore, in a real sea scenario, the estimate has to be calculated based on either up-wave measurements or WEC motion. In order to estimate/predict η, based on up-wave measurements in a real-sea scenario, several measurement points are required [115], which can be expensive to install. Additionally, using motion measurements to estimate η is suboptimal, since two estimation stages errors are accumulated, while directly estimating f_{e} based on WEC motion is a more straightforward approach.

5.2 Estimation in a physical environment

This section shows the results obtained during experimental tank tests, carried out at Aalborg University, Aalborg, Denmark, in Summer 2019. First, in Section 5.2.1, information on the experimental WEC system and the test facility is provided. Then, Section 5.2.2, shows the identification experiments that were carried out to characterise the system and, finally, in Section 5.2.3, the obtained estimation results are presented and discussed.

5.2.1 System description

The device, investigated during the tank tests, is a 1:20th scale version of the Wave Star device [109], shown in Figure 5.17. The device consists of a hemispherical hull with a single DoF in pitch (which oscillates around point A, see Figure 5.17(a)), with an electrical direct drive actuator as a PTO system. At equilibrium, the floater arm stands at (approximately) 30° with respect to the still water level. The interested reader is referred to [156] for a more detailed description of the physical system.

Since the motion of the device is rotational, but the PTO force acts always at the same point of the device arm (point C in Figure 5.17(a)), the angle between the motor axis and the floater arm (the angle ACB in Figure 5.17(a)) varies. Therefore, the model of the considered WEC is nonlinear, since the PTO torque explicitly depends on the angular position of the arm. To simplify the problem, avoiding the representation of such mechanical nonlinearities, instead of considering the motion of the device, only the linear displacement along the PTO axis (χ_{pto}) is considered. Thus, instead of the angular position of the device, the linear position of the motor is considered, given by the relative distance between points B and C of Figure 5.17(a), with 0 the distance

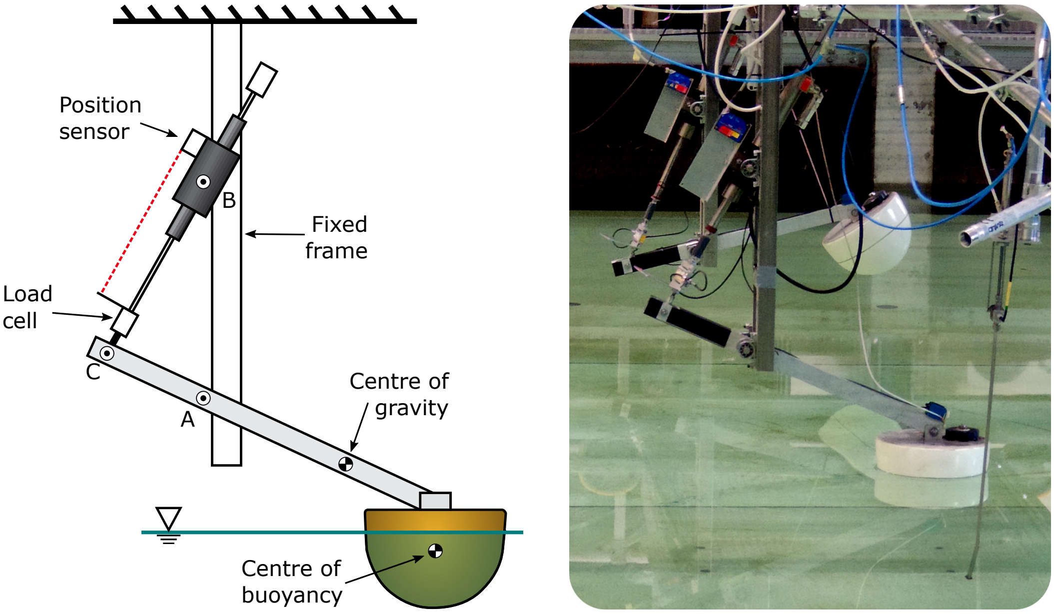

(a) Sketch of the scaled Wave Star device. **(b)** Picture of the scaled Wave Star device.

Figure 5.17: (a) Sketch and (b) picture of the scaled Wave Star device used for the tank test experiments.

at equilibrium. Similarly, instead of the excitation torque acting on the device hull, the equivalent excitation force acting on the PTO axis is considered.

Finally, Figure 5.18 shows a schematic of the tank in which the experiments were carried out, including all relevant dimensions. The water depth of the tank was 0.9 m.

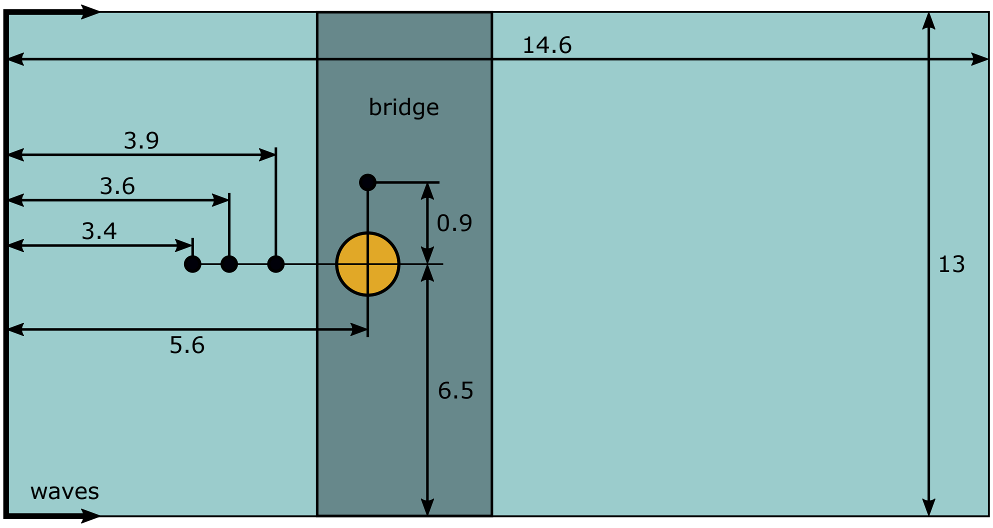

Figure 5.18: Sketch with the approximate dimensions (in meters) of the physical wave tank. The black dots represent the wave gauges, and the orange circle the WEC.

5.2.2 System characterisation

The force-to-motion model of the device (at the motor axis) is identified using a *black-box-identification* methodology, as explained in [75]. For the force-to-position system identification, a set of four different classical up-chirp experiments were performed, where the system is forced into motion by a chirp control force f_{pto}, while no incident waves are present. Knowing the approximate location of the natural resonance frequency of the system *a-priori* (≈ 7 rad/s), f_{pto} is defined as a linear frequency sweep in the range[12] $[0.7, 30]$ rad/s. Additionally, it should be noted that, to check for nonlinearities, chirps of different amplitudes are considered, in particular, $[5, 7.5, 10, 15]$ N. The performed control force chirps, along with the obtained motor position results, are shown in Figure 5.19(a) and (b), respectively.

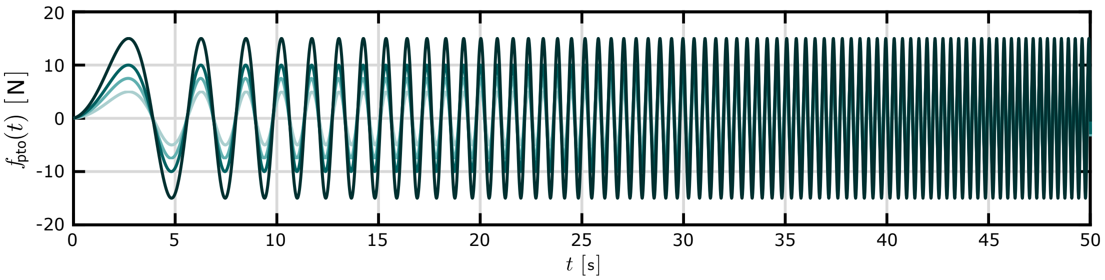

(a) The applied control force chirp, with different amplitudes.

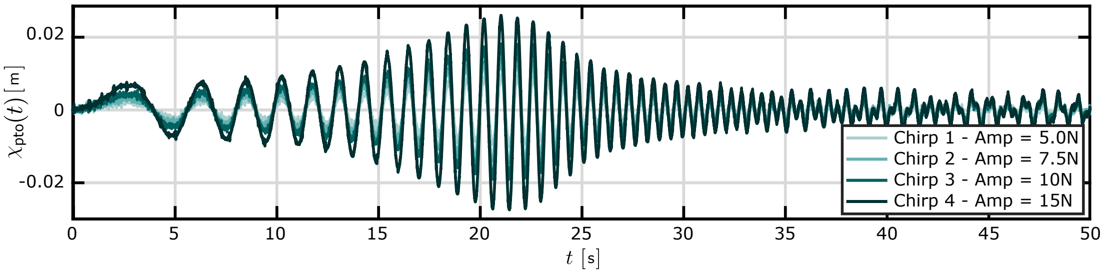

(b) The obtained motor position, for the different chirp amplitudes.

Figure 5.19: The set of (a) control force chirps performed to identify the system, along with (b) the obtained motor position.

The estimate of the empirical transfer function of the force-to-position system can then be computed using the chirp control force and the corresponding motor position as

$$\tilde{H}^{\text{emp}}_{f_{\text{pto}}\chi_{\text{pto}}}(\jmath\omega) = \frac{X_{\text{pto}}(\jmath\omega)}{F_{\text{pto}}(\jmath\omega)}, \tag{5.35}$$

where $X_{\text{pto}}(\jmath\omega)$ and $F_{\text{pto}}(\jmath\omega)$ represent the frequency-domain equivalent of the motor position ($\chi_{\text{pto}}(t)$) and force ($f_{\text{pto}}(t)$). As shown in Figure 5.20, the obtained frequency

---

[12] Note that covering the resonance frequency of the system with a decade below and above is usually recommended but, due to the limitations of the system, it was not possible to run the chirp signal up to 70 rad/s.

responses (magnitude and phase) for the four different amplitudes are similar, indicating linear behaviour of the system. Finally, and in order to reduce the measurement uncertainty of the frequency responses shown in Figure 5.20, the four signals are averaged. The obtained frequency response is then utilised to identify a parametric model of the system (also shown in Figure 5.20), using the frequency-domain moment-matching-based identification method introduced in Section 4.1. An 8th order model is enough to identify a parametric model with an approximation error of NRMSE=4.13%.

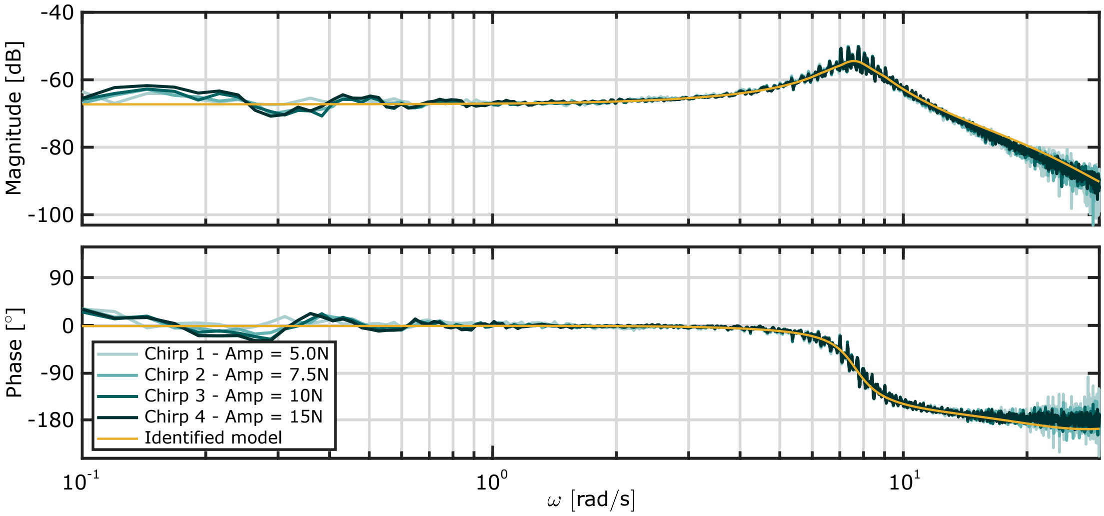

Figure 5.20: Frequency response of the obtained empirical transfer functions for the different chirp amplitudes based on the experimental data.

Note that the estimator used for this experiments is the KFHO since, as shown earlier in Section 5.1.5, this strategy is one of the most accurate estimators among the different strategies available in the literature. The only difference with respect to the KFHO used for the comparison is that no velocity measurements were used, since the motor position was the only directly available measurement.

5.2.3 Estimation results

The waves used for the experiments were generated based on three different JONSWAP SDFs (generated following Equation (2.4)), shown in Figure 5.21, inspired by the International WEC Control Competition (WECCCOMP) [156]. From Figure 5.21, one can see that the energy content of the three sea states is different, with $S^1_{\eta\eta}$ and $S^3_{\eta\eta}$ being the least and most energetic sea states, respectively. In full scale, the peak period and significant wave height of $S^1_{\eta\eta}$, $S^2_{\eta\eta}$, and $S^3_{\eta\eta}$ correspond to ($T_\text{p} \approx 4.4\,\text{s}$ and $H_\text{s} \approx 0.4\,\text{m}$), ($T_\text{p} \approx 6.3\,\text{s}$ and $H_\text{s} \approx 1.3\,\text{m}$), and ($T_\text{p} \approx 8.7\,\text{s}$ and $H_\text{s} \approx 2.1\,\text{m}$), respectively.

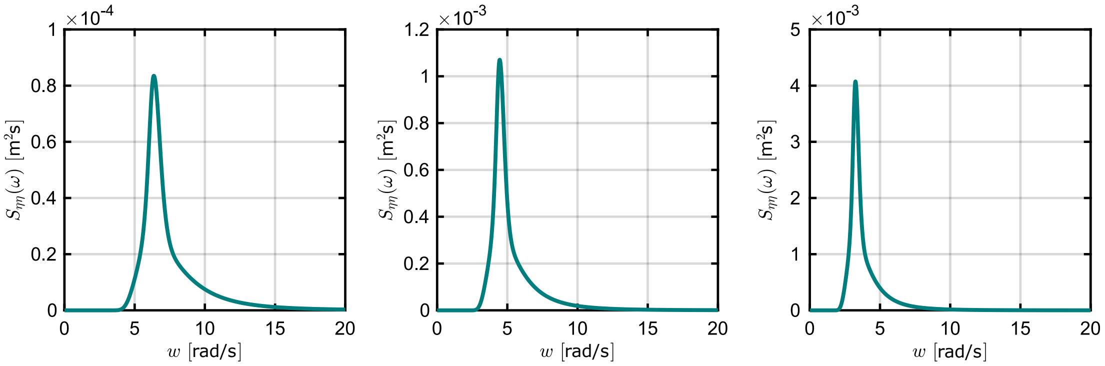

(a) $S^1_{\eta\eta}$: $\gamma = 3.3$, $T_\text{p} = 0.988$ s, and $H_\text{s} = 2.08$ cm.

(b) $S^2_{\eta\eta}$: $\gamma = 3.3$, $T_\text{p} = 1.412$ s, and $H_\text{s} = 6.25$ cm.

(c) $S^3_{\eta\eta}$: $\gamma = 3.3$, $T_\text{p} = 1.936$ s, and $H_\text{s} = 10.42$ cm.

Figure 5.21: The three JONSWAP SDFs considered for the tank tests.

Due to time constraints, the fixed body experiments, from which a measured f_e can be obtained (as explained in Section 5.1.3), were only run for one realisation of each of the sea states of Figure 5.21, which are shown in Figures 5.22 and 5.23.

In Figure 5.22, it can be seen that the performance of the KFHO estimator, using experimental tank test data, is not as good as the performance shown in the comparison of Section 5.1.5. In particular, it is worth highlighting the high-frequency content of the estimated f_e, which is more visible when the H_s of the sea state decreases. This is mainly due to the signal-to-noise ratio of the motor position measurements used for the estimator. For the sea state with the smallest H_s, $S^1_{\eta\eta}$, the signal-to-noise ratio is lower (higher noise content) and, therefore, the estimated f_e is significantly noise-polluted. In contrast, for $S^3_{\eta\eta}$, the device motion is larger and, hence, the signal-to-noise is higher, thus, obtaining a less noisy f_e estimate.

Figure 5.23 shows the measured and estimated position of the motor in the same time window shown in Figure 5.22. For $S^1_{\eta\eta}$, shown in Figure 5.23(a), one can notice that, at some time instances (as, for example, $t \approx 50.5$ s or $t \approx 58.4$ s), the noise amplitude is larger than the motor position. Thus, even though the estimated χ_pto can be considered smooth, which indicates that the KF was effectively filtering out a large part of the measurement noise, the small high-frequency content of the estimated χ_pto is amplified in the estimated f_e, as shown in Figure 5.22(a).

In contrast, as shown in Figure 5.23(c) for $S^3_{\eta\eta}$, the maximum χ_pto is around 1.5 cm, compared to the 3 mm of $S^1_{\eta\eta}$, and, therefore, the signal-to-noise ratio is not as significant as for $S^1_{\eta\eta}$. Hence, the obtained f_e estimate, shown in Figure 5.22(c), is also more accurate and less noise-polluted than the estimate obtained for $S^1_{\eta\eta}$, shown in Figure 5.22(a).

For the cases shown in Figure 5.22, the estimation could probably be improved by more accurately tuning the KF weighting matrices; however, such rigorous tuning

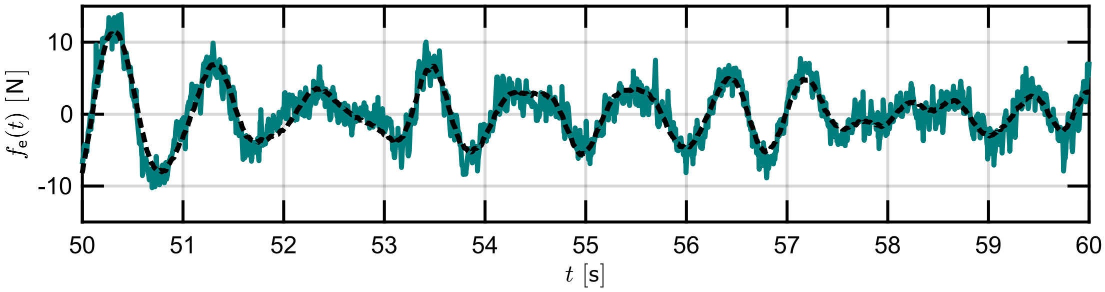

(a) Estimated and measured f_e for $S^1_{\eta\eta}$, obtaining a $\text{NRMSE}^{\text{est}}_{f_e}$ of 0.515.

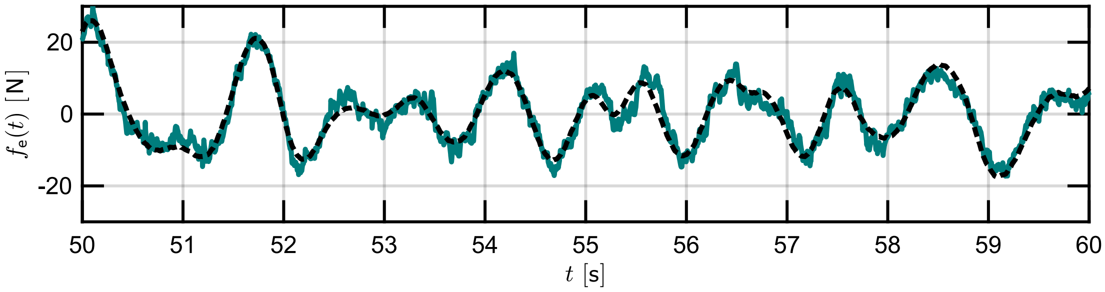

(b) Estimated and measured f_e for $S^2_{\eta\eta}$, obtaining a $\text{NRMSE}^{\text{est}}_{f_e}$ of 0.394.

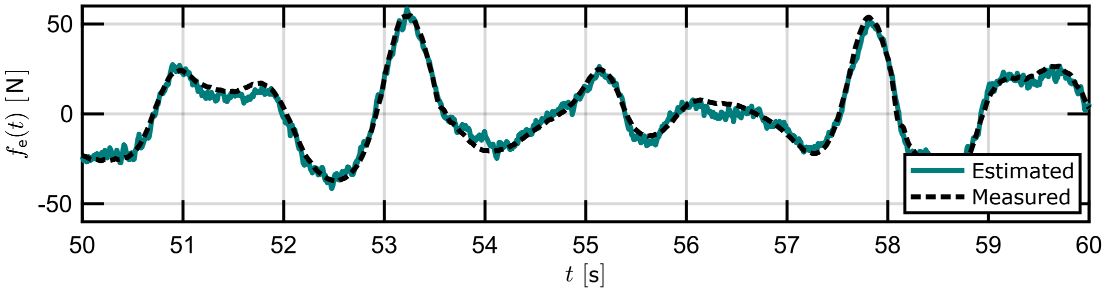

(c) Estimated and measured f_e for $S^3_{\eta\eta}$, obtaining a $\text{NRMSE}^{\text{est}}_{f_e}$ of 0.202.

Figure 5.22: Estimated and measured f_e for the three JONSWAP SDFs analysed.

was not possible during the time-limited experimental campaign. Additionally, the frequencies used for the HO description of the KF are [3.25, 4.45, 6.36] rad/s, which correspond to the peak periods of the three sea states. The choice of a specific set of frequencies for each sea state (or choosing more frequencies) could also improve the obtained estimation accuracy. However, the decision of choosing a constant set of frequencies was made to simulate a real scenario, where the HO description would not change for different sea states.

5.3 Conclusions

From the results shown in the comparison of Section 5.1, it can be concluded that estimation techniques using WEC motion measurements are the most feasible techniques, specifically the KFHO, ULISE, and UIO approaches. In particular, the

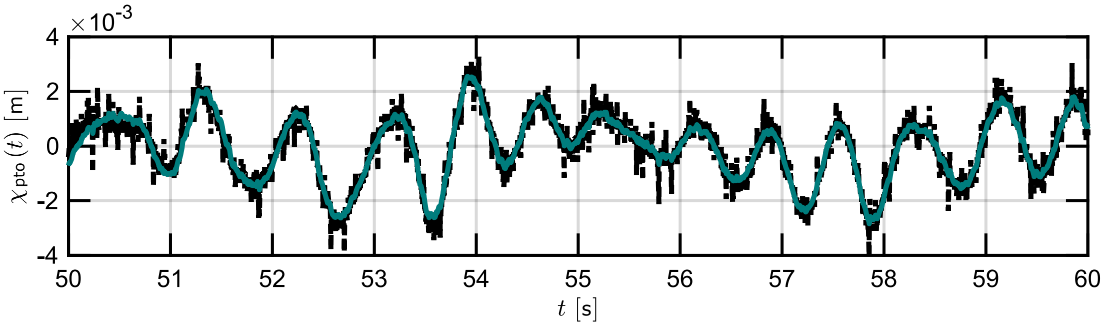

(a) Estimated and measured motor position for $S^1_{\eta\eta}$, obtaining a NRMSE$^{\text{est}}_{\chi_{\text{pto}}}$ of 0.221.

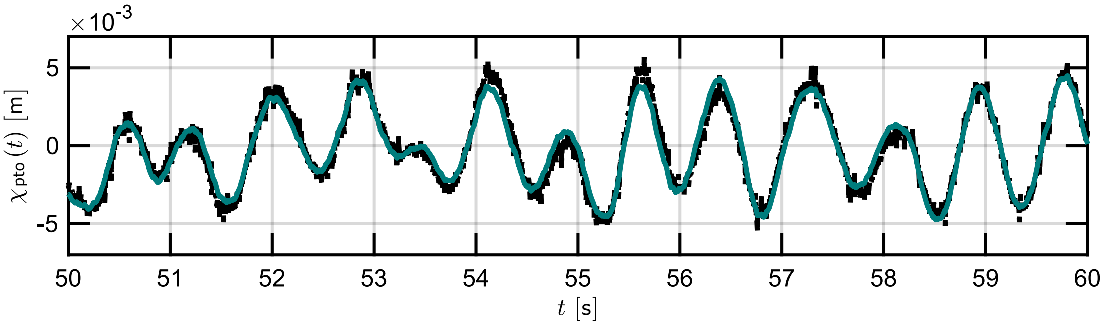

(b) Estimated and measured motor position for $S^2_{\eta\eta}$, obtaining a NRMSE$^{\text{est}}_{\chi_{\text{pto}}}$ of 0.179.

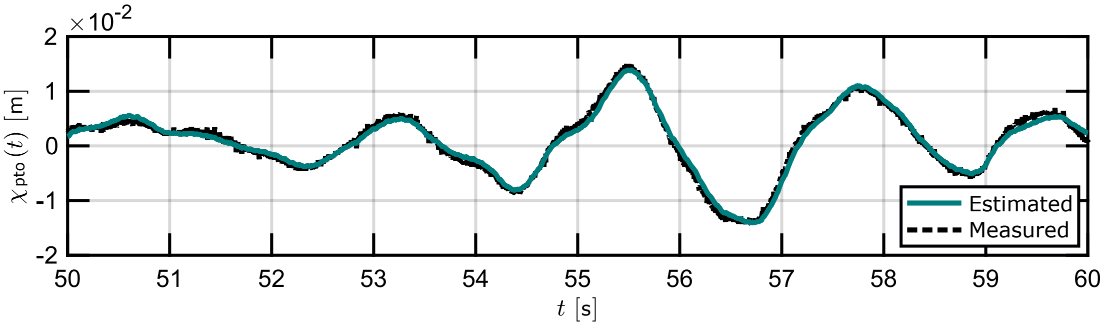

(c) Estimated and measured motor position for $S^3_{\eta\eta}$, obtaining a NRMSE$^{\text{est}}_{\chi_{\text{pto}}}$ of 0.114.

Figure 5.23: Estimated and measured χ_{pto} for the three JONSWAP SDFs analysed.

KFHO and ULISE approaches show good performance in terms of achieved accuracy and no phase shift between the estimated and the reference signal. Regarding the UIO method, even though this strategy is not the most accurate, it is the only approach able to consider model uncertainty, which could be important in a real WEC device scenario. Additionally, from the comparison, three different estimation errors can be distinguished: a delay in the obtained $\tilde{f}_{\text{e}}$, a difference in the amplitude between the estimated and actual f_{e}, and noise (variance) in the obtained $\tilde{f}_{\text{e}}$. Chapter 8 presents an investigation on how such estimation errors affect the performance of a moment-matching-based receding horizon optimal control strategy.

From the results obtained using physical tank experiments, shown in Section 5.2, it is important to highlight the difficulty associated with estimating f_{e} (or any other non-measurable quantity) for small-scale devices. In the shown case, using a 1:20$^{\text{th}}$ scale device, the amplitude of the position measurement noise is comparable to the actual position measurement at some time instants, which challenges the f_{e} estimation. However, it is expected that, when increasing the scale of the device, the motion amplitude of the device should increase proportionally with the scale, while the amplitude of the noise added by the sensors should increase at a lower rate. Therefore, the signal-to-noise ratio should increase, leading to an improvement in the estimation accuracy.

6

Short-term forecasting of excitation force and free surface elevation

Contents

As mentioned in Chapter 3, this chapter considers short-time forecasting strategies that were first applied (within the wave energy community) to η prediction, and afterwards to f_e prediction. Therefore, the results shown in this chapter are for η forecasting, rather than f_e forecasting. However, as mentioned in Section 3.3, the same strategies introduced and analysed in this chapter can be applied for f_e prediction, as shown in Chapters 7 and 8 for some of the forecasting strategies. Specifically, this chapter investigates the comparative performance of the η forecasting methods shown in references [67] and [76] in Section 6.1 and analyses the performance of autoregressive AR models for wave energy applications in Section 6.2.

6.1 AR and ARMA model comparison

As mentioned in Section 3.3.2, the results shown in [67] and [76] are inconsistent since, in [67], the ARMA model is shown not to provide any improvement for the η prediction, compared to simple AR models while, in [76], the ARMA model is shown to outperform the AR model introduced in [67]. To clarify the observed inconsistency, the current section aims to critically compare both forecasting strategies (AR and ARMA models) under the same conditions, to determine potential differences in the performance and, thereby, the comparative advantages and disadvantages of the two predictors for wave energy applications.

In order to compare the AR and ARMA models under the same conditions, a number of processes must be carried out in the same way for the two models as, for example, the identification method used to determine the coefficients of the models. To this end, different identification procedures can be found in the literature [23], such as the Yule-Walker or Hannan-Rissanen (HR) methods. However, none of those methods can be used for both AR and ARMA models since, as will be explained in Section 6.1.1.2, for the ARMA model, future η values not only depend on the past measurable values of η, but also on the unmeasurable values of the process noise and, therefore, requires two identification stages as opposed to the AR model which, as explained in Section 6.1.1.1, are identified from a single identification stage, in this case, solving a linear least square LLS problem. The most similar approach for both predictors is to identify the AR model parameters from a LLS method and, for the ARMA model, use a variation of the HR algorithm which includes two LLS problems, which is also the identification strategy adopted in [76]. By identifying the coefficients of both models using similar processes, the impact of the identification method on the performance of the prediction models is minimised, enabling, thus, a fair comparison of the model structures for η prediction.

Section 6.1.1 introduces the theory behind the AR and ARMA models, used for the comparison, the real wave time series are introduced in Section 6.1.2, and, in Section 6.1.3, the results obtained for the comparison are presented and discussed.

6.1.1 Prediction strategies

For the sake of clarity, the different forecasting strategies are termed using the predictor structure as name and the identification method in the subindex. For example, the forecasting strategy which has the AR predictor structure and identifies the parameters solving a LLS problem is referred to as AR_{LLS}.

6.1.1.1 AR model

The AR model assumes that $\eta(k)$ depends linearly on its own previous values through the parameters $\varphi^{\mathsf{AR}} \in \mathbb{R}^{n_{\mathsf{ord}}^{\mathsf{AR}}}$, with $n_{\mathsf{ord}}^{\mathsf{AR}}$ being the order of the model, following

$$\eta(k) = \sum_{i=1}^{n_{\mathsf{ord}}^{\mathsf{AR}}} \varphi^{\mathsf{AR}}(i)\eta(k-i) + \epsilon(k), \tag{6.1}$$

where $\epsilon(k)$ is the modelling error (or a disturbance term). Therefore, the n_{hor}^{*}-step-ahead predicted value of the wave elevation ($\bar{\eta}(k+n_{\mathsf{hor}}^{*}|k)$), where $n_{\mathsf{hor}}^{*} \in \{1, ..., n_{\mathsf{hor}}\}$ and $t_{\mathsf{hor}} = t_{\mathsf{s}} n_{\mathsf{hor}}$, can be expressed as

$$\bar{\eta}(k+n_{\mathsf{hor}}^{*}|k) = \sum_{i=1}^{n_{\mathsf{ord}}^{\mathsf{AR}}} \varphi^{\mathsf{AR}}(i)\bar{\eta}(k+n_{\mathsf{hor}}^{*}-i|k). \tag{6.2}$$

In Equation (6.2), $\bar{\eta}(k+n_{\mathsf{hor}}^{*}-i|k) = \eta(k+n_{\mathsf{hor}}^{*}-i)$ when $(k+n_{\mathsf{hor}}^{*}-i) \leq k$, since the value of $\eta(k+n_{\mathsf{hor}}^{*}-i)$ is known and there is no need for prediction. Thus, the process to calculate the n_{hor}^{*}-step-ahead predicted η is an iterative process, where all the values of $\eta(k)$ from $k=1$ to $(n_{\mathsf{hor}}^{*}-1)$ have to be predicted first.

Several methods to determine the optimal order $n_{\mathsf{ord}}^{\mathsf{AR}}$ of an AR model (e.g. Akaike's Information Theoretic Criterion [6]) can be found in the literature. However, the different methods for the optimal order determination are not discussed in this thesis since the aim is to show how the AR model performs for different orders, rather than how the best order can be obtained.

Given a set of training data of dimension n_{tr}, the coefficients φ^{AR} are identified by minimising the following cost function

$$J_{\mathsf{LLS}}^{\mathsf{AR}} = \sum_{i=n_{\mathsf{ord}}^{\mathsf{AR}}+1}^{n_{\mathsf{tr}}} \left(\eta(i) - \bar{\eta}(i|i-1)\right)^2, \tag{6.3}$$

which is a LLS problem, and can be solved by the following matrix product

$$\varphi_{\mathsf{LLS}}^{\mathsf{AR}} = \left(\boldsymbol{\eta}_{\mathsf{LLS}}^{\mathsf{AR}\,\mathsf{T}} \boldsymbol{\eta}_{\mathsf{LLS}}^{\mathsf{AR}}\right)^{-1} \left(\boldsymbol{\eta}_{\mathsf{LLS}}^{\mathsf{AR}\,\mathsf{T}} \boldsymbol{\eta}_{\mathsf{LLS}}^{*}\right), \tag{6.4}$$

where $\boldsymbol{\eta}_{\mathsf{LLS}}^{\mathsf{AR}} \in \mathbb{R}^{\left(n_{\mathsf{tr}}-n_{\mathsf{ord}}^{\mathsf{AR}}-1\right)\times n_{\mathsf{ord}}^{\mathsf{AR}}}$ and $\boldsymbol{\eta}_{\mathsf{LLS}}^{*} \in \mathbb{R}^{\left(n_{\mathsf{tr}}-n_{\mathsf{ord}}^{\mathsf{AR}}-1\right)}$ are defined as

$$\boldsymbol{\eta}_{\mathsf{LLS}}^{\mathsf{AR}} = \begin{bmatrix} \eta(n_{\mathsf{ord}}^{\mathsf{AR}}) & \eta(n_{\mathsf{ord}}^{\mathsf{AR}}-1) & \cdots & \eta(1) \\ \eta(n_{\mathsf{ord}}^{\mathsf{AR}}+1) & \eta(n_{\mathsf{ord}}^{\mathsf{AR}}) & \cdots & \eta(2) \\ \vdots & \vdots & \ddots & \vdots \\ \eta(n_{\mathsf{tr}}-1) & \eta(n_{\mathsf{tr}}-2) & \cdots & \eta(n_{\mathsf{tr}}-n_{\mathsf{ord}}^{\mathsf{AR}}) \end{bmatrix}, \tag{6.5a}$$

$$\boldsymbol{\eta}_{\mathsf{LLS}}^{*} = \left[\eta(n_{\mathsf{ord}}^{\mathsf{AR}}+1) \quad \eta(n_{\mathsf{ord}}^{\mathsf{AR}}+2) \quad \cdots \quad \eta(n_{\mathsf{tr}})\right]^{\mathsf{T}}. \tag{6.5b}$$

Thus, the AR model based forecasting strategy, whose coefficients are identified by minimising the one-step-ahead prediction error, solving the LLS problem of Equation (6.4), is termed $\mathsf{AR}_{\mathsf{LLS}}$.

6.1.1.2 ARMA model

The ARMA model, considered in this thesis and proposed in [76][1], assumes that $\eta(k)$ can be expressed as

$$\eta(k) = \sum_{i=1}^{n_{\text{ord}}^{\text{ARma}}} \varphi^{\text{ARma}}(i)\eta(k-i) + \sum_{j=1}^{n_{\text{ord}}^{\text{arMA}}} \varphi^{\text{arMA}}(j)\epsilon(k-j) + \epsilon(k), \tag{6.6}$$

where $\varphi^{\text{ARma}} \in \mathbb{R}^{n_{\text{ord}}^{\text{ARma}}}$ and $\varphi^{\text{arMA}} \in \mathbb{R}^{n_{\text{ord}}^{\text{arMA}}}$ are the coefficients of the AR and MA parts of the ARMA model, respectively. As in Equation (6.1), ϵ stands for the modelling error (or a disturbance term) [76] in Equation (6.6). Thus, the n_{hor}^{*}-step-ahead predicted value of η can be expressed as

$$\bar{\eta}(k+n_{\text{hor}}^{*}|k) = \sum_{i=1}^{n_{\text{ord}}^{\text{ARma}}} \varphi^{\text{ARma}}(i)\bar{\eta}(k+n_{\text{hor}}^{*}-i|k) + \sum_{j=1}^{n_{\text{ord}}^{\text{arMA}}} \varphi^{\text{arMA}}(j)\bar{\tilde{\epsilon}}(k+n_{\text{hor}}^{*}-j|k), \tag{6.7}$$

where, as explained for Equation (6.2), $\bar{\eta}(k + n_{\text{hor}}^{*} - i|k)$ refers to $\eta(k + n_{\text{hor}}^{*} - i|k)$ for $(k + n_{\text{hor}}^{*} - i) \leq k$, and $\bar{\tilde{\epsilon}}(k + n_{\text{hor}}^{*} - j|k)$ refers to estimated values of ϵ $(\tilde{\epsilon}(k + n_{\text{hor}}^{*} - j|k))$ for $(k + n_{\text{hor}}^{*} - i) \leq k$.

Since the disturbance cannot be measured, two LLS problems have to be solved to identify the parameters of the ARMA model [76]. With the first LLS problem, neglecting the moving average part, the parameters of the autoregressive part are obtained as shown in Equation (6.4), by considering $n_{\text{ord}}^{\text{ARma}\star}$ instead of $n_{\text{ord}}^{\text{AR}}$ as

$$\varphi_{\text{LLS}}^{\text{ARma}\star} = \left(\boldsymbol{\eta}_{\text{LLS}}^{\text{ARma}\mathsf{T}}\boldsymbol{\eta}_{\text{LLS}}^{\text{ARma}}\right)^{-1}\left(\boldsymbol{\eta}_{\text{LLS}}^{\text{ARma}\mathsf{T}}\boldsymbol{\eta}_{\text{LLS}}^{*}\right), \tag{6.8}$$

where $\boldsymbol{\eta}_{\text{LLS}}^{\text{ARma}} \in \mathbb{R}^{\left(n_{\text{tr}}-n_{\text{ord}}^{\text{ARma}\star}-1\right)\times n_{\text{ord}}^{\text{ARma}\star}}$ and $\boldsymbol{\eta}_{\text{LLS}}^{*} \in \mathbb{R}^{\left(n_{\text{tr}}-n_{\text{ord}}^{\text{ARma}\star}-1\right)}$ are defined as

$$\boldsymbol{\eta}_{\text{LLS}}^{\text{ARma}} = \begin{bmatrix} \eta(n_{\text{ord}}^{\text{ARma}\star}) & \eta(n_{\text{ord}}^{\text{ARma}\star}-1) & \cdots & \eta(1) \\ \eta(n_{\text{ord}}^{\text{ARma}\star}+1) & \eta(n_{\text{ord}}^{\text{ARma}\star}) & \cdots & \eta(2) \\ \vdots & \vdots & \ddots & \vdots \\ \eta(n_{\text{tr}}-1) & \eta(n_{\text{tr}}-2) & \cdots & \eta(n_{\text{tr}}-n_{\text{ord}}^{\text{ARma}\star}) \end{bmatrix}, \tag{6.9a}$$

$$\boldsymbol{\eta}_{\text{LLS}}^{*} = \begin{bmatrix} \eta(n_{\text{ord}}^{\text{ARma}\star}+1) & \eta(n_{\text{ord}}^{\text{ARma}\star}+2) & \cdots & \eta(n_{\text{tr}}) \end{bmatrix}^{\mathsf{T}}. \tag{6.9b}$$

Note that, since the obtained $\varphi_{\text{LLS}}^{\text{ARma}}$ are not the final coefficients, they are denoted as $\varphi_{\text{LLS}}^{\text{ARma}\star} \in \mathbb{R}^{n_{\text{ord}}^{\text{ARma}\star}}$. Once the parameters $\varphi_{\text{LLS}}^{\text{ARma}\star}$ are determined, the estimate of the noise $\epsilon(k)$ can be obtained as

$$\tilde{\epsilon}(k) = \eta(k) - \sum_{i=1}^{n_{\text{ord}}^{\text{ARma}\star}} \varphi_{\text{LLS}}^{\text{ARma}\star}(i)\eta(k-i). \tag{6.10}$$

---

[1] Note that the definition of the ARMA model is adopted from [76] since, even though it was first proposed in [67], no model or identification method description is provided in [67].

With $\tilde{\epsilon}$, the parameters of both AR and MA parts can be identified by minimising the following cost function

$$J_{\mathsf{LLS}}^{\mathsf{ARMA}} = \sum_{i=n_{\mathsf{max}}^{\mathsf{ARMA}}+1}^{n_{\mathsf{tr}}} (\eta(i) - \bar{\eta}(i|i-1))^2, \tag{6.11}$$

where $n_{\mathsf{max}}^{\mathsf{ARMA}} = \max\{n_{\mathsf{ord}}^{\mathsf{ARma}}, n_{\mathsf{ord}}^{\mathsf{arMA}}\}$. Equation (6.11), which is again a LLS problem, can be solved by the following matrix product

$$\varphi_{\mathsf{LLS}}^{\mathsf{ARMA}} = \left(\boldsymbol{\eta}_{\mathsf{LLS}}^{\mathsf{ARMA}\mathsf{T}} \boldsymbol{\eta}_{\mathsf{LLS}}^{\mathsf{ARMA}}\right)^{-1} (\boldsymbol{\eta}_{\mathsf{LLS}}^{\mathsf{ARMA}\mathsf{T}} \boldsymbol{\eta}_{\mathsf{LLS}}^{\star}), \tag{6.12}$$

where $\varphi_{\mathsf{LLS}}^{\mathsf{ARMA}} = \left[\varphi_{\mathsf{LLS}}^{\mathsf{ARma}} \;\; \varphi_{\mathsf{LLS}}^{\mathsf{arMA}}\right] \in \mathbb{R}^{n_{\mathsf{ord}}^{\mathsf{ARMA}}}$, with $n_{\mathsf{ord}}^{\mathsf{ARMA}} = n_{\mathsf{ord}}^{\mathsf{ARma}} + n_{\mathsf{ord}}^{\mathsf{arMA}}$, and $\boldsymbol{\eta}_{\mathsf{LLS}}^{\mathsf{ARMA}} \in \mathbb{R}^{n_{\mathsf{ord}}^{\mathsf{ARMA}} \times \left(n_{\mathsf{tr}} - n_{\mathsf{ord}}^{\mathsf{ARma}\star} - n_{\mathsf{max}}^{\mathsf{ARMA}} - 1\right)}$ includes now the ϵ estimates as

$$\boldsymbol{\eta}_{\mathsf{LLS}}^{\mathsf{ARMA}} = \begin{bmatrix} \eta(n_{\mathsf{ord}}^{\mathsf{ARma}\star} + n_{\mathsf{max}}^{\mathsf{ARMA}}) & \cdots & \eta(n_{\mathsf{tr}} - 1) \\ \vdots & \ddots & \vdots \\ \eta(n_{\mathsf{ord}}^{\mathsf{ARma}\star} + n_{\mathsf{max}}^{\mathsf{ARMA}} - n_{\mathsf{ord}}^{\mathsf{ARma}} + 1) & \cdots & \eta(n_{\mathsf{tr}} - n_{\mathsf{ord}}^{\mathsf{ARma}}) \\ \tilde{\epsilon}(n_{\mathsf{ord}}^{\mathsf{ARma}\star} + n_{\mathsf{max}}^{\mathsf{ARMA}}) & \cdots & \tilde{\epsilon}(n_{\mathsf{tr}} - 1) \\ \vdots & \ddots & \vdots \\ \tilde{\epsilon}(n_{\mathsf{ord}}^{\mathsf{ARma}\star} + n_{\mathsf{max}}^{\mathsf{ARMA}} - n_{\mathsf{ord}}^{\mathsf{arMA}} + 1) & \cdots & \tilde{\epsilon}(n_{\mathsf{tr}} - n_{\mathsf{ord}}^{\mathsf{arMA}}) \end{bmatrix}^{\mathsf{T}}, \tag{6.13a}$$

$$\boldsymbol{\eta}_{\mathsf{LLS}}^{\star} = \left[\eta(n_{\mathsf{ord}}^{\mathsf{ARma}\star} + n_{\mathsf{max}}^{\mathsf{ARMA}} + 1) \;\; \eta(n_{\mathsf{ord}}^{\mathsf{ARma}\star} + n_{\mathsf{max}}^{\mathsf{ARMA}} + 2) \;\; \cdots \;\; \eta(n_{\mathsf{tr}})\right]^{\mathsf{T}}. \tag{6.13b}$$

Once the parameters $\varphi_{\mathsf{LLS}}^{\mathsf{ARma}}$ and $\varphi_{\mathsf{LLS}}^{\mathsf{arMA}}$ are identified, the ARMA model can be expressed by the following discrete-time SS

$$x^{\mathsf{ARMA}}(k+1) = A_{\mathsf{ss}}^{\mathsf{ARMA}} x^{\mathsf{ARMA}}(k) + B_{\mathsf{ss}}^{\mathsf{ARMA}} \epsilon(k+1), \tag{6.14a}$$

$$y^{\mathsf{ARMA}}(k) = C_{\mathsf{ss}}^{\mathsf{ARMA}} x^{\mathsf{ARMA}}(k), \tag{6.14b}$$

where $x^{\mathsf{ARMA}}(k) \in \mathbb{R}^{n_{\mathsf{ss}}^{\mathsf{ARMA}}}$, $A_{\mathsf{ss}}^{\mathsf{ARMA}} \in \mathbb{R}^{n_{\mathsf{ss}}^{\mathsf{ARMA}} \times n_{\mathsf{ss}}^{\mathsf{ARMA}}}$, $B_{\mathsf{ss}}^{\mathsf{ARMA}} \in \mathbb{R}^{n_{\mathsf{ss}}^{\mathsf{ARMA}}}$, and $C_{\mathsf{ss}}^{\mathsf{ARMA}} \in \mathbb{R}^{n_{\mathsf{ss}}^{\mathsf{ARMA}}}$, with $n_{\mathsf{ss}}^{\mathsf{ARMA}} = \max\{n_{\mathsf{ord}}^{\mathsf{ARma}}, n_{\mathsf{ord}}^{\mathsf{arMA}} + 1\}$, are defined as

$$x^{\mathsf{ARMA}}(k) = \left[\; \bar{\eta}(k) \;\; \bar{\eta}(k-1) \;\; \cdots \;\; \bar{\eta}(k - n_{\mathsf{ss}}^{\mathsf{ARMA}})\right]^{\mathsf{T}}, \tag{6.15a}$$

$$A_{\mathsf{ss}}^{\mathsf{ARMA}} = \begin{bmatrix} \varphi_{\mathsf{LLS}_1}^{\mathsf{ARma}} & \varphi_{\mathsf{LLS}_2}^{\mathsf{ARma}} & \cdots & \varphi_{\mathsf{LLS}_{n_{\mathsf{ss}}^{\mathsf{ARMA}}}}^{\mathsf{ARma}} \\ 1 & 0 & \cdots & 0 \\ 0 & 1 & \cdots & 0 \\ \vdots & \vdots & \ddots & \vdots \\ 0 & 0 & \cdots & 0 \end{bmatrix}, \tag{6.15b}$$

$$B_{\mathsf{ss}}^{\mathsf{ARMA}} = \left[\; 1 \;\; 0 \;\; \cdots \;\; 0\right]^{\mathsf{T}}, \tag{6.15c}$$

$$C_{\mathsf{ss}}^{\mathsf{ARMA}} = \left[\; 1 \;\; \varphi_{\mathsf{LLS}_1}^{\mathsf{arMA}} \;\; \cdots \;\; \varphi_{\mathsf{LLS}_{n_{\mathsf{ss}}^{\mathsf{ARMA}}-1}}^{\mathsf{arMA}}\right]. \tag{6.15d}$$

In $A_{\mathsf{ss}}^{\mathsf{ARMA}}$ and $C_{\mathsf{ss}}^{\mathsf{ARMA}}$, $\varphi_{\mathsf{LLS}_i}^{\mathsf{ARma}} = 0$ for $i > n_{\mathsf{LLS}}^{\mathsf{ARma}}$ and $\varphi_{\mathsf{LLS}_i}^{\mathsf{arMA}} = 0$ for $i > n_{\mathsf{LLS}}^{\mathsf{arMA}}$.

With System (6.14), the n^{*}_{hor}-step-ahead predicted value of η can be obtained using a discrete-time linear KF. To this end, the steady-state error covariance matrix P^{∞}_{kf} can be obtained by solving the discrete algebraic Riccati equation defined as

$$\begin{aligned} P^{\infty}_{\mathsf{kf}} =& A^{\mathsf{ARMA}}_{\mathsf{ss}} P^{\infty}_{\mathsf{kf}} A^{\mathsf{ARMA}\intercal}_{\mathsf{ss}} + B^{\mathsf{ARMA}}_{\mathsf{ss}} \tilde{Q}^{\mathsf{ARMA}}_{\epsilon} B^{\mathsf{ARMA}\intercal}_{\mathsf{ss}} \\ & - A^{\mathsf{ARMA}}_{\mathsf{ss}} P^{\infty}_{\mathsf{kf}} C^{\mathsf{ARMA}\intercal}_{\mathsf{ss}} (C^{\mathsf{ARMA}}_{\mathsf{ss}} P^{\infty}_{\mathsf{kf}} C^{\mathsf{ARMA}\intercal}_{\mathsf{ss}})^{-1} C^{\mathsf{ARMA}}_{\mathsf{ss}} P^{\infty}_{\mathsf{kf}} A^{\mathsf{ARMA}\intercal}_{\mathsf{ss}}, \end{aligned} \tag{6.16}$$

while the steady-state Kalman gain (K^{∞}_{kf}) can be computed as

$$K^{\infty}_{\mathsf{kf}} = (P^{\infty}_{\mathsf{kf}} C^{\mathsf{ARMA}\intercal}_{\mathsf{ss}})(C^{\mathsf{ARMA}}_{\mathsf{ss}} P^{\infty}_{\mathsf{kf}} C^{\mathsf{ARMA}\intercal}_{\mathsf{ss}})^{-1}, \tag{6.17}$$

and, as shown in [76], the process covariance matrix $Q^{\mathsf{ARMA}}_{\epsilon}$ can be estimated as

$$\tilde{Q}^{\mathsf{ARMA}}_{\epsilon} = \frac{J^{\mathsf{ARMA}}_{\mathsf{LLS}}}{n_{\mathsf{tr}} - n^{\mathsf{ARma}^{\star}}_{\mathsf{ord}} - n^{\mathsf{ARMA}}_{\mathsf{max}}}. \tag{6.18}$$

Thus, the KF can now be defined using just two equations as

Time Update (*A Priori*) :

$$\tilde{x}^{\mathsf{ARMA}^{-}}(k) = A^{\mathsf{ARMA}}_{\mathsf{ss}} \tilde{x}^{\mathsf{ARMA}}(k-1). \tag{6.19a}$$

Measurement Update (*A Posteriori*) :

$$\tilde{x}^{\mathsf{ARMA}}(k) = \tilde{x}^{\mathsf{ARMA}^{-}}(k) + K^{\infty}_{\mathsf{kf}} \left(y^{\mathsf{ARMA}}(k) - C^{\mathsf{ARMA}}_{\mathsf{ss}} \tilde{x}^{\mathsf{ARMA}^{-}}(k) \right), \tag{6.19b}$$

and, once the state $\tilde{x}^{\mathsf{ARMA}}$ is determined, it is possible to recursively predict future η values as

$$\bar{\eta}(k + n^{*}_{\mathsf{hor}}|k) = C^{\mathsf{ARMA}}_{\mathsf{ss}} A^{\mathsf{ARMA}^{n^{*}_{\mathsf{hor}}}}_{\mathsf{ss}} \tilde{x}^{\mathsf{ARMA}}(k). \tag{6.20}$$

6.1.2 Wave data

Real sea η measurements, used for the comparison, were measured at three different locations:

- The **Pico WEC plant**, which is located on Pico island, approximately at global coordinates (38.56, -28.45), in the Azores. This data has been recorded using an Aquadopp sensor [80] with a sampling frequency of 2Hz. Data consist of 30 minutes sets recorded continually.
- **Belmullet** is located off the west coast of Ireland, approximately at global coordinates (54.27, -10.28). Data consist of 30 minutes sets recorded with a Waverider buoy [36] with a sampling frequency of 1.28Hz. The data are provided by the Irish Marine Institute [94].

- **Galway Bay**, west coast of Ireland, data are provided by the Irish Marine Institute [94]. This data consist of 20-minute records for each hour, measuring values with a sampling frequency of 2.56Hz recorded with a Waverider buoy [36]. The buoy is located approximately at global coordinates (53.23, -9.26).

The selected data fragments, from the three locations, are chosen so that the prediction strategies are tested for a diverse set of sea states. Figure 6.1 shows the SDFs[2] of the selected data fragments. Note that the data fragments are named with the initial of the location they were recorded at; i.e. data recorded at the Pico plant is referred to as **P**, data from Belmullet as **B**, and data from Galway bay as **G**.

Figure 6.1 indicates that the spectra of the Pico plant wave data are narrow banded at low-frequencies, showing that the sea state is mainly composed of swell waves, with small high-frequency components. The SDFs of η from Belmullet are also narrow banded at low frequencies, but with larger high-frequency components. Finally, the wave data fragments selected for Galway Bay are mostly composed of wind waves which, though not optimal for WEC power extraction, are chosen to assess the performance of the predictors in a wider set of sea conditions.

6.1.3 Comparative results

Identification of the forecasting coefficients is carried out using the first half of every data fragment, while the second half is used to assess the performance of the predictors on unseen data. By way of example, considering $\mathbf{P_3}$, Figure 6.2 shows how the obtained $\text{NRMSE}_{\eta}^{\text{pred}}$, defined as shown in Equation (4.21), changes for different model orders, in the case of (a) the AR model and (b) the ARMA model.

As shown in Figure 6.2(a), the minimum prediction error ($\text{NRMSE}_{\eta}^{\text{pred}} \approx 0.11$) for the AR model occurs at a model order of $n_{\text{ord}}^{\text{AR}} \approx 40$ and, for higher orders, the obtained $\text{NRMSE}_{\eta}^{\text{pred}}$ increases. This can be justified by the fact that, real sea wave conditions, characterised by the wave spectrum, vary in time and, hence, the wave condition evolves between the η data fragment during which the coefficients are identified and the one over which the models are used to perform prediction. In this case, as shown in Figure 6.2(a), for orders higher than 40, the AR model identifies characteristics of the signal that are in the first half of the data fragment (with which the identification is performed), but not in the second half (where the performance is assessed). However, it should be highlighted that the $\text{NRMSE}_{\eta}^{\text{pred}}$ only varies from 0.11 to 0.15, so the order of the model does not significantly affect the obtained error.

---

[2] To create the smoothed spectra shown in Figure 6.1, the wave time series data is processed as explained in [36].

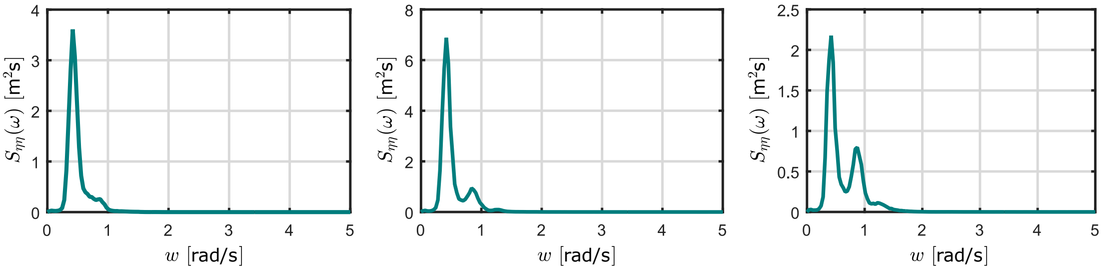

(a) SDF obtained for $\mathbf{P_1}$. **(b)** SDF obtained for $\mathbf{P_2}$. **(c)** SDF obtained for $\mathbf{P_3}$.

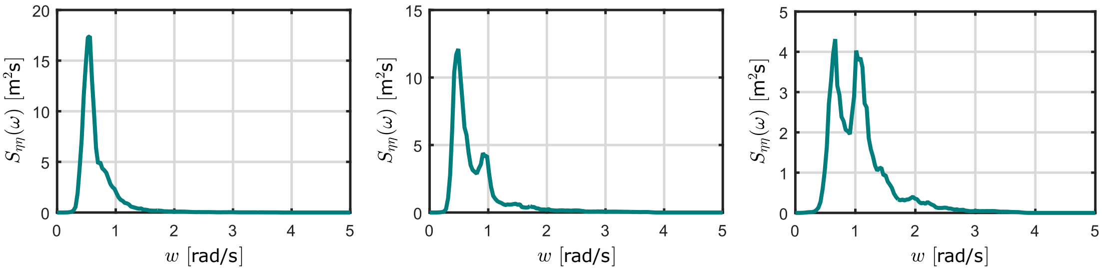

(d) SDF obtained for $\mathbf{B_1}$. **(e)** SDF obtained for $\mathbf{B_2}$. **(f)** SDF obtained for $\mathbf{B_3}$.

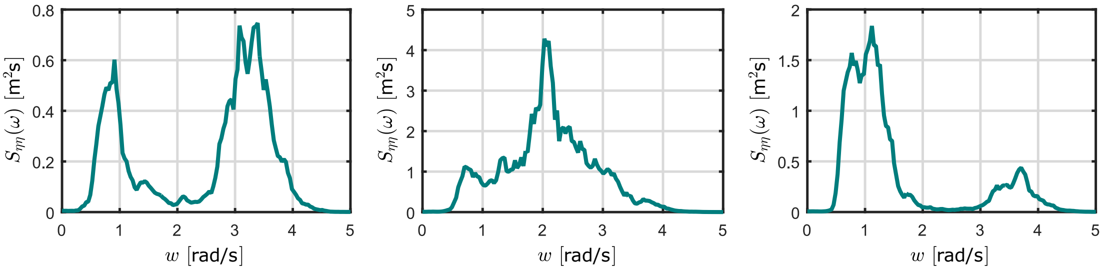

(g) SDF obtained for $\mathbf{G_1}$. **(h)** SDF obtained for $\mathbf{G_2}$. **(i)** SDF obtained for $\mathbf{G_3}$.

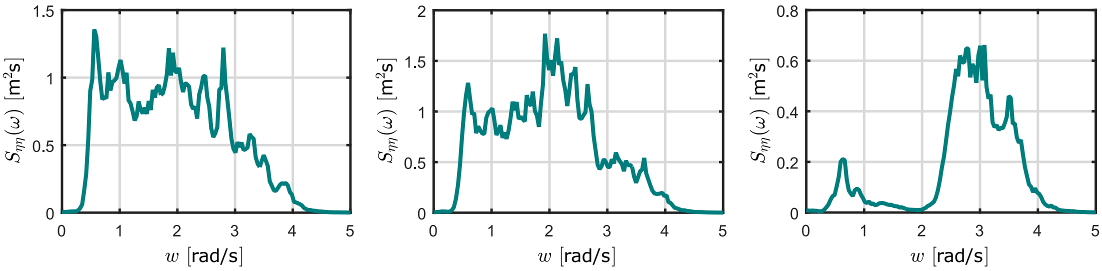

(j) SDF obtained for $\mathbf{G_4}$. **(k)** SDF obtained for $\mathbf{G_5}$. **(l)** SDF obtained for $\mathbf{G_6}$.

Figure 6.1: The SDFs of the data fragments selected for the comparison, obtained from η time series recorded at (a-c) Pico island, (d-f) Belmullet, and (g-l) Galway bay.

Similarly, the NRMSE$^{\text{pred}}_{\eta}$ obtained using the ARMA model does not vary significantly for a large set of $n^{\text{ARma}}_{\text{ord}}$ and $n^{\text{arMA}}_{\text{ord}}$ combinations, as shown in Figure 6.2(b). Additionally, one can notice that there is a minimum $n^{\text{ARma}}_{\text{ord}}$ required (approximately $n^{\text{ARma}}_{\text{ord}} > 15$) to obtain reasonably accurate results. However, the obtained NRMSE$^{\text{pred}}_{\eta}$ is not affected if small $n^{\text{arMA}}_{\text{ord}}$ are chosen, which means that, while a minimum order of 15 is needed for the AR part of the ARMA model to obtain reasonable results, the MA part does

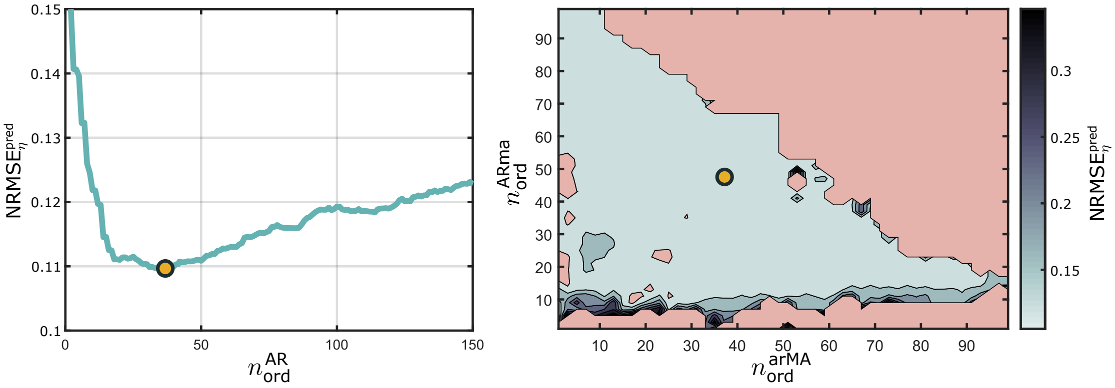

(a) One-step-ahead $\text{NRMSE}_{\eta}^{\text{pred}}$ for different AR model orders.

(b) One-step-ahead $\text{NRMSE}_{\eta}^{\text{pred}}$ for different ARMA model orders, where the red areas represent $n_{\text{ord}}^{\text{ARma}}$ and $n_{\text{ord}}^{\text{arMA}}$ order combinations for which the ARMA model obtains prediction errors higher than 100%.

Figure 6.2: Variation of the one-step-ahead (0.5 s) $\text{NRMSE}_{\eta}^{\text{pred}}$ for different model orders of both (a) AR and (b) ARMA models, for $\mathbf{P_3}$. The orange dots denote the selected orders.

not significantly affect the obtained performance. The order $n_{\text{ord}}^{\text{ARma}*}$, as explained in [76], does not affect the obtained $\text{NRMSE}_{\eta}^{\text{pred}}$ as long as is higher than $n_{\text{ord}}^{\text{ARma}}$ and, therefore, $n_{\text{ord}}^{\text{ARma}*} = 110$ is selected for all the ARMA models.

The considered AR and ARMA model orders (selected such that the obtained NRMSE is minimised) and the obtained one-step-ahead $\text{NRMSE}_{\eta}^{\text{pred}}$ for all the analysed sea states are shown in Table 6.1. It is shown that the one-step-ahead $\text{NRMSE}_{\eta}^{\text{pred}}$ achieved by the AR model is always slightly lower than that obtained using the ARMA predictor.

Table 6.1: Model orders and obtained one-step-ahead $\text{NRMSE}_{\eta}^{\text{pred}}$ for the different data sets considered. Since the sampling frequency differs for each location, the one-step-ahead refers to 0.5 s, 0.78 s, and 0.39 s for the data-sets from Pico, Belmullet, and Galway Bay, respectively.

		Pico			**Belmullet**			**Galway**					
		$\mathbf{P_1}$	$\mathbf{P_2}$	$\mathbf{P_3}$	$\mathbf{B_1}$	$\mathbf{B_2}$	$\mathbf{B_3}$	$\mathbf{G_1}$	$\mathbf{G_2}$	$\mathbf{G_3}$	$\mathbf{G_4}$	$\mathbf{G_5}$	$\mathbf{G_6}$
AR	$n_{\text{ord}}^{\text{AR}}$	89	40	40	62	66	55	7	38	41	42	26	31
	$\text{NRMSE}_{\eta}^{\text{pred}}$	0.05	0.08	0.11	0.22	0.34	0.36	0.32	0.2	0.23	0.27	0.23	0.29
ARMA	$n_{\text{ord}}^{\text{ARma}}$	58	14	49	46	22	16	7	7	28	19	19	16
	$n_{\text{ord}}^{\text{arMA}}$	29	21	37	10	16	7	4	16	37	25	16	13
	$\text{NRMSE}_{\eta}^{\text{pred}}$	0.07	0.1	0.15	0.32	0.52	0.57	0.37	0.23	0.28	0.28	0.28	0.34

The differences between the $\text{NRMSE}_{\eta}^{\text{pred}}$ obtained using the AR and ARMA models is further visualised in Figure 6.3, which shows the obtained $\text{NRMSE}_{\eta}^{\text{pred}}$ for different n_{hor}^{*} for all the considered time series. It is shown that, overall, the results obtained using the AR and ARMA models are similar for all the analysed cases. The most accurate predictions are obtained for η recorded at the Pico plant, obtaining a $\text{NRMSE}_{\eta}^{\text{pred}}$

of around 60% for $t_{\text{hor}} = 5\,\text{s}$ (averaged over the three sea states), compared to the 80% and 100% of error obtained for Belmullet and Galway, respectively. This can be explained by the fact that, as shown in Figure 6.1, the SDFs of the time series recorded at Pico plant are narrow banded, with almost no high-frequency content, while the SDFs from Belmullet have more high-frequency components and, finally, the SDFs of the waves recorded at Galway Bay have significant high-frequency components.

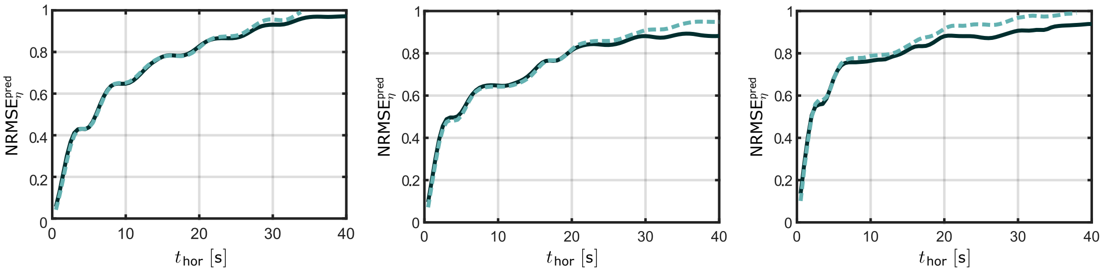

(a) $\text{NRMSE}_\eta^{\text{pred}}$ obtained for $\mathbf{P_1}$. **(b)** $\text{NRMSE}_\eta^{\text{pred}}$ obtained for $\mathbf{P_2}$. **(c)** $\text{NRMSE}_\eta^{\text{pred}}$ obtained for $\mathbf{P_3}$.

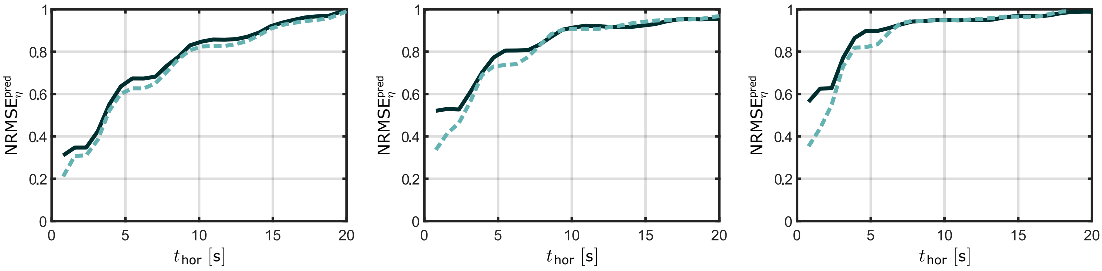

(d) $\text{NRMSE}_\eta^{\text{pred}}$ obtained for $\mathbf{B_1}$. **(e)** $\text{NRMSE}_\eta^{\text{pred}}$ obtained for $\mathbf{B_2}$. **(f)** $\text{NRMSE}_\eta^{\text{pred}}$ obtained for $\mathbf{B_3}$.

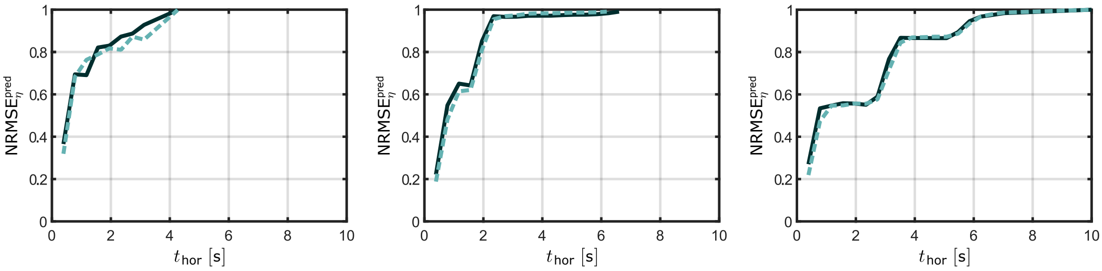

(g) $\text{NRMSE}_\eta^{\text{pred}}$ obtained for $\mathbf{G_1}$. **(h)** $\text{NRMSE}_\eta^{\text{pred}}$ obtained for $\mathbf{G_2}$. **(i)** $\text{NRMSE}_\eta^{\text{pred}}$ obtained for $\mathbf{G_3}$.

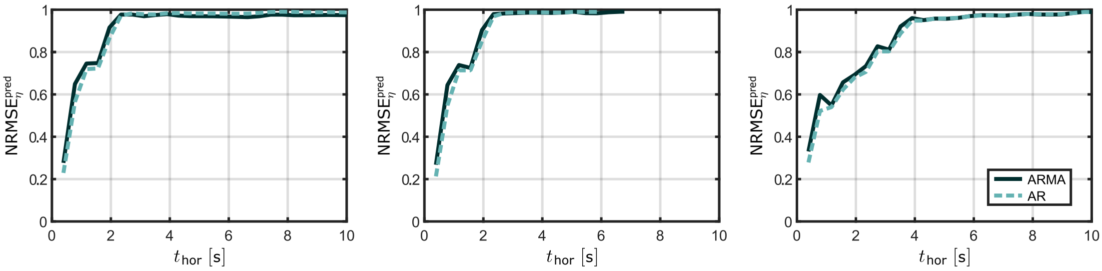

(j) $\text{NRMSE}_\eta^{\text{pred}}$ obtained for $\mathbf{G_4}$. **(k)** $\text{NRMSE}_\eta^{\text{pred}}$ obtained for $\mathbf{G_5}$. **(l)** $\text{NRMSE}_\eta^{\text{pred}}$ obtained for $\mathbf{G_6}$.

Figure 6.3: The obtained $\text{NRMSE}_\eta^{\text{pred}}$ for the different sea states.

Finally, regarding the time needed by both models to predict future η values, it should be noted that, even though both AR and ARMA compute the η predictions quickly, the AR model is slightly faster than the ARMA model (approximately 1.3 times faster). However, this is not a problem for any of the models, since both are around three orders of magnitude below real time and, therefore, there will not be any issue to apply these predictors for online η or f_e prediction.

In summary, this section shows that, while the ARMA model is significantly more complex than the AR model, the obtained results are similar for both models and, therefore, the conclusion presented in [67] is confirmed. With the discrepancy on the results of [76] and [67] solved, the next section, Section 6.2, analyses the capabilities of the AR model by comparing the obtained results to two theoretical prediction accuracy limits.

6.2 Analysis of AR models

Since Fusco and Ringwood compared different short-term η prediction strategies in [67], the AR model is been one of the most popular predictors for wave energy applications. In fact, as explained in Section 3.3.2, several new η prediction techniques have been proposed since [67], often concluding that there is no significant improvement with respect to the results obtained using the AR model in [67].

To assess the capabilities of the AR model for wave energy applications, this section proposes the following three analyses:

- The results obtained with the AR model are compared with two theoretical accuracy limits for the prediction. The first one is given by a predictor that, by directly identifying the forecasting parameters from the SDF, yields, in theory, the best achievable prediction of η. While the AR predictor structure uses a single set of parameters (for the one-step-ahead prediction), and multi-step-ahead prediction is carried out iteratively, the theoretically-optimal predictor has a different set of coefficients for each n^*_hor and, thus, directly predicts the multi-step ahead wave elevation with no need for iteration. In the following, the predictor structure with a different set of coefficients for each prediction horizon will be termed DMS model. Additionally, since the theoretically optimal predictor identifies the parameters from the wave spectrum, it is referred to as DMS$_\mathrm{SDF}$ hereinafter. The second theoretical limit is given by the Kolmogoroff-Szego's formula [132], and provides the theoretical lowest one-step-ahead prediction error associated to a given SDF, under a set of assumptions specified in Section 6.2.1.4.

- Two different identification methods for the AR predictor are compared. The first one, termed AR$_{\mathsf{LLS}}$ and introduced in Section 6.1.1.1, is based on solving a LLS problem, which minimises the one-step-ahead forecasting error. In contrast, the second identification method, proposed in [67], optimises the n^*_{hor}-step-ahead prediction through a NLS problem, termed Long-Range Predictive Identification (LRPI) [67, 131] and, therefore, termed AR$_{\mathsf{LRPI}}$.
- Additionally, the idea of using filtered η values for the prediction is investigated. In some studies [67, 131], it is shown that, when using an AR model, offline filtering can improve the forecasting accuracy. However, for real time operation, since online filters add a delay to the filtered signal (t_{del}), online filtering may not improve the overall forecasting accuracy. To assess the filtering problem, the prediction accuracy obtained using online and offline filtering of η are compared.

An additional forecasting strategy is introduced which, having the DMS model structure (as the theoretical optimal predictor DMS$_{\mathsf{SDF}}$), identifies the parameters from a time series by solving a LLS problem. Finally, since in real conditions the data available for identification are imperfect and the sea-state is not perfectly stationary, the relative performance of the different strategies may differ. Therefore, for the analysis of this section both simulated and real wave data is used.

Section 6.2.1 introduces the LRPI identification method for the AR model, the DMS$_{\mathsf{SDF}}$ strategy, the one-step-ahead theoretical prediction accuracy limit, and the forecasting strategy that, with the DMS structure, identifies the parameters from a LLS (termed DMS$_{\mathsf{LLS}}$). The idea of filtering η before using it for prediction is investigated in Section 6.2.2, while the results obtained using simulated and real η data are shown and discussed in Sections 6.2.3 and 6.2.4, respectively.

6.2.1 Prediction strategies

6.2.1.1 LRPI identification strategy

Since, usually, the required prediction horizons are longer than one-step-ahead, an identification method which minimises the n^*_{hor}-step-ahead prediction error may be more pertinent. To this end, the LRPI technique can be applied to identify the forecasting parameters of the AR model (introduced in Section 6.1.1.1). The LRPI identification method is based on minimising the following multi-step ahead cost function

$$J^{\mathsf{AR}}_{\mathsf{LRPI}} = \sum_{j=1}^{n_{\mathsf{hor}}} \sum_{i=n^{\mathsf{AR}}_{\mathsf{ord}}+1}^{n_{\mathsf{tr}}} \left(\eta(i) - \bar{\eta}(i|i-j)\right)^2 . \tag{6.21}$$

Since Equation (6.21) represents a NLS problem, the minimisation problem is computationally more complex than solving Equation (6.4). Thus, the time needed to identify the parameters of AR$_{\mathsf{LRPI}}$ ($\varphi^{\mathsf{AR}}_{\mathsf{LRPI}}$) is significantly longer than the time needed to solve the LLS problem of Equation (6.4) for the coefficients of the AR$_{\mathsf{LLS}}$ strategy ($\varphi^{\mathsf{AR}}_{\mathsf{LLS}}$).

6.2.1.2 DMS model

While the AR model structure uses a single set of parameters (for one-step-ahead prediction), and the multi-step ahead prediction is carried out iteratively, the DMS model has n_{hor} different sets of coefficients, one set for each n^*_{hor}, and, thus, directly predicts the n^*_{hor}-step-ahead η, with no need for iteration. The structure of the DMS predictor is defined as follows:

$$\bar{\eta}(k+n^*_{\mathsf{hor}}|k) = \sum_{i=1}^{n_{\mathsf{ord}}^{\mathsf{DMS}}} \varphi^{\mathsf{DMS}}(n^*_{\mathsf{hor}}, i)\eta(k-i). \tag{6.22}$$

As for the AR model, the parameters of Equation (6.22) can be identified using previous η values. To this end, the identification is carried out by minimising a separate cost function for each n^*_{hor} defined as

$$J_{\mathsf{LLS}}^{\mathsf{DMS}}(n^*_{\mathsf{hor}}) = \sum_{i=n_{\mathsf{ord}}^{\mathsf{DMS}}+1}^{n_{\mathsf{tr}}} \left(\eta(i+n^*_{\mathsf{hor}}) - \bar{\eta}(i+n^*_{\mathsf{hor}}|i)\right)^2 \tag{6.23}$$

which, as in Equation (6.11), is a LLS problem. In fact, the only difference with respect to Equation (6.4) is the vector $\boldsymbol{\eta}^*_{\mathsf{LLS}}$, which is now given by a matrix ($\boldsymbol{\eta}^*_{\mathsf{LLS}} \in \mathbb{R}^{n_{\mathsf{ord}}^{\mathsf{DMS}} \times \left(n_{\mathsf{tr}} - n_{\mathsf{ord}}^{\mathsf{DMS}} - 1\right)}$) defined as

$$\boldsymbol{\eta}^*_{\mathsf{LLS}} = \begin{bmatrix} \eta(n_{\mathsf{ord}}^{\mathsf{DMS}}+1) & \eta(n_{\mathsf{ord}}^{\mathsf{DMS}}+2) & \cdots & \eta(n_{\mathsf{ord}}^{\mathsf{DMS}}+n_{\mathsf{hor}}) \\ \eta(n_{\mathsf{ord}}^{\mathsf{DMS}}+2) & \eta(n_{\mathsf{ord}}^{\mathsf{DMS}}+3) & \cdots & \eta(n_{\mathsf{ord}}^{\mathsf{DMS}}+n_{\mathsf{hor}}+1) \\ \vdots & \vdots & \ddots & \vdots \\ \eta(n_{\mathsf{tr}}-n_{\mathsf{hor}}+1) & \eta(n_{\mathsf{tr}}-n_{\mathsf{hor}}+1) & \cdots & \eta(n_{\mathsf{tr}}) \end{bmatrix}. \tag{6.24}$$

Henceforth, the forecasting strategy, that is based on the DMS structure and identifies the parameters using past η values, is termed $\mathsf{DMS}_{\mathsf{LLS}}$.

6.2.1.3 $\mathsf{DMS}_{\mathsf{SDF}}$ – A theoretically-optimal predictor

As mentioned in Chapter 2, in the vast majority of cases within the power production region of WECs, ocean waves can be described as a Gaussian, zero-mean, linear process, only excluding shallow water conditions (for a more detailed discussion, see Chapter 9 of [126]). Additionally, if a short duration time signal is considered, with respect to the typical time-length in which the sea condition changes (typically 30 minutes to 3 hours), the wave elevation process can be considered stationary [126]. Finally, the wave elevation process is also considered to be ergodic, which means that the statistics of the process, obtained from a time series, are equal to the ensemble statistics [126]. A stationary, ergodic, Gaussian process is fully described by its mean, which is 0 for the case of ocean waves, and its Auto-CoVariance Function (ACVF), which is defined as follows:

$$R_{\eta\eta}(\tau) = \lim_{t\to\infty} \frac{1}{2t} \int_{-t}^{t} \eta(t)\eta(t+\tau)dt. \tag{6.25}$$

One can notice that $R_{\eta\eta}$ only depends on τ, due to the stationarity of the process. Additionally, the maximum of $R_{\eta\eta}(\tau)$ is at $\tau = 0$, where $R_{\eta\eta}(0) = \sigma_\eta^2$, the variance of the process.

The ACVF can be obtained directly from the SDF, since they are a Fourier transform pair, according to the Wiener-Khintchine theorem [31]. Therefore, the statistical properties of a stationary Gaussian sea are fully characterised by its ACVF or, equivalently, by its SDF [115]. By way of example, Figure 6.4 shows (a) a JONSWAP spectrum ($H_\mathsf{s} = 2\,\mathsf{m}$, $T_\mathsf{p} = 10\,\mathsf{s}$ and $\gamma = 3.3$) and (b) its corresponding ACVF.

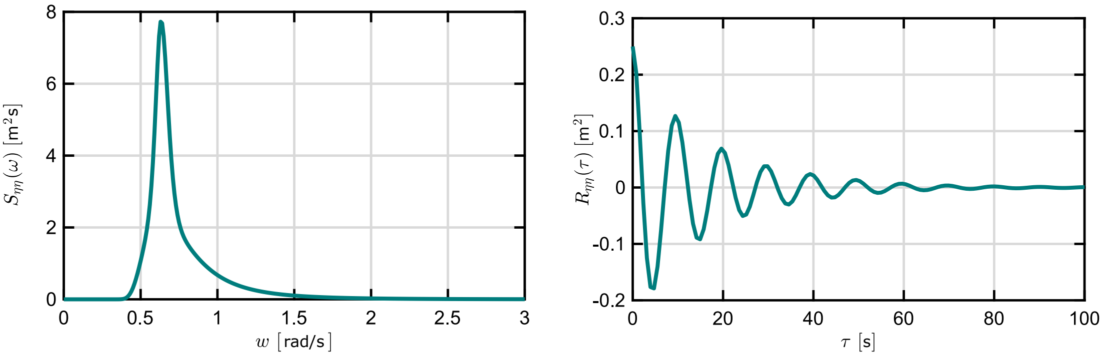

(a) SDF. **(b)** ACVF.

Figure 6.4: Example of (a) a JONSWAP spectrum with $T_\mathsf{p} = 10\,\mathsf{s}$, $H_\mathsf{s} = 2\,\mathsf{m}$ and $\gamma = 3.3$ and (b) its corresponding ACVF.

Once the statistical properties of ocean waves are well-defined, and assuming perfect knowledge of the SDF, it is possible to derive a theoretically-optimal predictor, in a mean-square error sense. Define the sequences of vectors $\boldsymbol{\eta}_\mathsf{ord}(k) \in \mathbb{R}^{n_\mathsf{ord}^\mathsf{DMS}}$ and $\boldsymbol{\eta}_\mathsf{hor}(k) \in \mathbb{R}^{n_\mathsf{hor}}$, which contain, respectively, $n_\mathsf{ord}^\mathsf{DMS}$ past consecutive measurements and n_hor consecutive forecast samples, as

$$\boldsymbol{\eta}_\mathsf{ord}(k) = \begin{bmatrix} \eta(k) \\ \eta(k-1) \\ \vdots \\ \eta(k - n_\mathsf{ord}^\mathsf{DMS} + 1) \end{bmatrix}, \quad \boldsymbol{\eta}_\mathsf{hor}(k) = \begin{bmatrix} \eta(k + n_\mathsf{hor}) \\ \vdots \\ \eta(k+2) \\ \eta(k+1) \end{bmatrix}, \tag{6.26}$$

for any positive integer $k > n_\mathsf{ord}^\mathsf{DMS}$, and let $\boldsymbol{\eta}^*(k) \in \mathbb{R}^{n_\mathsf{ord}^\mathsf{DMS} + n_\mathsf{hor}}$ be a vector containing both $\boldsymbol{\eta}_\mathsf{ord}(k)$ and $\boldsymbol{\eta}_\mathsf{hor}(k)$ as

$$\boldsymbol{\eta}^*(k) = \begin{bmatrix} \boldsymbol{\eta}_\mathsf{ord}(k) \\ \boldsymbol{\eta}_\mathsf{hor}(k) \end{bmatrix}. \tag{6.27}$$

From the definition of a Gaussian process, $\boldsymbol{\eta}^*(k)$ follows a multivariate normal distribution, characterised by its mean, which is 0, and its variance-covariance matrix, $\Sigma_{\eta\eta} \in \mathbb{R}^{(n_\mathsf{ord}^\mathsf{DMS} + n_\mathsf{hor}) \times (n_\mathsf{ord}^\mathsf{DMS} + n_\mathsf{hor})}$, whose components $\Sigma_{\eta\eta_{ij}}$ are defined as:

$$\Sigma_{\eta\eta_{ij}} = \mathbb{E}\left[\eta(k + n_\mathsf{hor} + 1 - i)\eta(k + n_\mathsf{hor} + 1 - j)\right], \tag{6.28}$$

where the operator $\mathbb{E}[\cdot]$ stands for the expected value, and $i, j \in \{1, 2, ..., n_{\text{ord}}^{\text{DMS}} + n_{\text{hor}}\}$. All the diagonal elements of $\Sigma_{\eta\eta_{ij}}$ are equal to the variance of the process (σ_η^2). Defining $r_{\eta\eta}(k) = R_{\eta\eta}(kt_{\text{s}})$, each row of $\Sigma_{\eta\eta}$ is a discretised and time-shifted version of the ACVF (see Equation (6.25)), as

$$\Sigma_{\eta\eta} = \begin{bmatrix} r_{\eta\eta}(0) & r_{\eta\eta}(1) & \cdots & r_{\eta\eta}(n_{\text{ord}}^{\text{DMS}} + n_{\text{hor}} - 1) \\ r_{\eta\eta}(1) & r_{\eta\eta}(0) & \cdots & r_{\eta\eta}(n_{\text{ord}}^{\text{DMS}} + n_{\text{hor}} - 2) \\ \vdots & \vdots & \ddots & \vdots \\ r_{\eta\eta}(n_{\text{ord}}^{\text{DMS}} + n_{\text{hor}} - 1) & r_{\eta\eta}(n_{\text{ord}}^{\text{DMS}} + n_{\text{hor}} - 1) & \cdots & r_{\eta\eta}(0) \end{bmatrix}. \tag{6.29}$$

Splitting $\Sigma_{\eta\eta}$ into past-measurement and forecasting blocks as

$$\Sigma_{\eta\eta} = \begin{bmatrix} \Sigma_{\eta_{\text{hor}}\eta_{\text{hor}}} & \Sigma_{\eta_{\text{hor}}\eta_{\text{ord}}} \\ \Sigma_{\eta_{\text{ord}}\eta_{\text{hor}}} & \Sigma_{\eta_{\text{ord}}\eta_{\text{ord}}} \end{bmatrix}, \tag{6.30}$$

where $\Sigma_{\eta_{\text{hor}}\eta_{\text{hor}}} \in \mathbb{R}^{n_{\text{hor}} \times n_{\text{hor}}}$, $\Sigma_{\eta_{\text{ord}}\eta_{\text{ord}}} \in \mathbb{R}^{n_{\text{ord}}^{\text{DMS}} \times n_{\text{ord}}^{\text{DMS}}}$, $\Sigma_{\eta_{\text{hor}}\eta_{\text{ord}}} \in \mathbb{R}^{n_{\text{hor}} \times n_{\text{ord}}^{\text{DMS}}}$, and $\Sigma_{\eta_{\text{ord}}\eta_{\text{hor}}} \in \mathbb{R}^{n_{\text{ord}}^{\text{DMS}} \times n_{\text{hor}}}$ are defined as

$$\begin{aligned} \Sigma_{\eta_{\text{hor}}\eta_{\text{hor}}} &= \begin{bmatrix} r_{\eta\eta}(0) & \cdots & r_{\eta\eta}(n_{\text{hor}} - 1) \\ \vdots & \ddots & \vdots \\ r_{\eta\eta}(n_{\text{hor}} - 1) & \cdots & r_{\eta\eta}(0) \end{bmatrix}, \\ \Sigma_{\eta_{\text{ord}}\eta_{\text{ord}}} &= \begin{bmatrix} r_{\eta\eta}(0) & \cdots & r_{\eta\eta}(n_{\text{ord}}^{\text{DMS}} - 1) \\ \vdots & \ddots & \vdots \\ r_{\eta\eta}(n_{\text{ord}}^{\text{DMS}} - 1) & \cdots & r_{\eta\eta}(0) \end{bmatrix}, \\ \Sigma_{\eta_{\text{ord}}\eta_{\text{hor}}} = \Sigma_{\eta_{\text{hor}}\eta_{\text{ord}}}^{\mathsf{T}} &= \begin{bmatrix} r_{\eta\eta}(n_{\text{ord}}^{\text{DMS}}) & \cdots & r_{\eta\eta}(n_{\text{ord}}^{\text{DMS}} + n_{\text{hor}} - 1) \\ \vdots & \ddots & \vdots \\ r_{\eta\eta}(1) & \cdots & r_{\eta\eta}(n_{\text{ord}}^{\text{DMS}}) \end{bmatrix}. \end{aligned} \tag{6.31}$$

The conditional distribution of $\boldsymbol{\eta}_{\text{hor}}(k)$ and $\boldsymbol{\eta}_{\text{ord}}(k)$ (from Equation (6.26)), $\eta_{\text{hor}}(k)|\eta_{\text{ord}}(k)$, is a multivariate Gaussian process [39]. Since the mean of $\boldsymbol{\eta}_{\text{hor}}(k)$ and $\boldsymbol{\eta}_{\text{ord}}(k)$ is 0, the mean $\mu_{\eta_{\text{hor}}(k)|\eta_{\text{ord}}(k)}$ and variance $\Sigma_{\eta_{\text{hor}}(k)|\eta_{\text{ord}}(k)}$ are given as follows:

$$\mu_{\eta_{\text{hor}}(k)|\eta_{\text{ord}}(k)} = \Sigma_{\eta_{\text{hor}}\eta_{\text{ord}}} \Sigma_{\eta_{\text{ord}}\eta_{\text{ord}}}^{-1} \boldsymbol{\eta}_{\text{ord}}(k), \tag{6.32a}$$

$$\Sigma_{\eta_{\text{hor}}(k)|\eta_{\text{ord}}(k)} = \Sigma_{\eta_{\text{hor}}\eta_{\text{hor}}} - \Sigma_{\eta_{\text{hor}}\eta_{\text{ord}}} \Sigma_{\eta_{\text{ord}}\eta_{\text{ord}}}^{-1} \Sigma_{\eta_{\text{ord}}\eta_{\text{hor}}}. \tag{6.32b}$$

Furthermore, the best predictor of $\boldsymbol{\eta}_{\text{hor}}$ is given by $\mu_{\eta_{\text{hor}}(k)|\eta_{\text{ord}}(k)}$ as,

$$\bar{\boldsymbol{\eta}}_{\text{hor}}(k) = \mu_{\eta_{\text{hor}}(k)|\eta_{\text{ord}}(k)} = \Sigma_{\eta_{\text{hor}}\eta_{\text{ord}}} \Sigma_{\eta_{\text{ord}}\eta_{\text{ord}}}^{-1} \boldsymbol{\eta}_{\text{ord}}(k) \tag{6.33}$$

and the corresponding mean-square prediction error value, for every prediction horizon from 1 to n_{hor}, is given by the diagonal terms of $\Sigma_{\eta_{\text{hor}}(k)|\eta_{\text{ord}}(k)}$.

Explicitly, the set of optimal parameters $\varphi_{\text{SDF}}^{\text{DMS}} \in \mathbb{R}^{n_{\text{hor}} \times n_{\text{ord}}^{\text{DMS}}}$, which gives the best linear combination of the measurements of the vector $\boldsymbol{\eta}_{\text{ord}}(k)$, is obtained by solving the following system of linear equations

$$\varphi_{\text{SDF}}^{\text{DMS}} = \Sigma_{\eta_{\text{hor}}\eta_{\text{ord}}} \Sigma_{\eta_{\text{ord}}\eta_{\text{ord}}}^{-1}, \tag{6.34}$$

and the model structure is as defined in Equation (6.22).

Given the Gaussian nature of ocean waves, $\mathrm{DMS}_{\mathrm{SDF}}$ can be considered as an upper bound for the prediction accuracy of any linear or nonlinear forecasting method which predicts η by a function of the same set of previous values, provided that Equation (6.34) can be accurately solved.

6.2.1.4 Theoretical 1-step-ahead accuracy limit

If the spectrum of a stationary process is zero up to some frequency f_1, and then, from f_2, zero up to infinity (being non-zero for the complete frequency range $[f_1, f_2]$, with $f_1 < f_2$), the spectrum is defined as Band-Limited (BL) spectrum [132]. For time series generated from BL spectra, there exists a linear predictor whose one-step-ahead prediction error is less than ε for any $\varepsilon > 0$ and, therefore, the prediction error could be made arbitrarily small by increasing the order of the predictor [132]. This is not a reasonable assumption for ocean waves, since they are composed of an infinite number of frequency components and, therefore, are non-Band-Limited (nBL) processes. Furthermore, any realistic wave elevation measurement or estimation method would carry some level of measurement noise. In view of those considerations, it is reasonable to assume that the process, as recorded by a measurement device, would present some degree of unpredictability.

One can notice, from Figure 6.4(a), that the simulated JONSWAP spectral values are zero for low and high frequencies and is, therefore, band-limited (i.e. the one-step-ahead prediction error should tend to zero when increasing the predictor order). In order to make simulations more realistic, an arbitrarily small white-noise component (for example $1 \cdot 10^{-10}$ of amplitude) can be added to the SDF used to generate η. Note that, when spectra are computed from real wave data, no such modification is necessary since the recorded low-frequency spectral content is non-zero.

Provided that the SDF is nBL and that its logarithm is integrable (*Paley-Wiener condition* [132]), the Kolmogoroff-Szego's mean square error formula [132] can provide the theoretical lowest one-step-ahead prediction error, which would be obtained by increasing the predictor order to infinity, as

$$\varepsilon_{\infty}^{2} = e^{2\int_{0}^{\pi} \log \mathsf{SDF}(\omega) d\omega} \tag{6.35}$$

or, equivalently, the one-step-ahead NRMSE formula corresponding to the Kolmogoroff-Szego formula can be derived as

$$\mathsf{NRMSE}_{\mathsf{KS}} = \sqrt{\frac{\varepsilon_{\infty}^{2}}{\sigma_{\eta}^{2}}}. \tag{6.36}$$

Similar to the theoretically optimal predictor, introduced in Section 6.2.1.3, the theoretical one-step-ahead accuracy limit NMSE_{KS} can be considered as an upper bound for the one-step-ahead prediction accuracy. Thus, both accuracy limits are used to characterise the performance of AR models for η prediction and show how different configuration of the AR model affect the obtained prediction accuracy.

6.2.2 Wave signal filtering

It is well known that, if a signal is decomposed into a part containing the low-frequency content and another part containing the high-frequency content, the signal with the higher frequencies is less predictable [160]. Since the low-frequency wave components are the most energetic [125], some studies [131, 67] apply, offline[3], a low-pass filter to the η signal before the prediction process. However, for online filtering, the filtered signal (η_{f}) is delayed with respect to the original signal η [128]. Note that, if a prediction of t_{hor} seconds is required, $t_{\text{hor}} + t_{\text{del}}$ needs to be predicted, where t_{del} refers to the delay time added by the filtering process. Even though the phase distortion added by the filter does not necessarily have to be a pure delay (since the filter delays some frequency components more than others), for this analysis, such distortion is approximated using a pure delay of t_{del} seconds.

t_{del} depends mostly on the cut-off frequency (ω_{c}) and the order of the filter. By way of example, Figure 6.5 shows how η_{f} is delayed with respect to η for (a) different orders of a Butterworth filter and (b) different ω_{c}. The wave elevation time series of this section are generated from a JONSWAP SDF with $H_{\text{s}} = 2\,\text{m}$, $T_{\text{p}} = 10\,\text{s}$ and $\gamma = 3.3$, with a sampling period of $t_{\text{s}} = 1\,\text{s}$.

For the example shown in Figure 6.5(a), η is filtered by using 3rd, 6th and 9th order Butterworth filters with $\omega_{\text{c}} = 1\,{}^{\text{rad}}\!/\!_{\text{s}}$, corresponding to a t_{del} of, approximately, 2.3, 3.9 and 6.2 seconds respectively. Additionally, Figure 6.5(b) illustrates the differences between η and η_{f} using a 6th order Butterworth filter with various ω_{c}. It is clear that the delay added by the filter increases when the order increases or when ω_{c} decreases, i.e. when more high-frequency components are filtered out.

As shown in Figure 6.6(a), the obtained $\text{NRMSE}_{\eta}^{\text{pred}}$ using an AR_{LLS} model, comparing $\bar{\eta}_{\text{f}}(t + t_{\text{hor}}^{*}|t)$ with $\eta_{\text{f}}(t + t_{\text{hor}})$, improves when increasing the order of the filter, since the roll-off rate of the filter increases (i.e. the sharpness of the frequency separation) and, therefore, more high-frequency components are filtered out. This is due to the fact that, as mentioned at the beginning of this section, low-frequency signals are more predictable than high-frequency signals.

---

[3] The main difference between online and offline filtering is that, while online filtering always adds a phase distortion on the filtered signal, there are techniques to avoid such distortion when considering offline filtering.

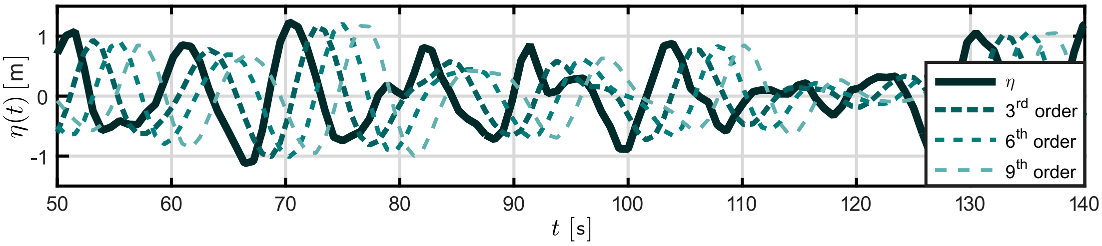

(a) η_f filtered with different order Butterworth filters ($\omega_c = 1$ rad/s).

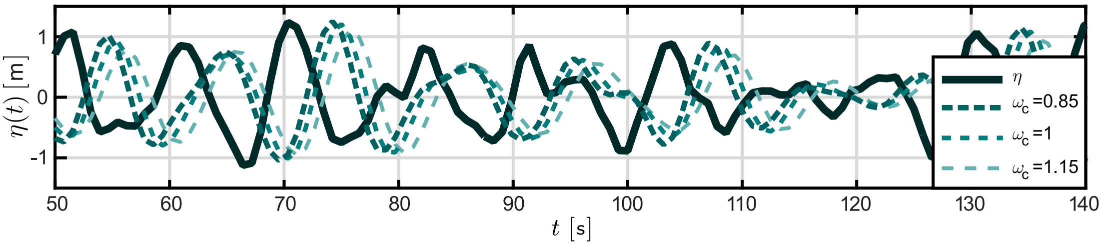

(b) η_f filtered with different cutting frequencies Butterworth filters (6th order filter).

Figure 6.5: Section of η_f using (a) Butterworth filters of 3rd, 6th and 9th orders with $\omega_c = 1$rad/s, and (b) the same section of η_f filtered with a 6th order Butterworth filter with $\omega_c = 0.85$, 1 and 1.15 rad/s.

However, if $\bar{\eta}_f(t + t^*_{hor}|t)$ is compared to $\eta(t + t_{hor})$, as shown in Figure 6.6(b), the obtained $\text{NRMSE}^{\text{pred}}_{\eta}$ decreases with the order of the filter. This can be explained by the fact that, when increasing the order of the filter, the differences between η_f and η increase, as shown before in Figure 6.5(a). Therefore, even though the prediction of η_f is more accurate, since the differences between η_f and η are more significant, the obtained predicted signal looks less like the original, unfiltered η, which increases the prediction error.

Furthermore, Figure 6.6(c) shows the performance of the AR_{LLS} forecasting strategy when using η_f, with the filtering carried out online. It is shown that the NRMSE of the prediction is higher than the NRMSE of the prediction using non-filtered η, which is due to the combination of two effects: firstly, because $\bar{\eta}_f(t + t^*_{hor}|t)$ is compared with $\eta(t + t_{hor})$; and, secondly, the delay introduced by the filter t_{del} is taken into account. The results shown in this subsection clearly illustrate how real-time filtering fails to improve the prediction of the non-filtered η. However, the above considerations do not discard the idea of online filtering within the scope of real-time measurement or estimation of the wave elevation, especially in the presence of measurement noise.

6.2.3 Simulation results

The data sets of the simulated η are 30 minutes long and both the identification of the parameters and the prediction are carried out using a complete (and different)

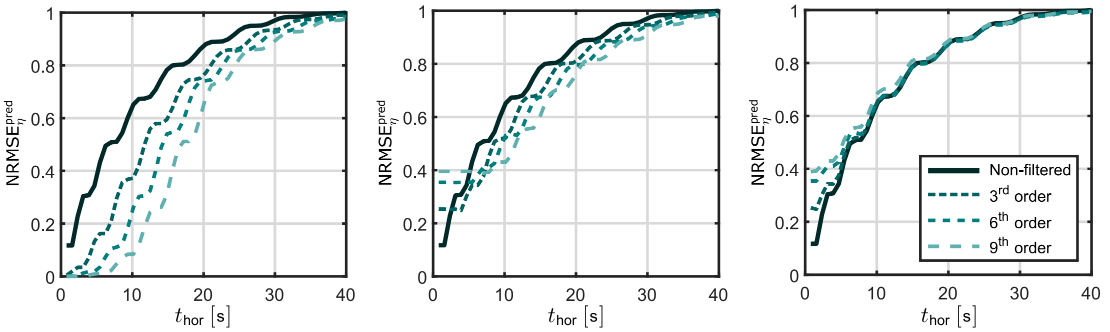

(a) NRMSE$_\eta^{\text{pred}}$ of the predicted η_{f}, compared to η_{f}.

(b) NRMSE$_\eta^{\text{pred}}$ of the predicted η_{f}, compared to η.

(c) NRMSE$_\eta^{\text{pred}}$ of the predicted η_{f}, compared to η, and considering the delay added by the filter.

Figure 6.6: The NRMSE$_\eta^{\text{pred}}$ of the prediction computed with an AR$_{\text{LLS}}$ model ($n_{\text{ord}}^{\text{AR}} = 100$) for filtered η (using Butterworth filters with $\omega_{\text{c}} = 1\,\text{rad/s}$) when comparing the results with (a) η_{f}, (b) η, or (c) with η and considering the added t_{del}.

data-set ($n_{\text{tr}} = 1800$ points). The AR$_{\text{LLS}}$, AR$_{\text{LRPI}}$, and DMS$_{\text{LLS}}$ strategies require that the identification of their prediction coefficients is carried out using a sufficiently large learning data set. Typically, regardless of the method, it is found that, to obtain accurate identification of the forecasting coefficients, the length of the training data should be 15 times the order of the model ($n_{\text{tr}} \approx 15\, n_{\text{ord}}$), and using more learning data points does not lead to any significant improvement of the prediction accuracy. In addition to the NRMSE, a Multi-Step Performance Index (MSPI) is used for this analysis, which takes into account all the prediction horizons considered between 1 and n_{hor}. Therefore, the MSPI provides an overview of the performance achieved by a given forecasting strategy for all time horizons at once. The MSPI is expressed as

$$\text{MSPI} = 1 - \frac{1}{\sigma_\eta^2 n_{\text{hor}}} \sum_{i=1}^{n_{\text{hor}}} \left(\frac{1}{n_{\text{dat}}} \sum_{j=1}^{n_{\text{dat}}} (\eta(j+i) - \bar{\eta}(j+i|j))^2 \right). \tag{6.37}$$

Some authors use correlation as a performance metric to quantify the accuracy of their forecasting strategies [16]. However, since correlation principally represents the phase difference between two signals, the amplitude differences are not reflected in the obtained correlation measure and is, therefore, not used in the current study.

Note that the two performance metrics used in this analysis, NRMSE and MSPI, are based on the root-mean-square error between actual and predicted values of η. Therefore, both NRMSE and MSPI statistically measure the magnitude of the difference between actual and predicted η values, instead of measuring only the difference in amplitude or phase, giving a more realistic measure of the prediction error.

Figure 6.7 illustrates the MSPI obtained for the different prediction strategies. For the analysed predictors, the achieved prediction accuracy increases with the model order, up to a given order, beyond which the MSPI does not improve significantly. The order, beyond which the MSPI improvement is not significant, is similar for all the strategies analysed, as can be seen in Figure 6.7. One can notice that the $\mathrm{DMS}_{\mathrm{SDF}}$ and $\mathrm{DMS}_{\mathrm{LLS}}$ strategies perform identically below $n_{\mathrm{ord}} \approx 80$, and outperform the two AR-model-based strategies. Moreover, for $n_{\mathrm{ord}} > 110$, the $\mathrm{DMS}_{\mathrm{LLS}}$, $\mathrm{AR}_{\mathrm{LLS}}$, and $\mathrm{AR}_{\mathrm{LRPI}}$ strategies achieve the same prediction accuracy, while the $\mathrm{DMS}_{\mathrm{SDF}}$ strategy performs slightly better than the other three.

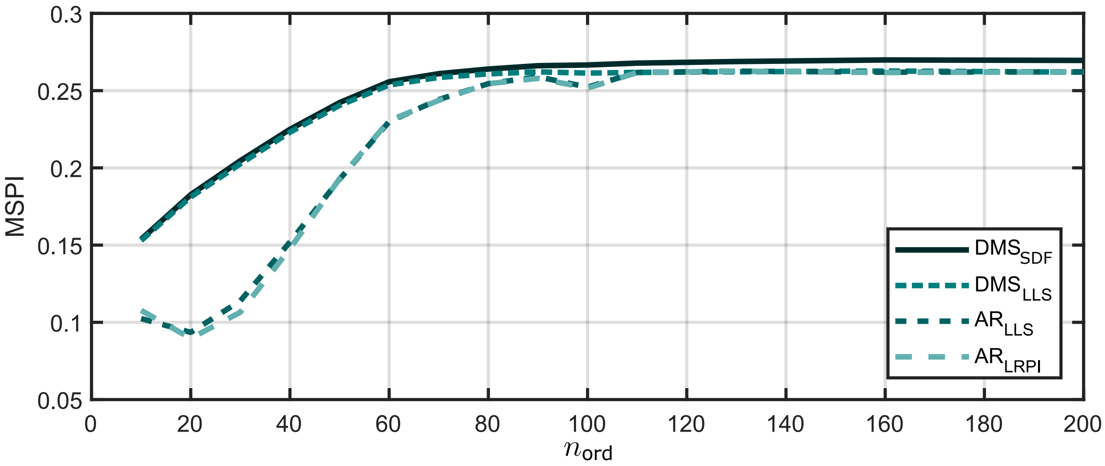

Figure 6.7: The MSPI obtained by the different forecasting methods for different n_{ord}.

In Figure 6.8, the comparison between the forecasting strategies is further exemplified in terms of NRMSE. Figure 6.8(a) shows that, for $n_{\mathrm{ord}} = 50$, the $\mathrm{DMS}_{\mathrm{SDF}}$ and $\mathrm{DMS}_{\mathrm{LLS}}$ strategies perform identically and, again, outperform the $\mathrm{AR}_{\mathrm{LLS}}$ and $\mathrm{AR}_{\mathrm{LRPI}}$ strategies, which achieve the same NRMSE. Note that the difference between the DMS and AR predictors increases with t_{hor}, due to the error accumulated within the iterations, required by AR models to obtain the n_{hor}-step-ahead forecast. Additionally, Figure 6.8(b) shows that, for $n_{\mathrm{ord}} = 150$, all strategies perform virtually identically, although the $\mathrm{DMS}_{\mathrm{SDF}}$ strategy is slightly more accurate. It should further be noted that the $\mathrm{AR}_{\mathrm{LRPI}}$ strategy achieves almost the same results as the $\mathrm{AR}_{\mathrm{LLS}}$, while requiring significantly more time for identification. For example, for $n_{\mathrm{ord}} = 50$, solving the LRPI nonlinear problem is typically around 20 times slower than solving the LLS problem of $\mathrm{AR}_{\mathrm{LLS}}$, and the relative difference increases with the order.

Since, as explained in Section 6.2.1.4, the SDF used for the simulation is a nBL SDF, it is possible to compute the theoretical minimum one-step-ahead NRMSE by using Equation (6.36), and compare it to the one-step-ahead NRMSE obtained by the $\mathrm{DMS}_{\mathrm{SDF}}$, $\mathrm{DMS}_{\mathrm{LLS}}$, $\mathrm{AR}_{\mathrm{LLS}}$, and $\mathrm{AR}_{\mathrm{LRPI}}$ strategies. As shown in Figure 6.9, the four strategies achieve almost identical one-step-ahead NRMSE (identical for the case of $\mathrm{AR}_{\mathrm{LLS}}$ and $\mathrm{DMS}_{\mathrm{LLS}}$). In fact, the difference between the $\mathrm{NRMSE}_{\mathrm{KS}}$ related to the SDF and the one-step-ahead NRMSE achieved by the $\mathrm{DMS}_{\mathrm{SDF}}$, $\mathrm{DMS}_{\mathrm{LLS}}$, $\mathrm{AR}_{\mathrm{LLS}}$, and $\mathrm{AR}_{\mathrm{LRPI}}$ strategies decreases asymptotically when the order increases.

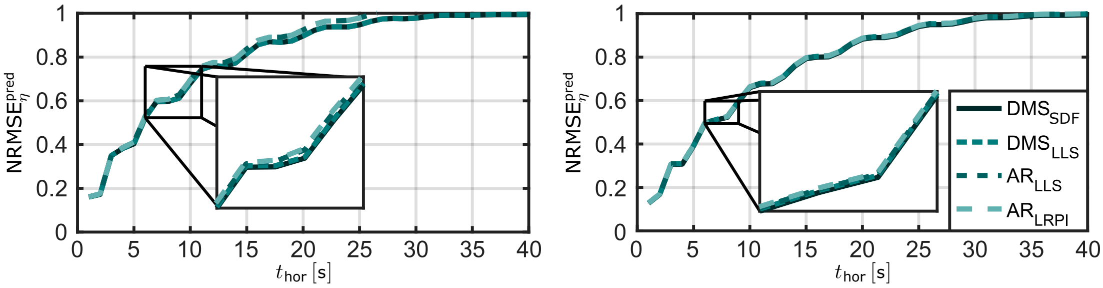

(a) NRMSE$_{\eta}^{\text{pred}}$ for $n_{\text{ord}} = 50$. **(b)** NRMSE$_{\eta}^{\text{pred}}$ for $n_{\text{ord}} = 150$.

Figure 6.8: The NRMSE$_{\eta}^{\text{pred}}$ obtained by the different forecasting strategies with (a) $n_{\text{ord}} = 50$ and (b) $n_{\text{ord}} = 150$.

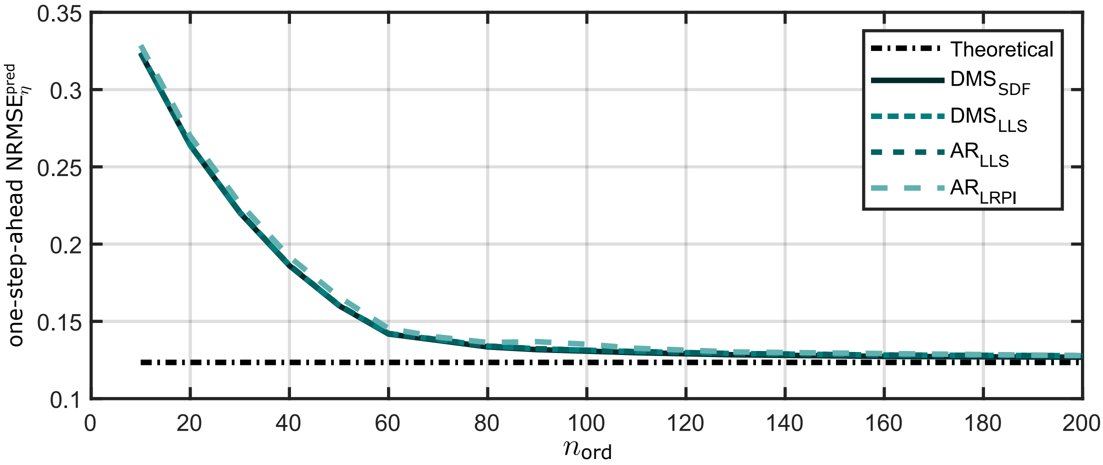

Figure 6.9: The one-step-ahead prediction of the different forecasting strategies for different orders and the theoretical best one-step-ahead prediction associated to the SDF.

6.2.3.1 Use of a band-limited spectrum

The use of a BL simulated spectrum for η generation requires a brief discussion. In this section, as opposed to the previous subsections, no white-noise component is added to the JONSWAP SDF and, therefore, the η time series utilised are BL processes. Figure 6.10(a) shows the one-step-ahead prediction obtained by AR$_{\text{LLS}}$ (or DMS$_{\text{LLS}}$) for different model orders, using wave data generated from both the nBL and BL JONSWAP spectra. It can be seen that, while for the nBL spectrum the minimum one-step-ahead NRMSE is achieved with an order of $n_{\text{ord}} \approx 60$, for a BL spectrum the one-step-ahead NRMSE continues decreasing up to an order of $n_{\text{ord}} \approx 250$.
Additionally, Figure 6.10(b) shows the MSPI obtained by the different strategies, in order to show how their prediction accuracies are affected by the use of a simulated noisy spectrum. The prediction accuracy achieved by the DMS$_{\text{LLS}}$ strategy continues to increase up to orders larger than $n_{\text{ord}} \approx 300$. Additionally, one can notice that the DMS$_{\text{SDF}}$ strategy does not achieve an accuracy as good as the other three strategies while, when using a nBL spectrum, it is always the most accurate. The reason

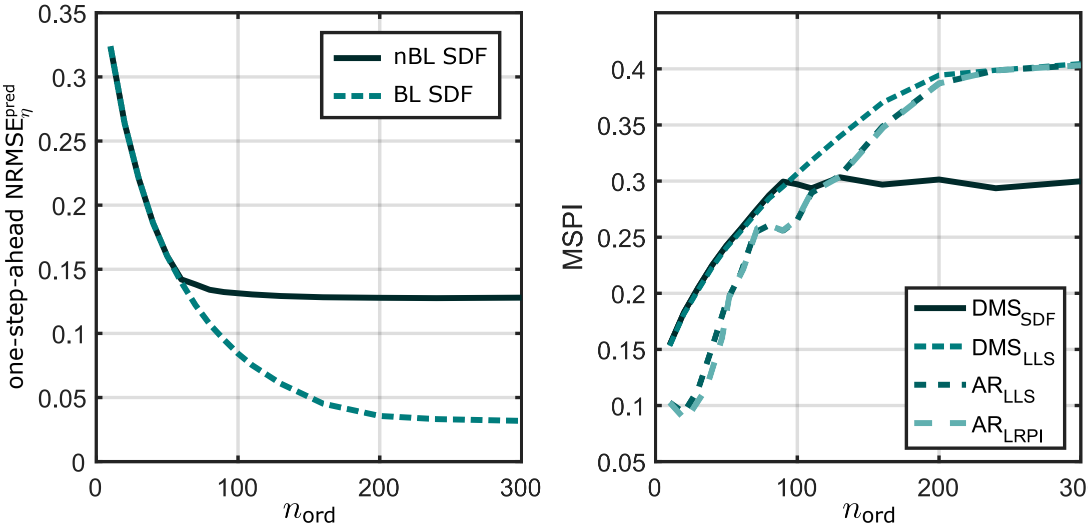

(a) The one-step-ahead NRMSE of the prediction achieved by AR_{LLS} (or DMS_{LLS}) using different orders, when using wave data generated from a nBL or from a BL spectrum.

(b) The MSPI obtained by the different forecasting methods using simulated wave data generated from a BL spectrum.

Figure 6.10: Results obtained for wave data generated from a BL spectrum.

for the increased error in the prediction obtained by DMS_{LLS} is that, when using a nBL spectrum, the result obtained from Equation (6.34), although theoretically consistent with the assumption of stationary Gaussian waves, may be subject to numerical inaccuracies. Indeed, since the process is BL, the SDF used for the calculations is zero for some frequency intervals and, therefore, the covariance matrix in Equation (6.34) is ill-conditioned.

The simulated results obtained from a nBL spectrum depend, to some extent, on the level of white noise added to the JONSWAP formulation. However, as will be shown in Section 6.2.4, the results obtained using real data are closer to those obtained from the nBL spectrum than to those obtained from the BL spectrum.

6.2.4 Results using real wave data

In Section 6.2.3, identification and prediction are performed on different data sets, generated from the same wave spectrum (shown in Figure 6.4(a)), thus, both data sets share identical statistical properties, characterised by the wave spectrum. In such a case, the use of higher-order models always results in a more accurate prediction, because more statistical information from the spectrum can be taken into account. However, real sea wave conditions, and therefore the wave spectrum, vary in time. Hence, the forecasting strategies may be subject to some additional errors, due to the fact that the wave condition evolves, between the η data-set during which the coefficients are identified and the data-set over which the models are used to perform prediction. In particular, high-order models may be more affected by the inherent non-stationarity of ocean waves. Overall, the impact of using real wave data is assessed in this section. The data used in this subsection is representative for Belmullet, Ireland, and has been provided by the Irish Marine Institute [94]. As explained in Section 6.1.2, the η time series have been recorded using a Datawell Waverider [36] data buoy, and each data set is 30-minute long, recorded at a sampling frequency of 1.28Hz. In particular, the results shown in this subsection are for December 2010.

To derive the DMS_{SDF} parameters, it is important to use an appropriate procedure for wave SDF estimation. By considering a 30-min wave signal window, it can be assumed that the sea is purely stationary, i.e. that the wave spectrum does not evolve over time. This 30-min signal carries some statistical characteristics of the underlying wave spectrum, but also has some inherent randomness. Therefore, in theory, to obtain a perfect estimate of the spectrum, an infinitely long record would be necessary. However, if only a 30-min data set is available, applying signal processing techniques, such as windowing and smoothing, can help to separate the effects of the short-term variability from the statistical information specific to the underlying spectrum [147]. For real sea records, it can be considered that the underlying wave spectrum slowly evolves over time, but such an underlying, slowly evolving spectrum must still be distinguished from the effect of short-term randomness. In order to compute the half-hourly SDF, the same procedure as introduced in [36] is used. Each 30-min data set is divided into t_{w}-second overlapping windows, with each section multiplied by a windowing function (such as, for example, a Tukey windowing function), before applying a FFT to obtain a SDF estimate. Then, the half-hourly SDF is computed as the average of the SDFs of all sections. The resulting SDF is smoother when reducing t_{w} (and, consequently, increasing the number of overlapping sections). However, a smaller t_{w} also implies a lower frequency resolution for the SDF ($\omega_{\text{s}} = {}^{2\pi}/_{t_{\text{w}}}$). For this case, it has been found that $t_{\text{w}} = 5\,\text{minutes}$ gives the best estimate of the underlying wave spectrum.

The DMS_{SDF} parameters are derived from the SDF computed in the half-hourly data set previous to the data set where such parameters are used to predict η, so that, overall, only past information is used to forecast η. Similarly, for the strategies whose identification is based on a time series of η, the parameters are identified in the half-hourly data set previous to that used for wave prediction. It should be noted that the results from the AR_{LRPI} strategy are not shown since they are identical to AR_{LLS}, while requiring a computationally expensive identification procedure.

As shown in Figure 6.11, for orders lower than $\text{n}_{\text{ord}} < 60$, the DMS_{SDF} and DMS_{LLS} strategies achieve very similar prediction accuracies, and AR_{LLS} obtains less accurate results. For $\text{n}_{\text{ord}} = 60$ the three methods perform almost identically and, for

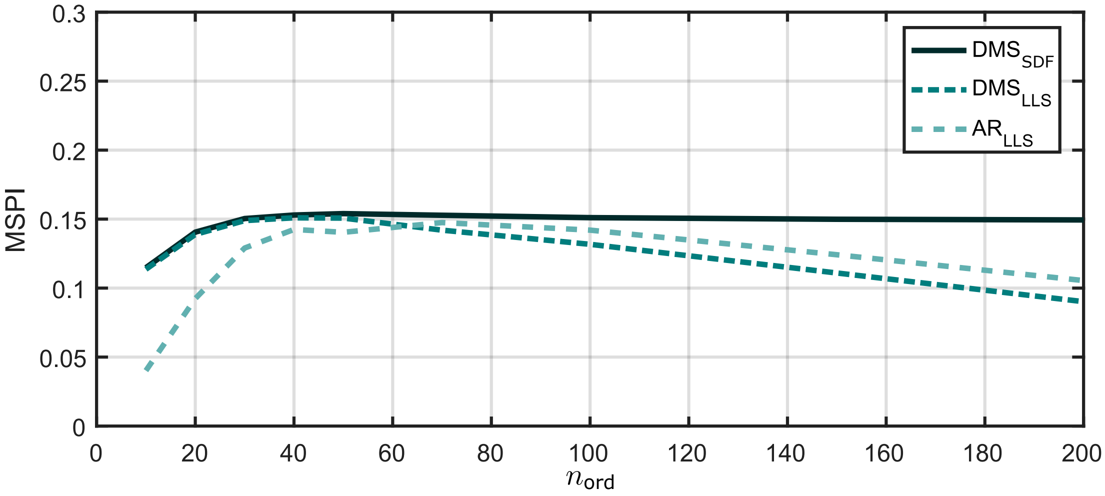

Figure 6.11: The MSPI obtained by the different forecasting methods for different n_{ord} using real η data.

orders larger than $\mathrm{n}_{\mathrm{ord}} > 60$, $\mathrm{DMS}_{\mathrm{Sp}}$ obtains the most accurate results among the three strategies.

For the strategies for which the identification is based on time series ($\mathrm{AR}_{\mathrm{LLS}}$ and $\mathrm{DMS}_{\mathrm{LLS}}$), there is an order n_{ord} beyond which the model seems to 'over learn' statistical information due to the short-term randomness (as opposed to the underlying spectrum), thus decreasing the prediction accuracy. As far as $\mathrm{DMS}_{\mathrm{SDF}}$ is concerned, since the effect of short-term randomness is mitigated by the appropriate SDF computation methodology, the prediction accuracy does not decrease once the maximum accuracy is achieved (see Figure 6.11).

A significant difference between predicting simulated or real waves using a forecasting strategy identified based on previous values of η ($\mathrm{AR}_{\mathrm{LLS}}$ and $\mathrm{DMS}_{\mathrm{LLS}}$) is that, compared to the simulated waves case, the choice of the order of the model n_{ord} can have a greater impact on the prediction performance for the case where real waves are used. In particular, for simulated waves, the performance is similar for any chosen order higher than the 'optimal' order ($n_{\mathrm{ord}}^{\mathrm{opt}}$) which, for the simulated waves in the previous section is $n_{\mathrm{ord}}^{\mathrm{opt}} \approx 80$ (as shown in Figure 6.7). However, when using real waves, the performance decreases if the chosen n_{ord} is greater than the 'optimal' order, in this case $n_{\mathrm{ord}}^{\mathrm{opt}} \approx 40$ (see Figure 6.11).

Overall, one can notice that the predictions obtained using real data are significantly less accurate than those achieved using simulated data, which may be due to several reasons:

- The sea-state is non-stationary, which implies that the statistical characterisation, learned in one given data set by any model is, in general, not the same in the next data set.

- The SDFs of real wave data have significantly more high-frequency content than idealised sea-states, such as JONSWAP spectra (see the difference between the SDF of Figure 6.4(a) and Figures 6.12(a-c)).
- Finally, real wave data may be subject to measurement noise, which influences the frequency content of the signal.

To assess the relative importance of the above factors in the performance of the predictors, the following comparison is performed and illustrated in Figure 6.12. For three different real-data sea states (shown in Figures 6.12(a-c)), the empirical NRMSE achieved by $\mathrm{DMS_{SDF}}$, identified using the SDF from the previous half-hourly data set, is compared to the theoretical best NRMSE, associated to the SDF of the data set where the prediction is carried out (using Equation (6.32b)), which is shown in Figures 6.12(d-f). In other words, the solid curve indicates how the optimal predictor would perform, assuming perfect knowledge of the underlying spectrum. It can be observed that the difference between the two NRMSEs is minimal, thus suggesting that the difference between simulated and actual prediction performances is mainly induced by the fact that real wave spectra have more high-frequency content, rather than resulting from the non-stationarity of wave conditions.

Although the considered data is from a single location, the results obtained for real sea states confirm the results obtained for simulated data, since all the strategies perform similarly and, in particular, the results obtained using the AR model are as accurate as those obtained with the theoretically optimal predictor.

6.3 Conclusions

From the comparison between AR and ARMA models, generally, it is fair to say that both models achieve similar performance, which is not surprising due to the fact that the ARMA model is a sum of an AR model and a noise which is estimated using another AR model [24]. Therefore, the conclusion presented in [67], stating that, for wave energy applications, ARMA models do not provide any improvement on η prediction compared to AR models, is confirmed.

It is demonstrated that the spectra used to generate simulated η time series should be nBL, in order to avoid unreasonably optimistic prediction results.

Considering the results obtained by the $\mathrm{DMS_{SDF}}$ strategy as an upper bound for the achievable prediction accuracy (provided that the method is free of numerical issues), the $\mathrm{DMS_{LLS}}$, $\mathrm{AR_{LLS}}$, and $\mathrm{AR_{LRPI}}$ strategies yield results close to the best achievable prediction, if their parameters are correctly identified. From this point of view, all strategies studied here seem to be suitable tools for short-term wave forecasting.

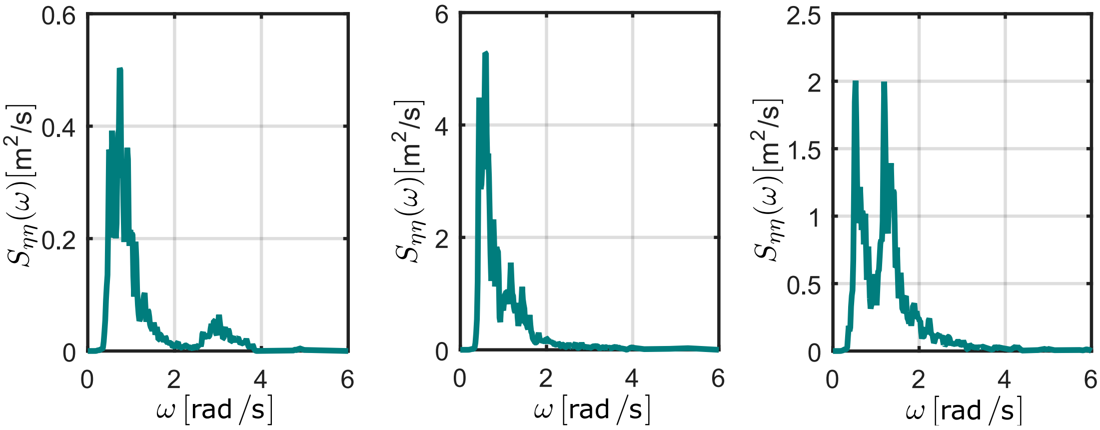

(a) Half-hourly SDF computed from real wave data ($S^1_{\eta\eta}$).

(b) Half-hourly SDF computed from real wave data ($S^2_{\eta\eta}$).

(c) Half-hourly SDF computed from real wave data ($S^3_{\eta\eta}$).

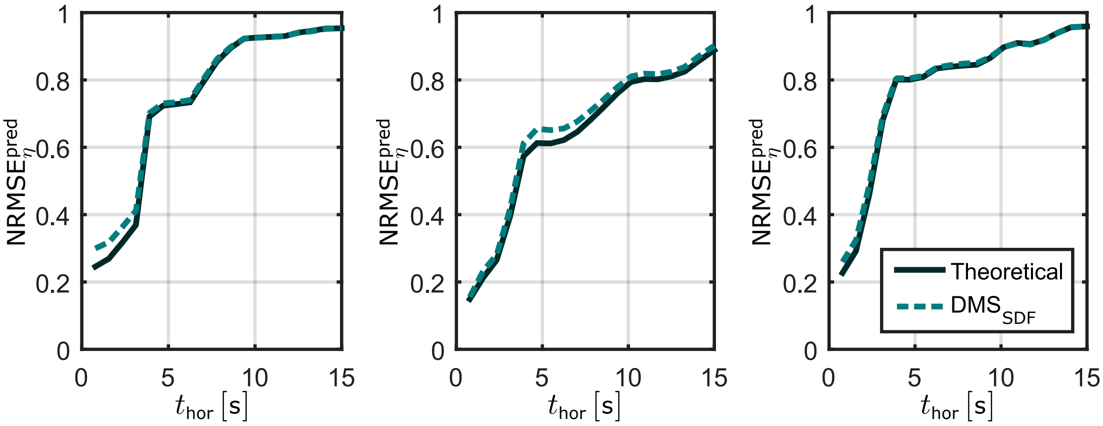

(d) NRMSE obtained for $S^1_{\eta\eta}$. **(e)** NRMSE obtained for $S^2_{\eta\eta}$. **(f)** NRMSE obtained for $S^3_{\eta\eta}$.

Figure 6.12: (a-c) Three different half hourly SDFs, and (d-f) the NRMSE of the prediction achieved by DMS$_{\mathrm{SDF}}$ and the theoretical best NRMSE.

In particular, the AR$_{\mathrm{LLS}}$ strategy and its multi-step analogous, the DMS$_{\mathrm{LLS}}$, are particularly simple and are not significantly outperformed by DMS$_{\mathrm{SDF}}$ representing, thus, convenient forecasting strategies for η or f_{e} prediction. Regarding computational requirements, even though all methods compute η prediction relatively fast (2-3 orders of magnitude below real time), the identification process of the AR$_{\mathrm{LRPI}}$ strategy is computationally more expensive than for the other strategies analysed.

It should be noted that, even the best achievable predictions remain relatively inaccurate, with a NRMSE higher than 50% for one wave period ahead in the favourable case of simulated data, and 80% in real sea-states. Such high values are in contrast to the results of [67, 131] (which obtain 0-10% of error for predictions of more than one wave period ahead), suggesting that the accuracies obtained from data, filtered offline, are unreasonably optimistic. Based on simple numerical examples, it is demonstrated in this chapter that the use of online filtered wave elevation data for the prediction always leads to inferior results compared to non-filtered wave elevation data. This can be explained by the fact that any realisable online filter is necessarily causal and, therefore, consists of some (usually linear) function of the previous measurements. Indeed, the use of a filter, combined with an AR model, simply results in some other function of the past values, which is then necessarily sub-optimal with respect to DMS_{SDF} (provided that the same set of previous measurements is used and that DMS_{SDF} avoids numerical inaccuracies). In view of the results shown in Section 6.2.3, showing the performance of the DMS_{SDF} strategy, it should not be possible to obtain results as favourable as in Figure 6.6(a), when using an online filter. Therefore, more accurate predictions may require the use of several measurement points in the vicinity of the WEC [115].

7

Estimation and forecasting for WEC arrays

Contents

As mentioned in Section 2.2.6, commercial WECs are likely to be deployed in arrays, in order to minimise total infrastructural and operational costs [159]. Similarly to the WEC array control problem [13], the estimation and forecasting problem for arrays can either be considered from an independent device perspective, where each device has no knowledge of the other devices (distributed or independent control/estimation/forecasting) or from a coordinated, or global, perspective, where the global controller/estimator/forecaster has complete knowledge of the motion of all the devices in the array.

Compared to the isolated WEC case (i.e. an 'array' of just a single device), the wave field for multiple devices in an array is significantly more complex, due to the

diffraction of the incident waves by each device and the waves which are radiated by each device, by virtue of their motion. A question exists as to whether the increase in information available for the full array is sufficient to counteract this increased wave field complexity for the estimation and forecasting problems. To this end, an estimation and forecasting model, with the ability to utilise the full set of WEC device motion available in the array, is designed in this chapter, and compared to the estimation/forecasting model utilising only motion measurements from a single device. For the control case, several studies (e.g. [13]) demonstrate that global array control always outperforms independent control.
The analysed array configurations are introduced in Section 7.1, while Section 7.2 describes the chosen f_e estimation and forecasting strategies. Section 7.3 shows the obtained results and, finally, in Section 7.4, some conclusions are drawn.

7.1 Arrays configurations

In this chapter, four different array layouts, shown in Figure 7.1, are examined. In addition, three different wave directions β_η and 18 different inter-device distances d_b are considered for each layout. The examined arrays comprise a set of cylindrical bodies, and all devices are assumed to be identical, with a diameter of 10 m, a draft of 10 m, and a mass of $m = 7.9 \cdot 10^5$ kg, representing a full-size scale case. In addition, it is assumed that each device is limited to heave-only motion.

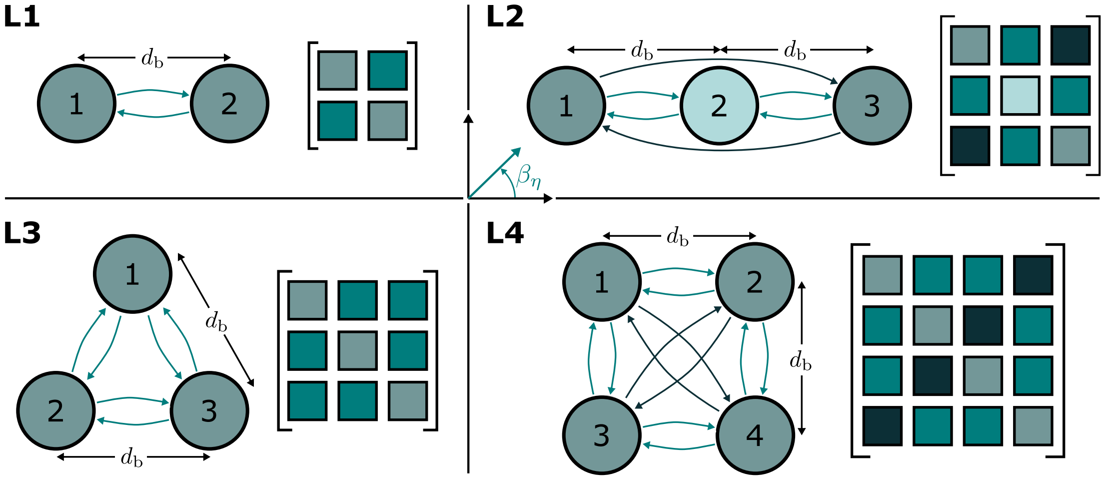

Figure 7.1: The different array layouts considered for the analysis.

The colour boxes to the right of each layout in Figure 7.1 show the symmetries of the transfer function matrices (defined as shown in Equation (2.44)) of the MIMO systems. By way of example, for the simplest layout, **L1**, since the geometry of the two bodies is the same, so are the inner dynamics of each device (the diagonal terms of the transfer matrix); furthermore, for the same reason, the interactions from body 1 to body 2, and vice-versa, are also identical (cross-coupling terms of the transfer matrix are symmetric).

Note that the dynamics of the devices of the array do not vary with the wave direction β_η, since they only depend on the geometry of the devices and the layout of the array, rather than the incident wave field. The wave direction, along with the diffraction effects on the different devices, is included in the excitation force frequency-domain parameter $\hat{F}_\mathsf{e}(\omega)$. As an example, Figure 7.2 shows how the $\hat{F}_\mathsf{e}(\omega)$ coefficients change, for **L2**[1] with inter-device distance $d_\mathsf{b} = 20\,\text{m}$, for different wave directions. For this array layout, when $\beta_\eta = 90°$, following the convention of the wave direction β_η shown in Figure 7.1, the incoming wave affects the three bodies at the same time. Therefore, as shown in Figure 7.2(b), both magnitude and phase of the excitation force for the three devices is similar to the magnitude and phase of the isolated body.

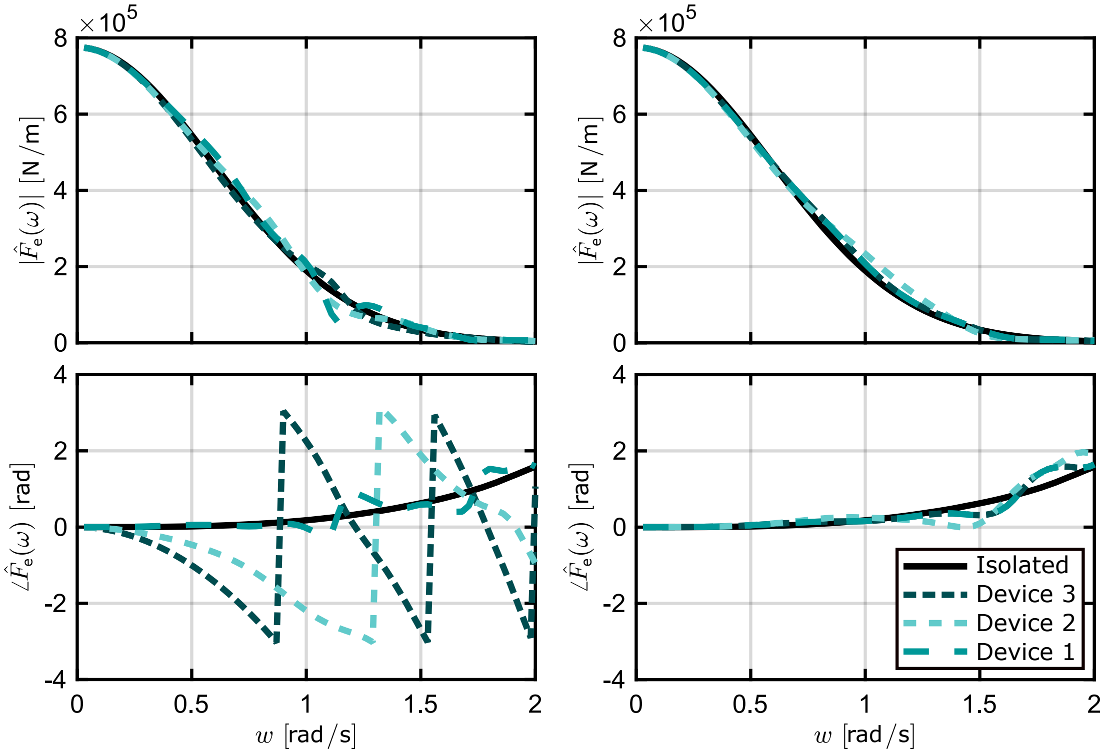

(a) $\hat{F}_\mathsf{e}(\omega)$ coefficients for $\beta_\eta = 0°$. **(b)** $\hat{F}_\mathsf{e}(\omega)$ coefficients for $\beta_\eta = 90°$.

Figure 7.2: Magnitude and phase of the excitation force coefficients for the different bodies of **L2** (with $d_\mathsf{b} = 20\,\text{m}$), for (a) $\beta_\eta = 0°$ and (b) $\beta_\eta = 90°$, along with the coefficients for the isolated WEC case.

In contrast, for $\beta_\eta = 0°$, two different effects can be observed in Figure 7.2(a). First, the magnitude of $\hat{F}_\mathsf{e}$ for Device 1 is the most disturbed one between the three devices,

---

[1] Note that **L2** is shown in Figure 7.2 since, due to its geometry, it adequately shows the effect of the wave direction on the excitation force coefficients $\hat{F}_\mathsf{e}(\omega)$.

which is due to the waves diffracted from Devices 2 and 3, and Device 3 is the most similar to the $\hat{F}_\text{e}$ magnitude of the isolated device. Note that the differences between the $\hat{F}_\text{e}$ magnitude for Device 3 and the isolated body are (mainly) due to the shadowing effect from the previous devices [17]. Secondly, by looking at the phases of the different devices in Figure 7.2(a), it can be seen that Device 1 and the isolated device have similar phases (since the isolated body is located at the location of Device 1), while the phase of Devices 2 and 3 tend to negative angles. This is because the excitation force of the three devices is computed from the same η signal (using the convolution calculation shown in Equation (2.37)) and, therefore, the different phases of $\hat{F}_\text{e}$ add the time delays on the f_e signals associated with the location of the devices, i.e. a phase delay is added to the f_e signal of Device 1 (which is the same as the isolated device) to obtain the f_e acting on Devices 2 and 3.

It should be noted that, for some coupling terms, the hydrodynamic coefficients are expected to be equal. For example, the excitation force coefficients of the two bodies in **L1**, with $\beta_\eta = 90°$, or some of the $A_\text{r}(\omega)$ coefficients of **L3** for any β_η, etc. However, in practice, the coefficients obtained from BEM solvers, like NEMOH or WAMIT, are not exactly the same. Those small differences between the coefficients of the model may be magnified during simulation, estimation, and forecasting, resulting in a disparity of up to 10% between the forecasting NRMSE of devices whose NRMSE would be expected to be identical, due to symmetry. In this chapter, that issue is addressed by equalizing the values of the coefficients that should be equal, from symmetric considerations.

7.2 Excitation force estimation and forecasting

For each of the analysed cases, two alternative estimation and forecasting models are tested, both global (using all the available measurements) and independent (where the f_e estimate/forecast for a WEC depends only on the motion information local to the specific WEC). For the independent estimator, no information from radiated or diffracted waves from other devices is explicitly taken into account, and each device cannot distinguish between such waves and the incident (far field) waves. With regard to the forecasting models, the independent model only takes into account past f_e values of one device to forecast the future f_e acting on that specific body. In contrast, the global forecasting model uses past f_e values of all the bodies of the array to forecast the f_e acting on a given device.

7.2.1 Global and independent estimation

The f_{e} estimation strategy selected for this analysis is the KFHO scheme since, as shown in the comparison of Section 5.1, this strategy is one of the most accurate and simple estimation approaches available for wave energy applications. The main difference between the independent and the global estimator analysed in this chapter is the model used to describe the WEC array and the f_{e} dynamics within the KF. On the one hand, the independent estimator utilises a different KFHO estimator for each body of the array (i.e. n_{b} different estimators, with n_{b} bodies in the array), defined as explained in Section 5.1.1.3, and using a SS model describing the single-DoF WEC shown in System (2.41).

On the other hand, for the global estimator, even though the KF process is as introduced in Section 5.1.1.3, the description of the model and the dynamical model of the f_{e} differs. In order to compare the independent and global estimator under similar conditions, the array SS model of the global estimator is defined as a set of multi-SISO SS systems, as opposed to directly identifying the complete MIMO array system using moment matching which, as shown in Section 4.3, provides a lower order representations of the array. By using the multi-SISO approach, the same SISO models used to define the models of the independent estimator can be used and, therefore, minimise the effect that the used model has on the final results. However, a brief analysis showing the advantages of using the MIMO models, identified using the moment-matching identification approach for the global estimator, is shown in Section 7.3.3. Note that the order of the SS model used to approximate the different radiation subsystems is $n_{\mathsf{r}} = 4$, obtaining final MIMO array systems of order ($n_{\mathsf{ss}}^{\mathsf{array}} = 2n_{\mathsf{b}} + n_{\mathsf{r}}n_{\mathsf{b}}^2$) 20, 42, and 72 for the cases of 2, 3, and 4 devices, respectively. For the HO describing the excitation force of the global estimator, the following changes have to be made to the matrices shown in Equation (5.7):

$$
\begin{aligned}
\Omega^{\mathsf{HO}} &= \mathbb{I}_{n_{\mathsf{b}}} \otimes \bigoplus_{i=1}^{n_\omega} \begin{bmatrix} 0 & \omega_i \\ -\omega_i & 0 \end{bmatrix}, \\
\Theta(k) &= \sum_{j=1}^{n_{\mathsf{b}}} \mathbb{e}_j^{n_{\mathsf{b}}} \otimes \left(\sum_{i=1}^{n_\omega} \mathbb{e}_i^{n_\omega} \otimes \begin{bmatrix} f_{e_{j\omega_i}}^{\mathsf{KFHO}}(k) \\ \dot{f}_{e_{j\omega_i}}^{\mathsf{KFHO}}(k) \end{bmatrix} \right).
\end{aligned}
\tag{7.1}
$$

Here, $f_{e_{j\omega_i}}^{\mathsf{KFHO}}$ are the different components of the HO describing the excitation force of the device j, and C^{HO} is now defined as $C^{\mathsf{HO}} = \mathbb{1}_{1,n_\omega n_{\mathsf{b}}} \otimes \begin{bmatrix} 1 & 0 \end{bmatrix}$.

7.2.2 Global and independent forecasting

For the f_{e} prediction, the AR model is used since, as shown in Chapter 6, it is simple and (if correctly identified) yield prediction accuracies close to those obtained by the theoretically optimal predictor. The independent estimator is, basically, the AR$_{\mathsf{LLS}}$ model introduced in Section 6.1.1.1, but operating on f_{e} instead of η. Note that the LLS is dropped in this chapter, since no identification method, other than LLS, is employed.

For the global predictor, a variation of the AR model is used, termed autoregressive with exogenous variable, or ARX, model in the literature [27]. The ARX predictor not only uses past f_{e} estimated values from the device under analysis, but also the f_{e} estimated by the other devices as 'external' inputs. Thus, the ARX model assumes that f_{e} is defined as

$$f_{\mathsf{e}_{\mathsf{b}*}}(k) = \sum_{i=1}^{n_{\mathsf{ord}}^{\mathsf{ARx}}} \varphi^{\mathsf{ARX}_{\mathsf{b}*}^{\mathsf{b}^*}}(i) f_{\mathsf{e}_{\mathsf{b}*}}(k-i) + \sum_{\substack{j=1 \\ j \neq \mathsf{b}^*}}^{n_{\mathsf{b}}} \sum_{i_2=1}^{n_{\mathsf{ord}}^{\mathsf{arX}}} \varphi^{\mathsf{ARX}_{\mathsf{b}*}^{j}}(i_2) f_{\mathsf{e}_j}(k-i_2) + \epsilon(k), \tag{7.2}$$

where $f_{\mathsf{e}_{\mathsf{b}*}}(k) \in \mathbb{R}$ is the excitation force of the body b*, with b$^* = \{1, ..., n_{\mathsf{b}}\}$, and $\varphi^{\mathsf{ARX}_{\mathsf{b}*}^{j}}$ are the regression coefficients of body b* for the past values of body j. In Equation (7.2), $n_{\mathsf{ord}}^{\mathsf{ARx}}$ and $n_{\mathsf{ord}}^{\mathsf{arX}}$ refer to the number of past values considered of the device under analysis (the order of the autoregressive part) and for the other devices (the order of the exogenous input part), respectively.

The coefficients of the ARX for the body i can be identified by solving a set of n_{b} LLS problems, described by the matrix product

$$\varphi_i^{\mathsf{ARX}} = \left(\boldsymbol{f}_{\mathbf{e}_i}^{\mathsf{ARX}^{\mathsf{T}}} \boldsymbol{f}_{\mathbf{e}_i}^{\mathsf{ARX}}\right)^{-1} \left(\boldsymbol{f}_{\mathbf{e}_i}^{\mathsf{ARX}^{\mathsf{T}}} \boldsymbol{f}_{\mathbf{e}_i}^{\star}\right), \tag{7.3}$$

where $\boldsymbol{f}_{\mathbf{e}_i}^{\star} \in \mathbb{R}^{(n_{\mathsf{tr}} - n_{\mathsf{max}}^{\mathsf{ARX}} - 1)}$, with $n_{\mathsf{max}}^{\mathsf{ARX}} = \max\{n_{\mathsf{ord}}^{\mathsf{ARx}}, n_{\mathsf{ord}}^{\mathsf{arX}}\}$, is a vector containing the $f_{\mathsf{e}}(k)$ values of body i from $k = n_{\mathsf{max}}^{\mathsf{ARX}} + 1$ to n_{tr}, and the matrix $\boldsymbol{f}_{\mathbf{e}_i}^{\mathsf{ARX}} \in \mathbb{R}^{(n_{\mathsf{tr}} - n_{\mathsf{max}}^{\mathsf{ARX}} - 1) \times (n_{\mathsf{ord}}^{\mathsf{ARx}} + (n_{\mathsf{b}} - 1) n_{\mathsf{ord}}^{\mathsf{arX}})}$ is defined as follows:

$$\boldsymbol{f}_{\mathbf{e}_i}^{\mathsf{ARX}} = \left[\boldsymbol{f}_{\mathbf{e}_i}^{\mathsf{ARx}} \quad \boldsymbol{f}_{\mathbf{e}_{(i-1+\alpha_{\mathsf{b}})}}^{\mathsf{arX}} \quad \cdots \quad \boldsymbol{f}_{\mathbf{e}_{(i-(n_{\mathsf{b}}-1)+\alpha_{\mathsf{b}})}}^{\mathsf{arX}}\right], \tag{7.4}$$

where

$$\boldsymbol{f}_{\mathbf{e}_i}^{\mathsf{ARx}} = \begin{bmatrix} f_{\mathsf{e}_i}(n_{\mathsf{max}}^{\mathsf{ARX}}) & \cdots & f_{\mathsf{e}_i}(n_{\mathsf{max}}^{\mathsf{ARX}} - n_{\mathsf{ord}}^{\mathsf{ARx}}) \\ f_{\mathsf{e}_i}(n_{\mathsf{max}}^{\mathsf{ARX}} + 1) & \cdots & f_{\mathsf{e}_i}(n_{\mathsf{max}}^{\mathsf{ARX}} - n_{\mathsf{ord}}^{\mathsf{ARx}} + 1) \\ \vdots & \ddots & \vdots \\ f_{\mathsf{e}_i}(n_{\mathsf{tr}} - 1) & \cdots & f_{\mathsf{e}_i}(n_{\mathsf{tr}} - n_{\mathsf{ord}}^{\mathsf{ARx}}) \end{bmatrix}, \tag{7.5}$$

$$\boldsymbol{f}_{\mathbf{e}_i}^{\mathsf{arX}} = \begin{bmatrix} f_{\mathsf{e}_i}(n_{\mathsf{max}}^{\mathsf{ARX}}) & \cdots & f_{\mathsf{e}_i}(n_{\mathsf{max}}^{\mathsf{ARX}} - n_{\mathsf{ord}}^{\mathsf{arX}}) \\ f_{\mathsf{e}_i}(n_{\mathsf{max}}^{\mathsf{ARX}} + 1) & \cdots & f_{\mathsf{e}_i}(n_{\mathsf{max}}^{\mathsf{ARX}} - n_{\mathsf{ord}}^{\mathsf{arX}} + 1) \\ \vdots & \ddots & \vdots \\ f_{\mathsf{e}_i}(n_{\mathsf{tr}} - 1) & \cdots & f_{\mathsf{e}_i}(n_{\mathsf{tr}} - n_{\mathsf{ord}}^{\mathsf{arX}}) \end{bmatrix}. \tag{7.6}$$

In Equation (7.4), for the subindices defined as $i-j+\alpha_{\mathsf{b}}$, α_{b} is defined as

$$\alpha_{\mathsf{b}} = \begin{cases} 0 & \text{if} \qquad i-j>0, \\ n_{\mathsf{b}} & \text{if} \qquad i-j \leq 0, \end{cases} \tag{7.7}$$

which ensures that, regardless of the value of i, the excitation force from all the devices is included in the matrix $\boldsymbol{f}_{\mathbf{e}_i}^{\mathsf{ARX}}$.

7.3 Results

It should be noted that the order of the estimator/predictor could be optimised for each case, which would improve the results presented in this section. However, it is appealing, from comparison purposes, to keep such estimator/predictor orders constant for every case analysed (selected as explained in Sections 7.3.1 and 7.3.2 for the estimator and predictor, respectively). Additionally, for estimation, instead of showing the NRMSE obtained by the different estimation techniques, the Relative Error (RE) is shown, which relates the results obtained within the WEC to the results obtained for the isolated WEC case as:

$$\mathsf{RE}_i = \frac{\mathsf{NRMSE}_i^{\mathsf{array}}}{\mathsf{NRMSE}^{\mathsf{isol}}}, \tag{7.8}$$

where $\mathsf{NRMSE}_i^{\mathsf{array}}$ refers to the estimation NRMSE obtained for device i and $\mathsf{NRMSE}^{\mathsf{isol}}$ to the comparable estimation NRMSE obtained for the isolated WEC case.

The η time series are generated from a JONSWAP SDF with $H_{\mathsf{s}} = 1.5\,\mathrm{m}$, $T_{\mathsf{p}} = 8\,\mathrm{s}$, and $\gamma = 3.3$. Each time series consists of 450 s, with $t_{\mathsf{s}} = 0.01\,\mathrm{s}$. In order to obtain meaningful results, it is found that the average of 35 simulations is necessary (according to the central limit theorem [28]). The coefficients of the predictors are identified during the first 150 s of the simulation, which is one third of the total length (450 s). The prediction is carried out over the remaining 300 s.

It should be noted that, for the graphs showing results as a function of the inter-device distance d_{b}, such distances are shown using integer multiples of the device diameter $\varnothing_{\mathsf{b}}$. Finally, in order to simulate the electrical noise on the real motion measurement sensors, the position and velocity measurements of the devices are artificially polluted with white noise, with standard deviations of 0.02 m and 0.08 m/s, respectively.

7.3.1 Estimation results

As shown in Section 5.1.1.3, the accuracy of the estimator increases with the number of frequencies considered in the HO model describing f_{e}. As shown in Figure 7.3(a), for this case, the $\mathsf{NRMSE}_{f_{\mathsf{e}}}^{\mathsf{est}}$ improvement, when considering more than 7 frequencies, is not

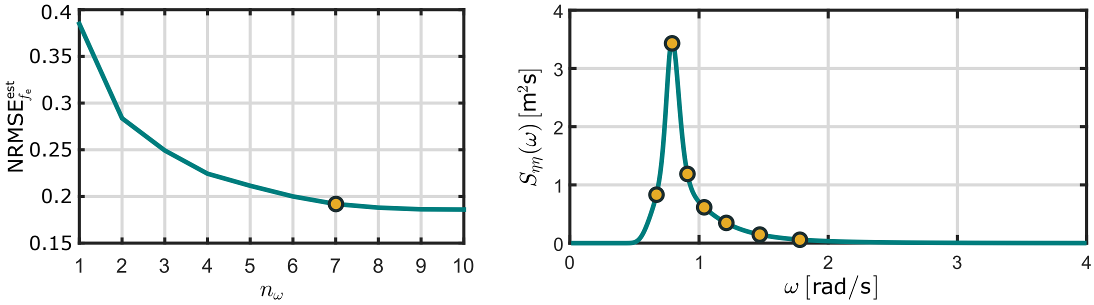

(a) $\mathrm{NRMSE}^{\mathrm{est}}_{f_\mathrm{e}}$ for different n_ω considered in the HO model, where the orange dot represents the selected order.

(b) JONSWAP SDF, with $H_\mathrm{s} = 1.5\,\mathrm{m}$, $T_\mathrm{p} = 8\,\mathrm{s}$, and $\gamma = 3.3$, along with the frequencies chosen for the HO of the KFHO (orange dots).

Figure 7.3: (a) The variation of the $\mathrm{NRMSE}^{\mathrm{est}}_{f_\mathrm{e}}$ for different n_ω, and (b) the JONSWAP SDF considered to generate η with the frequencies of the HO ($n_\omega = 7$).

significant. Therefore, for this case, seven frequencies are used, which are chosen evenly spaced and include the peak frequency of the sea state, as shown in Figure 7.3(b). Note that the results shown in Figure 7.3(a) are obtained for the isolated WEC case. For the array case, such results could be improved by optimising both the number of frequencies and their value for each array layout, separation distance d_b, and wave direction β_η. However, it is appealing to use the same HO configuration for all the cases of this comparison and, therefore, $n_\omega = 7$ is the order chosen for both global or independent estimators with the frequency values shown in Figure 7.3(b).

Figure 7.4 shows the RE on the estimation obtained using the global and independent estimators for the four layouts in Figure 7.1, averaged over the three wave directions[2]. Note that the RE values, shown in Figure 7.4, represent the values of the RE averaged over the different devices of the array. As the distance between devices increases, the power density of the radiated and diffracted waves decreases, reducing the magnitude of the interactions. Therefore, as shown in Figure 7.4, the global and independent estimator accuracies converge towards that achieved in the isolated body case, i.e. $\lim_{d_\mathrm{b}\to\infty}\mathrm{RE} = 1$. Figure 7.4 also shows that, overall, the magnitude of the interaction increases for a larger number of bodies in the array, which decreases the performance of the independent estimator, increasing the obtained $\mathrm{NRMSE}^{\mathrm{est}}_{f_\mathrm{e}}$ and the RE. In contrast, the RE obtained by the global estimator is always close to unity. Therefore, one can deduce that the extra complexity due to interactions among devices is balanced by the provision of the extra information available to the global estimator.

Table 7.1 shows the estimation RE obtained for **L1** with different β_η and d_b. When $\beta_\eta = 0°$ and $\beta_\eta = 45°$, the two bodies of the array achieve similar RE using global estimation. However, there is a difference on the performance obtained for the two

---

[2] The average RE over $\beta_\eta = 0°$, $45°$, and $90°$ is shown in Figure 7.4, due to the similarities of the results obtained for three wave directions analysed.

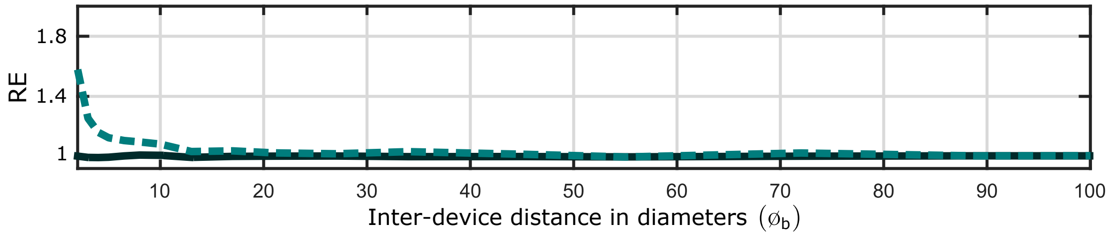

(a) Estimation relative error for **L1**.

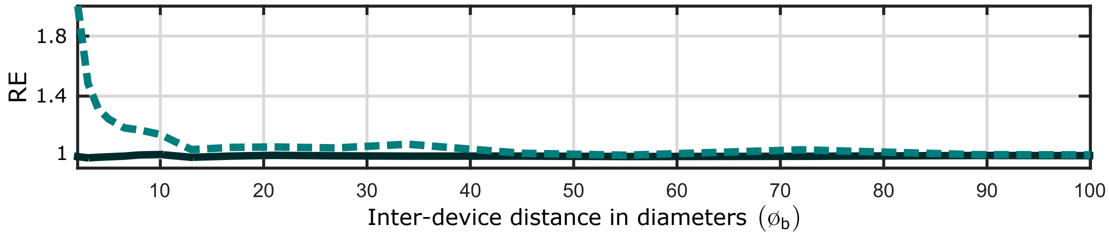

(b) Estimation relative error for **L2**.

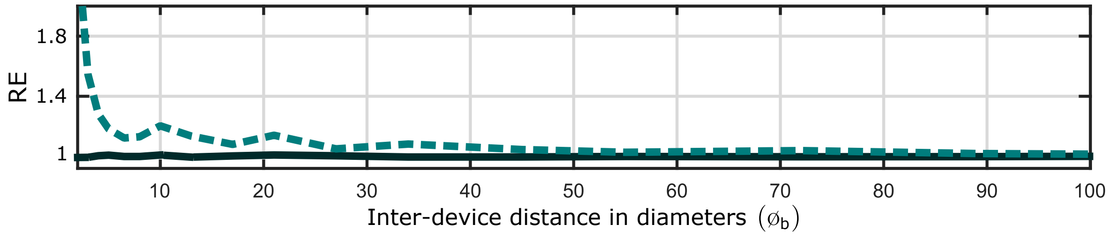

(c) Estimation relative error for **L3**.

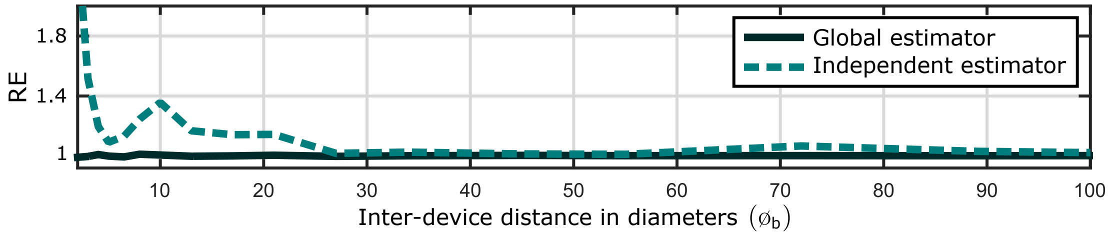

(d) Estimation relative error for **L4**.

Figure 7.4: The relative error of the estimation for the different layouts **L1**–**L4**, averaged over the three wave directions, for the global and independent estimator.

devices when using the independent estimator for close spacing ($d_\mathrm{b} < 6.5\varnothing_\mathrm{b}$). When $\beta_\eta = 90°$, both bodies achieve almost identical RE results for all d_b with global and independent estimators, due to the symmetry of that case[3]. As for Figure 7.4, Table 7.1 demonstrates that the global estimator always achieves a $\mathrm{NRMSE}^{\mathrm{est}}_{f_\mathrm{e}}$ comparable to the one obtained in the isolated body case, while the independent estimator achieves significantly poorer estimates, particularly for small d_b values.

---

[3] Note that if the results obtained for both devices are not exactly the same is due to the randomness of the noise added to the position and velocity measurements at the estimation stage.

Table 7.1: The RE of estimation for **L1**, for different distances and wave directions

		Global estimator					**Independent estimator**				
	$\boldsymbol{d}_\mathrm{b}$	$2\varnothing_\mathrm{b}$	$3\varnothing_\mathrm{b}$	$6.5\varnothing_\mathrm{b}$	$21\varnothing_\mathrm{b}$	$200\varnothing_\mathrm{b}$	$2\varnothing_\mathrm{b}$	$3\varnothing_\mathrm{b}$	$6.5\varnothing_\mathrm{b}$	$21\varnothing_\mathrm{b}$	$200\varnothing_\mathrm{b}$
$\beta_\eta = 0°$	Device 1	0.964	0.980	0.976	0.984	0.988	1.348	1.148	1.048	1.004	0.984
	Device 2	0.988	0.992	0.996	0.976	0.976	2.272	1.484	1.104	0.988	1.000
$\beta_\eta = 45°$	Device 1	0.984	0.976	0.992	0.984	1.000	1.260	1.084	1.088	1.268	0.996
	Device 2	0.992	0.996	0.988	0.992	0.988	1.936	1.48	1.076	1.036	0.988
$\beta_\eta = 90°$	Device 1	0.984	0.980	0.988	0.995	0.990	1.584	1.251	1.096	1.012	0.988
	Device 2	0.984	0.980	0.988	0.996	0.989	1.584	1.250	1.096	1.013	0.986

7.3.2 Forecasting results

As shown in Chapter 6, the accuracy of the prediction obtained with AR models depends (mostly) on the amount of past signal history considered to predict future values, which is given by the order of the model and the sampling period of the signal. Since, for this case, the AR model order giving the best prediction accuracy is $n_\mathrm{ord}^\mathrm{AR} = 160$, the estimated f_e is re-sampled, in order to reduce the order of the predictor. By way of example, Figure 7.5 shows the $\mathrm{NRMSE}_{f_\mathrm{e}}^\mathrm{pred}$, for $t_\mathrm{hor} = 4\,\mathrm{s}$, computed for different re-sampled sampling periods using the isolated WEC case. Note that the minimum prediction error for each t_s occurs approximately when 16 s of past values are taken into account, equivalent to two times T_p. Therefore, the estimated f_e is re-sampled to $t_\mathrm{s} = 0.04\,\mathrm{s}$ before using it at the prediction stage. Even though Figure 7.5 is computed for the isolated WEC case, the best $n_\mathrm{ord}^\mathrm{AR}$ remains the best order for an independent predictor in the array case and, therefore, $n_\mathrm{ord}^\mathrm{AR} = 40$ is chosen.

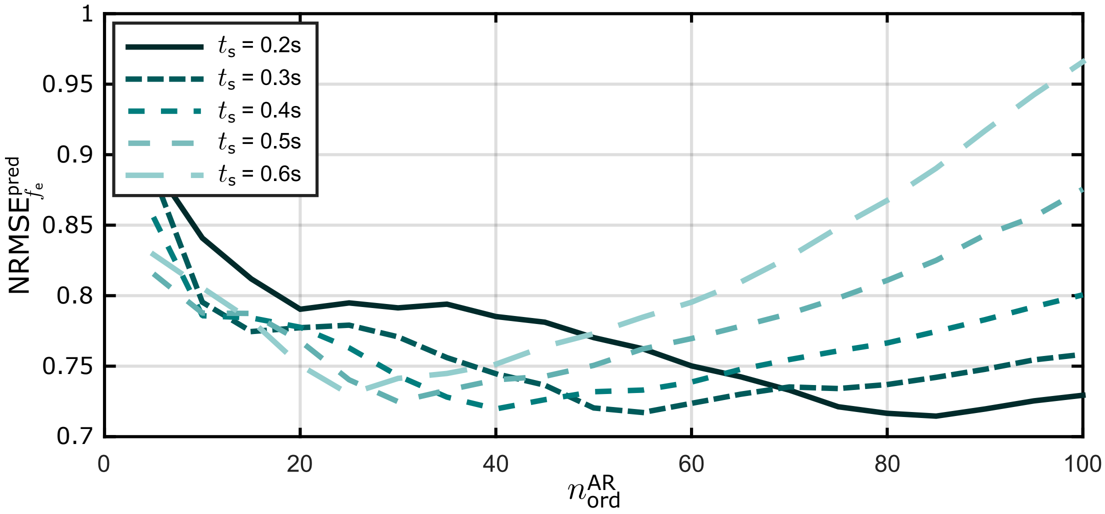

Figure 7.5: The different array layouts considered for the analysis.

Regarding the global predictor, the model order which gives the most accurate prediction varies depending on the layout, spacing d_b, and wave direction β_η. It is appealing, for comparison purposes, to use a consistent order for all cases, with an overall best choice of $n_{\text{ord}}^{\text{ARx}} = 40$ and $n_{\text{ord}}^{\text{arX}} = 40$.

Figure 7.6 illustrates the variation in the prediction performance when the $\tilde{f}_{\text{e}}$ signal used to identify the forecasting parameters is obtained from global and independent estimators, illustrated in Figure 7.6(a) and (b), respectively. Even though only the case for **L2**, with $\beta_\eta = 0°$ and $d_{\text{b}} = 20\,\text{m}$, is shown in Figure 7.6, this case is representative of all the considered array layouts. Three main details are highlighted in Figure 7.6. Firstly, the $\text{NRMSE}_{f_{\text{e}}}^{\text{pred}}$ obtained by the predictor using $\tilde{f}_{\text{e}}$ from the global estimator (Figure 7.6(a)) is, overall, lower than that obtained using $\tilde{f}_{\text{e}}$ from the independent estimator. This is due to the error added by the independent estimator. Note that the lowest prediction errors start at around $\text{NRMSE}_{f_{\text{e}}}^{\text{pred}} = 0.2$, which correspond to the estimation error.

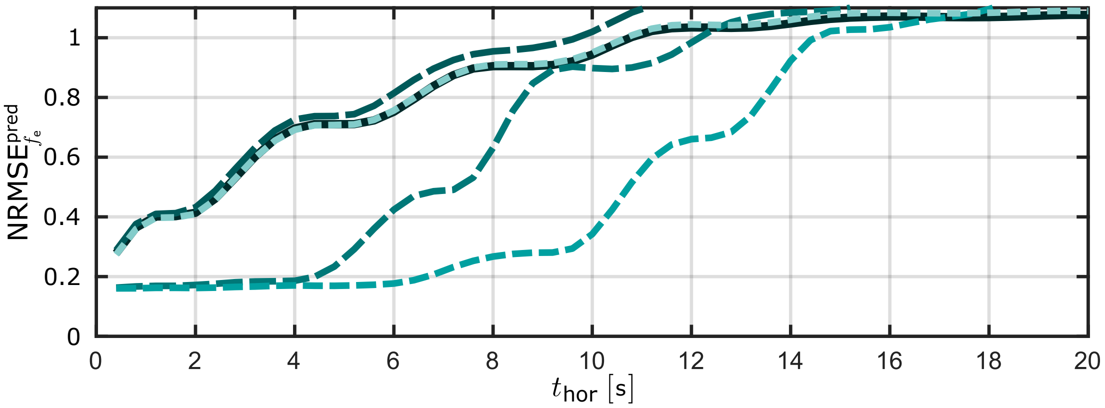

(a) $\text{NRMSE}_{f_{\text{e}}}^{\text{pred}}$ obtained using the $\tilde{f}_{\text{e}}$ from the global estimator.

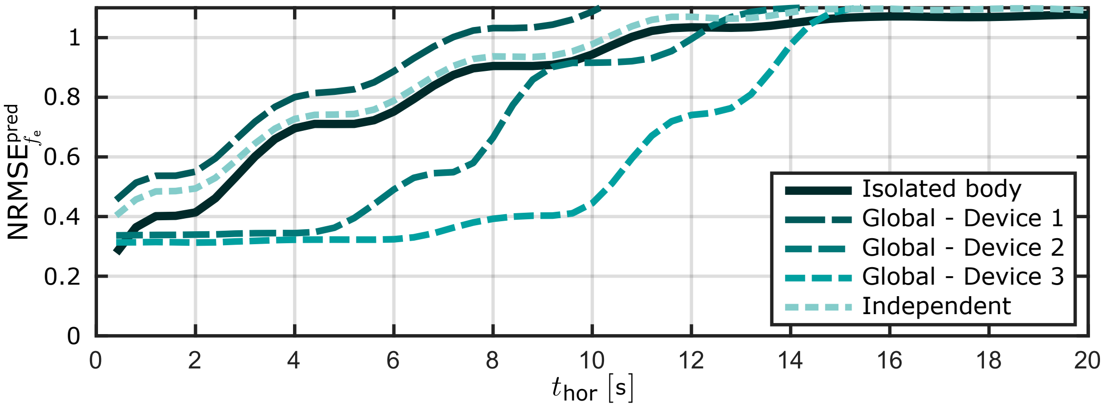

(b) $\text{NRMSE}_{f_{\text{e}}}^{\text{pred}}$ obtained using the $\tilde{f}_{\text{e}}$ from the independent estimator.

Figure 7.6: Comparison of the $\text{NRMSE}_{f_{\text{e}}}^{\text{pred}}$ of the forecasting using the values obtained from the global estimator and independent estimator for **L2** with (a) $\beta_\eta = 0°$ and (b) $d_{\text{b}} = 20\,\text{m}$.

Secondly, the $\text{NRMSE}_{f_e}^{\text{pred}}$ obtained by the independent predictor[4] is always similar to that obtained in the isolated WEC case, or worse in the case of using $\tilde{f}_e$ from the independent estimator. Finally, since incoming waves first impact Device 1 and, later, Devices 2 and 3, the knowledge of $\tilde{f}_e$ acting on Device 1 leads to an improvement of the prediction accuracy for Devices 2 and 3. The degree of improvement depends on the distance between the devices, i.e. the amount of time in advance the incoming wave is known. Thus, Device 3 achieves the best prediction performance, while the prediction performance of Device 1 is similar to that achieved in the isolated body case.

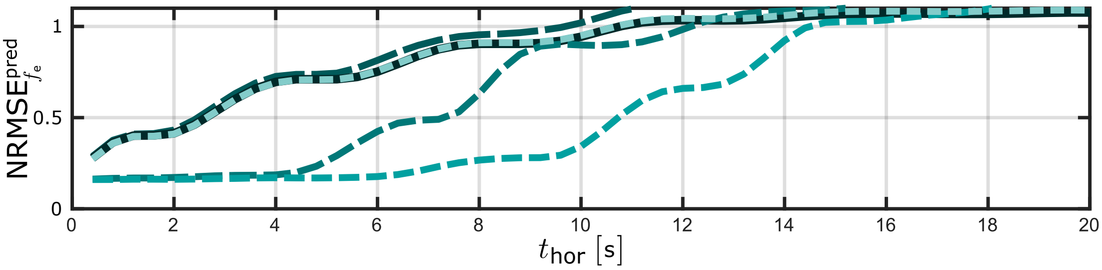

(a) $\text{NRMSE}_{f_e}^{\text{pred}}$ obtained using the $\tilde{f}_e$ from the global estimator and $\beta_\eta = 0°$.

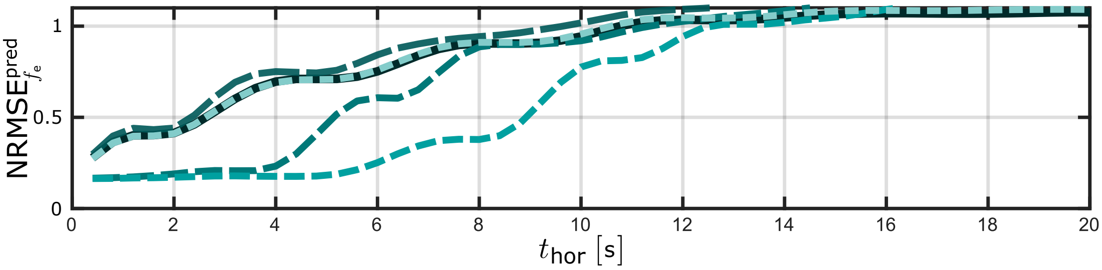

(b) $\text{NRMSE}_{f_e}^{\text{pred}}$ obtained using the $\tilde{f}_e$ from the global estimator and $\beta_\eta = 45°$.

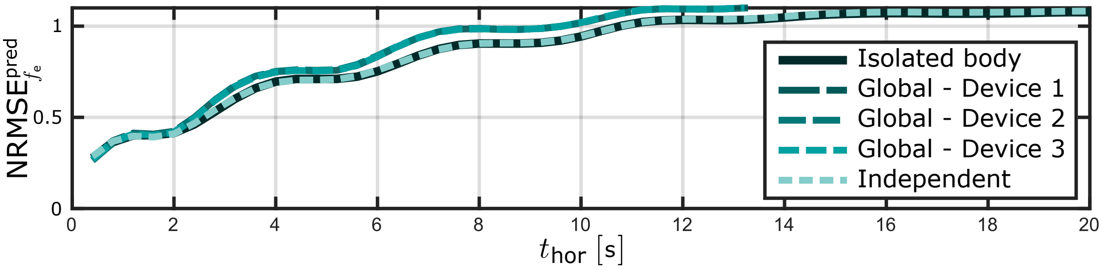

(c) $\text{NRMSE}_{f_e}^{\text{pred}}$ obtained using the $\tilde{f}_e$ from the global estimator and $\beta_\eta = 90°$.

Figure 7.7: Comparison of the $\text{NRMSE}_{f_e}^{\text{pred}}$ of the forecasting using the values obtained from the global estimator for **L2**, with $d_b = 20\,\text{m}$, for (a) $\beta_\eta = 0°$, (b) $\beta_\eta = 45°$, and (c) $\beta_\eta = 90°$.

Figure 7.7 illustrates the prediction $\text{NRMSE}_{f_e}^{\text{pred}}$ for different β_η, with **L2** and $d_b = 20\,\text{m}$. For such case, when the incident wave direction is perpendicular to the main axis

---

[4] Note that a single trace is shown for the independent predictor, representing the $\text{NRMSE}_{f_e}^{\text{pred}}$ averaged over the three bodies.

of the array, $\beta_\eta = 90°$ (see Figure 7.7(c)), all devices are affected by the wave front at the same time. Therefore, there is no significant extra information from the array motion, compared to the information from any single device. Consequently, the global forecaster achieves a similar $\text{NRMSE}_{f_e}^{\text{pred}}$ compared to the independent forecaster, and to the isolated single WEC case.

However, as explained for Figure 7.6, the $\text{NRMSE}_{f_e}^{\text{pred}}$ for some devices improves when the incoming wave affects the other bodies of the array first. Thus, for $\beta_\eta = 45°$, the f_e estimated from Device 1 helps Devices 2 and 3 to obtain better f_e predictions than for the isolated WEC case. This $\text{NRMSE}_{f_e}^{\text{pred}}$ is further improved for $\beta_\eta = 0°$, since the distance between Device 1 and Devices 2 and 3 is larger compared to the case of $\beta_\eta = 45°$.

A section of simulated, estimated, and predicted f_e, for a specific sea state realisation, is shown in Figure 7.8, when using (a) an independent estimator/predictor and (b) a global estimator/predictor, for Device 2 of **L1** with $d_b = 20\,\text{m}$, $\beta_\eta = 0°$, and $t_{\text{hor}} = 4\,\text{s}$. Figure 7.8 again confirms that the estimation of f_e is more accurate when using the global estimator. Additionally, it is shown that, when using the global predictor, the prediction achieved is quasi-identical to the estimated f_e, due to the anticipative information provided by Device 1.

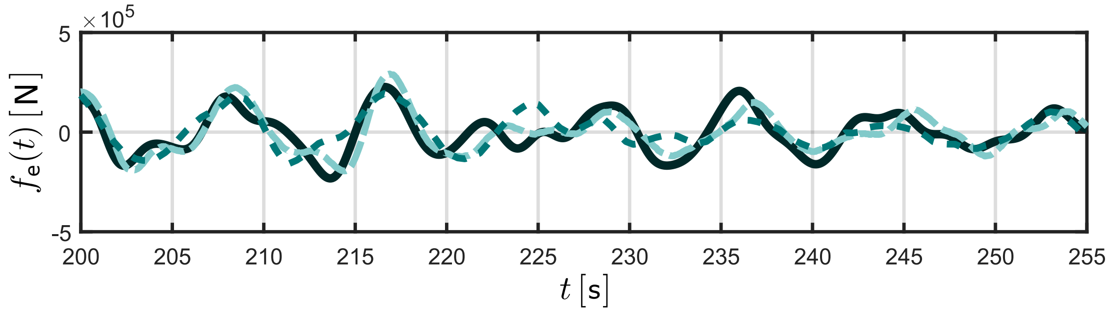

(a) Using independent estimator along with the independent predictor.

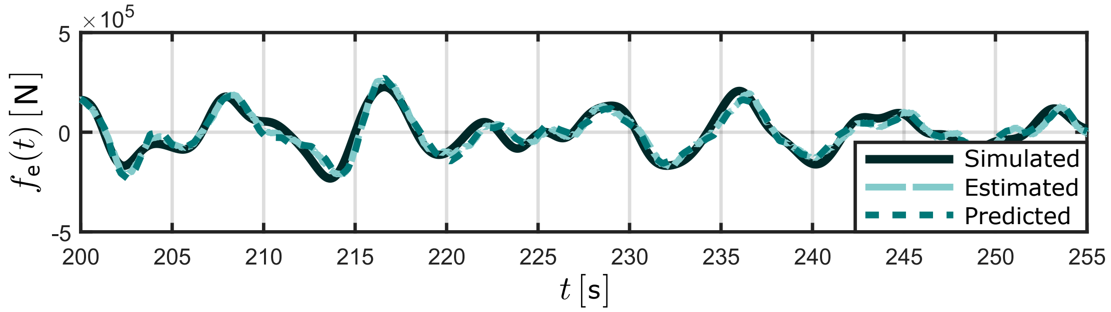

(b) Using the global estimator along with the global predictor.

Figure 7.8: Section of simulated, estimated, and predicted f_e using two different combinations of estimator/predictor, for a specific realisation. The device shown is Device 2 of the **L1** with $d_b = 20\,\text{m}$ and $\beta_\eta = 0°$. The prediction shown is for $t_{\text{hor}} = 4\,\text{s}$.

Finally, as explained in Section 7.2.1, for the independent estimation case, an estimator is used in each device and, therefore, the computational time will not change if larger arrays are considered. In contrast, since the global estimator takes into account the interactions between all the bodies of the array, the size of the A_{ss} matrix for the global estimator increases with n_{b}. In fact, by defining the MIMO SS model of the array as a set of multi-SISO SS systems, the A_{ss} matrix increases proportionally with n_{b}^2, which could hamper the online application of the global estimator in a real sea-state scenario with large arrays. However, Section 7.3.3 details how the MIMO parametric models, introduced in Section 4.3, can reduce the computational time required by the global estimator.

7.3.3 Using the moment-based MIMO identification strategy

One can notice that the HO model, used in the KFHO estimator, is defined exactly like the dynamical model used to describe the excitation force input in the moment-matching based identification approach (see Equation (4.4)). This means that there is a natural synergy between the moment-matching-based parameterisation strategy, introduced in Section 4.1.1, and the KFHO estimation technique. This mathematical connection can be exploited to substantially improve the performance of the KFHO, through a wise selection of the set of interpolation points of the parametric model describing the WEC system.

In particular, for the array case, if the MIMO SS model is directly identified from the original MIMO system by interpolating the same set of frequencies used in the HO model, the performance of the global KFHO estimator improves, compared to the case where the standard multi-SISO MIMO SS model is used to describe the system (which is the model used for the global estimator of the previous section). It should be noted that such an improvement in performance is given in terms of not only computational effort required by the observer, but also of estimation accuracy, as demonstrated in the remainder of this section.

To illustrate the advantages of using the MIMO moment-based parameterisation method within the global KFHO estimation technique, the same four body array configuration used in the previous section, **L4**, is used. Thus, the array is composed of four cylindrical devices (10 m diameter and 10 m draft), laid out in the square layout **L4** with $d_{\text{b}} = 20\,\text{m}$ and $\beta_{\eta} = 0^{\circ}$ (see Figure 7.1).

In order to emphasise the effect of the WEC model used in the estimator, rather than the capacity of the KFHO estimator to deal with measurement noise, no measurement noise is considered in this analysis. Additionally, to accentuate the effect of choosing the correct frequencies for the HO model of the KFHO estimator, HO models composed of a maximum of two frequencies are considered for this section, instead of using seven frequencies as for the analysis of the previous section. To this end, the global KFHO estimator is designed using the following set of frequencies:

$$\begin{aligned} \mathcal{F}_1^{\text{est}} &= \{0.79\}, \\ \mathcal{F}_2^{\text{est}} &= \{0.79, 1.17\}, \end{aligned} \tag{7.9}$$

where the selection of the frequencies is made using explicit knowledge of the SDF of the wave input, since 0.79 $^{\text{rad}}/_{\text{s}}$ corresponds to the peak period of the JONSWAP spectrum shown in Figure 7.3(b). The second interpolation frequency, 1.17 $^{\text{rad}}/_{\text{s}}$, represents the largest peak of the MIMO frequency response of the force-to-velocity dynamics of the array (shown later in Figure 7.9).

Using the frequency sets defined in Equation (7.9), the moment-based MIMO SS models $\tilde{\boldsymbol{H}}_{\mathcal{F}_1^{\text{est}}}$ and $\tilde{\boldsymbol{H}}_{\mathcal{F}_2^{\text{est}}}$ are identified, as shown in Section 4.3. Additionally, another two moment-based MIMO SS models are identified, termed $\tilde{\boldsymbol{H}}_{\mathcal{F}_1^{\text{sim}}}$ and $\tilde{\boldsymbol{H}}_{\mathcal{F}_2^{\text{sim}}}$, where the interpolation frequencies are selected so that the approximation error between the frequency responses of the target MIMO system and obtained parametric model is minimised. In particular, $\mathcal{F}_1^{\text{sim}}$ and $\mathcal{F}_2^{\text{sim}}$ are defined as:

$$\begin{aligned} \mathcal{F}_1^{\text{sim}} &= \{1.17\}, \\ \mathcal{F}_2^{\text{sim}} &= \{1.17, 1.11\}, \end{aligned} \tag{7.10}$$

where 1.11 $^{\text{rad}}/_{\text{s}}$ represents the location of the second largest peak of the MIMO frequency response of the dynamics of the array. It should be clarified that, for the estimators using the models $\tilde{\boldsymbol{H}}_{\mathcal{F}_1^{\text{sim}}}$ and $\tilde{\boldsymbol{H}}_{\mathcal{F}_2^{\text{sim}}}$, the set of frequencies defining the HO model are also $\mathcal{F}_1^{\text{est}}$ and $\mathcal{F}_2^{\text{est}}$.

Table 7.2 shows the estimation results obtained with the different identified MIMO models, as well as with the multi-SISO parametric model, of the force-to-velocity relationship of the WEC array. Note that Table 7.2 shows the results in terms of the following characteristics:

Dim Dimension of the MIMO force-to-velocity parametric model.

NRMSE$_{H(\omega)}$ Approximation error computed against the target MIMO WEC array frequency response (for $\omega \in [0.3,2.5]$ $^{\text{rad}}/_{\text{s}}$).

NRMSE$_{f_e}^{\text{est}}$ NRMSE of the f_{e} estimate, averaged over 35 randomly-generated realisations of the JONSWAP SDF.

N-Time The time required[5] for the f_{e} estimation, normalised against the slowest model, in this case the model computed with the multi-SISO approach ($2{\cdot}10^{-4}$s for one time step $t_{\text{s}} = 0.001\,\text{s}$).

Table 7.2: Estimation results obtained with the different identified MIMO and the multi-SISO parametric models of the force-to-velocity of the WEC array.

Model	**Dim**	**NRMSE$_{\boldsymbol{H}(\omega)}$**	**NRMSE$^{\text{est}}_{f_{\text{e}}}$**	**N-Time**
multi-SISO	72	0.0076	0.0437	1
$\tilde{\boldsymbol{H}}_{\mathcal{F}_1^{\text{sim}}}$	8	0.0482	0.2359	0.1984
$\tilde{\boldsymbol{H}}_{\mathcal{F}_1^{\text{est}}}$	8	0.3112	0.0982	0.1984
$\tilde{\boldsymbol{H}}_{\mathcal{F}_2^{\text{sim}}}$	16	0.0044	0.0428	0.3108
$\tilde{\boldsymbol{H}}_{\mathcal{F}_2^{\text{est}}}$	16	0.0502	0.0204	0.3108

One can notice, by analysing $\tilde{\boldsymbol{H}}_{\mathcal{F}_1^{\text{est}}}$ and $\tilde{\boldsymbol{H}}_{\mathcal{F}_1^{\text{sim}}}$ that, even though the order of both models is exactly the same, the performance results are significantly different. Figures 7.9 and 7.10 show the frequency responses obtained by $\tilde{\boldsymbol{H}}_{\mathcal{F}_1^{\text{sim}}}$ and $\tilde{\boldsymbol{H}}_{\mathcal{F}_1^{\text{est}}}$, respectively. From visual inspection of Figures 7.9 and 7.10, it can be observed that $\tilde{\boldsymbol{H}}_{\mathcal{F}_1^{\text{sim}}}$ obtains a more accurate representation of the target frequency response. This is further confirmed in Table 7.2, showing that $\tilde{\boldsymbol{H}}_{\mathcal{F}_1^{\text{sim}}}$ obtains a NRMSE$_{\boldsymbol{H}(\omega)} \approx 0.05$, compared to a NRMSE$_{\boldsymbol{H}(\omega)} \approx 0.31$ obtained by $\tilde{\boldsymbol{H}}_{\mathcal{F}_1^{\text{est}}}$.

However, the performance of the estimation obtained using $\tilde{\boldsymbol{H}}_{\mathcal{F}_1^{\text{sim}}}$ is significantly worse than that obtained using $\tilde{\boldsymbol{H}}_{\mathcal{F}_1^{\text{est}}}$ (NRMSE$^{\text{est}}_{f_{\text{e}}} \approx 0.24$ against NRMSE$^{\text{est}}_{f_{\text{e}}} \approx 0.10$). This can be explained by the fact that $\tilde{\boldsymbol{H}}_{\mathcal{F}_1^{\text{est}}}$ has exactly the same steady-state response as the WEC array at the frequency points selected to represent the HO of the estimator, which contains the majority of the spectral content of the input signal.

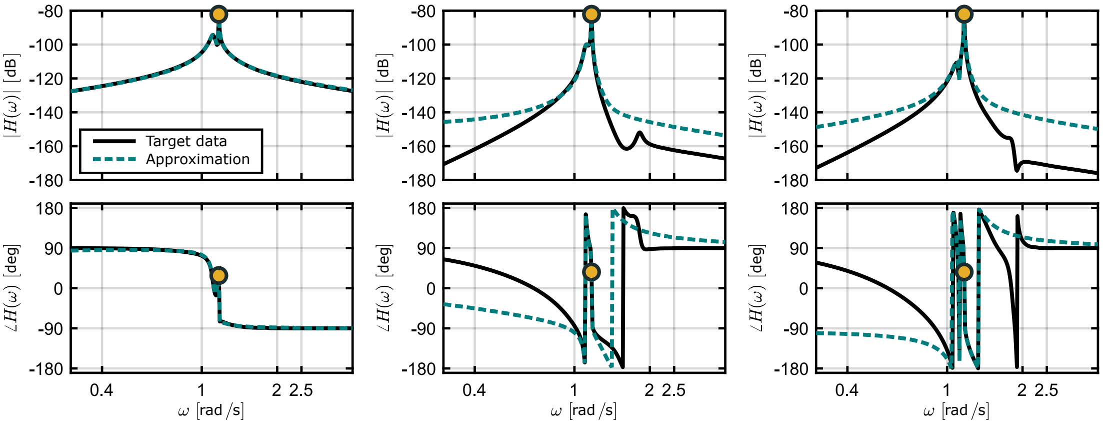

(a) Inner dynamics. **(b)** Interaction with the closest neighbour. **(c)** Interaction with the device on the diagonal.

Figure 7.9: Frequency response of $\tilde{\boldsymbol{H}}_{\mathcal{F}_1^{\text{sim}}}$, along with the target frequency domain data and the interpolation frequencies (orange-dots). NRMSE$_{\boldsymbol{H}(\omega)}$ ≈0.05.

Note that, using $\tilde{\boldsymbol{H}}_{\mathcal{F}_1^{\text{est}}}$, the f_{e} estimate is computed five times faster than using the multi-SISO model, while the obtained NRMSE$^{\text{est}}_{f_{\text{e}}}$ is only 0.06 worse (NRMSE$^{\text{est}}_{f_{\text{e}}} \approx 0.04$

---

[5] Measured using the MATLAB functions `Tic` and `Toc`.

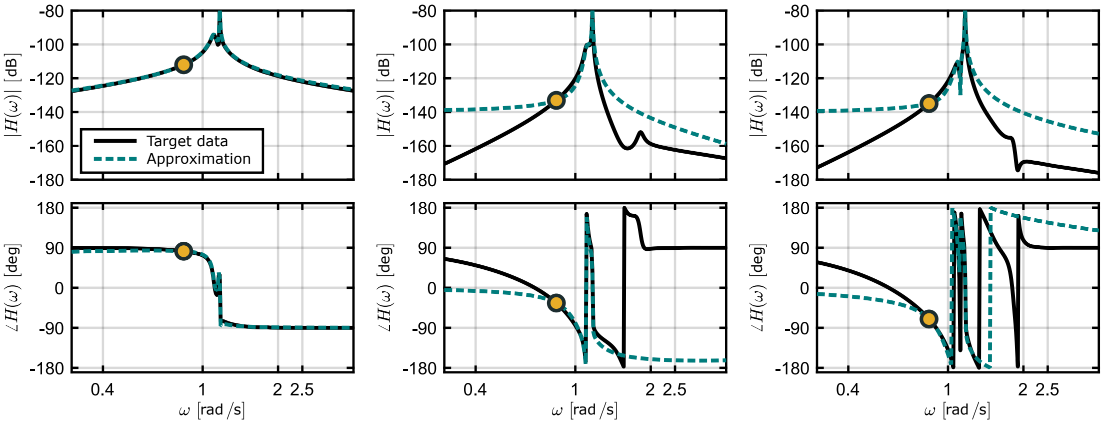

(a) Inner dynamics. **(b)** Interaction with the closest neighbour. **(c)** Interaction with the device on the diagonal.

Figure 7.10: Frequency response of $\tilde{\boldsymbol{H}}_{\mathcal{F}_1^{\text{est}}}$, along with the target frequency domain data and the interpolation frequencies (orange-dots).NRMSE$_{\boldsymbol{H}(\omega)}$ ≈0.31.

against NRMSE$_{f_\text{e}}^{\text{est}} \approx 0.10$). However, if two interpolation frequencies are chosen for the identification of the MIMO SS, as shown for the results using $\tilde{\boldsymbol{H}}_{\mathcal{F}_2}^{\text{est}}$, the obtained estimation error is half the error compared to the multi-SISO approach, while being more than three times faster. In contrast, if the frequencies are not chosen to specifically match those of the HO model in the KFHO estimator, as shown for $\tilde{\boldsymbol{H}}_{\mathcal{F}_2}^{\text{sim}}$, the estimate is as accurate as that obtained by the multi-SISO approach, while being also three times faster. Therefore, regardless on the way in which the interpolation frequencies are selected, it is important to use SS models identified using a MIMO identification strategy, in order to reduce the computational effort required by the global estimator.

Finally, it should be highlighted that, as explained in Section 4.3, the difference in the computational time required by the multi-SISO model and the MIMO moment-matching based identified models will increase with the size of the array since, while the order of the multi-SISO model increases quadratically with n_b, the order of the obtained model using the moment-based MIMO identification will increase linearly with n_b.

7.4 Conclusions

The results of this chapter show that the complex wave field of a WEC array degrades the independent estimator performance, compared to the global estimator, whose performance is relatively consistent with that of the isolated body case for all the layouts, distances, and wave directions analysed. This allows WEC array designers to optimise the array layout for any optimisation objective (such as, for example, enhancing constructive interaction between devices or maximising the absorbed power by each device) since, regardless of the final array layout, the global estimator always performs to a level comparable with the isolated body case.

Regarding forecasting of f_e, it has been demonstrated that the global forecaster not only achieves better prediction accuracy than the independent forecaster, but also outperforms the isolated body case for the devices positioned down-wave, since they get information of the incoming wave from the WECs positioned up-wave. In a real-sea scenario with large arrays and multidirectional waves, by using the global predictor, the devices in the middle of the array (which, depending on the layout, could be the majority of the devices) will always obtain better f_e prediction than in the isolated WEC case. Additionally, the prediction accuracy obtained by the devices located at the edges of the array, in the worst-case-scenario, will enjoy the same prediction accuracy as for the isolated WEC case. However, since waves potentially come from every direction, even the devices located at the edges of the array will have extra information of the incoming waves and, therefore, obtain a more accurate f_e prediction than for the isolated WEC case. However, since no location has an equal distribution of incidence angles around the compass rose, the prediction accuracy obtained by the different devices would depend on their location within the array.

It should be highlighted that, since no control strategy is employed for this analysis, stronger interaction can be expected when an optimal control strategy is implemented, due to the fact that the motion of the devices may increase considerably, with a consequent increase in the amplitude of radiated waves. Therefore, in case of an array under optimal control, there may be a greater disparity between the independent estimator model's performance and that achieved by the global estimator, or isolated body case.

The only drawback, regarding the global estimation/prediction techniques, is the computational time they would require for large WEC arrays. However, it is demonstrated that, when using the moment-based MIMO identification approach, the order of the final model only increases linearly with the number of devices composing the array (as opposed to quadratically, if the multi-SISO approach is used to generate the MIMO SS models of the array), which eases the implementation of the global strategies for large arrays in real-time. Nevertheless, if necessary, computational simplification (e.g. parallelising the estimators/predictors onto several processors or simplification of such models can be computed, considering only the interactions with the closest devices) could be effected, while retaining the spirit of the global approach.

8

Controller sensitivity to estimation/forecasting errors

Contents

As shown in Chapters 5 and 6, considerable uncertainties can intrinsically arise in the estimated/predicted excitation force. Therefore, it is important to analyse the effects that such uncertainties can potentially have on the performance of the control strategy. To this end, this chapter shows how the estimation/prediction errors affect a receding-horizon WEC optimal control strategy. Section 8.1 introduces, briefly, the WEC energy maximising control problem and, in particular, the receding-horizon WEC optimal control strategy considered in this chapter. Then, in Section 8.2, the sensitivity analysis of the controller to both estimation and prediction errors is shown and, finally, some conclusions are drawn in Section 8.3.

8.1 Energy maximising control

Energy-maximising control for WECs can be clearly divided into two categories: Optimisation-Based (OB) and non-Optimisation-Based (nOB) controllers [45]. In the case of OB controllers, the control objective is treated as an optimal control problem, for which both input and state variables are often discretised using different criteria, aiming to translate the WEC control problem into a computationally tractable nonlinear program. Model predictive control techniques are a typical example for OB controllers [45]. In contrast, nOB controllers do not rely on numerical routines but are mostly based on the fundamental principle behind maximum power transfer in electric circuits: the impedance-matching principle [60].

Naturally, OB and nOB control strategies have distinct differences, with individual strengths and weaknesses. An immediate advantage of OB approaches is that constraint handling becomes straightforward, i.e. limits on device motion and PTO force are naturally handled within a constrained optimisation problem. A clear disadvantage, however, is that the real-time capabilities of solving the required optimisation depend on a number of factors, primarily on the discretisation technique utilised to parameterise the state and input variables, as well as the hardware available for implementation [45]. Examples can be found in [101] for MPC, in [15] for spectral optimal control, or in [51, 52] for moment-matching-based control.

For the analysis in this chapter, an OB control strategy is chosen since, for most of the OB control strategies, energy-maximisation can only be achieved by having full (past, instantaneous, and future) knowledge of the wave excitation force f_e and, therefore, rely on estimation/prediction techniques[1]. In particular, a receding-horizon moment-matching-based energy-maximising optimal control strategy is applied, which was recently published in [50]. Such control strategy is a real-time version of the moment-based WEC control strategy, proposed in [51, 52], which assumes a sufficiently long time interval for which f_e is known in the future. However, as shown in Chapters 6 and 7, the f_e (or η) prediction error increases rapidly with the prediction horizon t_hor when considering realistic sea-state conditions, which limits the applicability of the original (non-receding-horizon) moment-matching-based controller. Hence, there is a trade-off between a long receding window (which is desired for control) and the fidelity degradation associated with longer prediction horizons. The moment-matching-based control strategy has the capability to effectively solve the energy maximising problem, guaranteeing existence and uniqueness of the optimal PTO force f_pto^opt, with real-time performance. The energy-maximising optimal control formulation to be solved by OB controllers is defined as

$$\begin{aligned} f_\text{pto}^\text{opt} &= \arg\max_{f_\text{pto}} \frac{1}{t_\text{w}} \int_0^{t_\text{w}} \dot{\chi}(t) f_\text{pto}(t)\text{d}t, \\ &\text{subject to: } \begin{cases} \text{WEC dynamics,} \\ \text{state and input constraints,} \end{cases} \end{aligned} \tag{8.1}$$

---

[1] Note that some nOB control strategies also need a f_e estimate to calculate the optimal control force but, usually, they do not require future knowledge of f_e.

with $t_\mathsf{w} \in \mathbb{R}$, and $t_\mathsf{w} > 0$, the receding time window over which the control force is optimised. As for the case of moment-based identification introduced in Section 4.1.1, the moment-based energy-maximising control strategy, introduced in [51, 52], provides an efficient and convenient way to parameterise the input and state variables in terms of the concept of moments [8]. Moments are intrinsically connected to the steady-state response characteristics of the system under analysis, allowing for a parameterisation of the problem, shown in Equation (8.1), in terms of the steady-state response of a suitably defined system.

As shown in Equation (4.4), the excitation force f_e, and now the control input f_pto, can be expressed as the solution of the signal generator

$$
\begin{aligned}
\dot{x}_\mathsf{e}^\mathsf{MM}(t) &= A_\mathsf{sg}^\mathsf{MM} x_\mathsf{e}^\mathsf{MM}(t), && \text{(8.2a)}\\
f_\mathsf{e}(t) &= C_\mathsf{sg}^\mathsf{MM} x_\mathsf{e}^\mathsf{MM}(t), && \text{(8.2b)}\\
f_\mathsf{pto}(t) &= C_{\mathsf{sg}_\mathsf{pto}}^\mathsf{MM} x_\mathsf{e}^\mathsf{MM}(t). && \text{(8.2c)}
\end{aligned}
$$

With the parameterisation of Equation (8.2), and the matrices $A_\mathsf{ss}^\mathsf{MM}$, $B_\mathsf{ss}^\mathsf{MM}$, and $C_\mathsf{ss}^\mathsf{MM}$ of the SS model describing the WEC dynamics, shown in Equation (4.3), the optimal control problem of Equation (8.1) can be defined as a QP optimisation problem. In other words, the optimal energy-maximising control input, $f_\mathsf{pto}^\mathsf{opt}(t) = C_{\mathsf{sg}_\mathsf{pto}}^{\mathsf{MM}^\mathsf{opt}} x_\mathsf{e}^\mathsf{MM}(t)$, can be computed as the unique global solution of the inequality-constrained concave quadratic optimisation problem defined as

$$
\begin{aligned}
&C_{\mathsf{sg}_\mathsf{pto}}^{\mathsf{MM}^\mathsf{opt}} = \arg\max_{C_{\mathsf{sg}_\mathsf{pto}}^\mathsf{MM}} -\frac{1}{2} C_{\mathsf{sg}_\mathsf{pto}}^\mathsf{MM} \Phi_\mathsf{pto}^\mathsf{MM} C_{\mathsf{sg}_\mathsf{pto}}^{\mathsf{MM}^\intercal} + \frac{1}{2} C_\mathsf{sg}^\mathsf{MM} \Phi_\mathsf{pto}^\mathsf{MM} C_{\mathsf{sg}_\mathsf{pto}}^{\mathsf{MM}^\intercal},\\
&\text{subject to:}\\
&\mathcal{A}_\chi C_{\mathsf{sg}_\mathsf{pto}}^{\mathsf{MM}^\intercal} \leq \mathcal{B}_\chi, \qquad \mathcal{A}_{\dot{\chi}} C_{\mathsf{sg}_\mathsf{pto}}^{\mathsf{MM}^\intercal} \leq \mathcal{B}_{\dot{\chi}}, \qquad \mathcal{A}_{f_\mathsf{pto}} C_{\mathsf{sg}_\mathsf{pto}}^{\mathsf{MM}^\intercal} \leq \mathcal{B}_{f_\mathsf{pto}},
\end{aligned}
\tag{8.3}
$$

where $\Phi_\mathsf{pto}^\mathsf{MM}$ contains both the WEC dynamics and input description as

$$
\begin{aligned}
\Phi_\mathsf{pto}^\mathsf{MM} &= \left(\mathbb{I}_{n_\mathsf{ss}} \otimes C_\mathsf{ss}^\mathsf{MM}\right) \phi_\mathsf{pto}^\mathsf{MM} \left(\mathbb{I}_{n_\mathsf{ss}} \otimes -B_\mathsf{ss}^\mathsf{MM}\right),\\
\phi_\mathsf{pto}^\mathsf{MM} &= A_\mathsf{sg} \hat{\oplus} A_\mathsf{ss}^\mathsf{MM} - R^\mathsf{MM} \otimes B_\mathsf{ss}^\mathsf{MM} C_\mathsf{ss}^\mathsf{MM}.
\end{aligned}
\tag{8.4}
$$

Note that, as shown in Equation (4.8), the matrix R^MM characterises the non-parametric impulse response function associated with radiation forces, using moment-based theory, without the need to pre-compute a parametric approximation (which is the case for most of the OB methods reported in the literature [45]). Additionally, as shown in [51, 52], the constant matrices $(\mathcal{A}_\chi, \mathcal{B}_\chi)$, $(\mathcal{A}_{\dot{\chi}}, \mathcal{B}_{\dot{\chi}})$, and $(\mathcal{A}_{f_\mathsf{pto}}, \mathcal{B}_{f_\mathsf{pto}})$ characterise the displacement, velocity, and control force constraints, respectively.

Given the concave nature of the QP expressed in Equation (8.3), the optimal control force $f_\mathsf{pto}^\mathsf{opt}$ can be effectively computed in real-time [51]. Nevertheless, this optimal control formulation requires knowledge of past, actual, and future wave excitation force f_e to compute the optimal control law. The associated estimation and prediction techniques increase the overall computational demand.

Every given receding window can be decomposed into two different parts: the first one with estimated f_e (of length t_w^est), and a second part containing the predicted f_e (of length t_w^pred and, therefore, $t_\text{hor} = t_\text{w}^\text{pred}$). Note that, without loss of generality, the current time instant is located at the centre of the receding window and, therefore, $t_\text{w}^\text{est} = t_\text{w}^\text{pred}$; however, different window configurations can be designed [50]. Thus, at every time instant t, the estimated and predicted f_e are used to calculate the optimal f_pto over the receding window, defined from $t - t_\text{w}^\text{est}$ to $t + t_\text{w}^\text{pred}$. The obtained f_pto^opt is applied from t to $t + t_{\text{s}_\text{w}}$, with t_{s_w} denoting the receding sampling period. Then, at $t + t_{\text{s}_\text{w}}$, a new, optimal f_pto is calculated using a new receding window.

This strategy assumes that the excitation force is periodic within the receding window where the optimal f_pto is computed. This can be ensured by multiplying the f_e of the receding window by a windowing function, which forces both ends of the f_e of the receding window to 0, as shown in [9]. By way of example, Figure 8.1 shows a fragment of f_e, with the estimated and predicted f_e signals composing the receding window, multiplied by the windowing function. Since $t_\text{w} = 60\,\text{s}$, the excitation force of the receding window is composed of $t_\text{w}^\text{est} = t_\text{w}^\text{pred} = 30\,\text{s}$ of estimated and predicted f_e. It is shown that, due to the windowing function, both the beginning of the estimated f_e and the end of the predicted f_e go to zero, making, thus, f_e periodic inside the receding window.

Note that the results shown in Figure 8.1, as well as the rest of the results shown in this chapter, are obtained for a η time series generated from a JONSWAP SDF (with $T_\text{p} = 8\,\text{s}$, $H_\text{s} = 2\,\text{m}$, and $\gamma = 3.3$) and using a CorPower-like device, shown in Figure 4.10(f).

8.2 Sensitivity Analysis

This section performs a sensitivity analysis of the moment-based controller, introduced in Section 8.1, to estimation and forecasting errors. For the sensitivity analysis to estimation errors, the excitation force signal is modified based on typical errors arising from the estimation process, observed in the comparison reported in Section 5.1. Regarding prediction, the possible errors arising from the prediction process, observed in Chapter 6, are simulated by changing the order of the predictor. To this end, an AR model is considered since, as shown in Section 6.2, if correctly identified (using a sensible order and sufficiently large identification data set), the obtained prediction accuracy is almost the same as the theoretically best achievable prediction.

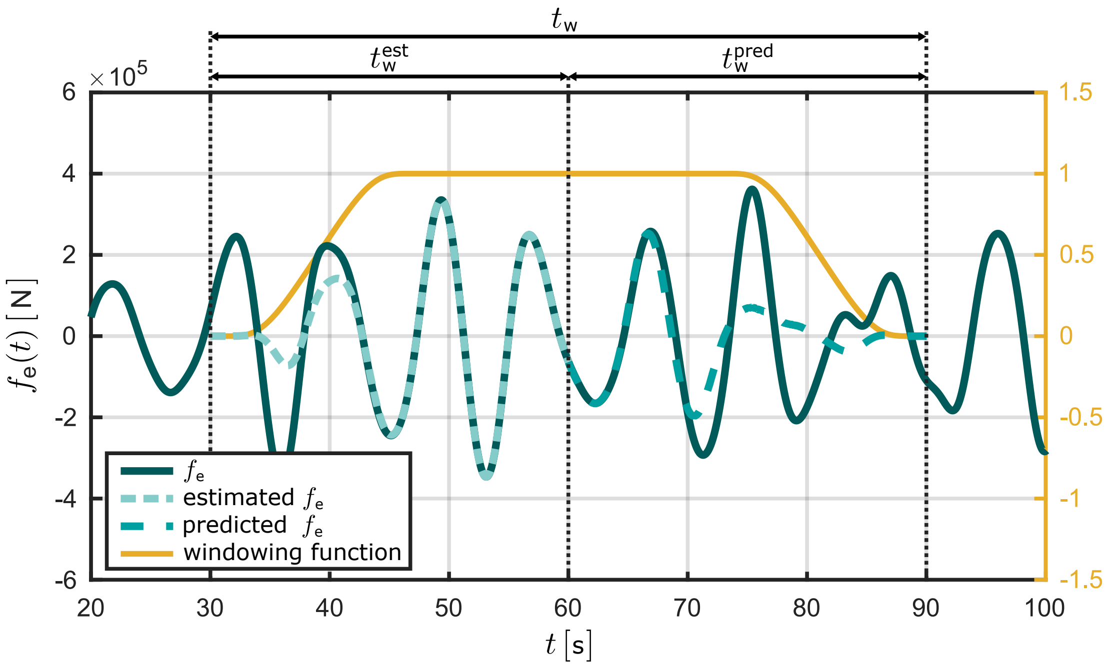

Figure 8.1: Target excitation force, along with the estimated and predicted f_e multiplied by the windowing function (yellow line, with the right axis).

In order to obtain meaningful results, it is found that, according to the central limit theorem [28], a mean of 30 simulations is required. The time-length of each simulation is set to 200 s, with a sampling period of $t_\mathrm{s} = 0.01$ s. The motion of the device is constrained to 2 m and 2 m/s for position and velocity, respectively. The receding horizon length t_w is set to 60 s, i.e. 30 s of both estimated and forecasted f_e, which provides sufficiently accurate results with mild computational requirements [50]. The windowing sampling period is set to $t_{\mathrm{s}_\mathrm{w}} = 1$ s, which means that the control force, optimised over a given receding window, is applied for 1 s, before a new receding window is considered, over which a new optimal control force is calculated.

8.2.1 Sensitivity to estimation errors

As discussed in the f_e estimators comparison, shown in Section 5.1, there are three main sources of errors affecting $\tilde{f}_\mathrm{e}$, arising from improper tuning of the estimator: errors in instantaneous amplitude (i.e. constant deviations in envelope), instantaneous phase errors (i.e. time-delays), and noise-polluted f_e estimation. Regarding the latter, the presence of measurement noise in $\tilde{f}_\mathrm{e}$, stems from the estimator tuning, such that high frequency noise (affecting motion sensors) is not filtered. Since the moment-domain representation of the input is composed of the frequencies in $A_\mathrm{sg}^\mathrm{MM}$ (see Equation (4.4)), any high frequency component in such input can be efficiently filtered out by a suitable selection of the frequencies in $A_\mathrm{sg}^\mathrm{MM}$. Therefore, the effect that a noisy f_e estimate could have on the controller is not analysed herein.

The imperfections, within the estimation stage, related to errors in instantaneous amplitude and phase are represented using the following criteria. First, define $\mathsf{F}_{a_\mathsf{e}} \in \Omega_\mathsf{F}$ and $\mathsf{F}_{\phi_\mathsf{e}} \in \Omega_\mathsf{F}$ as the error factors associated with the amplitude and phase of $\tilde{f}_\mathsf{e}$, respectively, with $\Omega_\mathsf{F} \in [0.75, 1.25]$. Additionally, $f_{\mathsf{e}_\mathsf{w}} \in \mathbb{R}^{n_\mathsf{w}}$ denotes the approximated wave excitation input in the receding window, composed of estimated and forecasted values (see Figure 8.1). The three following error sources are defined:

A: $f_{\mathsf{e}_\mathsf{w}}(t) \mapsto \mathsf{F}_{a_\mathsf{e}} f_{\mathsf{e}_\mathsf{w}}(t)$.
P: $f_{\mathsf{e}_\mathsf{w}}(t) \mapsto f_{\mathsf{e}_\mathsf{w}}(t + (\mathsf{F}_{\phi_\mathsf{e}} - 1)T_\mathsf{p})$.
AP: $f_{\mathsf{e}_\mathsf{w}}(t) \mapsto \mathsf{F}_{a_\mathsf{e}} f_{\mathsf{e}_\mathsf{w}}(t + (\mathsf{F}_{\phi_\mathsf{e}} - 1)T_\mathsf{p})$.

Case **A** assumes that[2] the amplitude of the estimated f_e is not estimated correctly, i.e. f_e is multiplied by a factor $\mathsf{F}_{a_\mathsf{e}}$, while case **P** considers the existence of a time delay (positive or negative) between estimated and true excitation force, proportional to the peak period T_p. Lastly, case **AP** combines both sources of error, by assuming that the estimated excitation force has both amplitude and phase errors, for all possible combinations of $\mathsf{F}_{a_\mathsf{e}}$ and $\mathsf{F}_{\phi_\mathsf{e}}$.

Figure 8.2 presents an illustrative example of an excitation force signal affected by amplitude and phase uncertainties, representing cases **A** and **P**, for a time-window t_w. In particular, the estimated and forecasted excitation force with $\mathsf{F}_{a_\mathsf{e}} = \mathsf{F}_{\phi_\mathsf{e}} = 1$, i.e. error-free, and for various values of $\mathsf{F}_{a_\mathsf{e}}$ and $\mathsf{F}_{\phi_\mathsf{e}}$ from 0.75 to 1.25, are shown.

It should be noted that, due to the underlying linearity of the AR model considered for the prediction, if $f_{\mathsf{e}_\mathsf{w}}$ is modified either by scaling, shifting in time, or superposing both cases for the estimation time window, this modification propagates within the forecasted time-window in the exact same manner. In other words, the sources of estimation error described in cases **A**, **P**, and **AP** affect the forecasted signal in the exact same proportions.

Lets define now the performance indicator $\mathsf{E}_\mathsf{rel}^\mathsf{est}(\mathsf{F}_{a_\mathsf{e}}, \mathsf{F}_{\phi_\mathsf{e}}) = {}^{\mathsf{E}_\mathsf{abs}(\mathsf{F}_{a_\mathsf{e}}, \mathsf{F}_{\phi_\mathsf{e}})}/_{\mathsf{E}_\mathsf{abs}(1,1)}$, where $\mathsf{E}_\mathsf{abs}(\mathsf{F}_{a_\mathsf{e}}, \mathsf{F}_{\phi_\mathsf{e}})$ is the absorbed energy, throughout the complete simulation time, for any pair of values $(\mathsf{F}_{a_\mathsf{e}}, \mathsf{F}_{\phi_\mathsf{e}})$, and $\mathsf{E}_\mathsf{rel}^\mathsf{est}$ represents the ratio between the absorbed energy under the moment-based control strategy, with and without the presence of estimation errors. Figures 8.3(a) and (b) show the performance results for cases **A** and **P**, in terms of $\mathsf{E}_\mathsf{rel}^\mathsf{est}(\mathsf{F}_{a_\mathsf{e}}, 1)$ and $\mathsf{E}_\mathsf{rel}^\mathsf{est}(1, \mathsf{F}_{\phi_\mathsf{e}})$, respectively. For case **A**, it can be observed that, even under an amplitude deviation of 25% from its true value, the absorbed energy always remains above 90% of its optimal achievable performance (computed without any estimation amplitude or phase errors). In other words, deviations in amplitude, for the estimated wave excitation force, generate only small deviations in absorbed

---

[2] Note that, from now on, the instantaneous amplitude and instantaneous phase are referred to as amplitude and phase, respectively.

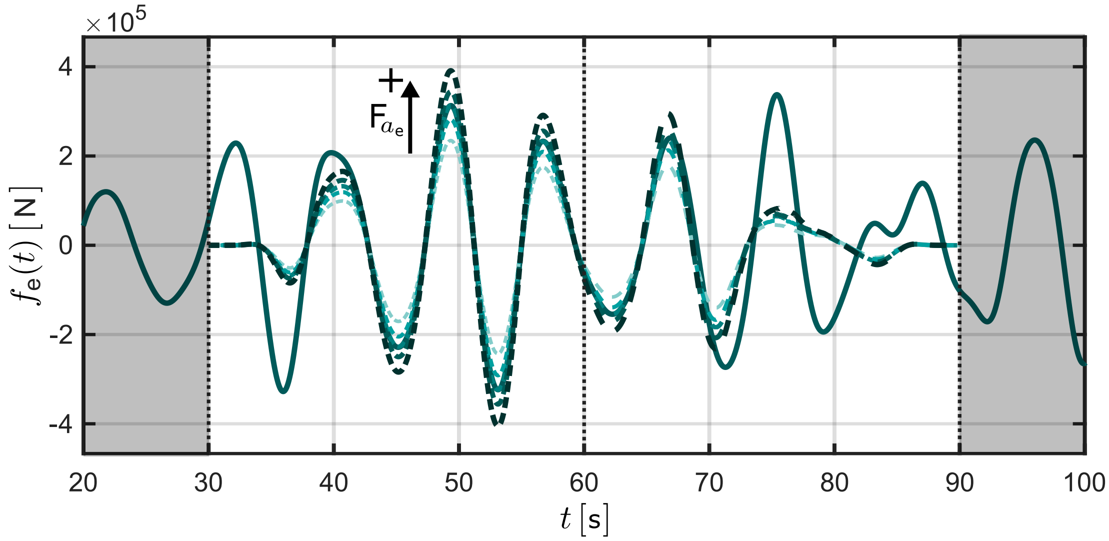

(a) $f_{\mathrm{e}_\mathrm{w}}(t)$ considering different amplitude errors (case **A**).

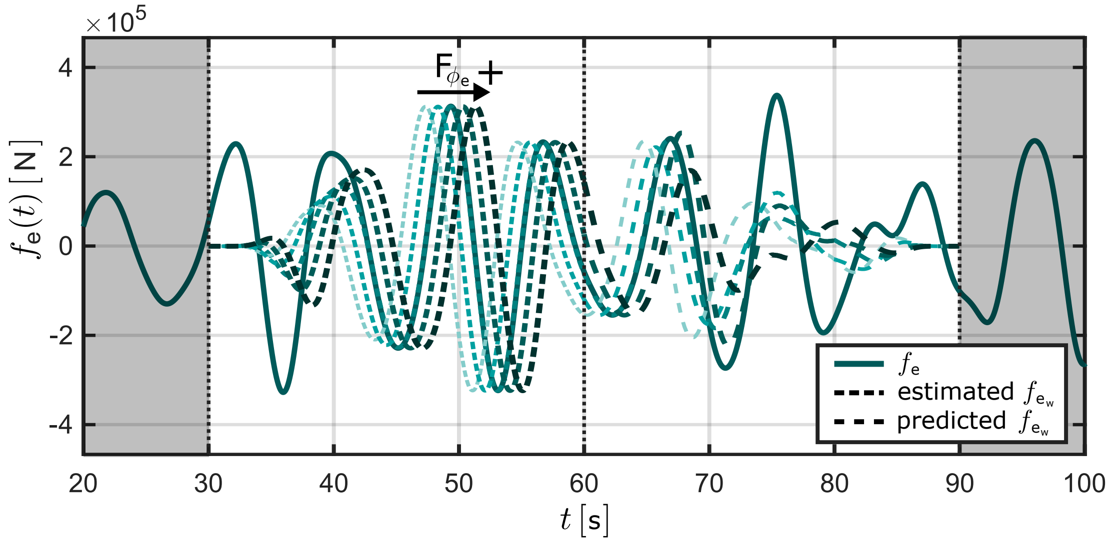

(b) $f_{\mathrm{e}_\mathrm{w}}(t)$ considering different phase errors (case **B**).

Figure 8.2: Illustrative example of cases (a) **A** and (b) **P**, for a particular $f_{\mathrm{e}_\mathrm{w}}$.

energy under controlled conditions. This is clearly not the case for phase deviations, i.e. case **P**, where a delay of ±10% of the peak period (around 0.8 s, for this case study) not only dramatically affects the energy absorption, but actually generates negative power (the device absorbs energy from the electric grid). This clearly indicates that great care should be taken to tune the estimator to guarantee phase synchronisation with the target wave excitation signal, hence achieving optimal energy absorption, under controlled conditions.

Finally, Figure 8.4 shows results for case **AP**, where errors in amplitude and phase are analysed simultaneously. Similarly to case **P**, Figure 8.3(b), it is clear that the presence of a time delay (positive or negative) has a much greater impact on energy absorption than any existing differences in estimated amplitude. Interestingly, while

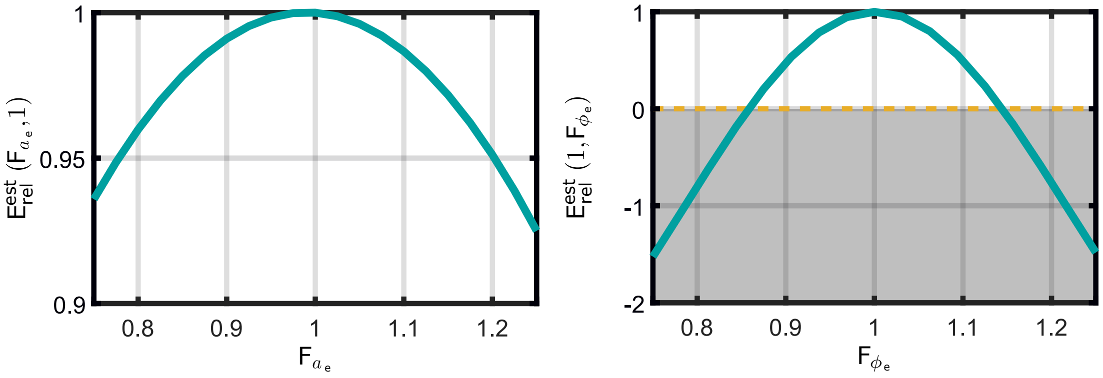

(a) E_{rel}^{est} considering case **A**. **(b)** E_{rel}^{est} considering case **P**.

Figure 8.3: $E_{rel}^{est}(F_{a_e}, F_{\phi_e})$ for cases (a) **A** and (b) **P**. A E_{rel}^{est} value below zero indicates negative energy absorption, as illustrated with the grey area in (b), with the dashed-orange line representing the zero energy absorption limit.

positive or negative delays have an almost symmetric effect, under-prediction of the wave excitation force amplitude has less impact on performance than over-prediction. Note that this behaviour is consistent with that of Figure 8.3.

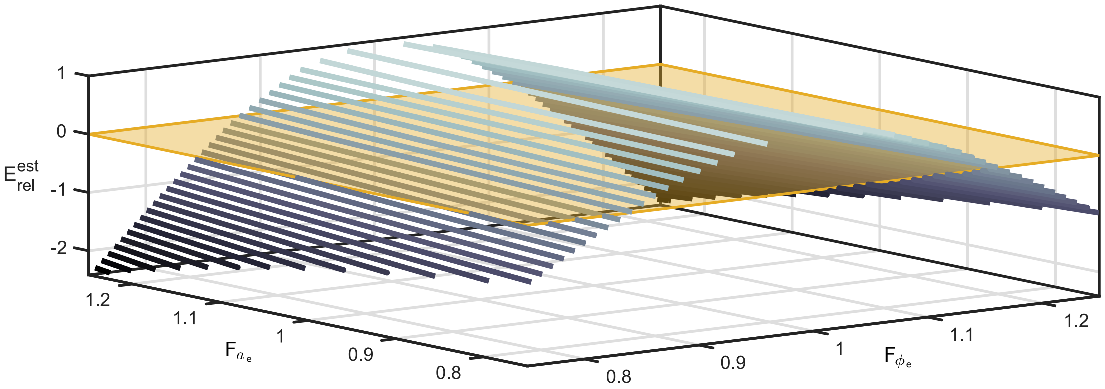

Figure 8.4: $E_{rel}^{est}(F_{a_e}, F_{\phi_e})$ for case **AP**. A E_{rel}^{est} value below zero indicates negative energy absorption, delimited with the orange plane.

8.2.2 Sensitivity to forecasting errors

This section considers errors arising purely from the forecasting procedure, i.e. assuming that the estimator is well tuned (achieving convergence towards the target f_e), and that any potential mismatch is only present within the forecasted window. Figure 8.5 presents performance results in terms of the indicator $E_{rel}^{pred}(t_{pred}^{0.99}) = E_{abs}(t_{pred}^{0.99})/E_{abs}(5)$, where the operator $E_{abs}(t_{pred}^{0.99})$ refers to the energy absorbed, assuming a forecast accuracy within 99% and 100%, for $t_{pred}^{0.99}$ seconds. In other words, E_{rel}^{pred} is the ratio of absorbed energy, under controlled conditions, between energy extraction assuming different $t_{pred}^{0.99}$ and with a forecast with more than 99% of accuracy 5-seconds-ahead, obtained using (in this case) an AR model order $n_{\text{ord}}^{\text{AR}} = 200$. Note that, even though the simulation sampling period is $t_{\text{s}} = 0.01\,\text{s}$, as explained in Section 6.2, the data is re-sampled to $t_{\text{s}} = 0.1\,\text{s}$ for the prediction stage, in order to reduce the order of the required AR model.

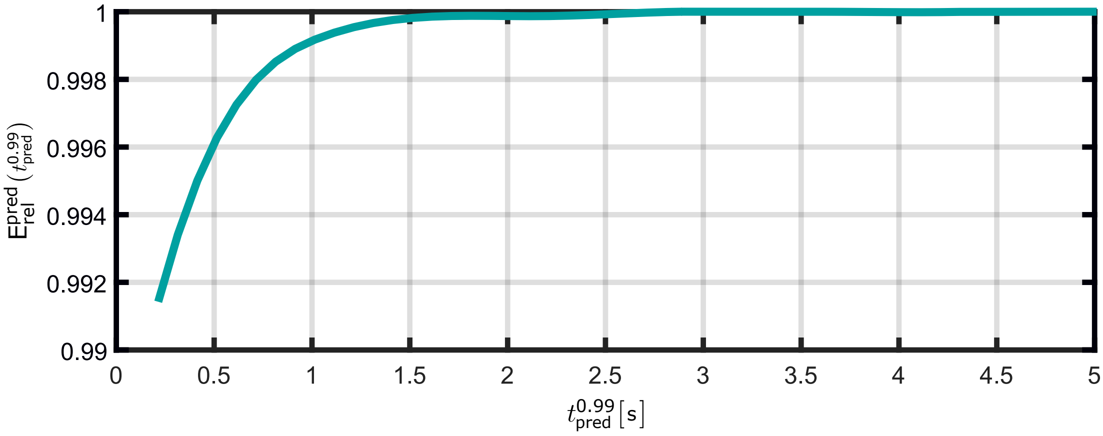

Figure 8.5: Sensitivity analysis with respect to forecasting errors in terms of the performance indicator $E_{\text{rel}}^{\text{pred}}$.

By way of example, Figure 8.6 illustrates a section of forecasted excitation force signal, predicted using an AR model of different orders. One can notice that, even with $n_{\text{ord}}^{\text{AR}} = 50$, i.e. considering five seconds of past values to predict future values, the prediction error over the first 3-4 seconds is close to zero. This can be explained by the fact that f_{e} can be considered as a low-pass filtered representation of η, since the high-frequency components of η are absorbed by the dynamics of the device. Therefore, as discussed in Section 6.2.2 (in Figure 6.6), where the accuracy obtained for the prediction of filtered and non-filtered η is compared, if the signal to be predicted does not contain significant high-frequency components, the predictor behaves accurately for a longer time horizon, which is clearly not the case for signals with high-frequency content. Unlike the estimation case discussed in Section 8.2.1, where it is shown that deviations from the target excitation force can effectively generate negative power absorption, the impact of forecasting errors alone, for the moment-based controller considered in this chapter, is almost negligible. Even with $t_{\text{pred}}^{0.99} = 1\,\text{s}$, the controller is able to perform within 99% of its optimal performance. This can be explained by the fact that, even though the optimal f_{pto} is calculated for the complete receding window, only the first $t_{\text{s}_{\text{w}}}$ seconds are applied. Therefore, even though the f_{e} prediction is not accurate for large t_{hor}, it does not significantly affect the obtained $f_{\text{pto}}^{\text{opt}}$ for the first seconds of the predicted window, provided that the first $t_{\text{s}_{\text{w}}}$ seconds of the predicted f_{e} represent (to some extent) accurately the target f_{e}.

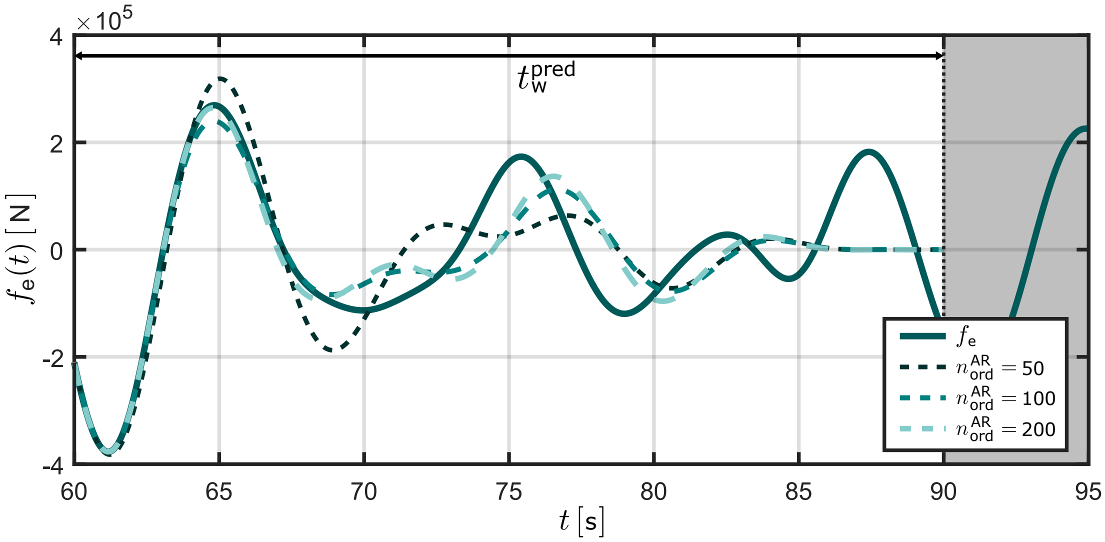

Figure 8.6: Illustrative example of a forecasted (and windowed) predicted excitation force signal for different AR model orders.

8.3 Conclusions

Two main conclusions can be directly drawn from this chapter: f_e forecasting errors have a negligible impact on the overall performance of the control strategy, while errors induced by the f_e estimators can effectively generate negative power absorption. This chapter shows that, for the analysed control strategy, errors in the f_e instantaneous phase are more important than errors in instantaneous amplitude or noise in the f_e estimate. In particular, phase errors (positive or negative) in the estimated excitation force have a substantial impact on the energy maximising performance of the controller, suggesting that great care should be taken in tuning the estimator such that (instantaneous) phase synchronisation is achieved with the target excitation force. Since the optimal control force is only applied over the first t_{sw} seconds, the forecasting accuracy for prediction horizons larger than $t_{hor} > t_{sw}$ does not significantly affect the performance of the absorbed energy. Therefore, using a simple AR model, which obtains accurate results over the first seconds of f_e prediction, even though the prediction accuracy fades out to zero relatively quickly, it is shown to be sufficient to obtain similar energy absorption to that obtained using almost one peak period of perfect knowledge of f_e (decreasing the energy absorption by less than 1%).

Finally, it should be noted that a separate sensitivity analysis (as the one shown in this chapter) should be carried out for the different control strategies, depending on the sensitivity of such control strategy to different estimation/prediction errors, to choose the most appropriate estimator/predictor strategy.

9

Conclusions

Contents

9.1 Conclusions

The conversion of the current global energy mix, from a fossil-fuel-dominated energy mix to a low-carbon energy mix, is one of the most important challenges of this century. To this end, wave energy can provide a significant complement to other renewable energy technologies. Despite the significant development of different wave energy converter technologies during the recent decades, none of the technologies has yet demonstrated economical viability. In order to reach such economic feasibility, several proposals can be found in the literature as, for example, optimal control of wave energy converters or the deployment of devices in large arrays.

As introduced in Chapters 1-3, the majority of WEC optimal control strategies require knowledge of previous, current, and future excitation force f_e acting on the device, which is an unmeasurable quantity for the WEC case. Thus, in order to provide the controller with knowledge of f_e, such force is usually estimated based on other measurements (such as WEC motion) and then predicted in the future using prediction strategies.

In essence, this thesis provides a comprehensive analysis of the estimation/prediction techniques available in the literature, in order to evaluate whether they are ready to be applied in real WEC control strategies or not. To this end, such estimation/prediction techniques, which have been developed mostly for linear hydrodynamic models, are investigated as a previous step to the analysis of estimation/prediction techniques under nonlinear conditions. From the sensitivity analysis of the controller to estimation/prediction errors it can be deduced that, since prediction errors have negligible impact on the controllers performance, simple and linear prediction strategies, such as the AR model, may provide sufficiently accurate results even under nonlinear conditions, avoiding the use of any nonlinear prediction strategy. On the contrary, while the necessity of extending the estimation techniques to include nonlinear WEC models is uncertain, this thesis highlights the estimation errors which affect the controller performance the most. As a result, the thesis provides an overview of the aspects which should be taken into account at the stage of tuning an estimation/prediction technique, in order to not affect the performance of the controller.

From the f_{e} estimators comparison, provided in Chapter 5, it is concluded that estimation techniques using WEC motion measurements are the most feasible techniques. In particular, the KFHO and ULISE approaches, which show good performance in terms of achieved accuracy and no phase shift between the estimated and the reference f_{e}, and the UIO method, which is the only approach able to consider model uncertainty, are found to be the most feasible estimators. However, from the sensitivity analysis shown in Chapter 8, it is found that the error in the f_{e} instantaneous phase is more important than the error in instantaneous amplitude or obtaining a noisy f_{e} estimate. Therefore, using other estimation techniques with the controller, such as EKFHO and ASMO, which, although they obtain higher estimation errors (2 or 3 times higher than the KFHO estimator, respectively), would obtain similar energy absorption performances to those obtained using the KFHO or ULISE estimators. On the contrary, the highest instantaneous phase delay reported in Table 5.2 is 0.16 s (obtained using the FAUIE estimator) which, for the moment-matching-based receding-horizon control strategy, would suggest a decrease of around 10% of the energy absorption, compared to the case where no phase delay is considered.

Regarding prediction strategies, Chapter 6 shows that the AR model is not only a simple and accurate predictor but, if correctly identified (using a large enough training dataset), the obtained prediction accuracy is close to the theoretically best achievable accuracy. Furthermore, Chapter 8 shows that, for the moment-matching-based receding-horizon controller, the f_{e} prediction obtained using an AR model is accurate enough for the controller to obtain a performance comparable to that obtained from exact knowledge of f_{e}. This can be reasoned by the fact that, even though the optimal control force is optimised over the entire receding window, only the first $t_{\mathrm{s_w}}$ seconds of the control force is applied to the WEC. Chapter 6 shows that the AR model usually obtains accurate prediction for prediction horizons relatively small compared to the wave peak period (as, for example, 1 or 2 s for a peak period of 8 s) and, then, the prediction accuracy fades to zero relatively quickly. Therefore, if t_{s_w} is also chosen to be relatively small compared to the wave peak period, the performance obtained by the controller is similar to that obtained from exact knowledge of f_e over the whole receding window. For WEC arrays, Chapter 7 shows that, while the complex wave field of a WEC array degrades the independent estimator performance, the performance of the global estimation strategy is relatively consistent with that of the isolated body case. This is important, since it allows for optimisation of the array layout, considering any optimisation objective, without affecting the obtained f_e estimation performance. The global predictor not only achieves better prediction accuracy than the independent predictor, but also outperforms the isolated body case for the devices of the array positioned down-wave (if there are any), since they get advance information of the incoming wave from the WECs positioned up-wave. As shown in Chapter 8, f_e prediction has almost negligible impact on the moment-matching-based receding-horizon controller and, therefore, the controller performance obtained using either independent or global predictors would be almost the same. However, this might not be the case for other controllers, for which longer prediction horizon are required and, hence, a global prediction technique may be necessary.

A moment-matching-based frequency-domain identification strategy is developed in Chapter 4, which obtains a monotonically decreasing error with the increasing order of the parametric model. Additionally, it is able to preserve almost all the physical properties of the radiation convolution term subsystem, which none of the other identification techniques available in the literature achieves. Additionally, by using the MIMO extension of the moment-matching-based identification strategy for WEC arrays, Chapter 7 shows how the computational time required by the global estimator strategy can be reduced without affecting the obtained estimation accuracy.

9.2 Future work

The work presented in this thesis highlights several direction for further work:

- The comparison of estimators, presented in Chapter 5, considers linear WEC models for the estimators along with a CFD simulation. However, due to the reduced motion of the device, the simulation can be considered linear. Thus, it would be beneficial to investigate the effect that considering a nonlinear simulation of a WEC device under control conditions would have on the performance of the different estimators. One of the difficulties of such a comparison is that, under control conditions, the WEC motion is maximised and, therefore, the definition of a reference f_e, as used in Chapter 5, does not hold any more, since linear potential flow assumes small WEC motion (as explained in Chapter 2). Thus, a new way to address the performance of the estimators has to be considered. Additionally, how the estimation errors (arising from using a linear WEC model for the estimator on a nonlinear WEC system) affect the performance of the controller should be investigated, to assess if the analysed estimators have to be extended to include nonlinear WEC models.

- The sensitivity analysis shown in Chapter 8 should be carried out for other WEC control strategies, to see how the different estimation/prediction errors affect the obtained performance of the WEC. By doing so, it would be possible to select the most appropriate estimation/prediction strategy for each controller.
- As explained in Chapter 4, two extensions have been proposed for the moment-matching-based identification strategy: the first one to preserve passivity and, the second one, to consider multiple-input multiple-output systems. However, none of those extensions have been yet implemented in the FOAMM toolbox and, therefore, are part of pertinent future work.

Appendices

A

FOAMM Toolbox

Contents

This appendix provides a description of the FOAMM toolbox, with all the different operation modes and options, along with a step-by-step example and some using recommendations to illustrate how to fully exploit its potential.

Note that some of the variables recalled in this appendix have been previously introduced in the description of the moment-matching theory, in Section 4.1.1.

A.1 Toolbox description

In this section, how to get and install FOAMM, and which are the provided files is shown. Additionally, the different identification methods and options that FOAMM comprises are introduced and, finally, which are the input variables required by FOAMM, along with the provided output variables are detailed.

A.1.1 Platform requirements and installation

Even though, as shown in Equations (4.11) and (4.14), FOAMM requires of an optimisation procedure to obtain the final parametric model, since the application is created using the MATLAB compiler, FOAMM runs on a plain MATLAB distribution, i.e. no other toolboxes/applications are required. At the time of writing, two versions of FOAMM are available, one for the Windows Operating Systems (OSs) (tested for Windows 7, 8, and 10), and another one for Linux OSs (tested for Ubuntu 18, and CentOS 6.10 and 7.4). In both OSs, different MATLAB versions have been tested (years 2012, 2015, 2017, and 2018).

The files can be downloaded from [173] for free. Since FOAMM is an executable, having the correct Matlab runtime version installed on the computer is required[1], for which the installer is provided in the folder "Matlab Runtime" (among the downloaded files, as explained in Section A.1.2). After installing the MATLAB runtime, for which an active internet connection is needed, the application effectively runs in a stand-alone fashion on a plain MATLAB.

It should be noted that the first run of the application is considerably slower than the subsequent ones, which is indeed a known issue, when using the MATLAB compiler. Additionally, for the Linux version, administrative access is required for both the installation of the MATLAB Runtime, and the use of the application.

A.1.2 Provided files

In this subsection, the files compressed in "FOAMM.rar" are listed and explained:

MatlabRuntime This file, located inside the "Matlab Runtime" folder, is the executable, required to install the correct version of the MATLAB runtime.

Main.m This is the main file and the user interface to the application. The file loads the frequency-domain data contained in **Data.mat**, used to perform the identification, and allows to change between the different modes and options of the application. **'Main.m** set-ups the required variables, and explicitly calls the executable file **FOAMM**. It should be noted that this file provides the only way to select between the different modes of the application.

---

[1] Note that installing the Matlab runtime will not change any other functionality of the computer.

FOAMM This is the executable file of the application and is explicitly called by **"Main.m"**. For the Windows version, the extension of the file is ".exe".

Data.mat This file contains the frequency-domain data to be identified (computed with any BEM code) and it should be provided by the user, following the specific input format, detailed in the following subsections. In "FOAMM.rar" an example **Data.mat** file is provided, with the hydrodynamic coefficients of a cylinder with 5 m radius and 10 m draft.

A.1.3 Identification methods

In order to select the interpolation frequencies $\mathcal{F}$, FOAMM offers the following three identification methods:

Manual method The user selects the desired set of frequencies to achieve moment-matching. The order will be twice the number of frequencies selected.

Automatic method The user selects a final number of interpolation points (β^{MM}) and, additionally, a subset of frequencies to interpolate (with size denoted by α^{MM}). This method optimises the value of the $\beta^{\mathsf{MM}} - \alpha^{\mathsf{MM}}$ interpolation frequencies. It should be noted that, if the user does not pre-select a set of frequencies i.e. $\alpha^{\mathsf{MM}} = 0$, all the β^{MM} interpolation points are optimised by FOAMM.

Optimised-automatic method This method is essentially the automatic method for the selection of the matching frequencies, but it also selects the number of interpolation points β^{MM} automatically. Starting from α^{MM}, this method keeps adding (and optimising) interpolation frequencies until the approximated model satisfies both an absolute and a relative error thresholds specified by the user in the "Options" structure.

A.1.4 Application options

Every option of the application can (only) be changed using the structure **Options** from the **Main.m** file. The different variables stored in the structure can be accessed and tuned as follows:

Options.Mode (integer)

default **0** Identify the radiation impulse response $K_{\mathsf{r}}(\omega)$ of the device.

1 Identify the force-to-velocity dynamics $H(\omega)$ of the device.

Options.Method (integer)

default **0** Manual identification method.

1 Automatic identification method.

2 Optimised-automatic identification method.

Options.FreqRangeChoice (string or float)

default **'G'** Select the frequency range from a plot.

'C' When asked, enter a vector with the lower and upper bounds of the frequency range in MATLAB's command window, as $[\omega_l, \omega_u]$.

VEC Directly enter a vector with the lower and upper bounds of the frequency range as **VEC**$=[\omega_l, \omega_u]$.

Options.FreqChoice (string or float)

default **'G'** Select the set of desired interpolation frequencies from a plot.

'C' When asked, enter the desired set of interpolation frequencies in MATLAB's command window as a vector, $\left[\omega_1, \dots, \omega_{\beta^{\mathsf{MM}}}\right]$.

VEC Directly enter a vector with the set of interpolation frequencies as **VEC**$=\left[\omega_1, \dots, \omega_{\beta^{\mathsf{MM}}}\right]$.

Options.FreqNumChoice (string or integer) (if **Options.Method** $= 1$)

default **'C'** When asked, enter the number of frequencies to interpolate $\beta^{\mathsf{MM}} > 0$ in MATLAB's command window.

INT Directly enter the desired number of interpolation frequencies $\beta^{\mathsf{MM}} > 0$.

Options.Optim (optimisation-related options)

integer **Options.Optim.InitCond** Number of initial conditions considered on the optimisation. Default = 50.

float **Options.Optim.Tol** Tolerance on the final value of the optimisation. Default = $1e^{-5}$.

integer **Options.Optim.maxEval** Maximum number of evaluations considered for the optimisation. Default = $1e^{3}$.

integer **Options.Optim.maxIter** Maximum number of iterations considered for the optimisation. Default = 200.

float **Options.Optim.StepTol** Step tolerance value for the optimisation. Default = $1e^{-6}$.

float **Options.Optim.ThresRel** (if **Options.Method** = 2) Relative error threshold. Default = 0.03.

float **Options.Optim.ThresAbs** (if **Options.Method** = 2) Absolute error threshold. Default = 0.1.

If any of the labels inside the structure **Options** is changed, the application will not recognise the variables and the default values will be used. Additionally, if the selected value is wrong, the application will ask the user to correct it.

A.1.5 Input and output variables

The frequency-domain data, used to perform the moment-matching-based identification, is loaded from the user supplied file **Data.mat**. This file with ".mat" extension must contain all the information regarding the frequency-domain data, considered for the identification process. In the following, a detailed description of the required format is provided, so that the application can load the data correctly.

†**A** (vector, float, $n_\omega \times 1$) Radiation added mass ($A_{\text{r}}(\omega)$).
†**B** (vector, float, $n_\omega \times 1$) Radiation damping ($B_{\text{r}}(\omega)$).
†**w** (vector, float, $n_\omega \times 1$) Frequency vector (ω).
Mu (scalar, float, if **Options.Mode** $= 0$) Radiation infinite added mass (μ_∞). If this value is not supplied, the application will automatically calculate its value using Ogilvie's relations. However, the author recommends users to provide it in order to reduce possible inaccuracies.
Mass (scalar, float, if **Options.Mode** $= 1$) Sum of mass terms (usually the mass of the structure under analysis, M).
K (scalar, float, if **Options.Mode** $= 1$) Sum of stiffness terms (such as, for example, the sum of S_{h} and S_{pto}).
D (scalar, float, if **Options.Mode** $= 1$) Sum of damping terms (such as, for example, D_{pto}).

Note that, if any of the variables denoted with † is named differently, the application will halt. Once the identification process is finished, FOAMM will return the following variables:

A_ss (matrix, float, $2\beta^{\text{MM}} \times 2\beta^{\text{MM}}$) Dynamic matrix of the final model.
B_ss (matrix, float, $2\beta^{\text{MM}} \times 1$) Input matrix of the final model.
C_ss (matrix, float, $1 \times 2\beta^{\text{MM}}$) Output matrix of the final model.
MAPE (scalar, float) Mean absolute percentage error MAPE of the approximation, which is defined as

$$\text{MAPE} = \frac{1}{n}\sum_{i=1}^{n}\left|\frac{f(i)-\tilde{f}(i)}{f(i)}\right|, \tag{A.1}$$

where f and $\tilde{f}$ are the frequency responses of the target and the final model, respectively, and n is the number of frequencies contained in the considered frequency-range. Note that the obtained MAPE will vary from 0 to 1, being 1 a 100% of error.
Frequencies (vector, float, $1 \times \beta^{\text{MM}}$) Value of the chosen frequencies.
FreqRange (vector, float, 1×2) Value of the minimum and maximum frequencies of the chosen frequency range.
Mu (scalar, float, if **Options.Mode** $= 0$ and **Mu** not provided) Automatically calculated radiation infinite added mass.

A.2 Application example

In this subsection, a step-by-step example is shown of how to use FOAMM to identify a finite order parametric model of the radiation impulse response and complete force-to-motion dynamics. The hydrodynamic parameters used, correspond to a heaving cylinder with a 5 m radius, representing the example case provided in the **data.mat** file (see Section A.1.2). In the following, the three identification methods are explained and the options are varied between the subsections, in order to exemplify all the different operating modes and options.

A.2.1 Manual method

In the following, an example of how the **Main.m** file is shown, for the operation of the toolbox in the manual mode. For the sake of clarity, the majority of the comments and spaces of the original **Main.m** file are omitted:

Listing A.1: Example code of the **main.m** file.

```
 1 %% Load hydrodynamic parameters ----------------------------------------
 2 clear all; clc
 3 load('data.mat')
 4 K = Sh;
 5
 6 %% Options structure -------------------------------------------------
 7 Options.Mode = 0;
 8 Options.Method = 0;
 9 Options.FreqRangeChoice = 'G';
10 Options.FreqChoice = 'G';
11 Options.FreqNumChoice = [];
12 Options.Optim.InitCond = 50;
13 Options.Optim.Tol = 1E-6;
14 Options.Optim.maxEval = 100;
15 Options.Optim.StepTol = 1E-6;
16 Options.Optim.ThresRel = 0.1;
17 Options.Optim.ThresAbs = 0.03;
18
19 %% Run application ---------------------------------------------------
20 save('temp_file.mat')
21
22 system('FOAMM');
23
24 load('temp_file.mat')
25 delete('temp_file.mat')
26 %% -------------------------------------------------------------------
```

As shown in Listing A.1, the file **Main.m** is composed of three different parts. The commands in the first part (from line 1 to 5) clear the variables of the MATLAB workspace, and load the hydrodynamic parameters saved in **data.mat**. Since no PTO is considered, the only stiffness term in this example is the hydrostatic stiffness and, therefore, the variable **K** is defined by S_{h} (line 4). For the same reason, no damping term (**D**) needs to be defined. In the middle section of the code in **Main.m** (from line 6 to 18), the different working options are defined. Finally, at the end (from line 19 to 26), all the variables are saved in a temporary file (**temp_file.mat**), which is loaded by FOAMM to subsequently compute the identification. After the identification process is finished, the updated temporary file, which contains all the results obtained by the application, is loaded and deleted.

For this example, the parametric model of the radiation impulse response is identified (**Options.Mode=0**, line 7), using the manual method (**Options.Method=0**, line 8). Both, the frequency range and the frequencies are chosen, using the graphical interface (**Options.FreqRangeChoice='G'**, line 9, and **Options.FreqChoice='G'**, line 10, respectively). Therefore, when **Main.m** is run, a graph, as the one shown in Figure A.1, will appear, asking the user to specify the frequency range[2].

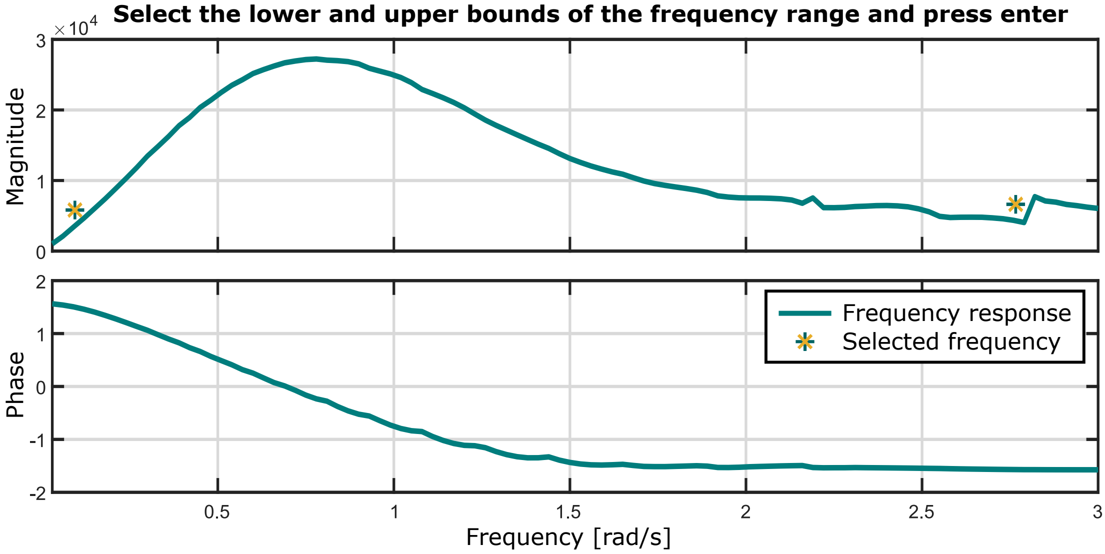

Figure A.1: Graphical interface to select the frequency range for the approximation.

As explained in Section 4.1.2, the frequency range will depend on the frequency distribution of the input signal. Thus, as shown in Figure 4.4, choosing a frequency range from around 0.1 to 2.75 $^{\mathrm{rad}}/_{s}$, the whole input frequency spectrum is covered and, therefore, for any possible operational point, the identified model will behave as the original system.

---

[2] It should be noted that the graphs shown by FOAMM are not exactly as shown in this thesis, for which the aspect ratio, colours and line-thicknesses are changed according to the format of the thesis.

Once the frequency range is correctly specified, another graphical interface appears, asking for the interpolation frequencies, showing the radiation impulse response just for the previously chosen frequency range (see Figure A.2). For this case, only a point around the resonant frequency is chosen as interpolation frequency.

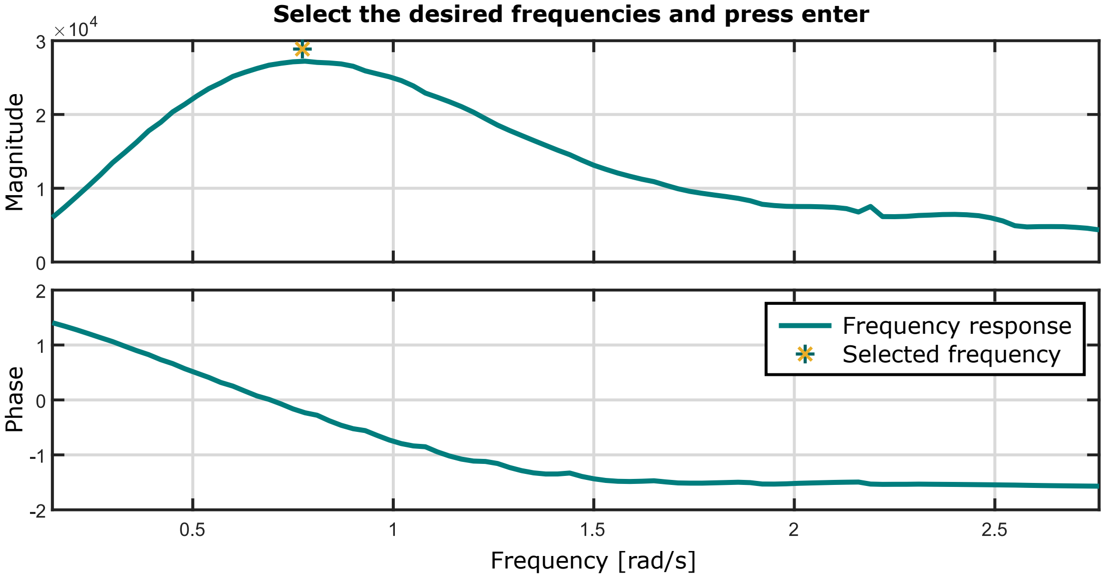

Figure A.2: Graphical interface to select the desired set of interpolation frequencies for the approximation.

While FOAMM is optimising the value of the eigenvalues, a wait bar, as shown in Figure A.3, is displayed. The wait bar shows the progress of the optimisation, along with a cancel button, which allows the user to stop the optimisation process. In case of stopping the optimisation (by pressing the cancel button), FOAMM will return the best model obtained before stopping the process. In the particular case of using the optimised-automatic method and cancelling the optimisation, the predefined error thresholds of such method (specified in **Options.Optim.ThresRel** and **Options.Optim.ThresAbs**) would not be taken into account, and the order which gives the best fitting accuracy will be returned as the resulting model.

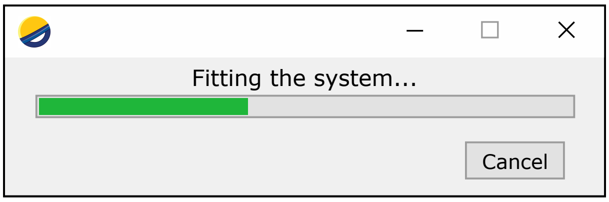
Fitting the system...

Figure A.3: Waiting bar showing the progress of the optimisation.

After the optimisation is finished, the resulting model, along with the target system, and the interpolation frequencies are displayed, as shown in Figure A.4. For this case, since a unique frequency was chosen, the error of the obtained model is MAPE≈0.22.

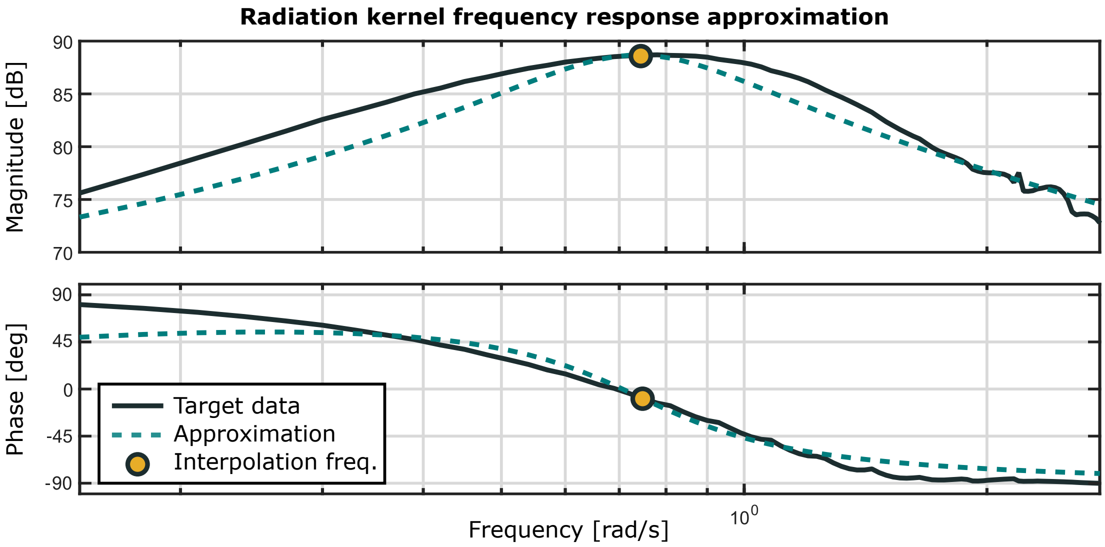

Figure A.4: Frequency response of the obtained parametric model of the radiation convolution term (dashed-blue), along with the target frequency response (solid-dark-blue) and the interpolation frequency (orange-dot) using the manual method. MAPE≈0.22.

A.2.2 Automatic method

In this subsection, apart from showing how to use the automatic method, which is selected by defining **Options.Method=1** (line 8 of Listing A.1), the force-to-velocity frequency response of the WEC is identified, instead of the radiation impulse response. Thus, in order to approximate the force-to-motion frequency response, the option **Options.Mode** needs to be set to 1 (line 7 of Listing A.1). Additionally, the following changes are made with respect to Listing A.1:

Listing A.2: Extra changes of the code shown in Listing A.1.

```
%% Options structure ------------------------------------------------
Options.FreqRangeChoice = 'C';
Options.FreqChoice = [];
Options.FreqNumChoice = 1;
```

In this case, the following message will appear in the command window of MATLAB, asking for the frequency range: *"Introduce a vector containing the lower and upper bounds of the desired frequency range (min=0.03, max=3):"*, where the shown minimum and maximum values correspond to the minimum and maximum values of the provided frequency vector. Then, the frequency range must be defined as a size 2 vector, with its values being inside the provided frequencies defined by the vector **w** from the file **data.mat**. If, as for this example case, enter is pressed without specifying anything (or writing an empty vector as [ ]), the whole vector of frequencies will be taken into account for the identification. Additionally, since no frequencies have been defined in **Options.FreqChoice**, the value of all the frequencies will be optimised.

Since **Options.FreqNumChoice=1** ($\beta^{\mathsf{MM}} = 1$), a parametric model with a single frequency is returned as result, depicted in Figure A.5, and with MAPE≈0.02.

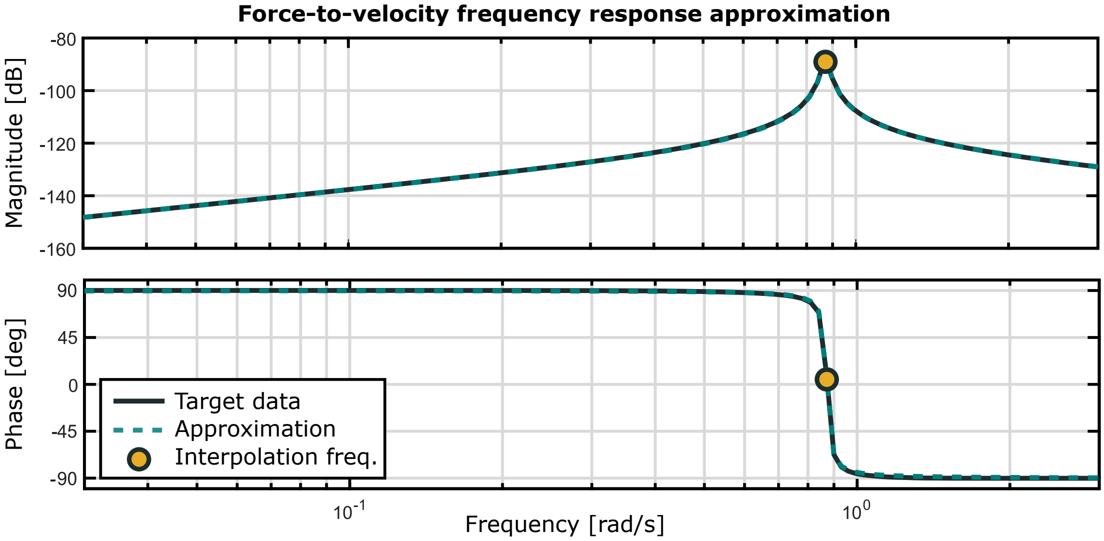

Figure A.5: Frequency response of the obtained parametric model of the complete force-to-velocity dynamics (dashed-blue), along with the target frequency response (solid-dark-blue) and the interpolation frequency (orange-dot) using the automatic method. MAPE≈0.02.

A.2.3 Optimised-automatic method

In order to run the optimised-automatic method, **Options.Method=2** needs to be selected (line 8 of Listing A.1). Additionally, the following changes are made with respect to Listing A.1:

Listing A.3: Extra changes of the code shown in Listing A.1.

```
%% Options structure ——————————————————————————
Options.FreqRangeChoice = [0.1 2.75];
Options.FreqChoice = 0.78;
```

Since the frequency range and an interpolation frequency are already defined for this case, FOAMM will directly proceed to the optimisation. During the optimisation, apart from the waiting bar, a graph (as shown in Figure A.6) will be displayed showing the MAPE, obtained for the different model orders that were tested.

This method will keep adding interpolation frequencies until the predefined absolute and relative error thresholds are satisfied, or the optimisation is stopped using the cancel button. It should be noted that the number of frequencies considered by the optimisation procedure will begin from the frequencies specified in **Options.FreqChoice**. Since a unique frequency is predefined for this example, it starts from 1, which would

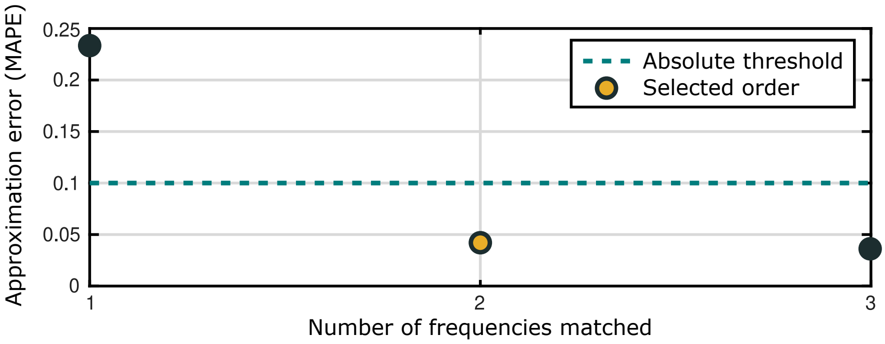

Figure A.6: Graph displayed while the optimised-automatic method is running.

also be the case if no frequency is predefined, with the only difference that the value of such interpolation frequency would also be subject to the optimisation.

The dash-blue line of Figure A.6 represents the defined absolute threshold, which is set to 0.1 (as the default value in **Options.Optim.ThresAbs**). For this application example, the optimisation considers up to three interpolation frequencies ($\beta^{\mathsf{MM}} = 3$) but, since the MAPE improvement with respect to $\beta^{\mathsf{MM}} = 2$ is less than the defined relative threshold (which is 0.03, as the default value in **Options.Optim.ThresRel**), the optimisation stops and chooses $\beta^{\mathsf{MM}} = 2$ as the optimal order. Finally, as for the other two methods, the resulting frequency response of the parametric model is displayed, shown in Figure A.7, which obtains MAPE≈0.04.

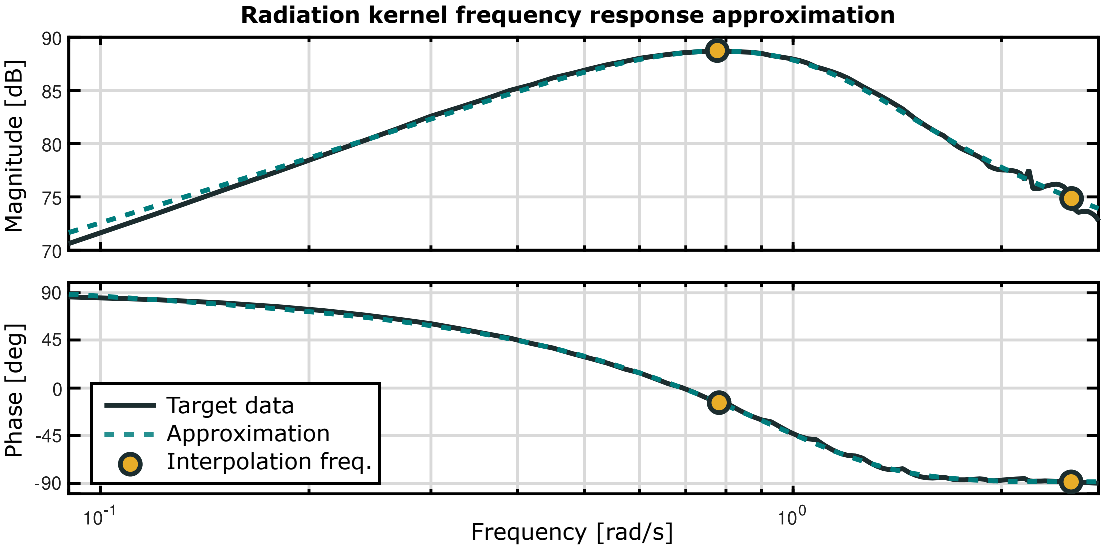

Figure A.7: Frequency response of the obtained parametric model of the radiation convolution term (dashed-blue), along with the target frequency response (solid-dark-blue) and the interpolation frequencies (orange-dots) using the optimised-automatic method. MAPE≈0.04.

A.3 Recommendations

This section provides some recommendations for the use of FOAMM, with which, based on the author's and other collaborators' opinion, the results obtained using FOAMM can be improved.

A.3.1 Use the manual method

Even though the application comes with different automated method, the author highly recommend a manual choice of the interpolation frequencies, based on the system dynamics to be identified. In fact, the option of performing a suitable selection of points to interpolate in the frequency-domain, is one of the most attractive characteristics of moment-matching. For example, the user might want to select, as one sensible choice, the resonant frequency of the structure to be identified, as shown in Figure A.2.

A.3.2 Specify the important frequencies

When not using the manual method, it is convenient to specify the most important frequencies to help the optimisation process and improve the accuracy of the obtained model. Thus, instead of giving the algorithm the freedom to look for the best frequency, a sensible choice would be to pre-select the resonant frequency and, if $\beta^{\mathsf{MM}} = 1$ is not enough to accurately represent the system (and there is no other important frequency), let the algorithm check for the best value of the subsequent frequencies. On the contrary, if the resonant frequency is not specified, and the optimisation variables are not correctly selected, FOAMM might not find the combination in which the resonant frequency is contained, obtaining a suboptimal parametric model. As an example, Figure A.8 shows a parametric model of the radiation impulse response of order 2 (as shown before in Figure A.4), where the resonant frequency is not pre-selected and the optimisation variables are not correctly selected, i.e. a single initial condition is chosen for the optimisation[3]. In this case, the obtained interpolation frequency is $1.5\,{}^{\mathsf{rad}}\!/_{s}$, which lead to an approximation error of MAPE≈0.38. However, if the resonant frequency is pre-selected, even though the optimisation variables are still not correctly selected, the obtained error is MAPE≈0.22 (as shown in Figure A.4).

---

[3] Even though it is not realistic to optimise using a unique initial condition, this option is chosen to emphasise the effect of this possible error.

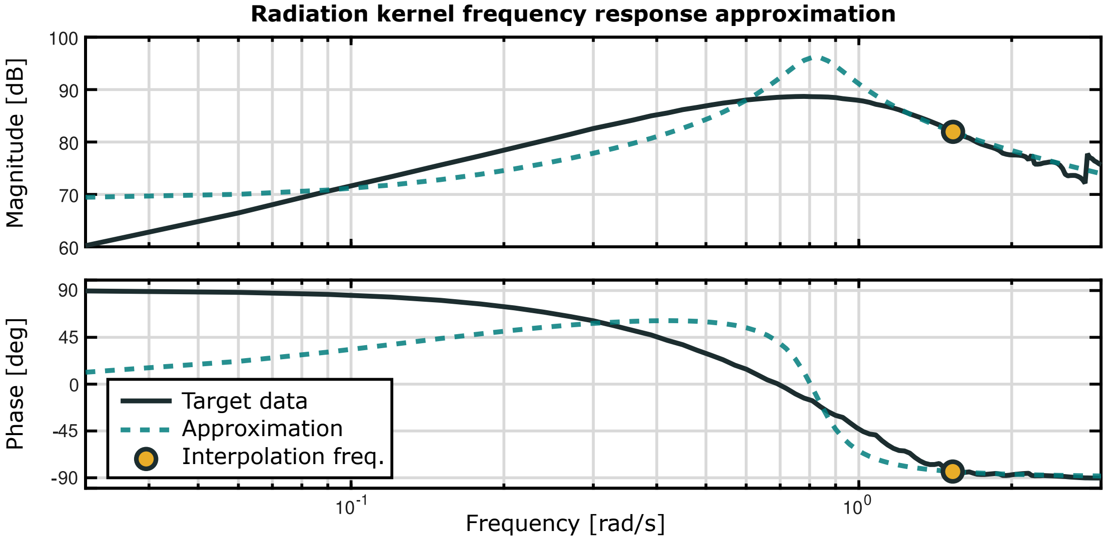

Figure A.8: Example of a suboptimal parametric model when using the automatic method (**Options.Method=1**) without specifying the most important frequency, and considering few initial conditions (for this example, **Options.Optim.InitCond=1**). MAPE≈0.38.

A.3.3 Increase the number of initial conditions

Since the initial conditions for the optimisation are chosen randomly using a normal distribution over a pre-selected set, it is more likely to find an accurate model if a high number of initial conditions is considered. Therefore, when trying to identify large order models, or when optimising the value of the interpolation frequencies (apart from the eigenvalues), using more initial conditions increases the chances of FOAMM to find the optimal model. For example, when using the optimised-automatic method, it may happen that, for some β^{MM}, the obtained error is higher than for a given smaller β^{MM} value. This can be fixed by increasing the number of initial conditions in **Options.Optim.InitCond**. As an example for this case, Figure A.9(a) shows the results obtained by the optimised-automatic method for the same case shown in Figure A.6, also shown in Figure A.9(b), but considering only a unique initial condition (**Options.Optim.InitCond=1**). It is shown how, apart from the obtained MAPE which is higher than in Figure A.9(b), when considering 3 frequencies the obtained MAPE is higher than the one obtained for $\beta^{\text{MM}} = 2$, which is due to the low number of initial conditions considered (a single one) in the example.

A.3.4 Use force-to-motion models

As can be observed from Figure A.5, force-to-motion frequency responses can be often approximated with a low order system. Additionally, as shown in Equation (2.41), two more states need to be added to the radiation impulse response approximated model, to obtain the complete WEC SS representation. Therefore, to characterise the

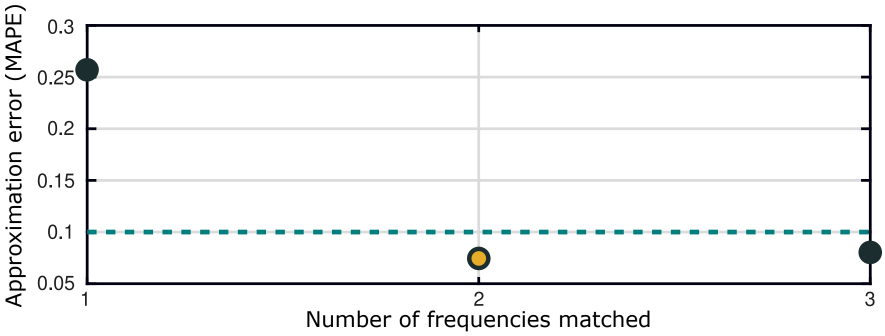

(a) Example of a possible error when using the optimised-automatic method (**Options.Method=2**) with few initial conditions (for this example, **Options.Optim.InitCond=1**).

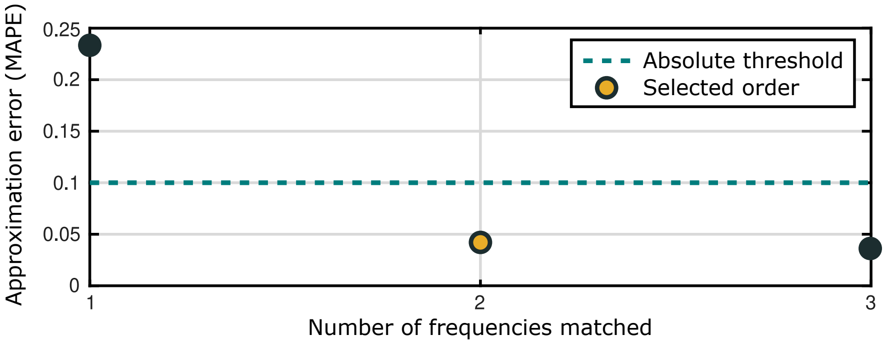

(b) Graph displayed while the optimised-automatic method (**Options.Method=2**) with the correct amount of initial conditions, also shown in Figure A.6.

Figure A.9: Example of a (a) possible error when using the optimised-automatic method with few initial conditions, along with (b) the same example using the correct amount of initial conditions.

input-output response of the WEC, the author recommends to directly parameterise the force-to-motion response of the target device.

Bibliography

[1] O. Abdelkhalik, S. Zou, G. Bacelli, R. D. Robinett, D. G. Wilson, and R. G. Coe. Estimation of excitation force on wave energy converters using pressure measurements for feedback control. In *Proceedings of the OCEANS 2016 MTS/IEEE, Monterey, USA*, pages 1–6, 2016.

[2] O. Abdelkhalik, S. Zou, R. Robinett, G. Bacelli, and D. Wilson. Estimation of excitation forces for wave energy converters control using pressure measurements. *International Journal of Control*, 90:1793–1805, 2017.

[3] M. Abdelrahman and R. Patton. Robust control of a wave energy converter with soft sensing of wave excitation force. In *Proceedings of the 12th European Wave and Tidal Energy Conference (EWTEC), Cork, Ireland*, pages 974–(1–10), 2017.

[4] M. Abdelrahman and R. Patton. Observer-based unknown input estimator of wave excitation force for a wave energy converter. *IEEE Transactions on Control Systems Technology (early access)*, 2019.

[5] M. Abdelrahman, R. Patton, B. Guo, and J. Lan. Estimation of wave excitation force for wave energy converters. In *Proceedings of the Conference on Control and Fault-Tolerant Systems (SysTol), Barcelona, Spain*, pages 654–659, 2016.

[6] H. Akaike. A new look at the statistical model identification. *IEEE Transactions on Automatic Control*, 19(6):716–723, 1974.

[7] N. Armaroli and V. Balzani. The future of energy supply: challenges and opportunities. *Angewandte Chemie International Edition*, 46(1-2):52–66, 2007.

[8] A. Astolfi. Model reduction by moment matching for linear and nonlinear systems. *IEEE Transactions on Automatic Control*, 55(10):2321–2336, 2010.

[9] C. Auger, A. Mérigaud, and J. V. Ringwood. Receding-horizon pseudo-spectral control of wave energy converters using periodic basis functions. *IEEE Transactions on Sustainable Energy*, 10(4):1644–1652, 2018.

[10] A. Babarit. *Ocean wave energy conversion: resource, technologies and performance*. Elsevier, 2017.

[11] A. Babarit, A. H. Clément, J. Ruer, and C. Tartivel. SEAREV: A fully integrated wave energy converter. In *Proceedings of the Offshore Wind and other marine renewable Energies in Mediterranean and European Seas (OWEMES), Rome, Italy*, pages 1–11, 2006.

[12] A. Babarit and G. Delhommeau. Theoretical and numerical aspects of the open source BEM solver NEMOH. In *Proceedings of the 11th European Wave and Tidal Energy Conference, Nantes, France*, pages 08C1–1–(1–12), 2015.

[13] G. Bacelli, P. Balitsky, and J. V. Ringwood. Coordinated control of arrays of wave energy devices — benefits over independent control. *IEEE Transactions on Sustainable Energy*, 4(4):1091–1099, 2013.

[14] G. Bacelli, R. G. Coe, D. Patterson, and D. Wilson. System identification of a heaving point absorber: Design of experiment and device modeling. *Energies*, 10:472, 2017.

[15] G. Bacelli and J. V. Ringwood. Numerical optimal control of wave energy converters. *IEEE Transactions on Sustainable Energy*, 6(2):294–302, 2014.

[16] M. R. Belmont, J. Christmas, J. Dannenberg, T. Hilmer, J. Duncan, J. M. Duncan, and B. Ferrier. An examination of the feasibility of linear deterministic sea wave prediction in multidirectional seas using wave profiling radar: Theory, simulation, and sea trials. *Journal of Atmospheric and Oceanic Technology*, 31(7):1601–1614, 2014.

[17] H. Bernhoff, E. Sjöstedt, and M. Leijon. Wave energy resources in sheltered sea areas: A case study of the baltic sea. *Renewable Energy*, 31(13):2164–2170, 2006.

[18] J. Blackledge, E. Coyle, D. Kearney, R. McGuirk, and B. Norton. Estimation of wave energy from wind velocity. *IAENG Engineering Letters*, 4:158–170, 2013.

[19] G. Bracco, E. Giorcelli, and G. Mattiazzo. ISWEC: A gyroscopic mechanism for wave power exploitation. *Mechanism and machine theory*, 46(10):1411–1424, 2011.

[20] C. L. Bretschneider. Wave variability and wave spectra for wind-generated gravity waves. Technical Report 118, Beach Erosion Board, US Army, Corps of Engineers, Washington D.C., 1959.

[21] J. Brewer. Kronecker products and matrix calculus in system theory. *IEEE Transactions on circuits and systems*, 25(9):772–781, 1978.

[22] P. E. Brockway, A. Owen, L. I. Brand-Correa, and L. Hardt. Estimation of global final-stage energy-return-on-investment for fossil fuels with comparison to renewable energy sources. *Nature Energy*, 4(7):612–621, 2019.

[23] P. J. Brockwell and R. A. Davis. *Introduction to Time Series and Forecasting*. springer, 2002.

[24] P. J. Brockwell, R. A. Davis, and S. E. Fienberg. *Time series: theory and methods*. Springer Science & Business Media, 1991.

[25] D. Cavaglieri, T. R. Bewley, and M. Previsic. Model Predictive Control leveraging Ensemble Kalman forecasting for optimal power take-off in wave energy conversion systems. In *Proceedings of the American Control Conference (ACC), Chicago, USA*, pages 5224–5230, 2015.

[26] C.-T. Chen. *Linear system theory and design*. Oxford University Press, Inc., 1998.

[27] H. Chen, Y. Du, and J. N. Jiang. Weather sensitive short-term load forecasting using knowledge-based ARX models. In *Proceedings of the IEEE Power Engineering Society General Meeting, San Francisco, USA*, pages 190–196. IEEE, 2005.

[28] Y. S. Chow and H. Teicher. *Probability theory: independence, interchangeability, martingales*. Springer Science & Business Media, 2003.

[29] R. Coe and G. Bacelli. State estimation for advanced control of wave energy converters. Technical report, Marine and Hydrokinetic Data Repository (MHKDR); Sandia National Laboratories, 2017.

[30] R. G. Coe, Y.-H. Yu, and J. Van Rij. A survey of WEC reliability, survival and design practices. *Energies*, 11(1):4, 2018.

[31] L. Cohen. The generalization of the Wiener-Khinchin theorem. In *Proceedings of the 1998 IEEE International Conference on Acoustics, Speech and Signal Processing, ICASSP'98 (Cat. No. 98CH36181)*, volume 3, pages 1577–1580. IEEE, 1998.

[32] J. L. Crassidis and J. L. Junkins. *Optimal estimation of dynamic systems*. Chapman and Hall/CRC, 2004.

[33] T. J. Crowley. Causes of climate change over the past 1000 years. *Science*, 289(5477):270–277, 2000.

[34] J. Cruz. *Ocean wave energy: current status and future prespectives*. Springer Science & Business Media, 2007.

[35] W. Cummins. The impulse response function and ship motion. Technical Report 9, Schiffstechnik, 1962.

[36] BV Datawell. *Datawell Waverider Installation Guide*, 2012. `http://www.datawell.nl/Portals/0/Documents/Manuals/datawell_manual_dwr4_2019-01-01.pdf` (last accessed on January 2020).

[37] G. De Prony. Essai éxperimental et analytique: sur les lois de la dilatabilité de fluides élastique et sur celles de la force expansive de la vapeur de l'alkool,a différentes températures. *Journal de l'école polytechnique*, 1(22):24–76, 1975.

[38] B. Drew, A. R. Plummer, and M. N. Sahinkaya. A review of wave energy converter technology. *Institution of Mechanical Engineers*, 223(JPE782):887–902, 2009.

[39] M. L. Eaton. *Multivariate statistics: A vector space approach*, volume 53. Institute of Mathematical Statistics, Beachwood, USA, 2007.

[40] O. Edenhofer, R. Pichs-Madruga, Y. Sokona, K. Seyboth, S. Kadner, T. Zwickel, P. Eickemeier, G. Hansen, S. Schlömer, and C. V. Stechow. *Renewable energy sources and climate change mitigation: Special report of the intergovernmental panel on climate change*. Cambridge University Press, 2011.

[41] C. Edwards and S. Spurgeon. *Sliding mode control: theory and applications*. Taylor and Francis Group, CRC Press, 1998.

[42] Mocean Energy. `https://www.corpowerocean.com/` (last accessed on August 2020).

[43] Mocean Energy. `https://www.mocean.energy/` (last accessed on August 2020).

[44] A. Etemad-Shahidi and J. Mahjoobi. Comparison between M5 model tree and neural networks for prediction of significant wave height in Lake Superior. *Ocean Engineering*, 36(15-16):1175–1181, 2009.

[45] N. Faedo, S. Olaya, and J. V. Ringwood. Optimal control, MPC and MPC-like algorithms for wave energy systems: An overview. *IFAC Journal of Systems and Control*, 1:37–56, 2017.

[46] N. Faedo, Y. Peña-Sanchez, G. Giorgi, and J. V. Ringwood. Moment-matching-based input-output parametric approximation for a multi-DoF WEC including hydrodynamic nonlinearities. In *Proceedings of the 13th European Wave and Tidal Energy Conference (EWTEC) Naples, Italy*, pages 1449–(1–10), 2019.

[47] N. Faedo, Y. Peña-Sanchez, and J. V. Ringwood. Finite-order hydrodynamic model determination for wave energy applications using moment-matching. *Ocean Engineering*, 163:251–263, 2018.

[48] N. Faedo, Y. Peña-Sanchez, and J. V. Ringwood. Passivity preserving moment-based finite-order hydrodynamic model identification for wave energy applications. In *Proceedings of the 3rd International Conference on Renewable Energies Offshore (RENEW), Lisbon, Portugal*, pages 351–359, 2019.

[49] N. Faedo, Y. Peña-Sanchez, and J. V. Ringwood. Parametric representation of arrays of wave energy converters for motion simulation and unknown input estimation: a moment-based approach. *Applied Ocean Research*, 98:102055, 2020.

[50] N. Faedo, Y. Peña-Sanchez, and J. V. Ringwood. Receding-horizon energy-maximising optimal control of wave energy systems based on moments. *IEEE Transactions on Sustainable Energies (early access)*, 2020.

[51] N. Faedo, G. Scarciotti, A. Astolfi, and J. V. Ringwood. Energy-maximising control of wave energy converters using a moment-domain representation. *Control Engineering Practice*, 81:85–96, 2018.

[52] N. Faedo, G. Scarciotti, A. Astolfi, and J. V. Ringwood. Moment-based constrained optimal control of an array of wave energy converters. In *Proceedings of the 2019 American Control Conference (ACC), Philadelphia, US*, pages 4797–4802. IEEE, 2019.

[53] A. F. de O. Falcão. Wave energy utilization: A review of the technologies. *Renewable and sustainable energy reviews*, 14(3):899–918, 2010.

[54] J. Falnes. On non-causal impulse response functions related to propagating water waves. *Applied Ocean Research*, 17:379–389, 1995.

[55] O. Faltinsen. *Sea loads on ships and offshore structures*, volume 1. Cambridge university press, 1993.

[56] A. Fernández Rodríguez, L. de Santiago Rodrigo, E. López Guillén, J. M. Rodríguez Ascariz, J. M. Jiménez, and L. Boquete. Coding prony's method in matlab and applying it to biomedical signal filtering. *BMC bioinformatics*, 19(1):1–14, 2018.

[57] F. Ferri, M. T. Sichani, and P. Frigaard. A case study of short-term wave forecasting based on FIR filter: Optimization of the power production for the Wavestar device. In *Proceedings of the 22nd International Offshore and Polar Engineering Conference (ISOPE), Rhodes, Greece*, pages 628–635. International Society of Offshore and Polar Engineers, 2012.

[58] J. Fiévez and T. Sawyer. Lessons learned from building and operating a grid connected wave energy plant. In *Proceedings of the 11th European Wave and Tidal Energy Conference (EWTEC), Nantes, France*, pages 08D1–4–(1–6), 2015.

[59] B. Fischer, P. Kracht, and S. Perez-Becker. Online-algorithm using adaptive filters for short-term wave prediction and its implementation. In *Proceedings of the 4th International Conference on Ocean Energy (ICOE), Dublin, Ireland*, pages 1–6, 2012.

[60] T. L. Floyd and E. Pownell. *Principles of electric circuits*. Prentice Hall, 1997.

[61] M. Folley. *Numerical modelling of wave energy converters: state-of-the-art techniques for single devices and arrays*. Academic Press, 2016.

[62] BEMIO Toolbox for Matlab. `https://wec-sim.github.io/WEC-Sim/index.html` (last accessed on january 2020).

[63] BEMIO Toolbox for Python. `https://wec-sim.github.io/bemio` (last accessed on january 2020).

[64] Ocean Energy Forum. Ocean energy strategic roadmap: building ocean energy for Europe, 2016. `https://webgate.ec.europa.eu/maritimeforum/sites/maritimeforum/files/OceanEnergyForum_Roadmap_Online_Version_08Nov2016.pdf` (last accessed on January 2020).

[65] T. I. Fossen and T. Perez. Marine Systems Simulator, `https://github.com/cybergalactic/MSS` (last accessed on August 2020).

[66] B. A. Francis and W. M. Wonham. The internal model principle of control theory. *Automatica*, 12(5):457–465, 1976.

[67] F. Fusco and J. V. Ringwood. Short-Term Wave Forecasting for Real-Time Control of Wave Energy Converters. *IEEE Transactions on Sustainable Energy*, 1(2):99–106, 2010.

[68] F. Fusco and J. V. Ringwood. Short-term wave forecasting with ar models in real-time optimal control of wave energy converters. In *Proceedings of the 2010 IEEE International Symposium on Industrial Electronics, Bari, Italy*, pages 2475–2480. IEEE, 2010.

[69] F. Fusco and J. V. Ringwood. A study of the prediction requirements in real-time control of wave energy converters. *IEEE Transactions on Sustainable Energy*, 3(1):176–184, 2011.

[70] F. Fusco and J. V. Ringwood. A simple and effective real-time controller for wave energy converters. *IEEE Transactions on sustainable energy*, 4(1):21–30, 2012.

[71] M. Garcia-Abril, F. Paparella, and J. V. Ringwood. Excitation force estimation and forecasting for wave energy applications. In *Proceedings of the IFAC World Congress, Toulouse, France*, pages 14692–14697, 2017.

[72] P. B. Garcia-Rosa, G. Bacelli, and J. V. Ringwood. Control-informed optimal array layout for wave farms. *IEEE Transactions on Sustainable Energy*, 6(2):575–582, 2015.

[73] A. Garcia-Teruel and D. Forehand. Optimal wave energy converter geometry for different modes of motion. In *Proceedings of the 3rd International Conference on Renewable Energies Offshore, Lisbon, Portugal*, pages 299–305, 2018.

[74] D. García Violini, Y. Peña-Sanchez, N. Faedo, C. Windt, and J. V. Ringwood. Experimental implementation and validation of a broadband LTI energy-maximising control strategy for the Wavestar device. *submitted to IEEE Transactions on Control Systems Technology*, 2020.

[75] D. García Violini, Y. Peña-Sanchez, N. Faedo, C. Windt, and J. V. Ringwood. LTI energy-maximising control for the Wave Star wave energy converter: identification, design, and implementation. In *Accepted for the 21st IFAC World Congress, Berlin, Germany*, 2020.

[76] M. Ge and E. C. Kerrigan. Short-term ocean wave forecasting using an autoregressive moving average model. In *Proceedings of the 2016 UKACC 11th International Conference on Control (CONTROL), Belfast, UK*, pages 1–6. IEEE, 2016.

[77] G. Giorgi, M. Penalba, and J. V. Ringwood. Nonlinear hydrodynamic models for heaving buoy wave energy converters. In *Proceedings of the 3rd Asian Wave and Tidal Energy Conference (AWTEC), Singapore*, pages 144–153, 2016.

[78] S. Giorgi, J. Davidson, and J. V. Ringwood. Identification of Nonlinear Excitation Force Kernels Using Numerical Wave Tank Experiments. In *Proceedings of the 11th European Wave and Tidal Energy Conference (EWTEC), Nantes, France*, pages 09C1–1–(1–10), 2015.

[79] A. R. Grilli, J. Merril, S. T. Grilli, and M. L. Spaulding. Experimental and numerical study of spar buoy-magnet/spring oscillators used as wave energy absorbers. In *Proceedings of the 17th International Offshore and Polar Engineering Conference, ISOPE, Lisbon, Portugal*, pages 489–496, 2007.

[80] Nortek Group. `https://www.nortekgroup.com/` (last accessed on january 2020).

[81] Seabased group. `https://www.seabased.com/` (last accessed on January 2020).

[82] K. Gunn and C. Stock-Williams. Quantifying the global wave power resource. *Renewable Energy*, 44:296–304, 2012.

[83] B. Guo, R. Patton, and S. Jin. Identification and Validation of Excitation Force for a Heaving Point Absorber Wave Energy Convertor. In *Proceedings of the 12th European Wave and Tidal Energy Conference (EWTEC), Cork, Ireland*, pages 956–(1–8), 2017.

[84] B. Guo, R. Patton, S. Jin, and J. Lan. Numerical and experimental studies of excitation force approximation for wave energy conversion. *Renewable Energy*, 125:877–889, 2018.

[85] J. R. Halliday, D. G. Dorrell, and A. Wood. A Fourier approach to short term wave prediction. In *Proceedings of the 16th International Offshore and Polar Engineering Conference (ISOPE), San Francisco, USA*, pages 444–451. International Society of Offshore and Polar Engineers, 2006.

[86] J. R. Halliday, D. G. Dorrell, and A. R. Wood. An application of the fast fourier transform to the short-term prediction of sea wave behaviour. *Renewable Energy*, 36(6):1685–1692, 2011.

[87] J. Hals. *Modelling and phase control of wave-energy converters*. PhD thesis, Norges teknisk-naturvitenskapelige universitet, 2010.

[88] K. Hasselmann, T. Barnett, E. Bouws, H. Carlson, D. Cartwright, K. Enke, J. Ewing, H. Gienapp, D. Hasselmann, P. Kruseman, A. Meerburg, P. Müller, D. Olbers, K. Richter, W. Sell, and H. Walden. Measurements of wind-wave growth and swell decay during the Joint North Sea Wave Project (JONSWAP). Technical Report A8 12, Ergänzungsheft zur Deutschen Hydrographischen Zeitschrift, 1973.

[89] R. Henderson. Design, simulation, and testing of a novel hydraulic power take-off system for the Pelamis wave energy converter. *Renewable energy*, 31(2):271–283, 2006.

[90] D. R. Herber and J. T. Allison. Approximating arbitrary impulse response functions with prony basis functions. Technical Report UIUC-ESDL-2019-01, University of Illinois at Urbana-Champaign, 2019.

[91] C. W. Hirt and B. D. Nichols. Volume of Fluid (VOF) Method for the Dynamics of Free Boundaries. *Journal of Computational Physics*, 39:201–225, 1981.

[92] ANSYS Inc. *AQWA v14.5 user manual*, 2012. `https://cyberships.files.wordpress.com/2014/01/wb_aqwa.pdf` (last accessed on January 2020).

[93] WAMIT Inc. *WAMIT v7.2 user manual*, 2016. `http://www.wamit.com/manualupdate/v72_manual.pdf` (last accessed on January 2020).

[94] Irish Marine Institute. `https://www.marine.ie` (last accessed on january 2020).

[95] N. G. Jacobsen, D. R. Fuhrmann, and J. Fredsø. A wave generation toolbox for the open-source CFD library: OpenFoam(R). *International Journal for Numerical Methods in Fluids*, 70:1073–1088, 2012.

[96] M.H. Kahn, M.S. Mackisack, M.R. Osborne, and G.K. Smyth. On the consistency of Prony's method and related algorithms. *Journal of Computational and Graphical Statistics*, 1(4):329–349, 1992.

[97] H. K. Khalil. *Nonlinear systems*. Prentice-Hall, New Jersey, 1996.

[98] J. P. Kofoed, P. Frigaard, E. Friis-Madsen, and H. C. Sørensen. Prototype testing of the wave energy converter Wave Dragon. *Renewable energy*, 31(2):181–189, 2006.

[99] I. Kollár, R. Pintelon, and J. Schoukens. Frequency domain system identification toolbox for matlab. *IFAC Proceedings Volumes*, 24(3):1243–1247, 1991.

[100] P. Kracht, S. Perez-Becker, J.-B. Richard, and B. Fischer. Performance improvement of a point absorber wave energy converter by application of an observer-based control: Results from wave tank testing. *IEEE Transactions on Industry Applications*, 51:3426–3434, 2015.

[101] G. Li and M. R. Belmont. Model predictive control of sea wave energy converters–Part I: A convex approach for the case of a single device. *Renewable Energy*, 69:453–463, 2014.

[102] L. Li, Y. Gao, and Z. Yuan. Real-time latching control of wave energy converter with consideration of wave force prediction. In *Proceedings of the 2018 OCEANS-MTS/IEEE Kobe Techno-Oceans (OTO), Piscataway, USA*, pages 1–6. IEEE, 2018.

[103] L. Li, Z. Gao, and Z.-M. Yuan. On the sensitivity and uncertainty of wave energy conversion with an artificial neural-network-based controller. *Ocean Engineering*, 183:282–293, 2019.

[104] L. Li, Z. Yuan, Y. Gao, and X. Zhang. Wave force prediction effect on the energy absorption of a wave energy converter with real-time control. *IEEE Transactions on Sustainable Energy*, 10(2):615–624, 2018.

[105] B. A. Ling. *Real-time Estimation and Prediction of Wave Excitation Forces for Wave Energy Control Applications*. PhD thesis, Oregon State University, 2015.

[106] B. A. Ling and B. A. Batten. Real time estimation and prediction of wave excitation forces on a heaving body. In *Proceedings of the ASME 2015 34th International Conference on Ocean, Offshore and Arctic Engineering (OMAE), Newfoundland, Canada*, pages 1–10. American Society of Mechanical Engineers, 2015.

[107] I. López, J. Andreu, S. Ceballos, I. Martínez de Alegría, and I. Kortabarria. Review of wave energy technologies and the necessary power-equipment. *Renewable and sustainable energy reviews*, 27:413–434, 2013.

[108] C. Maisondieu. WEC survivability threshold and extractable wave power. In *Proceedings of the 11th European Wave and Tidal Energy Conference (EWTEC), Nantes, France*, pages 07D4–2–(1–8), 2015.

[109] L. Marquis, M. Kramer, and P. Frigaard. First power production figures from the Wave Star roshage wave energy converter. In *Proceedings of the 3rd International Conference and Exhibition on Ocean Energy (ICOE), Bilbo, Basque Country*, pages 1–5, 2010.

[110] O. Masson. Développements du programme ACHIL3D. Technical Report UMR6598, Laboratoire de Mécanique des Fluides CNRS, Ecole Central de Nantes, 1998.

[111] E. Mehlum. Tapchan. In *Proceedings of the International Symposium on the Hydrodynamics of Ocean Wave-Energy Utilization, Lisbon, Portugal*, pages 51–55. Springer, 1986.

[112] M. Mekhiche and K. A. Edwards. Ocean power technologies Powerbuoy ®: System-level design, development and validation methodology. In *Proceedings of the 2nd Marine Energy Technology Symposium (METS), Seattle, USA*, pages 1–9, 2014.

[113] F. R. Menter. Two-Equation Eddy-Viscosity Turbulence Models for Engineering Applications. *American Institute of Aeronautics and Astronautics (AIAA) Journal*, 32(8):1598–1605, 1994.

[114] A. Mérigaud, V. Ramos, F. Paparella, and J. V. Ringwood. Ocean forecasting for wave energy production. *Journal of Marine Research*, 75(3):459–505, 2017.

[115] A. Mérigaud and J. V. Ringwood. Incorporating ocean wave spectrum information in short-term free-surface elevation forecasting. *IEEE Journal of Oceanic Engineering*, 44(2):401–414, 2018.

[116] S. Mhatre. Application of a linear optimal estimator on a wave energy converter using bang-singular-bang control. Master's thesis, Michigan Technological University, Michigan, USA, 2017.

[117] J. Moccia, A. Arapogianni, J. Wilkes, C. Kjaer, R. Gruet, S. Azau, and J. Scola. Pure power. Wind energy targets for 2020 and 2030, 2009. `http://www.ewea.org/fileadmin/ewea_documents/documents/publications/reports/Pure_Power_Full_Report.pdf` (last accessed on Jnauary 2020).

[118] G. Mork, S. Barstow, A. Kabuth, and M. T. Pontes. Assessing the global wave energy potential. In *Proceedings of the ASME 2010 29th International Conference on Ocean, Offshore and Arctic Engineering (OMAE), Sanghai, China*, pages 447–454. American Society of Mechanical Engineers Digital Collection, 2010.

[119] A. Mérigaud and J. V. Ringwood. Free-surface time-series generation for wave energy applications. *IEEE Journal of Oceanic Engineering*, 43(1):19–35, 2018.

[120] H.-N. Nguyen, G. Sabiron, P. Tona, M. M. Kramer, and E. Vidal Sanchez. Experimental validation of a nonlinear MPC strategy for a wave energy converter prototype. In *Proceedings of the ASME 2016 35th international conference on Ocean, Offshore and Arctic Engineering (OMAE), Busan, South Korea*, pages 1–10. American Society of Mechanical Engineers, 2016.

[121] H.-N. Nguyen and P. Tona. Wave excitation force estimation for wave energy converters of the point-absorber type. *IEEE Transactions on Control Systems Technology*, 26:2173–2181, 2017.

[122] R. Nie, J. Scruggs, A. Chertok, D. Clabby, M. Previsic, and A. Karthikeyan. Optimal causal control of wave energy converters in stochastic waves–accommodating nonlinear dynamic and loss models. *International Journal of Marine Energy*, 15:41–55, 2016.

[123] K. Nielsen, H. Bingham, and J. B. Thomsen. On the absorption of wave power using ship like structures. In *Proceedings of the 28th International Offshore and Polar Engineering Conference (ISOPE), Sapporo, Japan*, pages 719–727. International Society of Offshore and Polar Engineers, 2018.

[124] K. Northon. Long-term warming trend continued in 2017: NASA, NOAA, 2018. `https://www.nasa.gov/press-release/long-term-warming-trend-continued-in-2017-nasa-noaa` (last accessed on January 2020).

[125] M. K. Ochi. *Applied Probability and Stochastic Processes: In Engineering and Physical Sciences*. Wiley-Interscience, 1990.

[126] M. K. Ochi. *Ocean waves: The Stochastic Approach*, volume 6. Cambridge University Press, 2005.

[127] T. F. Ogilvie. Recent progress toward the understanding and prediction of ship motions. Technical Report 491, Office of Naval Research, 1966.

[128] A. V. Oppenheim. *Discrete-time signal processing*. Pearson Education India, 1999.

[129] A. Padoan, G. Scarciotti, and A. Astolfi. A geometric characterization of the persistence of excitation condition for the solutions of autonomous systems. *IEEE Transactions on Automatic Control*, 62(11):5666–5677, 2017.

[130] F. Paparella, K. Monk, V. Winands, M. F. P. Lopes, D. Conley, and J. V. Ringwood. Benefits of up-wave measurements in linear short-term wave forecasting for wave energy applications. In *Proceedings of the 2014 IEEE Conference on Control Applications (CCA), Antibes, France*, pages 2048–2053. IEEE, 2014.

[131] F. Paparella, K. Monk, V. Winands, M. F. P. Lopes, D. Conley, and J. V. Ringwood. Up-wave and autoregressive methods for short-term wave forecasting for an oscillating water column. *IEEE Transactions on Sustainable Energy*, 6(1):171–178, 2014.

[132] A. Papoulis and S. U. Pillai. *Probability, random variables, and stochastic processes*. Tata McGraw-Hill Education, 2002.

[133] S. Park, M.-S. Gil, H. Im, and Y.-S. Moon. Measurement noise recommendation for efficient Kalman filtering over a large amount of sensor data. *Sensors*, 19(5):1168–1187, 2019.

[134] Y. Peña-Sanchez, N. Faedo, M. Penalba, G. Giorgi, A. Mérigaud, C. Windt, D. García Violini, L. Wang, and J. V. Ringwood. Finite-Order hydrodynamic Approximation by Moment-Matching (FOAMM) toolbox for wave energy applications. In *Proceedings of the 13th European Wave and Tidal Energy Conference (EWTEC) Naples, Italy*, pages 1448–(1–9), 2019.

[135] Y. Peña-Sanchez, N. Faedo, and J. V. Ringwood. Hydrodynamic model fitting for wave energy applications using moment-matching: A case study. In *Proceedings of the 28th International Offshore and Polar Engineering Conference (ISOPE), Sapporo, Japan*, pages 641–648. International Society of Offshore and Polar Engineers, 2018.

[136] Y. Peña-Sanchez, N. Faedo, and J. V. Ringwood. A critical comparison between parametric approximation methods for radiation forces in wave energy systems. In *Proceedings of the 29th International Offshore and Polar Engineering Conference (ISOPE), Honolulu, Hawaii*, pages 174–181. International Society of Offshore and Polar Engineers, 2019.

[137] Y. Peña-Sanchez, N. Faedo, and J. V. Ringwood. Moment-based parametric identification of arrays of wave energy converters. In *Proceedings of the 2019 American Control Conference (ACC), Philadelphia, US*, pages 4785–4790. IEEE, 2019.

[138] Y. Peña-Sanchez, M. Garcia-Abril, F. Paparella, and J. V. Ringwood. Estimation and forecasting of excitation force for arrays of wave energy devices. *IEEE Transactions on Sustainable Energy*, 9:1672–1680, 2018.

[139] Y. Peña-Sanchez, A. Mérigaud, and J. V. Ringwood. Short-term forecasting of sea surface elevation for wave energy applications: The autoregressive model revisited. *IEEE Journal of Oceanic Engineering*, 45(2):462–471, 2018.

[140] Y. Peña-Sanchez and J. Ringwood. A critical comparison of AR and ARMA models for short-term wave forecasting. In *Proceedings of the 12th European Wave and Tidal Energy Conference (EWTEC), Cork, Ireland*, pages 961–(1–6), 2017.

[141] A. Pecher, J. P. Kofoed, J. Espedal, and S. Hagberg. Results of an experimental study of the Langlee wave energy converter. In *Proceedings of the 20th International Offshore and Polar Engineering Conference (ISOPE), Beijing, China*, pages 877–885. International Society of Offshore and Polar Engineers, 2010.

[142] M. Penalba, J. Davidson, C. Windt, and J. V. Ringwood. A high-fidelity wave-to-wire simulation platform for wave energy converters: Coupled numerical wave tank and power take-off models. *Applied Energy*, 226:655–669, 2019.

[143] M. Penalba, T. Kelly, and J. Ringwood. Using NEMOH for modelling wave energy convertes: A comparative study with WAMIT. In *Proceedings of the 12th European Wave and Tidal Energy Conference (EWTEC), Cork, Ireland*, pages 931–(1–10), 2017.

[144] M. Penalba and J. V. Ringwood. Linearisation-based nonlinearity measures for wave-to-wire models in wave energy. *Ocean Engineering*, 171:496–504, 2019.

[145] M. Penalba, I. Touzón, J. Lopez-Mendia, and V. Nava. A numerical study on the hydrodynamic impact of device slenderness and array size in wave energy farms in realistic wave climates. *Ocean Engineering*, 142:224–232, 2017.

[146] M. Penalba, A. Ulazia, G. Ibarra-Berastegui, J. V. Ringwood, and J. Sáenz. Wave energy resource variation off the west coast of Ireland and its impact on realistic wave energy converters' power absorption. *Applied energy*, 224:205–219, 2018.

[147] D. B. Percival and A. T. Walden. *Spectral Analysis for Physical Applications*. Cambridge University Press, 1993.

[148] T. Pérez and T. I. Fossen. Time-vs. frequency-domain identification of parametric radiation force models for marine structures at zero speed. *Modeling, Identification and Control*, 29(1):1–19, 2008.

[149] T. Perez and T. I. Fossen. A matlab toolbox for parametric identification of radiation-force models of ships and offshore structures. *Modeling, Identification and Control*, 30(1):1, 2009.

[150] J. L. Phillips. The triangular decomposition of hankel matrices. *Mathematics of Computation*, 25(115):559–602, 1971.

[151] W. J. Pierson Jr. and L. Moskowitz. A proposed spectral form for fully developed wind seas based on the similarity theory of SA Kitaigorodskii. *Journal of Geophysical Research*, 69(24):5181–5190, 1964.

[152] J. Portilla, J. Sosa, and L. Cavaleri. Wave energy resources: Wave climate and exploitation. *Renewable Energy*, 57:594–605, 2013.

[153] G. Reikard, P. Pinson, and J.-R. Bidlot. Forecasting ocean wave energy: The ECMWF wave model and time series methods. *Ocean Engineering*, 38(10):1089 – 1099, 2011.

[154] REN21. Renewables 2017: global status report. `http://www.ren21.net/gsr-2017/` (last accessed on January 2020).

[155] J. V. Ringwood, G. Bacelli, and F. Fusco. Energy-maximizing control of wave-energy converters: The development of control system technology to optimize their operation. *IEEE Control Systems*, 34:30–55, 2014.

[156] J. V. Ringwood, F. Ferri, K. Ruehl, Y. H. Yu, R. G. Coe, G. Bacelli, J. Weber, and M. M. Kramer. A competition for WEC control systems. In *Proceedings of the 12th European Wave and Tidal Energy Conference (EWTEC), Cork, Ireland*, pages 831–(1–9), 2017.

[157] H. Ritchie and M. Roser. Energy, our world in data, 2020. `https://ourworldindata.org/energy` (last accessed on January 2020).

[158] D. Ross. *Power from the Waves*. Oxford University Press, USA, 1995.

[159] K. Ruehl and D. Bull. Wave energy development roadmap: design to commercialization. In *Proceedings of the OCEANS'12 MTS/IEEE conference, Hampton Roads, VA, USA*, pages 1–10. IEEE, 2012.

[160] K. Sayood. *Introduction to Data Compression*. Morgan Kaufmann, 1996.

[161] G. Scarciotti and A. Astolfi. Model reduction by matching the steady-state response of explicit signal generators. *IEEE Transactions on Automatic Control*, 61(7):1995–2000, 2016.

[162] M. P. Schoen, J. Hals, and T. Moan. Wave prediction and robust control of heaving wave energy devices for irregular waves. *IEEE Transactions on energy conversion*, 26(2):627–638, 2011.

[163] P. D. Sclavounos and Y. Ma. Wave energy conversion using machine learning forecasts and model predictive control. In *Proceedings of the 33rd international workshop on water waves and floating bodies, Brest, France*, pages 1–4, 2018.

[164] J. T. Scruggs, S. M. Lattanzio, A. A. Taflanidis, and I. L. Cassidy. Optimal causal control of a wave energy converter in a random sea. *Applied Ocean Research*, 42:1–15, 2013.

[165] S. Shi, M. Abdelrahman, and R. Patton. Wave excitation force estimation and forecasting for WEC power conversion maximisation. In *Proceedings of the 2019 IEEE/ASME International Conference on Advanced Intelligent Mechatronics (AIM), Hong Kong, China*, pages 526–531. IEEE, 2019.

[166] S. Shi, R. Patton, and Y. Liu. Short-term wave forecasting using Gaussian process for optimal control of wave energy converters. *IFAC-PapersOnLine*, 51(29):44–49, 2018.

[167] R. Taghipour, T. Perez, and T. Moan. Hybrid frequency–time domain models for dynamic response analysis of marine structures. *Ocean Engineering*, 35(7):685–705, 2008.

[168] K. Tanizawa. The state of the art on numerical wave tank. In *Proceedings of the 4th Osaka Colloquium on Seakeeping Performance of Ships, Osaka, Japan*, pages 95–114, 2000.

[169] J. Tedd and P. Frigaard. Short term wave forecasting, using digital filters, for improved control of wave energy converters. In *Proceedings of the 7th International Offshore and Polar Engineering Conference (ISOPE), Lisbon, Portugal*, pages 388–394. International Society of Offshore and Polar Engineers, 2007.

[170] J. H. Todalshaug, G. S. Ásgeirsson, E. Hjálmarsson, J. Maillet, P. Möller, P. Pires, M. Guérinel, and M. Lopes. Tank testing of an inherently phase-controlled wave energy converter. *International Journal of Marine Energy*, 15:68–84, 2016.

[171] N. Tom, M. Lawson, and Y.-H. Yu. Demonstration of the recent additions in modelling capabilities for the WEC-Sim wave energy converter design tool. In *Proceedings of the 34th International Conference on Ocean, Offshore and Arctic Engineering (OMAE) Newfoundland, Canada*, pages 1–11. American Society of Mechanical Engineers, 2015.

[172] FDI Toolbox. `https://github.com/cybergalactic/MSS/tree/master/FDI` (last accessed on August 2020).

[173] FOAMM Toolbox. `http://www.eeng.nuim.ie/coer/downloads/` (last accessed on january 2020).

[174] Y. Torre-Enciso, I. Ortubia, L. I. López de Aguileta, and J. Marqués. Mutriku wave power plant: from the thinking out to the reality. In *Proceedings of the 8th European Wave and Tidal Energy Conference, Uppsala, Sweden*, volume 710, pages 319–329, 2009.

[175] A. Ulazia, M. Penalba, G. Ibarra-Berastegui, J. V. Ringwood, and J. Saénz. Wave energy trends over the bay of Biscay and the consequences for wave energy converters. *Energy*, 141:624–634, 2017.

[176] J. Umeda, H. Goto, T. Fujiwara, T. Taniguchi, and S. Inoue. Experimental study on model predictive control for a point absorber type wave energy converter with a linear generator. In *Proceedings of the ASME 2018 37th International Conference on Ocean, Offshore and Arctic Engineering (OMAE), Madrid, Spain*, pages 1–10. American Society of Mechanical Engineers, 2018.

[177] D. Valério, P. Beirão, and J. S. da Costa. Optimisation of wave energy extraction with the archimedes wave swing. *Ocean Engineering*, 34(17-18):2330–2344, 2007.

[178] M. Vaziri. Predicting Caspian sea surface water level by ANN and ARIMA models. *Journal of Waterway, Port, Coastal, and Ocean Engineering*, 123(4):158–162, 1997.

[179] V. Voronovich, B. Holmes, and G. Thomas. A preliminary numerical and experimental study of wave prediction. In *Proceedings of the 6th European Wave and Tidal Energy Conference (EWTEC), Glasgow, UK*, pages 1–9. International Society of Offshore and Polar Engineers, 2005.

[180] L. Wang and J. V. Ringwood. Geometric optimisation of a hinge-barge wave energy device. In *Proceedings of the 13th European Wave and Tidal Energy Conference (EWTEC) Naples, Italy*, pages 1389–(1–10), 2019.

[181] J. Weber. WEC technology readiness and performance matrix–finding the best research technology development trajectory. In *Proceedings of the 4th International Conference on Ocean Energy (ICOE), Dublin, Ireland*, volume 17, 2012.

[182] H. G. Weller, G. Tabor, H. Jasak, and C. Fureby. A tensorial approach to computational continuum mechanics using object-oriented techniques. *Computers in Physic*, 12:620 – 631, 1998.

[183] T. Whittaker, D. Collier, M. Folley, M. Osterried, A. Henry, and M. Crowley. The development of Oyster—a shallow water surging wave energy converter. In *Proceedings of the 7th European Wave and Tidal Energy Conference (EWTEC), Porto, Portugal*, pages 1–6, 2007.

[184] C. Windt, J. Davidson, and J. V. Ringwood. High-fidelity numerical modelling of ocean wave energy systems: A review of CFD-based numerical wave tanks. *Renewable and Sustainable Energy Reviews*, 93:610–630, 2018.

[185] C. Windt, J. Davidson, and J. V. Ringwood. High-fidelity numerical modelling of ocean wave energy systems: A review of computational fluid dynamics-based numerical wave tanks. *Renewable and Sustainable Energy Reviews*, 93:610–630, 2018.

[186] C. Windt, N. Faedo, M. Penalba, and J. V. Ringwood. Evaluation of energy maximising control systems for the Wavestar wave energy converter. In *Proceedings of the 2019 American Control Conference (ACC), Philadelphia, US*, pages 4791–4796. IEEE, 2019.

[187] S. Z. Yong, M. Zhu, and E. Frazzoli. A unified filter for simultaneous input and state estimation of linear discrete-time stochastic systems. *Automatica*, 63:321–329, 2016.

[188] N.-J. Young. The singular-value decomposition of an infinite Hankel matrix. *Linear Algebra and Its Applications*, 50:639–656, 1983.

[189] Y.-H. Yu, M. Lawson, K. Ruehl, and C. Michelen. Development and demonstration of the WEC-Sim wave energy converter simulation tool. In *Proceedings of the 2nd Marine Energy Technology Symposium, METS, Seattle, WA, USA*, pages 1–8, 2014.

[190] Y. Zhang, G. Li, and T. Zeng. Wave excitation force estimation for wave energy converters using adaptive sliding mode observer. In *Proceedings of the 2019 American Control Conference (ACC), Philadelphia, US*, pages 4803–4808. IEEE, 2019.

[191] Y. Zhang, T. Zeng, and G. Li. Robust excitation force estimation and prediction for wave energy converter M4 based on adaptive sliding-mode observer. *IEEE Transactions on Industrial Informatics*, 16(2):1163–1171, 2019.

[192] Q. Zhong and R. W. Yeung. Model-predictive control strategy for an array of wave-energy converters. *Journal of Marine Science and Application*, 18(1):26–37, 2019.

[193] S. Zou and O. Abdelkhalik. Consensus estimation in arrays of wave energy converters. *IEEE Transactions on Sustainable Energy*, 10(2):943–951, 2018.